BOUNDARY-LAYER FLOWS WITH SHORT-SCALE SPANWISE DISTURBANCES

A thesis submitted to the University of Manchester
for the degree of Doctor of Philosophy
in the Faculty of Science and Engineering

2018

Anthony James Williams
School of Mathematics

Contents

Word count 64832

List of Tables

List of Figures

The University of Manchester

Anthony James Williams
Doctor of Philosophy
Boundary-layer flows with short-scale spanwise disturbances
December 21, 2018

This work considers the three-dimensional laminar boundary layer on a semi-infinite plate aligned with a uniform oncoming stream or driven by a favourable pressure gradient of power-law type. The three dimensionality is induced by a wall injection that exists over a finite spanwise scale that is comparable to the boundary-layer thickness. These short-scale disturbances require the inclusion of spanwise and transverse diffusion in the boundary layer. As the spanwise extent of the disturbances maintains a constant ratio with the boundary-layer thickness a self-similar formulation is used. This self-similar formulation is later extended to allow for downstream variation in the injection profile.

In the absence of a pressure gradient, classical two-dimensional theory predicts separation when an injection into the boundary layer is of sufficient strength; injection over short spanwise scales leads to qualitatively different flow responses where no separation occurs. The flow exists in one of three distinct regimes depending upon the magnitude of the surface injection rate. These regimes take the form of low-speed streaks where the amplitude and spanwise width of the injection determines the geometry of the streaks. An asymptotic description in the limit of a large injection slot width and a fixed injection velocity is presented, this provides information on critical injection rates which distinguish the three regimes.

Applying a favourable pressure gradient reduces the extent of the streaks and removes the delineation between the three flow regimes. For sufficiently strong pressure gradients the Falkner–Skan solution is recovered throughout the domain, albeit with an injection boundary condition in the slot region. Near the centreline of the injection slot the asymptotic description does not agree with the full numerical calculations due to the presence of spatially unstable eigenmodes. These local spatial (cross-flow) eigenmodes are associated with a cross-flow collisional process at the centre of the injection slot.

The stability of the streak flow to a travelling wave disturbance is considered, both in terms of the fixed Reynolds number viscous stability and the inviscid limit. The inviscid analysis produces a two-dimensional analogue of the Rayleigh stability equation which forms a critical layer where the streak velocity is equal to the wave speed. The inviscid equations are well approximated by a two-dimensional analogue of the Orr-Sommerfeld equation when the Reynolds number is sufficiently large. The stability of the streak flow at various injection rates, pressure gradients, wavenumbers and Reynolds numbers is examined.

Declaration

No portion of the work referred to in the thesis has been submitted in support of an application for another degree or qualification of this or any other university or other institute of learning.

Copyright Statement

i. The author of this thesis (including any appendices and/or schedules to this thesis) owns certain copyright or related rights in it (the "Copyright") and s/he has given The University of Manchester certain rights to use such Copyright, including for administrative purposes.

ii. Copies of this thesis, either in full or in extracts and whether in hard or electronic copy, may be made **only** in accordance with the Copyright, Designs and Patents Act 1988 (as amended) and regulations issued under it or, where appropriate, in accordance with licensing agreements which the University has from time to time. This page must form part of any such copies made.

iii. The ownership of certain Copyright, patents, designs, trade marks and other intellectual property (the "Intellectual Property") and any reproductions of copyright works in the thesis, for example graphs and tables ("Reproductions"), which may be described in this thesis, may not be owned by the author and may be owned by third parties. Such Intellectual Property and Reproductions cannot and must not be made available for use without the prior written permission of the owner(s) of the relevant Intellectual Property and/or Reproductions.

iv. Further information on the conditions under which disclosure, publication and commercialisation of this thesis, the Copyright and any Intellectual Property and/or Reproductions described in it may take place is available in the University IP Policy (see http://documents.manchester.ac.uk/DocuInfo.aspx?DocID=487), in any relevant Thesis restriction declarations deposited in the University Library, The University Library's regulations (see http://www.manchester.ac.uk/library/aboutus/regulations) and in The University's Policy on Presentation of Theses.

Acknowledgements

First and foremost I would like to thank my supervisor Prof. Richard Hewitt for his guidance, support and insight. His incomparable knowledge and patience have helped me to learn and develop much more than would have been possible on my own. I would also like to thank my fiancée Rachel, my mother Gillian, my father Stephen, and my sister Lucy for their continued understanding, encouragement and kindness.

Chapter 1

Introduction

This thesis examines the effects of a localised short-scale spanwise injection into a fully three-dimensional boundary layer. Flows both with and without an applied freestream pressure gradient are considered. This work aims to expand upon previous work on three-dimensional boundary layers with a spanwise variation, that is comparable to the boundary-layer thickness, by analysing the 'boundary-region equations' first introduced by Kemp (1951) [45].

Firstly a general formulation will be given for a laminar incompressible boundary-layer flow adjacent to a flat plate, with a short-scale spanwise topography and/or injection. This more general formulation will allow the work to be extended in the future. By seeking solutions that are self-similar in the streamwise direction and determining the correct far-field boundary conditions the problem will be formulated in a computationally efficient manner. Chapter 2 continues by investigating the case of a short-scale injection into the boundary layer in the absence of an applied pressure gradient. A combination of numerical computation and asymptotic analysis provides a demonstration of the impact of different rates of injection; this gives an opportunity to explain the physical mechanisms involved. In chapter 3 the injection problem is extended to include the effects of an applied favourable pressure gradient allowing for a direct comparison with the solutions found in the zero pressure gradient case. Chapter 4 aims to expand upon the self-similar formulation presented in chapters 2 and 3 by allowing a general downstream variation. The fully-three dimensional formulation created allows different injection geometries to be analysed. The stability of the self-similar short-scale injection flow is examined in chapter 5. By disturbing

the self-similar flow with a travelling wave perturbation the stability of the flow is determined for a particular set of flow parameters.

1.1 General introduction

Until the 19th century the study of fluid mechanics mainly focused on so called ideal fluids which are incompressible and inviscid. The study of inviscid fluids leads to a set of hyperbolic partial differential equations, called the Euler equations, which describe the spatial and temporal development of the velocity field using the principles of conservation of mass and momentum. The inability of the Euler equations to predict certain phenomena motivated the study of viscous fluid dynamics. One of the main motivations for studying viscous flows is d'Alembert's paradox which predicts that a body moving with a constant velocity in an ideal fluid will experience zero drag [52]. This clearly contradicts physical observations of drag acting on bodies moving relative to fluids. In order to predict the drag forces acting on a body in relative motion to a fluid it is necessary to include the effects of viscosity.

Nondimensionalisation of the equations governing viscous fluid flow produces the dimensionless parameter Re, which is the Reynolds number. The Reynolds number quantifies the relative importance of inertial and viscous forces for given flow conditions and is useful, amongst other things, for predicting the transition between laminar and turbulent flow. The transition to turbulence, of a laminar flow, as the Reynolds number increases past some critical value can, in some cases, be described with the aid of a stability analysis [17]. Since many of the fluids considered in physical problems have very low viscosity it is beneficial to investigate the asymptotic behaviour of the governing equations for large Reynolds number. The limit $Re \to \infty$ corresponds to the flow of an ideal fluid with zero viscosity [59].

The concept of the boundary layer, first described by Ludwig Prandtl in 1904 [53], simplifies the equations governing viscous fluid flow. The flow over a body can be split into two regions: a thin boundary layer close to the surface, where viscous forces are important, and an inviscid flow outside the boundary layer where these forces are insignificant. The outer inviscid flow creates the boundary conditions at the upper edge of the boundary layer and therefore significantly impacts the velocity profile within the

layer. In contrast the boundary layer is so small that it is, at leading order, invisible to the outer flow. As such the boundary layer has no leading order effect on the inviscid flow provided that there is no flow separation. The equations governing the inviscid outer flow and the boundary layer are derived from the Navier-Stokes equations that describe the motion of viscous fluids.

The Navier-Stokes equations describe the motion of a fluid in $\mathbb{R}^n$ ($n = 2$ or 3). These equations are solved for an unknown velocity vector $\mathbf{u}(\mathbf{x}, t) \in \mathbb{R}^n$ and pressure $p(\mathbf{x}, t) \in \mathbb{R}$ as functions of position $\mathbf{x} \in \mathbb{R}^n$ and time $t \geq 0$. This thesis will mainly focus on steady incompressible fluids without body forces, in this case the Navier-Stokes equations are taken to be

$$\nabla \cdot \mathbf{u} = 0, \tag{1.1.1a}$$

$$(\mathbf{u} \cdot \nabla)\,\mathbf{u} = -\frac{1}{\rho}\nabla p + \nu \nabla^2 \mathbf{u}, \tag{1.1.1b}$$

with $\mathbf{u} = \mathbf{u}(\mathbf{x})$. Here ν is the kinematic viscosity of the fluid at a point and ρ is the density of the fluid, where both ν and ρ are taken to be constant in this work. The equations (1.1.1) are easily modified to include time dependency which is essential when conducting a stability analysis.

The dimensional Navier-Stokes equations may be written in index notation, using the summation convention, as

$$\frac{\partial u_i}{\partial x_i} = 0, \tag{1.1.2a}$$

$$u_j \frac{\partial u_i}{\partial x_j} = -\frac{1}{\rho}\frac{\partial p}{\partial x_i} + \nu \frac{\partial^2 u_i}{\partial x_j \partial x_j}. \tag{1.1.2b}$$

Now suppose that the spatial coordinates are rescaled such that $x_i = L\hat{x}_i$ where L is a characteristic length scale. The velocity components and the pressure are also rescaled such that $u_i = U_\infty \hat{u}_i$ and $p = \rho U_\infty^2 \hat{p}$ where U_∞ is the free-stream velocity, then it follows that

$$\frac{U_\infty}{L}\frac{\partial \hat{u}_i}{\partial \hat{x}_i} = 0, \tag{1.1.3a}$$

$$\frac{U_\infty^2}{L}\hat{u}_j \frac{\partial \hat{u}_i}{\partial \hat{x}_j} = -\frac{\rho U_\infty^2}{\rho L}\frac{\partial \hat{p}}{\partial \hat{x}_i} + \frac{\nu U_\infty}{L^2}\frac{\partial^2 \hat{u}_i}{\partial \hat{x}_j \partial \hat{x}_j}. \tag{1.1.3b}$$

Defining the Reynolds number for the flow $Re = U_\infty L/\nu$ and dividing through gives

$$\frac{\partial \hat{u}_i}{\partial \hat{x}_i} = 0, \tag{1.1.4a}$$

$$\hat{u}_j \frac{\partial \hat{u}_i}{\partial \hat{x}_j} = -\frac{\partial \hat{p}}{\partial \hat{x}_i} + \frac{1}{Re} \frac{\partial^2 \hat{u}_i}{\partial \hat{x}_j \partial \hat{x}_j}. \tag{1.1.4b}$$

These are the non-dimensional Navier-Stokes equations governing the steady flow of an incompressible fluid. The boundary layer approximation is achieved by performing an asymptotic expansion of the Navier-Stokes equations in the limit $Re \to \infty$.

Asymptotic expansion of the Navier-Stokes equations

In order to obtain asymptotic expansions for the solutions of the Navier-Stokes equations for large Reynolds numbers the singular perturbation problem

$$\frac{\partial \hat{u}_i}{\partial \hat{x}_i} = 0, \tag{1.1.5a}$$

$$\hat{u}_j \frac{\partial \hat{u}_i}{\partial \hat{x}_j} = -\frac{\partial \hat{p}}{\partial \hat{x}_i} + \epsilon^2 \frac{\partial^2 \hat{u}_i}{\partial \hat{x}_j \partial \hat{x}_j}, \tag{1.1.5b}$$

is proposed where $\epsilon = Re^{-1/2}$ is the perturbation parameter. The asymptotic expansion will be split into an outer and inner expansion which must be matched in the overlapping region. The outer expansion will govern the inviscid flow, away from the boundary, and the inner expansion will govern the thin region next to the boundary in which there is a large change in the velocity; this is the 'boundary-layer' [73].

For simplicity consider the two-dimensional Cartesian coordinates $\hat{x}_i = (x, y)$ and the velocity components $\hat{u}_i = (u, v)$. The following asymptotic expansions for the solutions of the Navier-Stokes equations in the outer flow are used:

$$\begin{aligned} u(x,y) &= U_0(x,y) + \epsilon U_1(x,y) + \epsilon^2 U_2(x,y) + \ldots, \\ v(x,y) &= V_0(x,y) + \epsilon V_1(x,y) + \epsilon^2 V_2(x,y) + \ldots, \\ p(x,y) &= P_0(x,y) + \epsilon P_1(x,y) + \epsilon^2 P_2(x,y) + \ldots. \end{aligned} \tag{1.1.6}$$

Substituting into the governing equations (1.1.5) it is found that to leading order

$$\frac{\partial U_0}{\partial x} + \frac{\partial V_0}{\partial y} = 0, \tag{1.1.7a}$$

$$U_0 \frac{\partial U_0}{\partial x} + V_0 \frac{\partial U_0}{\partial y} = -\frac{\partial P_0}{\partial x}, \tag{1.1.7b}$$

$$U_0 \frac{\partial V_0}{\partial x} + V_0 \frac{\partial V_0}{\partial y} = -\frac{\partial P_0}{\partial y}. \tag{1.1.7c}$$

Being a singular perturbation problem the Euler equations (1.1.7) for the outer flow are not valid close to the boundary. A different solution is required in the thin region next to the boundary.

The solution close to the boundary wall requires an alternative approach, so it is necessary to introduce the stretched coordinate $Y = y/\epsilon$ and the asymptotic expansions of Prandtl [53]

$$\begin{aligned} u(x,y) &= u_0(x,Y) + \epsilon u_1(x,Y) + \epsilon^2 u_2(x,Y) + \dots, \\ v(x,y) &= \epsilon v_0(x,Y) + \epsilon^2 v_1(x,Y) + \epsilon^3 v_2(x,Y) + \dots, \\ p(x,y) &= p_0(x,Y) + \epsilon p_1(x,Y) + \epsilon^2 p_2(x,Y) + \dots. \end{aligned} \tag{1.1.8}$$

Rescaling the governing equations (1.1.5) using the stretched coordinate Y gives

$$\epsilon\frac{\partial u}{\partial x} + \frac{\partial v}{\partial Y} = 0, \tag{1.1.9a}$$

$$\epsilon u\frac{\partial u}{\partial x} + v\frac{\partial u}{\partial Y} = -\epsilon\frac{\partial p}{\partial x} + \epsilon^3\frac{\partial^2 u}{\partial x^2} + \epsilon\frac{\partial^2 u}{\partial Y^2}, \tag{1.1.9b}$$

$$\epsilon u\frac{\partial v}{\partial x} + v\frac{\partial v}{\partial Y} = -\frac{\partial p}{\partial Y} + \epsilon^3\frac{\partial^2 v}{\partial x^2} + \epsilon\frac{\partial^2 v}{\partial Y^2}. \tag{1.1.9c}$$

Then substituting the asymptotic expansions (1.1.8) into the rescaled equations (1.1.9) it is found that the leading-order pressure is determined by

$$\frac{\partial p_0}{\partial Y} = 0, \tag{1.1.10}$$

which implies that $p_0 = p_0(x)$. The leading-order continuity and streamwise momentum equations, along with the second order pressure, are found at $O(\epsilon)$ to be

$$\frac{\partial u_0}{\partial x} + \frac{\partial v_0}{\partial Y} = 0, \tag{1.1.11}$$

$$u_0\frac{\partial u_0}{\partial x} + v_0\frac{\partial u_0}{\partial Y} = -p_0'(x) + \frac{\partial^2 u_0}{\partial Y^2}, \tag{1.1.12}$$

$$\frac{\partial p_1}{\partial Y} = 0, \tag{1.1.13}$$

this means that $p_1 = p_1(x)$. Finally the expansion gives the leading-order transverse momentum equation along with the second order continuity and streamwise momentum equations as

$$\frac{\partial u_1}{\partial x} + \frac{\partial v_1}{\partial Y} = 0, \tag{1.1.14}$$

$$u_0\frac{\partial u_1}{\partial x} + u_1\frac{\partial u_0}{\partial x} + v_0\frac{\partial u_1}{\partial Y} + v_1\frac{\partial u_0}{\partial Y} = -p_1'(x) + \frac{\partial^2 u_1}{\partial Y^2}, \tag{1.1.15}$$

$$u_0\frac{\partial v_0}{\partial x} + v_0\frac{\partial v_0}{\partial Y} = -\frac{\partial p_2}{\partial Y} + \frac{\partial^2 v_0}{\partial Y^2}. \tag{1.1.16}$$

So governing the leading order terms in the boundary layer are the equations

$$\frac{\partial u_0}{\partial x} + \frac{\partial v_0}{\partial Y} = 0, \tag{1.1.17a}$$

$$u_0\frac{\partial u_0}{\partial x} + v_0\frac{\partial u_0}{\partial Y} = -p_0'(x) + \frac{\partial^2 u_0}{\partial Y^2}, \tag{1.1.17b}$$

$$u_0\frac{\partial v_0}{\partial x} + v_0\frac{\partial v_0}{\partial Y} = -\frac{\partial p_2}{\partial Y} + \frac{\partial^2 v_0}{\partial Y^2}. \tag{1.1.17c}$$

It is worth noting that p_1 has no impact on the leading-order boundary-layer equations (1.1.17). In two-dimensional boundary layers, as described here, the transverse momentum equation (1.1.17c) becomes an equation for p_2 which is decoupled from the rest of the equations however, as shall be discussed later, in the three-dimensional case this is not so and role of the p_2 term is more complicated.

The equations governing the outer inviscid flow (1.1.7) and the inner boundary-layer flow (1.1.17) determine the leading-order behaviour in this asymptotic expansion. In principle this process could be continued and the equations governing the terms at subsequent orders could be determined. For large Reynolds numbers however there is already sufficient accuracy to gain an understanding of the flow characteristics without including higher order corrections. The utility of the boundary-layer equations (1.1.17) shall be demonstrated by examining the boundary layer on a semi-infinite flat plate.

1.1.1 Flat plate boundary layers

As it will be of some utility later it is necessary that the standard theory of two-dimensional flat plate boundary layers be explored. Later consideration is given to a class of flows of the Falkner-Skan type, of which the Blasius boundary layer is a specific case. These Falkner-Skan and Blasius flows will provide the two-dimensional far-field behaviour for the more general three-dimensional boundary-layer flows with short-scale spanwise disturbances.

A Blasius boundary layer is formed on a semi-infinite flat plate which is held parallel to a constant unidirectional flow, see figure 1.1.1. The two-dimensional laminar boundary layer which is formed is indicative of the effect of including the viscosity of the fluid close to the boundary of a surface and is thus illustrative of many other problems involving boundary-layer flow.

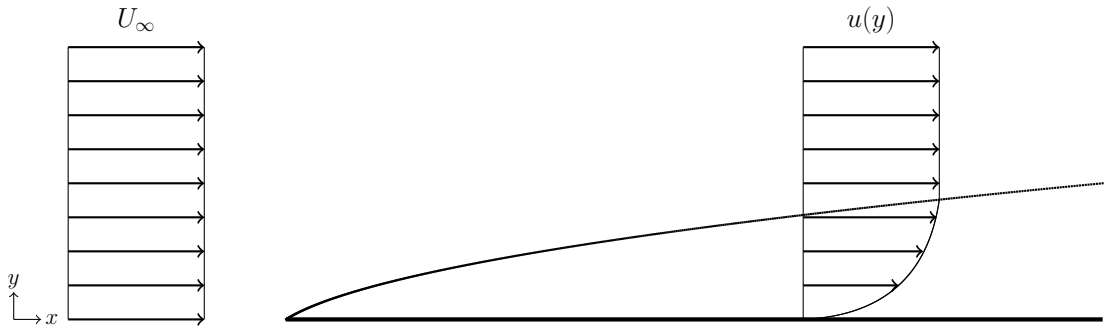

Figure 1.1.1: A Blasius boundary layer on a semi-infinite flat plate which is parallel to an oncoming unidirectional flow.

The flat plate, which is aligned with the x-axis, has a simple solution for the leading-order outer flow, namely U_0 in (1.1.6) is equal to unity throughout the domain. For the boundary-layer flow the two dimensional governing equations (1.1.17) must be solved. These equations are subject to boundary conditions of no-slip and impermeability at the wall such that $u_0 = v_0 = 0$ on $Y = 0$. It follows that at the top edge of the boundary layer the x velocity component must match the outer solution velocity so there is also the free-stream condition $u_0 \to 1$ as $Y \to \infty$.

In the outer flow the edge of the boundary layer is located at $y = 0$ and there is the leading-order impermeability condition $V_0 = 0$ at $y = 0$, which means that the x-momentum equation for the outer flow (1.1.7b) reduces to

$$U_0 \frac{\mathrm{d}U_0}{\mathrm{d}x} = -\frac{\mathrm{d}P_0}{\mathrm{d}x}. \tag{1.1.18}$$

Since $U_0 = 1$ it follows that P_0 is constant along the length of the boundary-layer edge. Since the pressure must match at the edge of the boundary layer, it follows that p_0 is constant throughout the boundary layer. This means the leading order pressure gradient is zero everywhere inside the boundary layer so the x-momentum equation (1.1.17b) reduces to

$$u_0 \frac{\partial u_0}{\partial x} + v_0 \frac{\partial u_0}{\partial Y} = \frac{\partial^2 u_0}{\partial Y^2}. \tag{1.1.19}$$

In order to solve these reduced equations the coordinate transformation

$$\eta = \frac{Y}{\delta} \tag{1.1.20}$$

is proposed where $\delta(x) = \sqrt{2x}$. Then seeking similarity solutions of the form

$$u_0 = U_0 U(\eta) = U(\eta), \quad v_0 = \frac{V(\eta)}{\delta}, \quad p_0 = P_0, \quad p_2 = \frac{\tilde{p}_2(\eta)}{\delta^2}, \tag{1.1.21}$$

such that

$$\frac{\partial}{\partial x} \to \frac{\partial}{\partial x} - \frac{\eta}{\delta^2}\frac{\partial}{\partial \eta} \quad \text{and} \quad \frac{\partial}{\partial Y} \to \frac{1}{\delta}\frac{\partial}{\partial \eta} \tag{1.1.22}$$

the continuity equation (1.1.17a) becomes

$$-\eta\frac{\partial U}{\partial \eta} + \frac{\partial V}{\partial \eta} = 0. \tag{1.1.23}$$

Proposing the change of variables $V = \eta U - f(\eta)$ the equation (1.1.23) reduces to $f' = U$ where the prime notation indicates differentiation with respect to η. Then the x-momentum equation (1.1.17b) becomes

$$-\frac{\eta}{\delta^2}UU' + \frac{1}{\delta^2}VU' = \frac{1}{\delta^2}U'', \tag{1.1.24}$$

which may be written as

$$U'' + [\eta U - V]\, U' = f''' + ff'' = 0. \tag{1.1.25}$$

The third order non-linear ordinary differential equation (1.1.25) is the Blasius equation and is subject to the boundary conditions $f(0) = f'(0) = 0$, due to impermeability at the plate and no-slip, and $f'(\eta) \to 1$ as $\eta \to \infty$ due to the free-stream condition [6].

The Blasius equation can be easily solved numerically using either a 'shooting' Runge-Kutta method or a finite-difference scheme. Figure 1.1.2 shows the solution using a finite-difference method. The numerical scheme used 2048 uniformly spaced mesh points and the far-field boundary $\eta_\infty = 20$. The $f' = U$ curve in figure 1.1.2 shows how rapidly the velocity in the boundary layer approaches the free-stream velocity. The value $f''(0) \approx 0.4696$ is important as it gives a value for the shear stress on the plate since

$$\tau_w = \mu Re^{\frac{1}{2}} \frac{\partial u_0}{\partial Y}\bigg|_{Y=0} = \mu Re^{\frac{1}{2}} \frac{U_0}{\delta} f''(0) \tag{1.1.26}$$

where τ_w is the wall shear stress and μ is the dynamic viscosity of the fluid. Since there is no pressure drag, on a thin flat plate aligned parallel to an oncoming flow, the shear stress is the cause of all of the drag acting on the plate. The frictional drag acting on the plate is found by integrating the shear stress over the surface.

A displacement thickness δ^* quantifies the effect of the boundary layer on the inviscid outer flow. The displacement thickness is the distance perpendicular to the

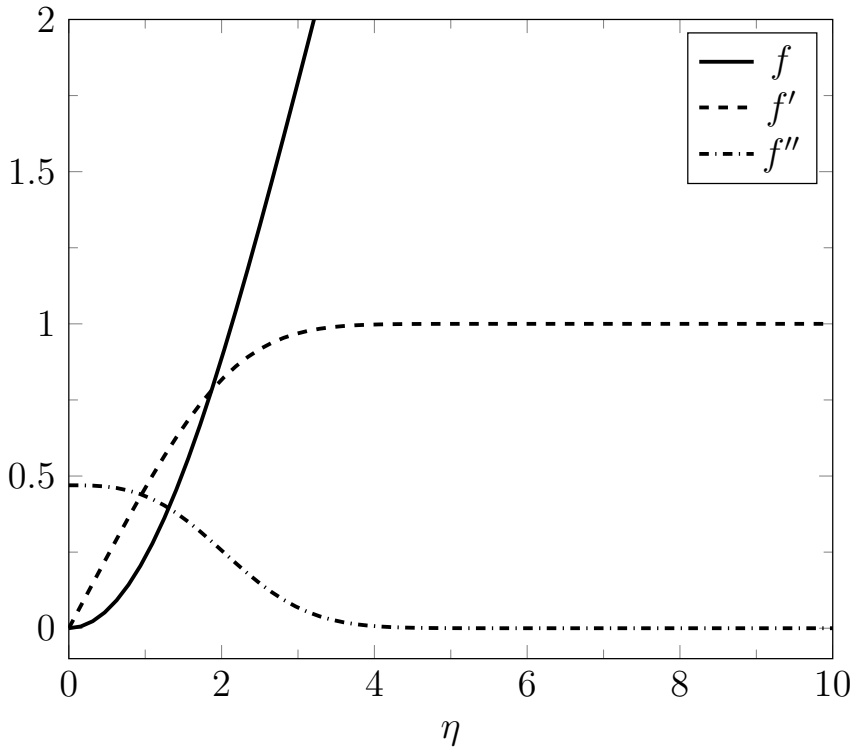

Figure 1.1.2: Numerical solution of the Blasius equation using a finite-difference scheme. Only part of the solution domain has been plotted.

surface by which the boundary layer pushes the inviscid flow outward, it may be supposed that the leading-order inviscid flow is over a body which has been extended at each wall position by this distance. The position $Y = \delta^*$ is defined as the position where the ideal flow has the same mass flux as the boundary layer [59], the displacement thickness is given by

$$\delta^* = \int_{Y=0}^{\infty} \left(1 - \frac{u_0}{U_0}\right) \mathrm{d}Y. \tag{1.1.27}$$

Using the similarity variable and dividing through by the scaling factor $\delta(x)$ gives the relation

$$\begin{aligned} \frac{\delta^*}{\delta(x)} &= \int_{Y=0}^{\infty} \frac{(1 - U(\eta))}{\delta(x)} \frac{\mathrm{d}Y}{\mathrm{d}\eta} \mathrm{d}\eta = \int_{\eta=0}^{\infty} (1 - U(\eta)) \, \mathrm{d}\eta \\ &= \int_{\eta=0}^{\infty} (1 - f'(\eta)) \, \mathrm{d}\eta = \lim_{\eta \to \infty} (\eta - f(\eta)) \,. \end{aligned} \tag{1.1.28}$$

This result can be approximated by using a suitably large value of η; it is found that the constant displacement associated with the Blasius boundary layer on a flat plate is given by

$$\delta_{Blasius} = \frac{\delta^*}{\delta(x)} \approx 1.2168. \tag{1.1.29}$$

In this section uniform flow over a flat plate has been explored, this analysis can be extended to include power law flow either on a wedge or uniform flow with an applied pressure gradient.

Falkner-Skan boundary layer

For flow along a flat plate $U_0 = 1$ is constant for all values of x. The Blasius boundary layer may be generalised by considering a wedge at an angle of attack, $\pi n/(n+1)$, to the uniform velocity field U_0, in this case the outer flow is of the form $U_0(x) = x^n$ where n is a constant. In this case the streamwise pressure gradient is no longer zero and is instead

$$\frac{\partial P_0}{\partial x} = -U_0 \frac{\partial U_0}{\partial x} = -\frac{n}{x} U_0^2. \tag{1.1.30}$$

Again proposing the coordinate transformation

$$\eta = \frac{Y}{\delta}, \tag{1.1.31}$$

where this time $\delta(x) = (2x/U_0(n+1))^{1/2}$, and seeking similarity solutions of the form given in (1.1.21), the continuity equation (1.1.17a) becomes

$$\frac{U_0}{2x}\left[2nU + (n-1)\eta U'\right] + \frac{1}{\delta^2} V' = 0. \tag{1.1.32}$$

Using the δ scaling this may be rewritten as

$$2nU + (n-1)\eta U' + (n+1)V' = 0. \tag{1.1.33}$$

Proposing the change of variables

$$V = \frac{(1-n)}{(n+1)}\eta U - f(\eta) \tag{1.1.34}$$

the equation (1.1.33) reduces to $f' = U$.

Applying the coordinate transformation (1.1.31) to the x-momentum equation (1.1.17b) gives

$$\frac{U_0^2}{2x} U\left[2nU + (n-1)\eta U'\right] + \frac{U_0}{\delta^2} V U' = \frac{U_0^2}{2x} 2n + \frac{U_0}{\delta^2} U'', \tag{1.1.35}$$

which, using the δ scaling, may be written as

$$\frac{2n}{n+1} U^2 - \left[\frac{(1-n)}{(n+1)}\eta U - V\right] U' = \frac{2n}{n+1} + U''. \tag{1.1.36}$$

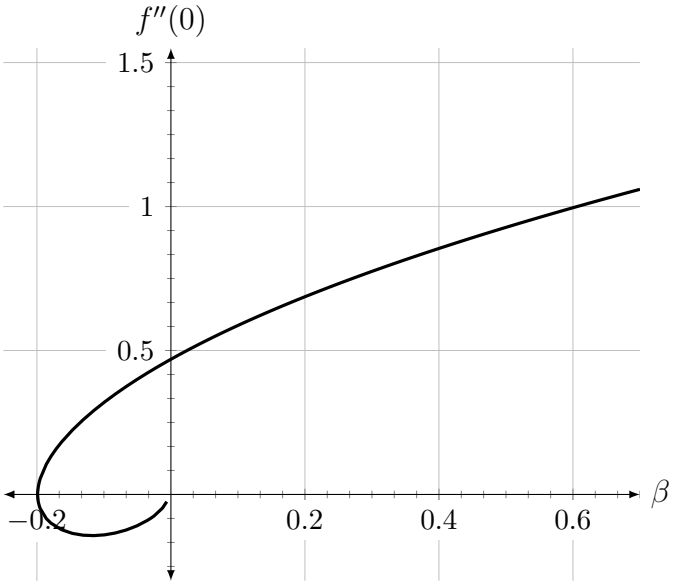

Figure 1.1.3: The dependence of $f''(0)$ on various values of the Hartree parameter β, a limit point occurs at $\beta \approx -0.199$. This is a numerical solution calculated using finite-differences. The solution is continued in β in order to find the solutions with negative shear stress when $\beta < 0$.

Since $U = f'$ and $f = \frac{(1-n)}{(n+1)}\eta U - V$ this reduces to an equation in f alone:

$$f''' + ff'' + \beta\left[1 - (f')^2\right] = 0, \tag{1.1.37a}$$

where

$$\beta = \frac{2n}{n+1} \tag{1.1.37b}$$

is the well known Hartree parameter. The nonlinear equation (1.1.37a) is the Falkner–Skan equation which describes boundary-layer profiles when the outer flow is of the form $U_0(x) = x^n$. It is worth noting how (1.1.37a) reduces to the Blasius equation (1.1.25) when $n = 0$. The Falkner–Skan equation is subject to the same boundary conditions as the Blasius equation namely $f(0) = f'(0) = 0$ and $f'(\eta) \to 1$ as $\eta \to \infty$ [21].

Figure 1.1.3 gives an indication of the wall shear stress for different values of the Hartree parameter. Note that for $-0.199 \lesssim \beta < 0$ there are two possible solutions of the Falkner-Skan equation; negative values of β correspond to an adverse pressure gradient. When β becomes smaller than this limiting value, $\beta_0 \approx -0.199$, an attached laminar boundary layer of this form can no longer exist. Hartree (1937) suggests that β_0 "determines the point at which the laminar boundary layer breaks away from the

solid" [30]. The standard Falkner-Skan equation considered in this section provides a basis for the more complicated three-dimensional scenarios that will be encountered later.

1.1.2 Boundary-layer suction and blowing

Sucking fluid from or blowing fluid into a boundary layer can have a significant impact on the stability of the boundary layer. If the wall of the body is permeable then the boundary layer can be modified by suction/blowing as this would modify the impermeability boundary condition such that $v_0 = v_w$ at the wall where v_w represents the rate of suction/blowing. Suction can be used to prevent flow separation since the low velocity fluid is removed from the boundary layer. Blowing on the other hand typically causes a reduction in both the wall shear stress and the drag due to skin friction. Blowing is used in transpiration cooling, as the injection layer reduces heat transfer to the boundary, and to induce turbulence by destabilising the boundary layer, which can be useful in enhancing mixing.

The rate of injection v_w is taken to be of the same order of magnitude as the boundary-layer scaling i.e. $O(Re^{-1/2})$ and so has no leading order effect on the outer inviscid flow. It can be shown that, in principle, the usual displacement caused by the boundary layer, shown in (1.1.29), can be prevented using a sufficient suction rate v_w [59]. The massive suction/blowing limit $|v_w| \to \infty$ is still only a small suction/blowing velocity when compared with the velocity of the outer flow, if $v_w Re^{-1/2} = o(1)$, but provides insight into the suction/blowing regimes.

In the case of massive *suction* the boundary layer becomes very thin being inversely proportional to the velocity of the suction. The velocity distribution within the boundary layer becomes the 'asymptotic suction profile' given by

$$\frac{u_0(x,y)}{U_0} = 1 - e^{-|v_w|y}, \tag{1.1.38}$$

where $U_0(x)$ is the outer inviscid velocity [69].

For a massive *blowing* the vertical velocity component, in the boundary layer, becomes extremely large causing the boundary layer to massively increase in size. In the massive blowing case the wall shear stress is very small as it becomes inversely proportional to the injection velocity [59]. The massive blowing solution can only exist

by inducing a pressure gradient in the outer inviscid fluid which regularises the flow, otherwise the boundary layer would be blown away from the plate. The thickening of the injectant layer creates a weak interaction with the outer flow which induces a small favourable pressure gradient. The pressure effect which this creates accelerates the injected fluid in a way that allows entrainment by the free shear layer thereby ensuring that the boundary layer remains attached [44]. In a thermal boundary the wall heat flux tends to zero exponentially when there is a large mass injection into the boundary layer [23]; this is why blowing is so useful in reducing aerodynamic heating. Suction and blowing are both particularly important as they are effective ways of providing boundary-layer control thereby allowing for manipulation of the physical properties of the flow [59].

1.1.3 Three-dimensional boundary layers

Three-dimensional boundary layers, with velocity components in all three spatial directions, are more complicated than planar boundary layers which only depend upon two spatial coordinates, as described in section 1.1. For a three-dimensional flow the Cartesian coordinates (x, y, z) and the velocity components (u, v, w) are used. In the usual three-dimensional boundary layer formulation the stretched coordinate $Y = y/\epsilon$ is used along with the asymptotic expansions

$$\begin{aligned} u(x,y,z) &= u_0(x,Y,z) + \epsilon u_1(x,Y,z) + \epsilon^2 u_2(x,Y,z) + \ldots, \\ v(x,y,z) &= \epsilon v_0(x,Y,z) + \epsilon^2 v_1(x,Y,z) + \epsilon^3 v_2(x,Y,z) + \ldots, \\ w(x,y,z) &= w_0(x,Y,z) + \epsilon w_1(x,Y,z) + \epsilon^2 w_2(x,Y,z) + \ldots, \\ p(x,y,z) &= p_0(x,Y,z) + \epsilon p_1(x,Y,z) + \epsilon^2 p_2(x,Y,z) + \ldots. \end{aligned} \tag{1.1.39}$$

Substituting (1.1.39) into (1.1.5) gives the three-dimensional boundary-layer equations

$$\frac{\partial u_0}{\partial x} + \frac{\partial v_0}{\partial Y} + \frac{\partial w_0}{\partial z} = 0, \tag{1.1.40a}$$

$$u_0\frac{\partial u_0}{\partial x} + v_0\frac{\partial u_0}{\partial Y} + w_0\frac{\partial u_0}{\partial z} = -p_0'(x) + \frac{\partial^2 u_0}{\partial Y^2}, \tag{1.1.40b}$$

$$u_0\frac{\partial v_0}{\partial x} + v_0\frac{\partial v_0}{\partial Y} + w_0\frac{\partial v_0}{\partial z} = -\frac{\partial p_2}{\partial Y} + \frac{\partial^2 v_0}{\partial Y^2}, \tag{1.1.40c}$$

$$u_0\frac{\partial w_0}{\partial x} + v_0\frac{\partial w_0}{\partial Y} + w_0\frac{\partial w_0}{\partial z} = -\frac{\partial p_0}{\partial z} + \frac{\partial^2 w_0}{\partial Y^2}. \tag{1.1.40d}$$

These equations govern three-dimensional boundary-layer flows when only one spatial dimension has a boundary-layer scaling.

This thesis concentrates on three-dimensional boundary layers that have two spatial dimensions that are both of boundary-layer scale $O(Re^{-1/2})$. This means that viscous diffusion is retained in two of the three spatial directions resulting in a parabolised version of the Navier-Stokes system. This is different to a typical three-dimensional boundary layer (1.1.40) as usually only one of the spatial dimensions is of boundary-layer scale (typically the coordinate that is transverse to the surface of the body, Y in the case above).

In the short-scale three-dimensional boundary-layer formulation the stretched coordinates $Y = y/\epsilon$ and $Z = z/\epsilon$ are used along with the asymptotic expansions

$$\begin{aligned} u(x,y,z) &= u_0(x,Y,Z) + \epsilon u_1(x,Y,Z) + \epsilon^2 u_2(x,Y,Z) + \ldots, \\ v(x,y,z) &= \epsilon v_0(x,Y,Z) + \epsilon^2 v_1(x,Y,Z) + \epsilon^3 v_2(x,Y,Z) + \ldots, \\ w(x,y,z) &= \epsilon w_0(x,Y,Z) + \epsilon^2 w_1(x,Y,Z) + \epsilon^3 w_2(x,Y,Z) + \ldots, \\ p(x,y,z) &= p_0(x,Y,Z) + \epsilon p_1(x,Y,Z) + \epsilon^2 p_2(x,Y,Z) + \ldots. \end{aligned} \tag{1.1.41}$$

Substituting (1.1.41) into (1.1.5) gives, for the three-dimensional short-scale boundary layer,

$$\frac{\partial u_0}{\partial x} + \frac{\partial v_0}{\partial Y} + \frac{\partial w_0}{\partial Z} = 0, \tag{1.1.42a}$$

$$u_0\frac{\partial u_0}{\partial x} + v_0\frac{\partial u_0}{\partial Y} + w_0\frac{\partial u_0}{\partial Z} = -p_0'(x) + \frac{\partial^2 u_0}{\partial Y^2} + \frac{\partial^2 u_0}{\partial Z^2}, \tag{1.1.42b}$$

$$u_0\frac{\partial v_0}{\partial x} + v_0\frac{\partial v_0}{\partial Y} + w_0\frac{\partial v_0}{\partial Z} = -\frac{\partial p_2}{\partial Y} + \frac{\partial^2 v_0}{\partial Y^2} + \frac{\partial^2 v_0}{\partial Z^2}, \tag{1.1.42c}$$

$$u_0\frac{\partial w_0}{\partial x} + v_0\frac{\partial w_0}{\partial Y} + w_0\frac{\partial w_0}{\partial Z} = -\frac{\partial p_2}{\partial Z} + \frac{\partial^2 w_0}{\partial Y^2} + \frac{\partial^2 w_0}{\partial Z^2}. \tag{1.1.42d}$$

The pressure term $p_1(x)$ does not affect the leading order equations (1.1.42) so may be ignored. Comparing (1.1.42) with (1.1.40) it can be seen that the short-scale equations have extra diffusive terms when compared with the usual three-dimensional boundary-layer formulation. In this section a general introduction to boundary-layer theory has been presented, now some of the research more directly related to this work shall briefly be described.

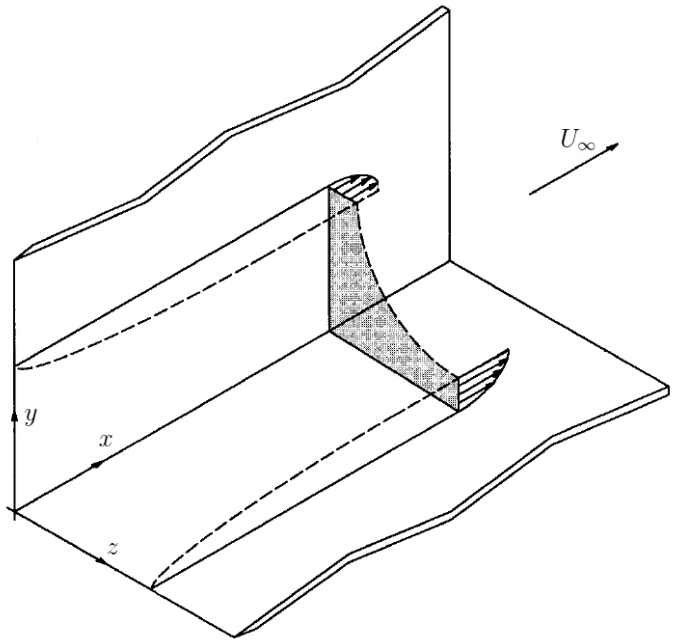

Figure 1.2.1: Schematic diagram for the corner boundary layer formed by streamwise aligned flow past two intersecting perpendicular semi-infinite planes. Taken from Dhanak & Duck (1997) [15].

1.2 Literature review

1.2.1 Boundary layers with short spanwise scales

Surfaces with short-scale spanwise features exist in many applications involving boundary-layer flows. In such scenarios viscous dissipation must be kept in the cross-sectional plane, perpendicular to the external flow direction. The equations governing the flow are parabolic in the streamwise coordinate with viscous diffusion over the entire downstream cross-section, this creates many difficulties for analysis.

Such three-dimensional parabolic flows have been studied extensively in the form of 'corner boundary layers'. Corner boundary layers are formed when two intersecting flat plates are aligned with an oncoming flow, as shown in figure 1.2.1. The first rigorous description of such flows, in the limit of large Reynolds number, was given by Rubin (1966) [58] who described the blending of the spanwise and transverse boundary layers created on the horizontal and vertical plates respectively. Despite this insight into the problem numerical solutions remained elusive until Dhanak & Duck (1997) [15] showed that these numerical difficulties were due to the use of incorrect far-field boundary conditions.

The corner boundary layer problem can be analysed using the 'corner boundary layer' or 'boundary-region' equations which describe any streamwise aligned feature of adequately short spanwise extent. These equations were used by Hewitt & Duck (2014) [35] to examine the three-dimensional boundary layers associated with flow over both a flat plate of narrow spanwise extent and a narrow gap in an otherwise infinite flat plate. This study showed the importance of properly chosen far-field boundary conditions for computational accuracy. Short-scale spanwise features impact the streamwise flow in the region of the disturbance, this alteration to the downstream volume flux must be substituted by lateral flow in the surface boundary layer or transverse flow to or from the free-stream. The short-scale spanwise feature creates a correction to the inviscid outer flow which must be accounted for and matched to the far-field boundary conditions for the boundary-layer. This modification to the outer flow and the corresponding effect on the far-field boundary conditions applies to all boundary-layer flows which have short-scale spanwise features. The effects discussed here are of vital importance in the work that follows and shall be considered in further detail later.

1.2.2 Injection into boundary layers

Injection into *two-dimensional* flat-plate boundary layers, both with and without an applied pressure gradient, has been extensively studied. For laminar uniform flow over a flat plate in the absence of a pressure gradient, with a boundary-layer scale injection v_w, there is a critical injection rate at which the boundary-layer solution ceases to exist. This so called 'blow-off' phenomena, illustrated by Emmons & Leigh (1954) [20], corresponds to a singular solution with zero wall shear and infinite displacement thickness. Figure 1.2.2 shows the behaviour of the self-similar boundary-layer velocity profile on the approach to this critical injection rate $K \approx 0.876$, where K parameterises the boundary-layer scale injection v_w [59].

Catherall et al. (1965) [10] analysed the downstream location of the separation due to a boundary-layer scale injection giving a description of the singularity at separation. Later Watson (1966) [70] showed that for two-dimensional boundary-layer injection any favourable pressure gradient prevents blow-off from occurring and instead leads to a displaced shear layer. In the zero pressure gradient case an analytical description

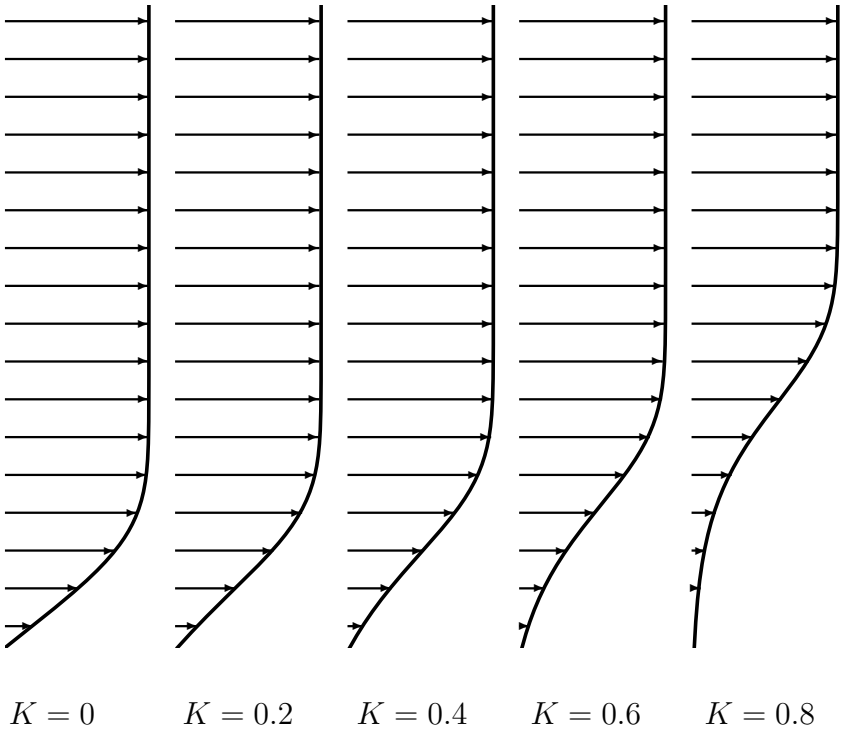

Figure 1.2.2: Boundary-layer velocity profiles for flow over a flat plate with a boundary-layer scale injection of varying magnitude. The injection rate is parameterised by the constant K where increasing K indicates a stronger injection. 'Blow-off' occurs at $K \approx 0.876$.

of the near blow-off behaviour was given by Kassoy (1970, 1971) [42] [43] using an asymptotic technique based on the limit of small wall shear and Prandtl's transposition theorem. For injection rates close to the critical value, there is an inviscid response near to the wall which is separated from the outer flow by a displaced shear layer. Kassoy (1971) [43] showed that, at injection rates above the critical value, when there is no favourable pressure gradient the interaction between the injected fluid and the external flow results in a favourable pressure gradient which prevents blow-off from occurring. Kassoy (1971) established an interacting solution which predicts decreasing wall shear for increasing injection rates below the critical value, increasing wall shear for increasing injection rates above the critical value and a singularity at the critical injection rate. Kassoy (1974) [44] then resolved the blow-off singularity at the critical injection rate by showing that weak pressure interactions, created by the boundary-layer displacement, and viscous effects regularise the problem and allow for a non-singular solution.

Smith & Stewartson (1973a) [62] and Smith & Stewartson (1973b) [63] investigated the case of a 'strong' blowing into a supersonic boundary. This is different to the above studies, and the rest of this thesis, as the injection is at least $O(Re^{-3/8})$ as compared with the boundary-layer scale blowing, $O(Re^{-1/2})$, which is considered to be 'weak' by Smith & Stewartson. These investigations into 'strong' injection through a plate of finite length into a supersonic free stream are useful for understanding heat transfer reduction. Stewartson (1974) [65] showed that the use of triple-deck theory, in these 'strong' injection flows, allows for an asymptotic solution of the Navier-Stokes equations which is uniformly valid in the limit of infinite Reynolds number by matching across different regions.

The two-dimensional theory for boundary-layer injection can be extended to three-dimensional flows with an injection over a finite spanwise extent that is comparable to the boundary-layer thickness. Recent work by van Dommelen & Yapalparvi (2014) [16] has given a theoretical description of the removal of boundary-layer separation by microjet injection with a short-scale spanwise variation. Such removal of separation is not possible for two-dimensional flow or three-dimensional flow with a long-scale (in comparison the the boundary-layer thickness) spanwise variation. This so called 'Görtler-scale' blowing can create an attached flow with a small wall shear where

otherwise one would expect to encounter a separated flow. The work by van Dommelen & Yapalparvi (2014) [16] considered a periodic arrangement of microjets on a surface with weak curvature. Herein, a continuous distribution of injection shall be allowed for, without the requirement for curvature, over a finite spanwise extent thus avoiding the periodic requirement. Chapters 2 and 3 seek to explain this study which demonstrates how microjets in a periodic arrangement can be used to remove separation from a boundary layer.

1.2.3 Experimental motivation for injection

Flow separation is undesirable in many industrial applications as it may reduce system performance, efficiency and stability. Kumar & Alvi (2006) [48] performed an experimental investigation in order to study the feasibility of using high-speed microjets to control boundary-layer separation. Activating microjets have been shown to reduce the extent of separated flow regions and increase the momentum of the flow near the surface. Experimental work by Fernandez et al. (2012) [22] showed that the lateral spacing between elements of a microjet array can have a significant impact on separation flow control effectiveness. The generation of streamwise vorticity, due to the counter rotating vortex pairs produced by the jets, is believed to be the main mechanism for separated flow reattachment.

The use of short-scale spanwise blowing as a mechanism for flow separation control compares favourably to traditional suction techniques as blowing repels contaminants away from the surface and sources of high pressure air/fluid are often readily available. However it is clear that further experimental and theoretical explorations are required in order to understand the underlying physical mechanisms and viability as a flow control technique. The work presented herein is a theoretical analysis and is not used to directly compare to any experimental findings, but offers insight on physical mechanisms and scaling with a focus on isolated injection.

1.2.4 Surface roughness

Surface roughness often plays a significant role in the transition from laminar to turbulent flow. The dimensions and spatial distribution of the roughness elements, along

with the boundary-layer flow structure, determine the amount of distortion in the downstream flow. Denier et al. (1991) [14] showed that wall roughness elements cause the stimulation of Görtler vortices in incompressible boundary layers with the induced vortex field growing at a finite distance downstream of the roughness element. Smith (1973) [60] examined the problem of two-dimensional boundary-layer flow over a flat plate which has a small hump situated downstream of the leading edge. A triple-deck description was given showing how the hump generates an interaction between the inviscid region just outside the boundary layer and the viscous region near the hump. Smith (1981) [61] showed that for a single obstacle, when the Reynolds number is large, the production of nonlinear interactions, and therefore the prospect of instability, depend on only the length and height scales of the obstacle in comparison to the triple-deck length scales.

Goldstein et al. (2010,2011) [24] [25] considered high-Reynolds-number flow over a spanwise periodic array of small roughness elements whose separation and dimensions are of the same order as the boundary-layer thickness. Goldstein et al. (2010) [24] showed that the local flow in the vicinity of the roughness has a double layer structure and that the wakes generated can persist over streamwise distances which are much longer than the distance between the roughness elements and the leading edge. Goldstein et al. (2011) [25] extended this to the case where the flow is nonlinear in the proximity of the roughness and showed that nonlinearity can have a dramatic effect on the evolution of the wake disturbances. Downstream wakes consist of streak-like perturbations that exhibit algebraic/transcendental growth. Recent work by Goldstein et al. (2016) [26] analysed larger roughness heights and streamwise elongated planform shapes which produce nonlinear behaviour in the downstream wakes. Surface roughness has a large effect on the stability of the flow downstream of the roughness and can be used as a source of short-scale spanwise disturbance to a boundary-layer flow. The studies by Goldstein et al. all involve the 'boundary-region' equations in some way as these equations are essential when investigating flow over obstacles of limited spanwise extent in comparison to the boundary-layer thickness.

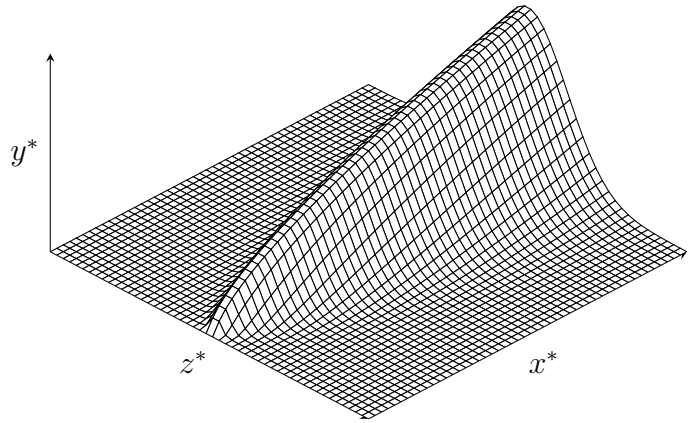

Figure 1.3.1: Schematic diagram of a short scale ridge surface as an example of a possible topographic feature.

1.3 A self-similar formulation

The general formulation for laminar incompressible boundary-layer flow adjacent to a semi-infinite plate with a short-scale spanwise injection through the plate surface, allowing for the possibility of a surface topography, is presented here. This formulation is essentially the same as that presented by Duck, Stow & Dhanak (2000) [18].

Consider a dimensional system of Cartesian coordinates (x^*, y^*, z^*) where x^* is increasing in the streamwise direction, y^* is the transverse coordinate and z^* is the spanwise coordinate. For $x^* > 0$ some non-planar surface lies in the path of the freestream flow, the leading edge of this surface is a straight line located at $x^* = 0$ as shown in figure 1.3.1. It is convenient to choose the undistorted, flat surface to be at $y^* = 0$. The velocity is written as $U^*_\infty(u^*, v^*, w^*)$, then at the outer edge of the boundary-layer the streamwise velocity is written as $U^*_\infty F(x^*)$. Power law external flows corresponding to $F(x^*) = (x^*/L^*)^n$ are considered here where n is the constant pressure gradient parameter and L^* is some arbitrary length scale. The local Reynolds number is defined as $Re_x = x^* U^*_\infty F(x^*)/\nu^*$ where ν^* is the kinematic viscosity of the fluid. In order to be of boundary-layer scale it is necessary to assume that the height of the surface topography profile $H^*(x^*, z^*)$ is $O(x^* Re_x^{-1/2})$ and that the cross-flow velocity scale is of the same order leading to transverse and spanwise velocities of $O(U^*_\infty Re_x^{-1/2})$. A non-dimensional solution is sought in a rescaled coordinate system

$$(z^*, y^*) = \left(\frac{2}{n+1}\right)^{\frac{1}{2}} x^* Re_x^{-\frac{1}{2}} \left(\zeta, \eta + H(\zeta)\right) \tag{1.3.1a}$$

where $H^*(x^*, z^*) = \sqrt{2}(n+1)^{-1/2} x^* Re_x^{-1/2} H(\zeta)$. This ζ variable allows for spanwise

scales that are comparable to the boundary-layer thickness. For the velocity field the expansion

$$u^* = U^*_\infty F(x^*) U(\zeta,\eta) + \ldots, \tag{1.3.1b}$$

$$(v^*, w^*) = \left(\frac{n+1}{2}\right)^{\frac{1}{2}} U^*_\infty F(x^*) Re_x^{-\frac{1}{2}} \left(V(\zeta,\eta) + \ldots, W(\zeta,\eta) + \ldots\right), \tag{1.3.1c}$$

is introduced. Then for the pressure field

$$p^* = -\frac{1}{2}\rho^* \left(U^*_\infty F(x^*)\right)^2 \left[1 + \left(\frac{n+1}{2}\right)^{\frac{1}{2}} Re_x^{-\frac{1}{2}} p_1(x^*) + \left(\frac{n+1}{2}\right) Re_x^{-1} p_2(\zeta,\eta) + \ldots\right], \tag{1.3.1d}$$

where ρ^* is the density of the fluid.

Substituting (1.3.1) into the Navier-Stokes and continuity equations (1.1.1) and assuming that the local Reynolds number is large, $Re_x \gg 1$, results in a system that retains viscous diffusion in both the transverse and spanwise directions. These three-dimensional equations are equivalent to the short-scale equations (1.1.42) and are simply parabolised Navier-Stokes equations. The explicit appearance of the pressure makes the primitive formulation (1.1.42) difficult to solve numerically, therefore it is computationally simpler to use an alternative formulation. Applying the change of variables

$$V(\zeta,\eta) = \frac{(1-n)}{(n+1)} (\eta + H) U(\zeta,\eta) - \Phi(\zeta,\eta), \tag{1.3.2a}$$

$$W(\zeta,\eta) = \frac{(1-n)}{(n+1)} \zeta U(\zeta,\eta) - \Psi(\zeta,\eta); \tag{1.3.2b}$$

and taking leading-order terms the 'boundary-region' equations are obtained as shown in Appendix A. The governing equations for a self-similar downstream solution are:

$$\frac{2}{n+1} U = \Phi_\eta + \Psi_\zeta - H'\Psi_\eta, \tag{1.3.3a}$$

$$\Theta = \Psi_\eta - \Phi_\zeta + H'\Phi_\eta, \tag{1.3.3b}$$

and

$$\nabla^2 U = \frac{2n}{n+1}\left[U^2 - 1\right] - \Phi U_\eta - \Psi\left[U_\zeta - H'U_\eta\right], \tag{1.3.4a}$$

$$\nabla^2 \Theta = \frac{2(1-n)}{(n+1)} \left[\zeta U U_\eta - (\eta + H) U \left(U_\zeta - H'U_\eta\right)\right] - \Phi\Theta_\eta - \Psi\left(\Theta_\zeta - H'\Theta_\eta\right) - \frac{2}{n+1} U\Theta. \tag{1.3.4b}$$

This less intuitive form of (1.1.42) has previously been stated by Dhanak & Duck (1997) [15] and Pal & Rubin (1971) [49] amongst others and is well known in relation to corner boundary-layer flows. In this formulation Φ and Ψ simply transform the transverse and spanwise velocity components and Θ is related to the vorticity of the flow.

Combining (1.3.3a) and (1.3.3b) by taking derivatives with respect η and ζ (1.3.3) may be rewritten as

$$\nabla^2\Phi = \frac{2}{n+1}U_\eta - \Theta_\zeta + H'\Theta_\eta, \tag{1.3.4c}$$

$$\nabla^2\Psi = \frac{2}{n+1}\left(U_\zeta - H'U_\eta\right) + \Theta_\eta. \tag{1.3.4d}$$

Here ∇^2 is defined by

$$\nabla^2 \equiv \left[1 + (H')^2\right]\frac{\partial^2}{\partial\eta^2} + \frac{\partial^2}{\partial\zeta^2} - 2H'\frac{\partial^2}{\partial\eta\partial\zeta} - H''\frac{\partial}{\partial\eta}. \tag{1.3.4e}$$

The general formulation (1.3.4) provides a basis for any subsequent problem formulations involving either a short-scale surface topography or a short-scale transpiration provided that any variation in the downstream coordinate remains in self-similar form.

1.3.1 Boundary conditions

In the dimensional coordinates the boundary conditions are defined by $u^* = w^* = 0$, $v^* = v_w^*(x^*, z^*)$ on the wall located at $y^* = H^*(x^*, z^*)$. The v_w^* term allows for the inclusion of transpiration through the surface. Focus shall be placed on transpiration through the surface of the plate of the form

$$v_w^*(x^*, z^*) = \left(\frac{n+1}{2}\right)^{\frac{1}{2}} U_\infty^* F(x^*) Re_x^{-\frac{1}{2}} V_{transp}(\zeta). \tag{1.3.5}$$

This similarity form is simply for convenience, more general x^* dependencies can be managed by marching in the downstream direction, this will be examined in chapter 4. So in the rescaled coordinate system the surface boundary conditions are

$$\Phi = \Phi_w(\zeta), \quad \Psi = U = 0, \quad \Theta = \Psi_\eta - \Phi_{w\zeta} \quad \text{on} \quad \eta = 0, \tag{1.3.6}$$

where $\Phi_w(\zeta) = -V_{transp}(\zeta)$ and $\Phi_{w\zeta}$ is the derivative of Φ_w with respect to ζ. Assuming a reflectional symmetry in the $z^* = 0$ plane gives the conditions

$$w^* = \frac{\partial u^*}{\partial z^*} = \frac{\partial v^*}{\partial z^*} = 0 \quad \text{on} \quad z^* = 0, \tag{1.3.7}$$

which become

$$U_\zeta - H'U_\eta = \Phi_\zeta - H'\Phi_\eta = \Psi = \Theta = 0, \quad \text{on} \quad \zeta = 0, \tag{1.3.8}$$

in the rescaled coordinate system. If the surface topography is symmetric about the centreline then $H'(0) = 0$ and the conditions (1.3.8) may be simplified. The surface and reflectional conditions (1.3.6) and (1.3.8) provide boundary conditions for the system (1.3.4) on $\eta = 0$ and $\zeta = 0$ respectively. Far away from the plate it is required that $u^* \to U^*_\infty F(x^*)$, $w^* \to 0$ as $y^* \to \infty$ in order to match with the external freestream with no cross flow. In the rescaled coordinates this leads to the conditions

$$U \to 1, \quad \Psi \to \left(\frac{1-n}{n+1}\right)\zeta \quad \text{and} \quad \Theta \to 0 \quad \text{as} \quad \eta \to \infty, \tag{1.3.9}$$

where the condition on Θ is due to the need to match to the outer inviscid freestream flow which has no vorticity at leading order.

1.3.2 Nonlinear correction formulation

The solution naturally divides into a two-dimensional boundary layer, without any short-scale spanwise features, and a correction due to any short-scale disturbance. The governing equations shall be rescaled based on the short-scale feature width ζ_0:

$$\zeta = \zeta_0\hat{\zeta}, \tag{1.3.10a}$$

$$U(\zeta,\eta) = \hat{U}(\hat{\zeta},\eta), \quad \Phi(\zeta,\eta) = \hat{\Phi}(\hat{\zeta},\eta) \tag{1.3.10b}$$

$$\Psi(\zeta,\eta) = \zeta_0\hat{\Psi}(\hat{\zeta},\eta), \quad \Theta(\zeta,\eta) = \zeta_0\hat{\Theta}(\hat{\zeta},\eta), \tag{1.3.10c}$$

then a nonlinear perturbation of the form

$$\hat{\Phi} = \Phi_B(\eta) + \tilde{\Phi}(\hat{\zeta},\eta), \tag{1.3.11a}$$

$$\hat{\Psi} = \hat{\zeta}\Psi_B(\eta) + \tilde{\Psi}(\hat{\zeta},\eta), \tag{1.3.11b}$$

$$\hat{U} = U_B(\eta) + \tilde{U}(\hat{\zeta},\eta), \tag{1.3.11c}$$

$$\hat{\Theta} = \hat{\zeta}\Theta_B(\eta) + \tilde{\Theta}(\hat{\zeta},\eta), \tag{1.3.11d}$$

is sought where subscript 'B' indicates a known base solution which exists far away from any short spanwise scale forcing. The ζ_0 rescaling is used as the large injection slot limit, $\zeta_0 \gg 1$, is of significant interest, especially for comparison with the two-dimensional injection solution. The surface profile is also restated in terms of the

scaled coordinate $\hat{\zeta}$ such that $H(\zeta) = \tilde{H}(\hat{\zeta})$. Substituting the above formulation into the governing equations (1.3.4) the response can be split into a base flow which exists far from the short spanwise scale region and a correction which is driven solely by the short-scale spanwise variation.

Base flow

Taking the leading order terms it is found that the two-dimensional base flow is governed by

$$\Phi_B' = \frac{2}{n+1}U_B - \Psi_B, \tag{1.3.12a}$$

$$\Psi_B' = \Theta_B, \tag{1.3.12b}$$

$$U_B'' = \frac{2n}{n+1}\left[U_B^2 - 1\right] - \Phi_B U_B', \tag{1.3.12c}$$

$$\Theta_B'' = \frac{2(1-n)}{n+1}U_B U_B' - \Phi_B\Theta_B' - \Psi_B\Theta_B - \frac{2}{n+1}U_B\Theta_B, \tag{1.3.12d}$$

subject to the boundary conditions

$$U_B(0) = \Psi_B(0) = 0, \quad \Phi_B(0) = \Phi_{Bw}, \tag{1.3.12e}$$

$$U_B \to 1, \quad \Theta_B \to 0, \quad \Psi_B \to \frac{1-n}{n+1} \quad \text{as} \quad \eta \to \infty. \tag{1.3.12f}$$

Here $\Phi_{Bw} = \Phi_w(\zeta \to \infty)$ is the constant base flow transpiration, usually this will be equal to zero. These base flow equations can be transformed into the Falkner-Skan equation (1.1.37a) or a three-dimensional alternative; this shall be discussed in more detail at the end of the chapter.

Nonlinear correction

The three-dimensional nonlinear correction quantities are governed by

$$\hat{\nabla}^2\tilde{\Phi} = \frac{2}{n+1}\tilde{U}_\eta - \tilde{\Theta}_{\hat{\zeta}} + \tilde{H}'\left(\hat{\zeta}\Theta'_B + \tilde{\Theta}_\eta\right) + \frac{1}{\zeta_0^2}\left[\tilde{H}''\Phi'_B - \left(\tilde{H}'\right)^2\Phi''_B\right], \tag{1.3.13a}$$

$$\hat{\nabla}^2\tilde{\Psi} = \left(\frac{2}{n+1}\right)\frac{1}{\zeta_0^2}\left[\tilde{U}_{\hat{\zeta}} - \tilde{H}'\left(U'_B + \tilde{U}_\eta\right)\right] + \tilde{\Theta}_\eta - \frac{1}{\zeta_0^2}\left(\tilde{H}'\right)^2\hat{\zeta}\Psi''_B + \frac{\Psi'_B}{\zeta_0^2}\left(2\tilde{H}' + \hat{\zeta}\tilde{H}''\right), \tag{1.3.13b}$$

$$\hat{\nabla}^2\tilde{U} = \frac{2n}{n+1}\left[2U_B\tilde{U} + \tilde{U}^2\right] - \left(\hat{\zeta}\Psi_B + \tilde{\Psi}\right)\left[\tilde{U}_{\hat{\zeta}} - \tilde{H}'\left(U'_B + \tilde{U}_\eta\right)\right] - \Phi_B\tilde{U}_\eta - \left(U'_B + \tilde{U}_\eta\right)\tilde{\Phi} + \frac{1}{\zeta_0^2}\left[\tilde{H}''U'_B - \left(\tilde{H}'\right)^2U''_B\right], \tag{1.3.13c}$$

$$\begin{aligned}\hat{\nabla}^2\tilde{\Theta} =& \frac{1}{\zeta_0^2}\left[\Theta'_B\left(2\tilde{H}' + \hat{\zeta}\tilde{H}''\right) - \hat{\zeta}\Theta''_B\left(\tilde{H}'\right)^2\right] + \frac{2(1-n)}{n+1}\left\{\hat{\zeta}\left(U_B + \tilde{U}\right)\tilde{U}_\eta\right.\\ &\left.+\hat{\zeta}U'_B\tilde{U} - \frac{1}{\zeta_0^2}\left(\eta + \tilde{H}\right)\left(U_B + \tilde{U}\right)\left(\tilde{U}_{\hat{\zeta}} - \tilde{H}'\left(U'_B + \tilde{U}_\eta\right)\right)\right\}\\ &- \left(\Phi_B + \tilde{\Phi}\right)\tilde{\Theta}_\eta - \hat{\zeta}\Theta'_B\tilde{\Phi} - \hat{\zeta}\Psi_B\left[\tilde{\Theta}_{\hat{\zeta}} - \tilde{H}'\left(\hat{\zeta}\Theta'_B + \tilde{\Theta}_\eta\right)\right]\\ &- \tilde{\Psi}\left[\Theta_B + \tilde{\Theta}_{\hat{\zeta}} - \tilde{H}'\left(\hat{\zeta}\Theta'_B + \tilde{\Theta}_\eta\right)\right]\\ &- \frac{2}{n+1}\left[\left(U_B + \tilde{U}\right)\tilde{\Theta} + \hat{\zeta}\Theta_B\tilde{U}\right],\end{aligned} \tag{1.3.13d}$$

where

$$\hat{\nabla}^2 \equiv \left[1 + \frac{1}{\zeta_0^2}\left(\tilde{H}'\right)^2\right]\frac{\partial^2}{\partial\eta^2} + \frac{1}{\zeta_0^2}\frac{\partial^2}{\partial\hat{\zeta}^2} - \frac{2}{\zeta_0^2}\tilde{H}'\frac{\partial^2}{\partial\eta\partial\hat{\zeta}} - \frac{1}{\zeta_0^2}\tilde{H}''\frac{\partial}{\partial\eta}. \tag{1.3.13e}$$

The surface boundary conditions (1.3.6) give the nonlinear correction boundary conditions

$$\tilde{\Phi} = \tilde{\Phi}_w(\hat{\zeta}), \quad \tilde{\Psi} = \tilde{U} = 0, \quad \tilde{\Theta} = \tilde{\Psi}_\eta - \frac{1}{\zeta_0^2}\tilde{\Phi}_{w\hat{\zeta}} \quad \text{on} \quad \eta = 0, \tag{1.3.14}$$

where $\tilde{\Phi}_w(\hat{\zeta}) = \Phi_w(\zeta) - \Phi_{Bw}$ is the spanwise varying injection. Then the symmetry boundary conditions are

$$\tilde{U}_{\hat{\zeta}} = \tilde{\Phi}_{\hat{\zeta}} = \tilde{\Psi} = \tilde{\Theta} = 0, \quad \text{on} \quad \hat{\zeta} = 0. \tag{1.3.15}$$

Appropriate far-field conditions must also be determined for the nonlinear correction to the base flow.

1.3.3 Far-field boundary conditions

The importance of the appropriate far-field boundary conditions was illustrated by Hewitt & Duck (2014) [35] in their work on a short-scale gap in a flat plate. The

presence of a short-scale spanwise variation alters the streamwise mass flux in the vicinity of the variation with this then inducing a spatially decaying boundary-layer transpiration. This short-scale transpiration region creates an $O(Re^{-1/2})$ half-line-source/sink alteration to the inviscid outer flow. Hewitt & Duck (2014) [35] showed that the mass flux associated with this source/sink should be directly included as part of the computational procedure for accurate numerical results to be obtained.

Far-field conditions for $\eta \gg 1$ at fixed $\hat{\zeta}$

Using the argument of Hewitt & Duck (2014) [35] presented in Appendix B it is found that, far away from the centreline at $\eta = \zeta = 0$, the proper far-field conditions for the nonlinear corrections are

$$\tilde{\Phi} \sim \left(\frac{1-n}{n+1}\right)\tilde{H} + \frac{A\left(\eta+\tilde{H}\right)}{\left(\eta+\tilde{H}\right)^2 + \zeta_0^2\hat{\zeta}^2}, \tag{1.3.16a}$$

$$\tilde{\Psi} \sim \frac{A\hat{\zeta}}{\left(\eta+\tilde{H}\right)^2 + \zeta_0^2\hat{\zeta}^2}, \tag{1.3.16b}$$

$$\tilde{U} = \tilde{\Theta} = 0, \tag{1.3.16c}$$

for $\zeta_0^2\hat{\zeta}^2 + \eta^2 \gg 1$. Here A is a measure of the mass flux towards ($A > 0$) and away from ($A < 0$) the centreline in the cross-sectional plane. A is unknown and must be calculated as part of the computational procedure. An extra complication is that the far-field conditions (1.3.16) are not valid near to the plate, where $\eta = O(1)$, as viscous effects must be taken into account.

Far-field conditions near the boundary for $\hat{\zeta} \gg 1$ and $\eta = O(1)$

For $\hat{\zeta} \gg 1$ and near the boundary where $\eta = O(1)$, a large-$\hat{\zeta}$ asymptotic solution exists in the form

$$\tilde{U} = A\bar{U}(\eta)/\zeta_0^2\hat{\zeta}^2 + \ldots, \tag{1.3.17a}$$

$$\tilde{\Phi} = A\bar{\Phi}(\eta)/\zeta_0^2\hat{\zeta}^2 + \ldots, \tag{1.3.17b}$$

$$\tilde{\Psi} = A\bar{\Psi}(\eta)/\zeta_0^2\hat{\zeta} + \ldots, \tag{1.3.17c}$$

$$\tilde{\Theta} = A\bar{\Theta}(\eta)/\zeta_0^2\hat{\zeta} + \ldots. \tag{1.3.17d}$$

Note that the asymptotic description in the far-field (1.3.17) is forced by A, which is why ensuring the correctness of the algebraically decaying far-field correct is so crucial.

Substituting (1.3.17) into the nonlinear correction equations (1.3.13) and taking the limit $\hat{\zeta} \to \infty$ the leading-order behaviour can be determined from the solution of the system

$$\bar{\Phi}'(\eta) = \frac{2}{n+1}\bar{U} + \bar{\Psi}, \tag{1.3.18a}$$

$$\bar{\Psi}'(\eta) = \bar{\Theta}, \tag{1.3.18b}$$

$$\bar{U}''(\eta) = \frac{4n}{n+1}U_B\bar{U} - U_B'\bar{\Phi} - \Phi_B\bar{U}' + 2\Psi_B\bar{U}, \tag{1.3.18c}$$

$$\begin{aligned}\bar{\Theta}''(\eta) =& \frac{2(1-n)}{n+1}\left[U_B\bar{U}' + \bar{U}U_B'\right] - \Phi_B\bar{\Theta}' - \Theta_B'\bar{\Phi} + \Psi_B\bar{\Theta} \\ &- \bar{\Psi}\Theta_B - \frac{2}{n+1}\left[U_B\bar{\Theta} + \Theta_B\bar{U}\right],\end{aligned} \tag{1.3.18d}$$

subject to the boundary conditions $\bar{U} = \bar{\Phi} = \bar{\Psi} = 0$ on $\eta = 0$ and $\bar{U}, \bar{\Theta} \to 0$, $\bar{\Psi} \to 1$ as $\eta \to \infty$ due to (1.3.14) and (1.3.16). Here it is assumed that the spanwise varying injection $\tilde{\Phi}_w(\hat{\zeta})$ and the surface profile $\tilde{H}(\hat{\zeta})$ decay sufficiently rapidly that they can be ignored when $\hat{\zeta}$ is large i.e. $\tilde{H}(\hat{\zeta}) = o(\hat{\zeta}^{-2})$.

Since (1.3.17) is only valid for $\eta = O(1)$ instead of imposing these conditions directly composite solutions are constructed instead. For example for large-$\hat{\zeta}$

$$\tilde{\Psi} \sim \frac{A\bar{\Psi}(\eta)}{\zeta_0^2\hat{\zeta}} + \frac{A\hat{\zeta}}{\eta^2 + \zeta_0^2\hat{\zeta}^2} - \tilde{\Psi}_{overlap}, \tag{1.3.19}$$

where

$$\tilde{\Psi}_{overlap} = \lim_{\eta\to\infty}\frac{A\bar{\Psi}(\eta)}{\zeta_0^2\hat{\zeta}} = \lim_{\eta\to 0}\frac{A\hat{\zeta}}{\zeta_0^2\hat{\zeta}^2 + \eta^2} = \frac{A}{\zeta_0^2\hat{\zeta}}. \tag{1.3.20}$$

Hence for $\hat{\zeta} \gg 1$ at fixed η the composite far-field conditions

$$\tilde{U} \sim \frac{A}{\zeta_0^2}\frac{\bar{U}(\eta)}{\hat{\zeta}^2}, \tag{1.3.21a}$$

$$\tilde{\Phi} \sim \frac{A}{\zeta_0^2}\left\{\frac{\bar{\Phi}(\eta)}{\hat{\zeta}^2} - \frac{\eta^3}{\hat{\zeta}^2\left(\zeta_0^2\hat{\zeta}^2 + \eta^2\right)}\right\}, \tag{1.3.21b}$$

$$\tilde{\Psi} \sim \frac{A}{\zeta_0^2}\left\{\frac{\bar{\Psi}(\eta)}{\hat{\zeta}} - \frac{\eta^2}{\hat{\zeta}\left(\zeta_0^2\hat{\zeta}^2 + \eta^2\right)}\right\}, \tag{1.3.21c}$$

$$\tilde{\Theta} \sim \frac{A}{\zeta_0^2}\frac{\bar{\Theta}(\eta)}{\hat{\zeta}}, \tag{1.3.21d}$$

are defined. In order to remove the dependence on the barred variables it is possible

to take combinations of the perturbation variables and their derivatives such that

$$\hat{\zeta}\tilde{U}_{\hat{\zeta}} + 2\tilde{U} = 0, \tag{1.3.22a}$$

$$\hat{\zeta}\tilde{\Phi}_{\hat{\zeta}} + 2\tilde{\Phi} = \frac{2A\eta^3}{\left(\zeta_0^2\hat{\zeta}^2 + \eta^2\right)^2}, \tag{1.3.22b}$$

$$\hat{\zeta}\tilde{\Psi}_{\hat{\zeta}} + \tilde{\Psi} = \frac{2A\eta^2\hat{\zeta}}{\left(\zeta_0^2\hat{\zeta}^2 + \eta^2\right)^2}, \tag{1.3.22c}$$

$$\hat{\zeta}\tilde{\Theta}_{\hat{\zeta}} + \tilde{\Theta} = 0. \tag{1.3.22d}$$

The conditions for large η are given by (1.3.16) and for large $\hat{\zeta}$ are given by (1.3.22) however the constraint on the volume flux coefficient A is also required. Using the far-field conditions for large-$\hat{\zeta}$ leads to the constraint

$$\zeta_0^2\hat{\zeta}\tilde{\Theta}(\hat{\zeta}, \eta = 0) = A\bar{\Theta}(0) \tag{1.3.23}$$

for $\hat{\zeta} \to \infty$. The nonlinear correction eqautions (1.3.13) must be solved subject to the boundary conditions (1.3.14), (1.3.15), (1.3.16) and (1.3.22) and the constraint (1.3.23). Combined with the base flow equations (1.3.12) the above nonlinear formulation provides a formulation for laminar incompressible boundary-layer flow adjacent to a semi-infinite plate with a short-scale spanwise topography and injection through the plate surface.

1.3.4 Non-similar formulation

The self-similar formulation presented above is not strictly necessary; a fully three-dimensional version with downstream variation is also possible. The approach can be generalised by parabolic marching in the downstream x^* coordinate, this allows for the inclusion of more general short-scale features. This downstream marching formulation requires a larger amount of computation and will be examined in chapter 4.

1.4 Two-dimensional boundary-layer injection

Pausing for a moment from the analysis of a short-scale three-dimensional injection; consider the problem of two-dimensional self-similar injection in the absence of any short-scale variation. In the presence of an applied pressure gradient the two-dimensional base flow is determined by the Falkner-Skan solution.

The boundary-region equations (1.3.4), in the absence of any surface topography, naturally reduce to the base flow equations (1.3.12) by removing the spanwise dependence such that $(\Phi_B, \Psi_B, U_B, \Theta_B)$ are functions of η only. Rewriting the base flow equations (1.3.12), using the Hartree parameter $\beta = 2n/(n+1)$, gives

$$\Phi_B' = (2-\beta)U_B - \Psi_B, \tag{1.4.1a}$$

$$\Psi_B' = \Theta_B, \tag{1.4.1b}$$

$$U_B'' = \beta\left[U_B^2 - 1\right] - \Phi_B U_B', \tag{1.4.1c}$$

$$\Theta_B'' = 2(1-\beta)U_B U_B' - \Phi_B\Theta_B' - \Psi_B\Theta_B - (2-\beta)U_B\Theta_B, \tag{1.4.1d}$$

subject to the boundary conditions

$$U_B(0) = \Psi_B(0) = 0, \quad \Phi_B(0) = -K_B, \tag{1.4.1e}$$

$$U_B \to 1, \quad \Theta_B \to 0, \quad \Psi_B \to 1-\beta \quad \text{as} \quad \eta \to \infty, \tag{1.4.1f}$$

where $K_B = -\Phi_{Bw}$ defines the magnitude of the injection through the surface.

The above two-point boundary value problem is known to have one solution which is two-dimensional and another solution which is a three-dimensional analogue for which there is a jet like cross-flow velocity component [56], see Appendix C. For the three-dimensional alternative solution the cross-flow jet vanishes at a line of symmetry ($\zeta = 0$) and grows linearly with ζ in the spanwise direction [15]. The equations (1.4.1) may be reformulated in order to emphasise both the two-dimensional and three-dimensional solutions. In this thesis only the two-dimensional base flow solution will be considered but it is worth noting that in everything that follows an equivalent version is available with the alternative base flow solution used instead.

1.4.1 Falkner-Skan family of solutions

In a similair manner to Duck et. al. (2000) [18] it is possible to seek a solution of the system (1.4.1) of the form

$$\begin{aligned} U_B &= F'(\eta), & \Phi_B &= F(\eta), \\ \Psi_B &= (1-\beta)F'(\eta), & \Theta_B &= (1-\beta)F''(\eta). \end{aligned} \tag{1.4.2}$$

Substituting into (1.4.1) clearly (1.4.1a) and (1.4.1b) are satisfied trivially and (1.4.1c) becomes the Falkner-Skan equation

$$F''' + FF'' + \beta\left[1 - (F')^2\right] = 0. \tag{1.4.3}$$

The Θ_B equation (1.4.1d) may be written as

$$F'''' = -F'F'' - FF''' + 2\beta F'F'', \tag{1.4.4}$$

or in terms of derivatives

$$(F''')' + (FF'')' - \beta\left((F')^2\right)' = 0. \tag{1.4.5}$$

Upon integration this yields

$$F''' + FF'' - \beta(F')^2 + c = 0, \tag{1.4.6}$$

where c is an arbitrary constant. Evaluating this as $\eta \to \infty$ it follows that $c = \beta$ then, as with (1.4.1c), the Θ_B equation (1.4.1d) is satisfied by the Falkner-Skan equation (1.4.3). When $\beta = 0$ there is no pressure gradient corresponding to the Blasius solution for two-dimensional flow over a flat plate. Solving equation (1.4.3) numerically, subject to the boundary conditions $F(0) = -K_B$, $F'(0) = 0$ and $F'(\eta) \to 1$ as $\eta \to \infty$, provides the two-dimensional solution of the system (1.4.1) governing the base flow with injection.

1.4.2 Shear stress

Figure 1.4.1 shows the surface shear stress as a function of the pressure gradient parameter, β, for various values of the blowing rate, K_B, for the Falkner–Skan solution. It can be seen that for $K_B \lesssim 0.876$ there are two solutions for decelerated flow ($\beta < 0$) with one solution displaying backflow ($U_B'(0) < 0$). When the blowing exceeds this critical value, $K_B \approx 0.876$, only one solution exists with $\beta > 0$ and no solutions exist with $\beta \leq 0$. This critical value is important for the phenomena of 'blow-off' which is discussed in section 1.4.3. In the limit of large injection an asymptotic expansion of the Falkner-Skan solution can be constructed; Kubota & Fernandez (1968) [47] showed that the leading order wall shear is given by $U_B'(0) \sim \beta/K_B$.

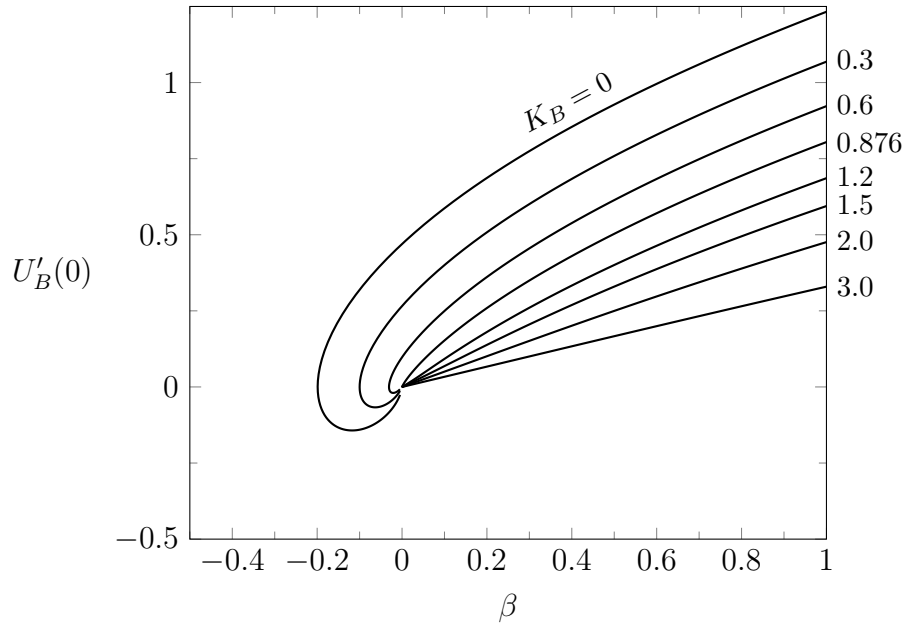

Figure 1.4.1: The scaled shear stress $U'_B(\eta = 0)$, for the Falkner-Skan solution, at the surface of the plate as a function of β for various base flow injection rates K_B. Recreation of a figure by Schlichting & Gersten (p303) [59].

1.4.3 Blow-off

Setting $\beta = 0$ in (1.4.1) the Falkner-Skan solution reduces to the Blasius solution governed by

$$F''' + FF'' = 0, \tag{1.4.7}$$

subject to the boundary conditions $F(0) = -K_B$, $F'(0) = 0$ and $F'(\eta) \to 1$ as $\eta \to \infty$. The equations are parameterised by the base flow injection rate K_B through the surface boundary condition.

Numerical experiments by Emmons & Leigh (1954) [20] showed that as K_B is increased, beyond a critical value of approximately 0.876, the self-similar solution no longer exists and the boundary layer is said to have been 'blown away'. At this critical value the solution becomes singular with the dimensionless wall shear approaching zero and the displacement thickness approaching infinity.

For the Blasius solution the approach to blow-off was described asymptotically by Kassoy (1970) [42]. Kassoy showed that there is an inviscid inner region, near the wall, and a viscous outer layer in which the basic flow is essentially a mixing layer system. The two regions are connected by a displaced shear layer which is blown away from the wall as the injection rate is increased towards its critical value.

The wall shear is shown to satisfy a transcendental equation with respect to a small perturbation about the critical injection rate, it is also seen to approach zero smoothly as the perturbation tends to zero. Kassoy (1971) [43] later showed that the interaction between the injection fluid and the free stream flow produces a favourable pressure gradient in the free stream which prevents the blow-off from occurring.

For any favourable pressure gradient in the free stream flow the blow-off singularity is removed and instead the shear layer connecting the low speed wall region and the outer region is displaced further away from the wall as the injection rate is increased [19]. In order to explain the difference between the singular blow-off when there is no pressure gradient and the gradual displacement of the shear layer when a pressure gradient is present Kassoy (1970) [43] and Klemp & Acrivos (1972) [46] developed weakly interacting theories of injection when the blowing is greater than the critical value. The weakly interacting solution developed predicts that the shear stress at the wall decreases as K_B increases when K_B is less than the critical value and then increases as K_B increases when K_B is greater than the critical value with a singularity occuring at $K_B \approx 0.876$.

The apparent problems at the critical value of K_B were later elucidated by Kassoy (1974) [44] as he showed that the asymptotic structure of the solution is easily disrupted. It was shown that as the shear layer displacement increases a weak favourable pressure is created in the outer flow which in turn avoids the singularity and regularises the flow. This phenomena of 'blow-off', in the absence of a pressure gradient, described above seems to only be present for the classical two-dimensional states. In this thesis the base flow injection will not be present, $K_B = 0$, however it will be replaced by a short-scale injection of finite width ζ_0. As the injection slot width becomes large, $\zeta_0 \to \infty$, it is predicted that this two-dimensional injection solution is recovered.

Chapter 2

Short-scale injection into a Blasius boundary layer

Chapter 1 presented an introduction to boundary-layer theory and gave a general formulation for laminar incompressible boundary-layer flow adjacent to a semi-infinite plate using a fully three-dimensional formulation. Section 1.4 examined two-dimensional boundary-layer injection and the phenomena of 'blow-off'. So if there is injection over an increasingly wide spanwise region in a fully three-dimensional boundary layer does 'blow-off' still occur at some finite injection rate? This chapter presents the work described by Hewitt, Duck & Williams (2017) [37], along with a few additional details.

The three-dimensionality is caused by a short-scale disturbance with a spanwise length scale that is comparable to the boundary-layer thickness. The general short-scale disturbance is due to a combination of a deformed geometry profile and an injection through the surface of the plate. This chapter examines the case of a flat plate, such that $H = H' = H'' = 0$, where the short-scale disturbance is caused only by an injection through the the plate surface.

2.1 Formulation

In order to formulate the problem it is assumed that the flow is laminar, steady and incompressible. The streamwise, transverse and spanwise directions (x^*, y^*, z^*) form a Cartesian coordinate system where the plate surface is defined by $y^* = 0$, $x^* \geq 0$. Suppose that the free-stream flow is uniform with magnitude U_∞^* and as such the

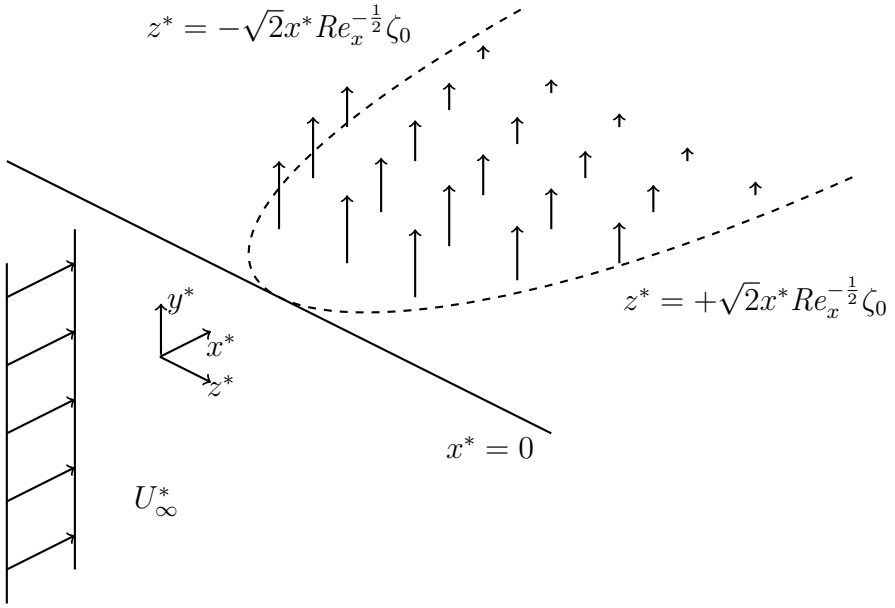

Figure 2.1.1: A schematic representation of the flow domain; the leading edge of the flat plate is located at $x^* = 0$ and the plate is aligned with an oncoming uniform flow U_∞^*. An injection perpendicular to the surface of the plate $v^* = v_w^*(x^*, z^*)$ is prescribed on $y^* = 0$ within the spanwise region specified by the dashed curve. The injection region grows downstream at the same rate as the boundary-layer thickness with ζ_0 specifying the relative width of the injection slot.

pressure gradient is given by $n = 0$ in $F(x^*) = (x^*/L^*)^n$. The injection velocity through the surface of the plate is given by $v^* = v_w^*(x^*, z^*)$ at $y^* = 0$ where v_w^* is $O(Re^{-1/2})$. A schematic diagram of the problem is given in figure 2.1.1. This set-up is difficult to achieve practically due to the self-similar nature of the injection however analogous non-similar flows would be easier to attain.

In this problem the governing equations (1.3.4) reduce to

$$2U = \Phi_\eta + \Psi_\zeta, \tag{2.1.1a}$$

$$\Theta = \Psi_\eta - \Phi_\zeta, \tag{2.1.1b}$$

$$\nabla^2 U = -\Phi U_\eta - \Psi U_\zeta, \tag{2.1.1c}$$

$$\nabla^2 \Theta = 2\left[\zeta U U_\eta - \eta U U_\zeta\right] - \Phi\Theta_\eta - \Psi\Theta_\zeta - 2U\Theta, \tag{2.1.1d}$$

where ∇^2 is the two-dimensional Laplacian in the plane spanned by the transverse and spanwise coordinates η and ζ. This system is to be solved subject to $U \to 1$, $\Psi \to \zeta$, $\Theta \to 0$ as $\eta \to \infty$ since the free-stream is uniform with no cross flow. The symmetry conditions (1.3.8) become $U_\zeta = \Phi_\zeta = \Psi = \Theta = 0$ on $\zeta = 0$ whilst for large ζ the solution is the usual flat-plate Blasius boundary layer. At the surface of the plate

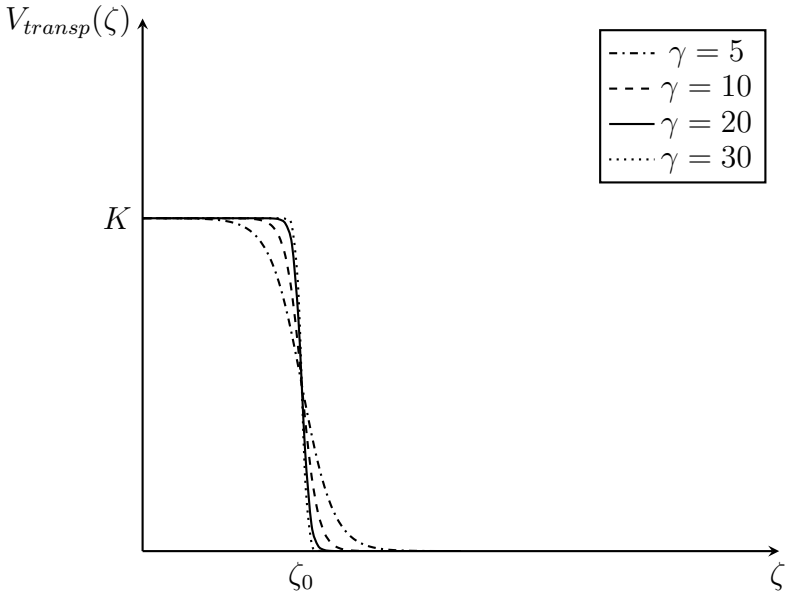

Figure 2.1.2: Injection profile given by (2.1.2) for various values of the steepness parameter γ.

($\eta = 0$) it is required that $\Psi = U = 0$, $\Theta = \Psi_\eta - \Phi_{w\zeta}$ and $\Phi = \Phi_w(\zeta) = -V_{transp}(\zeta)$. Attention is focused on the cases where the transpiration is almost uniform and exists only over a finite spanwise width, therefore the transpiration is taken to be of the form

$$V_{transp}(\zeta) = \frac{K}{2}\left(1 - \tanh\left(\gamma|\zeta/\zeta_0 - 1|\right)\right). \tag{2.1.2}$$

This functional form gives a 'top-hat' velocity profile at the surface of the plate, with ζ_0 defining the width of the injection and γ specifying the steepness of the transition from transpiration to no transpiration, see figure 2.1.2. K defines the magnitude of the short-scale transpiration with $K < 0$ indicating suction from the boundary layer and $K > 0$ indicating injection into the boundary layer. In the following analysis the steepness parameter is taken to be $\gamma = 20$ by default unless otherwise stated. The case of injection ($K > 0$) is examined throughout this chapter, rather than the simpler suction case, since fully-attached self-similar solutions exist for all $K < 0$ [69].

Two-dimensional base flow

Since for this problem there is no pressure gradient ($n = 0$) or base flow injection the base flow equations (1.3.12) reduce to

$$\Phi_B' = 2U_B - \Psi_B, \tag{2.1.3a}$$

$$\Psi_B' = \Theta_B, \tag{2.1.3b}$$

$$U_B'' = -\Phi_B U_B', \tag{2.1.3c}$$

$$\Theta_B'' = 2U_B U_B' - \Phi_B \Theta_B' - \Psi_B \Theta_B - 2U_B \Theta_B, \tag{2.1.3d}$$

subject to the boundary conditions

$$U_B(0) = \Psi_B(0) = \Phi_B(0) = 0, \tag{2.1.3e}$$

$$U_B, \Psi_B \to 1, \quad \Theta_B \to 0, \quad \text{as} \quad \eta \to \infty. \tag{2.1.3f}$$

If there is no injection into the boundary layer ($K = 0$) then the solution is provided, in terms of η only, by $(\Phi_B, \Psi_B, U_B, \Theta_B)$. The boundary value problem (2.1.3) provides two possible base flow solutions, the usual Blasius solution and a three-dimensional alternative solution. The two solutions differ in that for the Blasius solution $U_B = \Psi_B$ whereas for the alternative solution $U_B \neq \Psi_B$. Equivalently for the Blasius solution there is no cross flow ($W = 0$) unlike the alternative solution which has cross flow present ($W \neq 0$). In the following analysis it is assumed that $(\Phi_B, \Psi_B, U_B, \Theta_B)$ corresponds to the Blasius solution with no cross flow.

Short-scale nonlinear correction

For this problem the nonlinear correction equations (1.3.13) reduce to

$$\hat{\nabla}^2 \tilde{\Phi} = 2\tilde{U}_\eta - \tilde{\Theta}_{\hat{\zeta}}, \tag{2.1.4a}$$

$$\hat{\nabla}^2 \tilde{\Psi} = \frac{2}{\zeta_0^2} \tilde{U}_{\hat{\zeta}} + \tilde{\Theta}_\eta, \tag{2.1.4b}$$

$$\hat{\nabla}^2 \tilde{U} = -\left(\hat{\zeta}\Psi_B + \tilde{\Psi}\right)\tilde{U}_{\hat{\zeta}} - \Phi_B \tilde{U}_\eta - \left(U_B' + \tilde{U}_\eta\right)\tilde{\Phi}, \tag{2.1.4c}$$

$$\begin{aligned}\hat{\nabla}^2 \tilde{\Theta} =& 2\left\{\hat{\zeta}\left(U_B + \tilde{U}\right)\tilde{U}_\eta + \hat{\zeta} U_B' \tilde{U} - \frac{\eta}{\zeta_0^2}\left(U_B + \tilde{U}\right)\tilde{U}_{\hat{\zeta}}\right\} \\ & - \left(\Phi_B + \tilde{\Phi}\right)\tilde{\Theta}_\eta - \hat{\zeta}\Theta_B' \tilde{\Phi} - \hat{\zeta}\Psi_B \tilde{\Theta}_{\hat{\zeta}} - \tilde{\Psi}\left(\Theta_B + \tilde{\Theta}_{\hat{\zeta}}\right) \\ & - 2\left[\left(U_B + \tilde{U}\right)\tilde{\Theta} + \hat{\zeta}\Theta_B \tilde{U}\right],\end{aligned} \tag{2.1.4d}$$

where

$$\hat{\nabla}^2 \equiv \frac{\partial^2}{\partial\eta^2} + \frac{1}{\zeta_0^2}\frac{\partial^2}{\partial\hat{\zeta}^2}. \tag{2.1.4e}$$

It is worth noting that the nonlinear correction equations become independent of ζ_0 when $\zeta_0 \gg 1$. The surface boundary conditions remain the same as (1.3.14) such that

$$\tilde{\Phi} = \tilde{\Phi}_w(\hat{\zeta}), \quad \tilde{\Psi} = \tilde{U} = 0, \quad \tilde{\Theta} = \tilde{\Psi}_\eta - \frac{1}{\zeta_0^2}\tilde{\Phi}_{w\hat{\zeta}} \quad \text{on} \quad \eta = 0, \tag{2.1.5}$$

where the injection function is given by

$$\tilde{\Phi}_w(\hat{\zeta}) = -\frac{K}{2}\left[1 - \tanh\left(\gamma|\hat{\zeta} - 1|\right)\right]. \tag{2.1.6}$$

The symmetry boundary conditions (1.3.15) become

$$\tilde{U}_{\hat{\zeta}} = \tilde{\Phi}_{\hat{\zeta}} = \tilde{\Psi} = \tilde{\Theta} = 0, \quad \text{on} \quad \hat{\zeta} = 0. \tag{2.1.7}$$

Then for large η the far-field conditions (1.3.16) become

$$\left(\eta^2 + \zeta_0^2\hat{\zeta}^2\right)\tilde{\Phi}_\eta + \left[2\eta - \frac{\left(\eta^2 + \zeta_0^2\hat{\zeta}^2\right)}{\eta}\right]\tilde{\Phi} = 0, \tag{2.1.8a}$$

$$\left(\eta^2 + \zeta_0^2\hat{\zeta}^2\right)\tilde{\Psi}_\eta + 2\eta\tilde{\Psi} = 0, \tag{2.1.8b}$$

$$\tilde{U} = \tilde{\Theta} = 0. \tag{2.1.8c}$$

For large $\hat{\zeta}$ the far-field conditions are

$$\hat{\zeta}\tilde{U}_{\hat{\zeta}} + 2\tilde{U} = 0, \tag{2.1.9a}$$

$$\left(\eta^2 + \zeta_0^2\hat{\zeta}^2\right)\tilde{\Phi}_{\hat{\zeta}} + 2\zeta_0^2\hat{\zeta}\tilde{\Phi} = 0, \tag{2.1.9b}$$

$$\left(\eta^2 + \zeta_0^2\hat{\zeta}^2\right)\tilde{\Psi}_{\hat{\zeta}} + \left(2\zeta_0^2\hat{\zeta} - \frac{\left(\eta^2 + \zeta_0^2\hat{\zeta}^2\right)}{\hat{\zeta}}\right)\tilde{\Psi} = 0, \tag{2.1.9c}$$

$$\hat{\zeta}\tilde{\Theta}_{\hat{\zeta}} + \tilde{\Theta} = 0. \tag{2.1.9d}$$

The system (2.1.4) along with the conditions (2.1.5), (2.1.7), (2.1.8) and (2.1.9) must be solved numerically. Section 2.2 shows the results of the numerical solution of these equations.

2.2 Numerical results

Presented here is a numerical scheme for the solution of (2.1.4) which, when combined with the associated Blasius base flow, provide solutions to (2.1.1) governing flow over a flat plate with a short-scale injection through the plate surface.

2.2.1 Numerical scheme

The computational scheme used by Hewitt & Duck (2014) [35] is followed with a few modifications since a surface transpiration rather than a finite-width gap/plate is considered. The computational scheme uses a uniform grid in a stretched coordinate plane $(\bar{\zeta}, \bar{\eta})$ in order to concentrate nodes near to the injection region and close to the plate surface in the unstretched domain which is truncated at $\hat{\zeta} = \hat{\zeta}_\infty$ and $\eta = \eta_\infty$. The two functions $\bar{\zeta} = \bar{\zeta}(\hat{\zeta})$ and $\bar{\eta} = \bar{\eta}(\eta)$ are chosen in order to concentrate nodal points near to the boundary $\eta = 0$ and near to the transpiration region $\hat{\zeta} \leq 1$. For example the functions $\bar{\zeta}(\hat{\zeta}) = \left(\hat{\zeta} + a_1\right)^{a_2}$ and $\bar{\eta}(\eta) = (\eta + b_1)^{b_2}$ may be chosen where a_1, a_2, b_1 and b_2 are specified parameters. In the new $(\bar{\zeta}, \bar{\eta})$ variables the $\hat{\zeta}$ and η derivatives may be written as

$$\begin{aligned}
&\frac{\partial}{\partial\hat{\zeta}} = \bar{\zeta}'\frac{\partial}{\partial\bar{\zeta}}, \quad \frac{\partial}{\partial\eta} = \bar{\eta}'\frac{\partial}{\partial\bar{\eta}}, \quad \frac{\partial^2}{\partial\eta\partial\hat{\zeta}} = \bar{\eta}'\bar{\zeta}'\frac{\partial^2}{\partial\bar{\eta}\partial\bar{\zeta}}, \\
&\frac{\partial^2}{\partial\hat{\zeta}^2} = \bar{\zeta}''\frac{\partial}{\partial\bar{\zeta}} + \left(\bar{\zeta}'\right)^2\frac{\partial^2}{\partial\bar{\zeta}^2}, \quad \frac{\partial^2}{\partial\eta^2} = \bar{\eta}''\frac{\partial}{\partial\bar{\eta}} + \left(\bar{\eta}'\right)^2\frac{\partial^2}{\partial\bar{\eta}^2},
\end{aligned} \tag{2.2.1}$$

here $\bar{\zeta}'$ and $\bar{\eta}'$ are the derivatives with respect to $\hat{\zeta}$ and η respectively. Using these functions the perturbation equations (2.1.4) can be reformulated in the $(\bar{\zeta}, \bar{\eta})$-plane and then the resulting equations can be solved numerically on a uniform computational mesh in $(\bar{\zeta}, \bar{\eta})$.

The short-scale correction equations and boundary conditions are approximated by second-order finite difference equations. The partial derivatives in the transformed equations are approximated with central differences such that

$$\tilde{X}_{\bar{\eta}\bar{\eta}} = \frac{\tilde{X}(\bar{\zeta}, \bar{\eta} + \Delta\bar{\eta}) - 2\tilde{X}(\bar{\zeta}, \bar{\eta}) + \tilde{X}(\bar{\zeta}, \bar{\eta} - \Delta\bar{\eta})}{(\Delta\bar{\eta})^2}, \tag{2.2.2a}$$

$$\tilde{X}_{\bar{\zeta}\bar{\zeta}} = \frac{\tilde{X}(\bar{\zeta} + \Delta\bar{\zeta}, \bar{\eta}) - 2\tilde{X}(\bar{\zeta}, \bar{\eta}) + \tilde{X}(\bar{\zeta} - \Delta\bar{\zeta}, \bar{\eta})}{\left(\Delta\bar{\zeta}\right)^2}, \tag{2.2.2b}$$

$$\begin{aligned}
\tilde{X}_{\bar{\eta}\bar{\zeta}} = &\frac{\tilde{X}(\bar{\zeta} + \Delta\bar{\zeta}, \bar{\eta} + \Delta\bar{\eta}) + \tilde{X}(\bar{\zeta} - \Delta\bar{\zeta}, \bar{\eta} - \Delta\bar{\eta})}{4\left(\Delta\bar{\zeta}\right)(\Delta\bar{\eta})} \\
&- \frac{\tilde{X}(\bar{\zeta} + \Delta\bar{\zeta}, \bar{\eta} - \Delta\bar{\eta}) + \tilde{X}(\bar{\zeta} - \Delta\bar{\zeta}, \bar{\eta} + \Delta\bar{\eta})}{4\left(\Delta\bar{\zeta}\right)(\Delta\bar{\eta})},
\end{aligned} \tag{2.2.2c}$$

$$\tilde{X}_{\bar{\eta}} = \frac{\tilde{X}(\bar{\zeta}, \bar{\eta} + \Delta\bar{\eta}) - \tilde{X}(\bar{\zeta}, \bar{\eta} - \Delta\bar{\eta})}{2(\Delta\bar{\eta})}, \tag{2.2.2d}$$

$$\tilde{X}_{\bar{\zeta}} = \frac{\tilde{X}(\bar{\zeta} + \Delta\bar{\zeta}, \bar{\eta}) - \tilde{X}(\bar{\zeta} - \Delta\bar{\zeta}, \bar{\eta})}{2\left(\Delta\bar{\zeta}\right)}, \tag{2.2.2e}$$

where $\tilde{X}$ represents any of the correction variables. Here $\Delta\bar{\zeta}$ and $\Delta\bar{\eta}$ are the mesh interval sizes in the $\bar{\zeta}$ and $\bar{\eta}$ directions respectively given by

$$\Delta\bar{\zeta} = \frac{\bar{\zeta}(\hat{\zeta}_\infty) - \bar{\zeta}(0)}{N_{\hat{\zeta}} - 1} \quad \text{and} \quad \Delta\bar{\eta} = \frac{\bar{\eta}(\hat{\eta}_\infty) - \bar{\eta}(0)}{N_\eta - 1}, \tag{2.2.3}$$

where $N_{\hat{\zeta}}$ and N_η are the number of nodes in the $\bar{\zeta}$ and $\bar{\eta}$ directions. At the grid point $(\bar{\zeta}_i, \bar{\eta}_j) = (i\Delta\bar{\zeta} + \bar{\zeta}(0), j\Delta\bar{\eta} + \bar{\eta}(0))$ the approximation to each $\tilde{X}(\bar{\zeta}, \bar{\eta})$ is given by $\tilde{X}_{i,j} = \tilde{X}(\bar{\zeta}_i, \bar{\eta}_j)$ for $i = 0, 1, \ldots, N_{\hat{\zeta}} - 1$ and $j = 0, 1, \ldots, N_\eta - 1$. On this $N_{\hat{\zeta}} \times N_\eta$ grid each of the four equations in (2.1.4) is replaced by its finite difference approximation.

At the boundaries it is not possible to approximate derivatives by the above central differences as they would include points which are outside of the computational domain. In order to maintain second-order accuracy it is necessary to formulate a finite difference approximation based on the Lagrange interpolation of the points at the boundary. At $\hat{\zeta} = 0$ ($i = 0$) and $\bar{\zeta} = \bar{\zeta}(0)$ (2.2.2e) is replaced with

$$\tilde{X}_{\bar{\zeta}} = \frac{-3\tilde{X}(\bar{\zeta}, \bar{\eta}) + 4\tilde{X}(\bar{\zeta} + \Delta\bar{\zeta}, \bar{\eta}) - \tilde{X}(\bar{\zeta} + 2\Delta\bar{\zeta}, \bar{\eta})}{2\left(\Delta\bar{\zeta}\right)}, \tag{2.2.4}$$

and at $\eta = 0$ ($j = 0$) and $\bar{\eta} = \bar{\eta}(0)$ (2.2.2d) is replaced with

$$\tilde{X}_{\bar{\eta}} = \frac{-3\tilde{X}(\bar{\zeta}, \bar{\eta}) + 4\tilde{X}(\bar{\zeta}, \bar{\eta} + \Delta\bar{\eta}) - \tilde{X}(\bar{\zeta}, \bar{\eta} + 2\Delta\bar{\eta})}{2\left(\Delta\bar{\eta}\right)}. \tag{2.2.5}$$

Similarly at $\eta = \eta_\infty$ ($j = N_\eta - 1$) and $\bar{\eta} = \bar{\eta}(\eta_\infty)$ (2.2.2d) is replaced with

$$\tilde{X}_{\bar{\eta}} = \frac{3\tilde{X}(\bar{\zeta}, \bar{\eta}) - 4\tilde{X}(\bar{\zeta}, \bar{\eta} - \Delta\bar{\eta}) + \tilde{X}(\bar{\zeta}, \bar{\eta} - 2\Delta\bar{\eta})}{2\left(\Delta\bar{\eta}\right)} \tag{2.2.6}$$

and at $\hat{\zeta} = \hat{\zeta}_\infty$ ($i = N_{\hat{\zeta}} - 1$) and $\bar{\zeta} = \bar{\zeta}(\hat{\zeta}_\infty)$ (2.2.2e) is replaced with

$$\tilde{X}_{\bar{\zeta}} = \frac{3\tilde{X}(\bar{\zeta}, \bar{\eta}) - 4\tilde{X}(\bar{\zeta} - \Delta\bar{\zeta}, \bar{\eta}) + \tilde{X}(\bar{\zeta} - 2\Delta\bar{\zeta}, \bar{\eta})}{2\left(\Delta\bar{\zeta}\right)}. \tag{2.2.7}$$

The resulting nonlinear system is solved by Newton iteration, with the correction variables being split into a known/guessed part and a correction such that $\tilde{X} = \tilde{X}^G + \tilde{X}^C$. Here the superscript G indicates a known/guessed value and C indicates a correction to this known value. Linearising the equations and the boundary conditions, by ignoring terms of order correction squared, gives a linear system of equations for the correction terms. This gives, for example, central finite-difference approximations of the form

$$\tilde{X}_{\hat{\zeta}} = \frac{\bar{\zeta}_i'}{2\Delta\bar{\zeta}}\left(\tilde{X}^C_{i+1,j} - \tilde{X}^C_{i-1,j} + \tilde{X}^G_{i+1,j} - \tilde{X}^G_{i-1,j}\right), \tag{2.2.8}$$

and similar expressions for $\tilde{X}_{\eta}$, $\tilde{X}_{\hat{\zeta}\hat{\zeta}}$, $\tilde{X}_{\eta\hat{\zeta}}$ and $\tilde{X}_{\eta\eta}$ with slight modifications at the boundaries of the domain. This Newton iteration process is used to determine the four unknowns $(\tilde{\Phi}^C, \tilde{\Psi}^C, \tilde{U}^C, \tilde{\Theta}^C)$ at each nodal location along with the correction to the mass flux coefficient A^C. Using the above finite-difference approximations enables the system of equations to be written in the form $\mathbf{Au} = \mathbf{b}$ where

$$\mathbf{u} = \Big[\tilde{\Phi}^C_{0,0}, \tilde{\Psi}^C_{0,0}, \tilde{U}^C_{0,0}, \tilde{\Theta}^C_{0,0}, \tilde{\Phi}^C_{0,1}, \ldots, \tilde{\Theta}^C_{0,M}, \tilde{\Phi}^C_{1,0}, \tilde{\Psi}^C_{1,0}, \tilde{U}^C_{1,0}, \tilde{\Theta}^C_{1,0}, \tilde{\Phi}^C_{1,1}, \ldots, \\ \tilde{\Phi}^C_{N,0}, \tilde{\Psi}^C_{N,0}, \tilde{U}^C_{N,0}, \tilde{\Theta}^C_{N,0}, \tilde{\Phi}^C_{N,1}, \ldots, \tilde{\Phi}^C_{N,M}, \tilde{\Psi}^C_{N,M}, \tilde{U}^C_{N,M}, \tilde{\Theta}^C_{N,M}, A^C\Big]^T \tag{2.2.9}$$

and $\mathbf{A}$ and $\mathbf{b}$ are determined by the coefficients in the finite-difference equations for each variable at each nodal point. The resulting sparse linear system for the $4N_{\hat{\zeta}}N_{\eta} + 1$ unknowns, where $N_{\hat{\zeta}}$ and N_{η} are the number of nodes in the $\hat{\zeta}$ and η directions respectively, is solved at each iteration using supernodal LU factorization for general matrices implemented by the Eigen library Guennebaud et al. (2010) [27]. Newton iteration is continued until the correction terms are of sufficiently small magnitude that they may be neglected, usually 10^{-8} or smaller.

Typical computational parameters are $\hat{\zeta}_{\infty} = 16$, $\eta_{\infty} = 128$ and $N_{\hat{\zeta}} = N_{\eta} = 401$ i.e. approximately 6.4×10^5 degrees of freedom. The numerical results shown below are independent of the computational parameters $\hat{\zeta}_{\infty}$, η_{∞}, $N_{\hat{\zeta}}$, N_{η} and the spacing functions $\bar{\zeta}(\hat{\zeta})$ and $\bar{\eta}(\hat{\eta})$ as they have been performed on a range of different mesh sizes, with different values of $\hat{\zeta}_{\infty}$ and η_{∞} and using different spacing functions, including uniform spacing.

2.2.2 Results

When $K = 0$ there is no short-scale injection through the surface of the plate and the Blasius base flow solution is recovered. The short spanwise scale injection through the plate surface causes a three-dimensional correction to the underlying base flow which is determined by the parameters K and ζ_0 in (2.1.2) describing the injection rate and the width of the injection region respectively. Classical work on two-dimensional boundary layers ($\zeta_0 \to \infty$) predicts that increasing the injection rate leads to boundary-layer detachment at a critical injection rate of $K \approx 0.876$ as described in section 1.4.3. It is clearly important to understand to what extent are the classical two-dimensional results recovered for three-dimensional injections over increasing slot widths. When

$\zeta_0 \gg 1$ is there still a critical injection rate which produces boundary layer detachment? And is the two-dimensional critical injection rate $K \approx 0.876$ still significant?

Combining the numerical solution of the short-scale correction equations (2.1.4) with the two-dimensional base flow equations (2.1.3) provides a numerical solution of (2.1.1). For an injection through the plate surface, $K > 0$, the flow can be categorised into distinct types for increasing injection width ζ_0. The numerical results presented below are for a surface injection (2.1.2) with a large fixed injection slot width $\zeta_0 = 20$ and steepness parameter $\gamma = 20$. Using different values of the injection amplitude, $K = 0.5, 1.5, 2.5$, the different types of flow response are exemplified and the physical characteristics of each is discussed. The weak injection regime $0 < K < K_I$ is examined first, where K_I is the critical injection rate for the weak regime.

Weak injection $0 < K < K_I$

For a sufficiently small injection rate the flow response exists in the first regime as illustrated by figures 2.2.1(a,b) for $K = 0.5$. Figure 2.2.1(a) shows the streamwise velocity U and (b) shows the perturbation vorticity $\zeta_0\tilde{\Theta}$ along with the particle path lines in the $(\hat{\zeta}, \eta)$ plane. In this regime there is only a slight thickening of the boundary layer near to $\hat{\zeta} = 0$ however in the rest of the domain the response remains largely two-dimensional. The injection flow does not significantly impact the response as there is not sufficient blowing to cause the layer to be displaced from the surface. The shear at the surface of the plate, $U_\eta(\eta = 0)$, remains positive throughout the domain being equal to the Blasius value for $\hat{\zeta} \gg 1$ and reducing throughout the injection region until reaching a minimum at $\hat{\zeta} = 0$.

Although this weak injection does not cause displacement of the shear layer away from the surface it does cause a slight reduction in the streamwise mass flux due to the increase in the thickness of the layer. This reduction in the streamwise mass flux must be compensated for by an increase in the spanwise and transverse mass flux. This increased mass flux due to the injection and the displacement it induces means that as K increases so does the mass flux parameter A.

The flow response remains in this weak injection regime for values of the injection amplitude below $K_I \approx 0.876$. As shall be demonstrated in section 2.3 this critical 'blow-off' injection rate from the two-dimensional theory also plays a significant role

in the three-dimensional description by delineating the boundary between the weak and moderate injection regimes. Unlike the classical two-dimensional problem 'blow-off' does not occur at this critical value K_I; three-dimensional solutions for $K > K_I$ are still able to be found.

Moderate injection $K_I < K < K_{II}$

As the injection rate is increased above the first critical value K_I there is a significant alteration to the flow response in the injection region ($0 \leq \hat{\zeta} \leq 1$). In the three-dimensional problem, described by the boundary-region equations (2.1.1), 'blow-off' does not occur, instead a solution is obtained which has very low wall shear near to the centre of the injection region. When the injection rate is greater than the first critical value K_I but below a second critical value K_{II} a low-speed streak develops as shown in figure 2.2.2(a) where $U \approx 0$ inside the streak. In this moderate injection regime there is a vorticity component which is displaced away from the plate surface as shown in figure 2.2.2(b). Unlike the weak injection regime the moderate injection regime is characterised by a displaced shear layer which separates the low-speed streamwise flow inside the streak with the higher speed outer flow. It appears that the shear layer has almost constant curvature near to $\hat{\zeta} = 0$ however the shear layer ceases to be circular at a finite angle that is dependent upon the rate of injection.

As the width of the injection slot is increased the low-speed streak becomes more prominent which in turn creates a significant reduction in the streamwise mass flux. The reduction in the streamwise mass flux caused by the streak must be compensated for by an increase in the in-plane mass flux. This moderate injection regime exists for injection rates $K_I < K < K_{II}$ where $K_I \approx 0.876$ and the asymptotic theory presented in section 2.3, along with the numerical evidence, indicates that $K_{II} \approx 1.95$. The numerical evidence suggests that the transition between the regimes is a smooth function of the injection rate K. The asymptotic theory however provides a clear indication of when transition between the regimes occurs in a manner which is consistent with the numerical evidence.

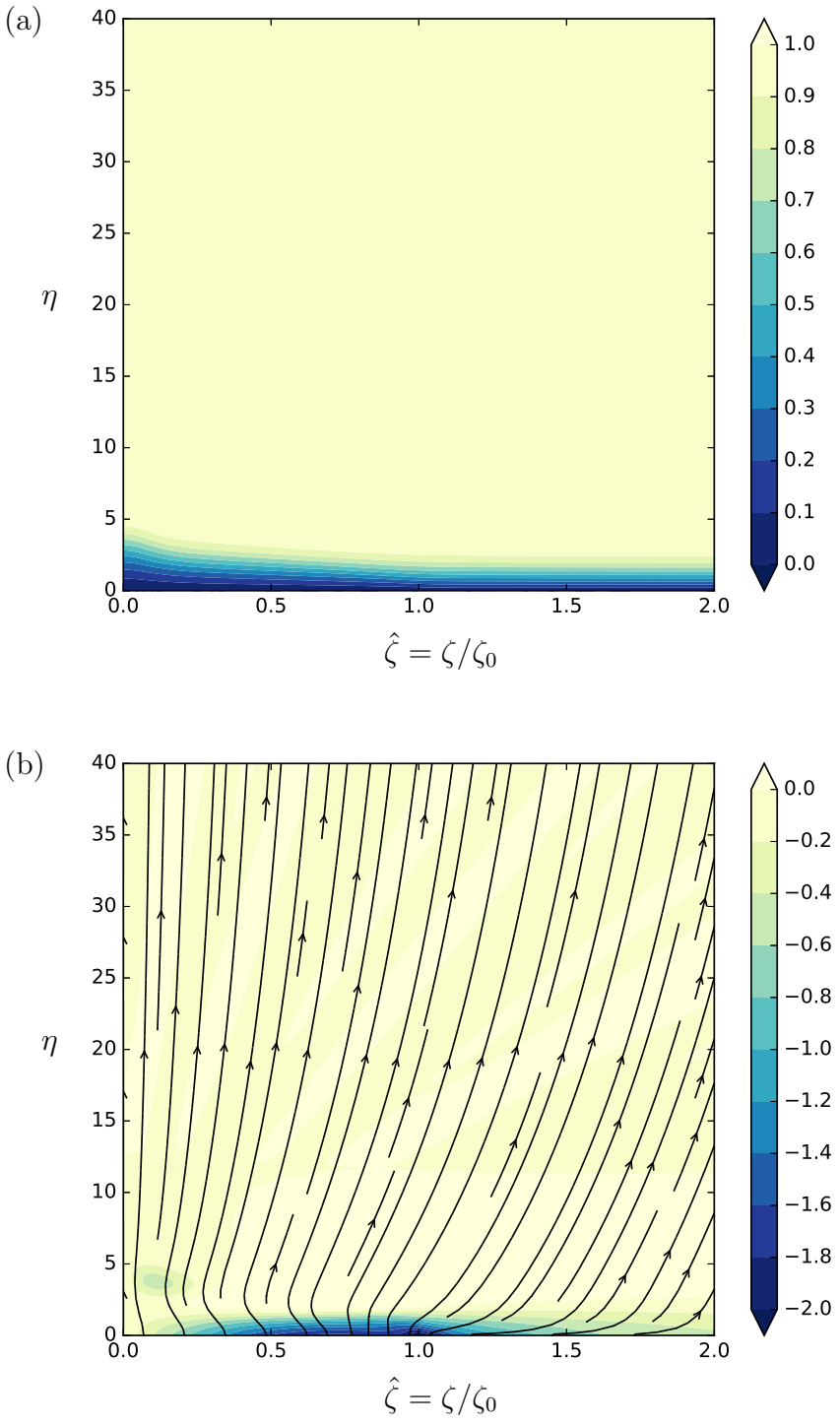

Figure 2.2.1: Results are shown for a wall transpiration (2.1.2), where $K = 0.5$. (a) shows contours of the streamwise velocity U and (b) shows the perturbation vorticity $\zeta_0\tilde{\Theta}$ and the (V, W) particle path lines (1.3.2).

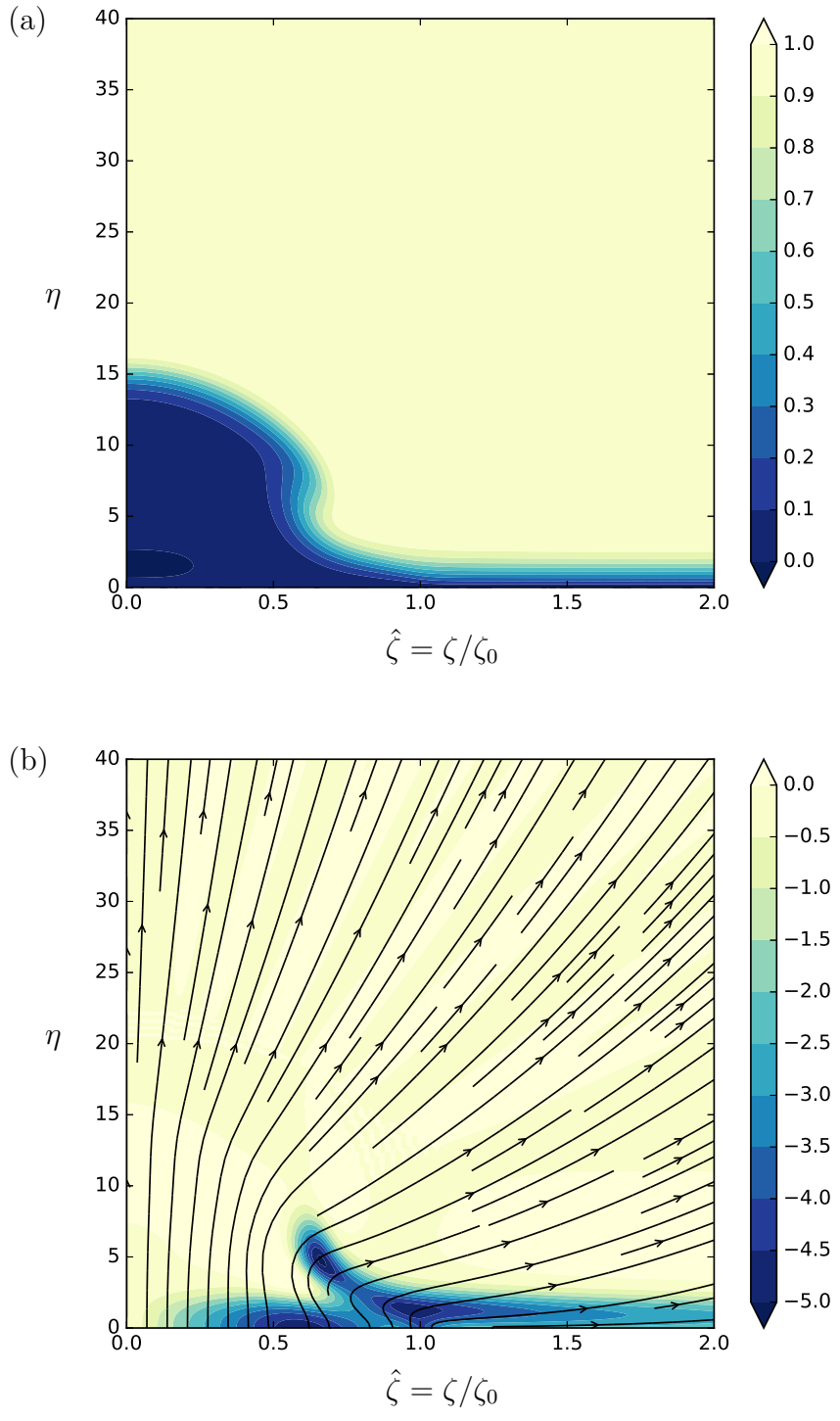

Figure 2.2.2: Results are shown for a wall transpiration (2.1.2), where $K = 1.5$. (a) shows contours of the streamwise velocity U and (b) shows the perturbation vorticity $\zeta_0\tilde{\Theta}$ and the (V, W) particle path lines (1.3.2).

Strong injection $K > K_{II}$

Increasing the injection rate past the second critical value K_{II} the flow response enters the strong injection regime. The strong injection regime is characterised by a semi-circular low-speed streak as shown in figure 2.2.3(a). The large low-speed streak extends past the edge of the injection slot located at $\zeta/\zeta_0 = 1$; the streak is approximately circular, with radius $O(\zeta_0)$, except for a small region near to the plate surface. The low-speed region inside the streak, where $U \approx 0$, is connected to the higher speed outer flow by a thin shear layer in which the velocity varies rapidly.

The significant impact of the fluid injection on the flow can be seen by the dramatic alteration to the (V, W) particle paths shown in figure 2.2.3(b) when compared with figure 2.2.1(b). The injection through the surface of the plate, and the resulting low-speed streak, causes a significant increase in the mass flux from the boundary layer. The small streamwise speeds inside the streak necessitates that the extra mass injected through the plate surface is ejected radially through the shear layer. Despite this being three-dimensional downstream developing flow, it is possible to predict the streak radius, along with the mass flux parameter A, by matching the mass exiting through the shear layer to the mass entering through the injection slot.

The three distinct regimes behave very differently from one another in regard to both the streamwise and cross-sectional flow response. In order to obtain a better understanding of the mechanisms involved in each of the regimes it useful to understand the behaviour of the flow as the injection slot becomes large. By taking the asymptotic limit $\zeta_0 \to \infty$ it is possible to gain a better understanding of the flow response and the delineation between the regimes.

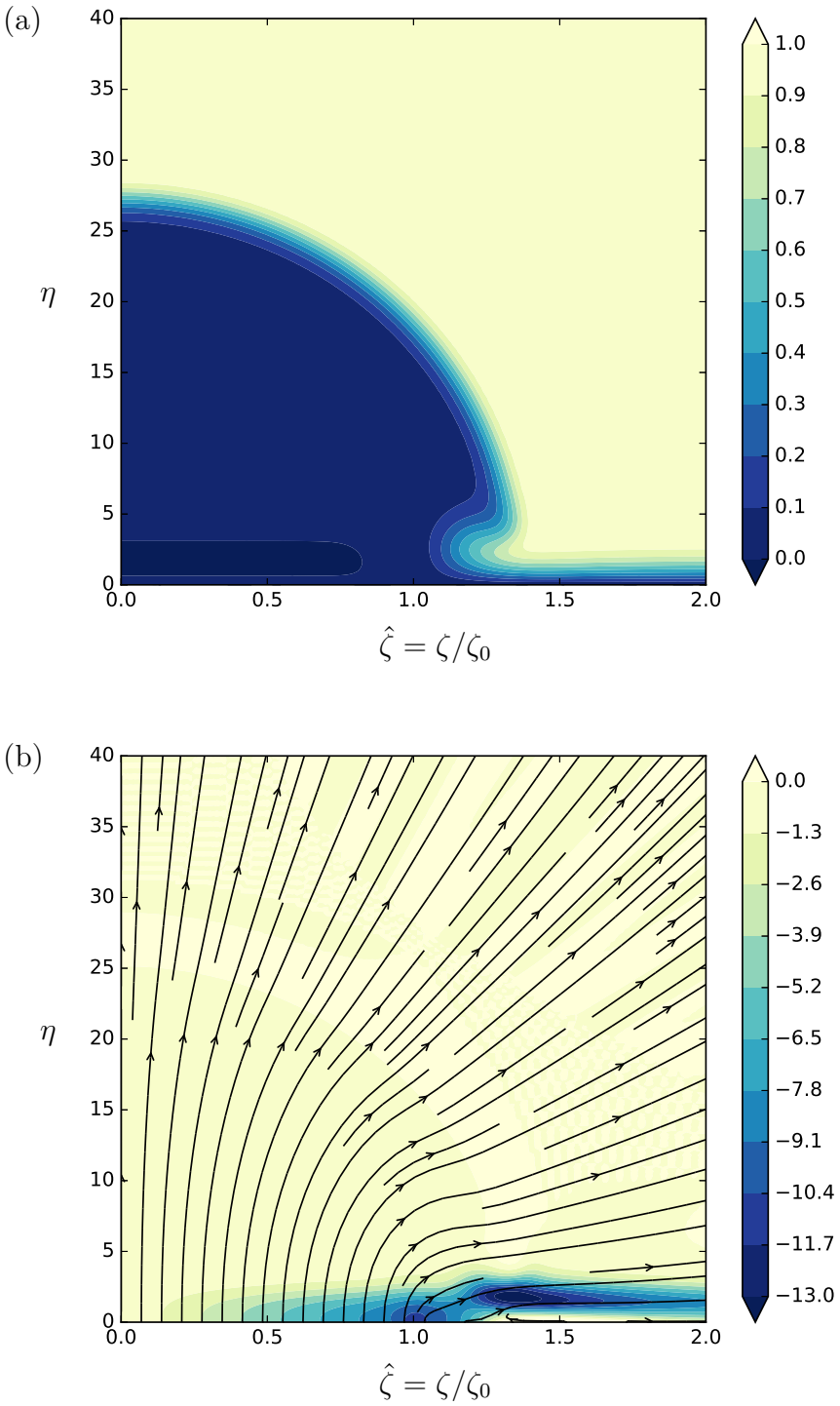

Figure 2.2.3: Results are shown for a wall transpiration (2.1.2), where $K = 2.5$. (a) shows contours of the streamwise velocity U and (b) shows the perturbation vorticity $\zeta_0\tilde{\Theta}$ and the (V, W) particle path lines (1.3.2).

2.3 Asymptotic results

In this section asymptotic descriptions for each of the three flow regimes described in the section 2.2 will be presented in the limit of a large injection slot, $\zeta_0 \to \infty$.

2.3.1 Weak injection

Firstly the weak injection regime shown in figure 2.2.1 for which $K < K_I$ is examined. For this regime a viscous layer is present across the injection slot hence there is an inner region where $\eta = O(1)$ and $\zeta = O(\zeta_0)$. It is advantageous to use the rescaled coordinate $\hat{\zeta} = \zeta/\zeta_0$ and

$$U(\zeta, \eta; \zeta_0) = U_0(\hat{\zeta}, \eta) + \ldots, \tag{2.3.1a}$$

$$\Phi(\zeta, \eta; \zeta_0) = \Phi_0(\hat{\zeta}, \eta) + \ldots, \tag{2.3.1b}$$

$$\Psi(\zeta, \eta; \zeta_0) = \zeta_0\hat{\zeta}\Psi_0(\hat{\zeta}, \eta) + \ldots, \tag{2.3.1c}$$

$$\Theta(\zeta, \eta; \zeta_0) = \zeta_0\hat{\zeta}\Theta_0(\hat{\zeta}, \eta) + \ldots. \tag{2.3.1d}$$

Substituting these into the governing equations (2.1.1), taking the limit $\zeta_0 \to \infty$, produces the system

$$2U_0 = \Phi_{0\eta} + \hat{\zeta}\Psi_{0\hat{\zeta}} + \Psi_0, \tag{2.3.2a}$$

$$\Theta_0 = \Psi_{0\eta}, \tag{2.3.2b}$$

$$U_{0\eta\eta} = -\Phi_0 U_{0\eta} - \hat{\zeta}\Psi_0 U_{0\hat{\zeta}}, \tag{2.3.2c}$$

$$\Theta_{0\eta\eta} = 2U_0U_{0\eta} - \Phi_0\Theta_{0\eta} - 2U_0\Theta_0 - \hat{\zeta}\Psi_0\Theta_{0\hat{\zeta}} - \Psi_0\Theta_0. \tag{2.3.2d}$$

In this system, which is parabolic in $\hat{\zeta}$, the terms involving the second derivative in ζ have been lost, due to the large slot width, therefore spanwise diffusion is neglected. This system of equations is subject to the boundary conditions $U_0 = \Psi_0 = 0$, $\Phi_0 = \Phi_w$ on $\eta = 0$ and $U_0, \Psi_0 \to 1$, $\Theta_0 \to 0$ as $\eta \to \infty$. If $\Psi_0 > 0$ for all $\eta > 0$ this system can be marched from $\hat{\zeta} = \hat{\zeta}_\infty$ towards $\hat{\zeta} = 0$, the starting solution at $\hat{\zeta} = \hat{\zeta}_\infty$ is the Blasius similarity solution without any transpiration. Starting the parabolic system from the Blasius solution in the far field requires that, $\Psi_0 = U_0$. which means there is no cross flow ($W = 0$) in (1.3.2). This absence of cross flow is retained as the system

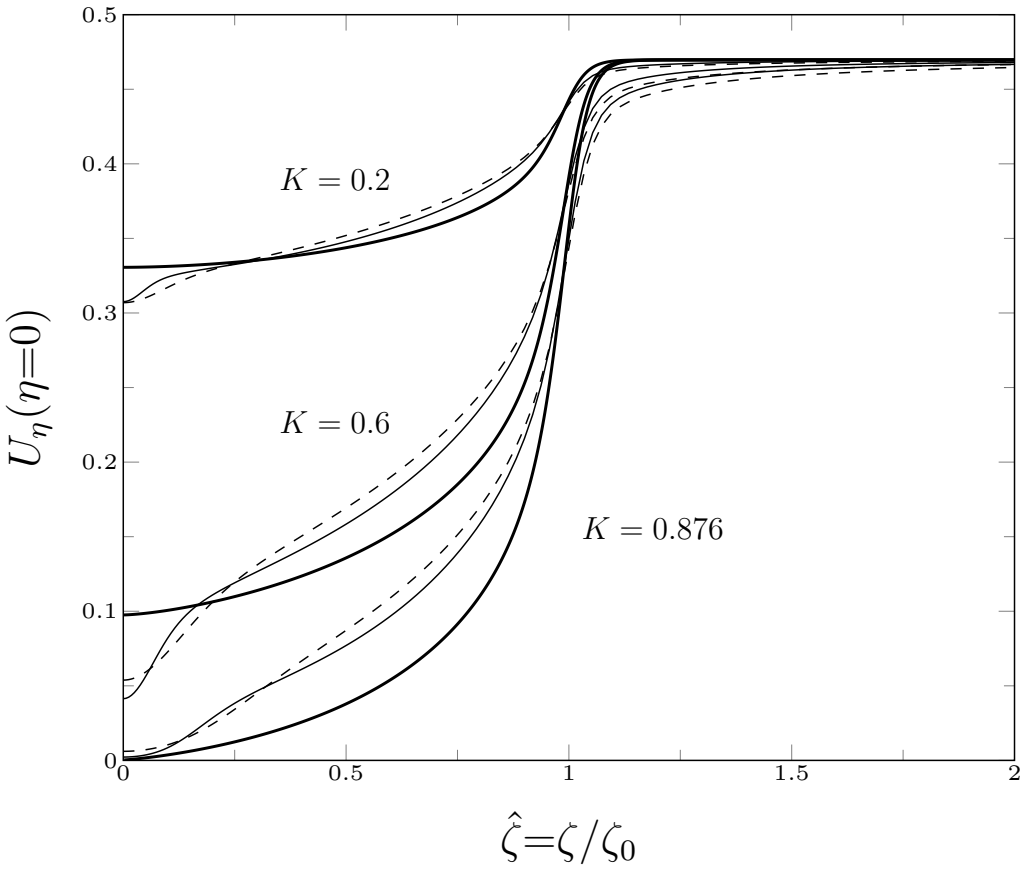

Figure 2.3.1: Shear stress distribution at the surface of the plate $U_\eta(\eta = 0, \hat{\zeta})$ for $\zeta_0 = 20$ (dashed) and $\zeta_0 = 40$ (solid) for $K = 0.2, 0.6$ and 0.876 from the solution of (2.1.1). The wall shear distribution predicted by the parabolic system (2.3.3) is also shown as the thicker solid lines.

is marched towards $\hat{\zeta} = 0$ hence the parabolic system (2.3.2) reduces to

$$U_0 = \Phi_{0\eta} + \hat{\zeta} U_{0\hat{\zeta}}, \tag{2.3.3a}$$

$$U_{0\eta\eta} = -\Phi_0 U_{0\eta} - \hat{\zeta} U_0 U_{0\hat{\zeta}}, \tag{2.3.3b}$$

with the boundary conditions $U_0 = 0$, $\Phi_0 = \Phi_w$ on $\eta = 0$ and $U_0 \to 1$ as $\eta \to \infty$.

Setting $\hat{\zeta} = 0$, with the assumption that $\hat{\zeta}$ derivatives can be neglected, (2.3.3) becomes the Blasius equation subject to an injection at the surface (1.4.7). It is tempting to assume that, for sufficiently large slot widths, the Blasius solution with injection is always recovered at the centreline of the injection region however this assumption is invalid. Figure 2.3.1 shows the shear stress distribution along the surface of the plate for solutions of the governing boundary-region equations (2.1.1) and the parabolic system (2.3.3). The full numerical solutions, given for $\zeta_0 = 20, 40$, approach the asymptotic prediction as the injection slot width ζ_0 is increased except in a small

region around $\hat{\zeta} = 0$. This deviation from the asymptotic prediction for $\hat{\zeta} \ll 1$ is due to spatially unstable, in $\hat{\zeta}$, three-dimensional eigensolutions which shall be discussed in section 2.4.

The parabolic solution, unlike the full solution, terminates at $\hat{\zeta} = 0$ with the two-dimensional Blasius state (1.4.7) for which solutions only exist for $K \leq K_I \approx 0.876$. Marching of the parabolic system (2.3.3) when $K > K_I$ leads to a singular response at a finite value of $\hat{\zeta}$ when the wall shear stress becomes equal to zero. Figure 2.3.1 shows how the shear stress distribution approaches to zero at $\hat{\zeta} = 0$ when $K = 0.876$.

For large η the first two equations in (2.3.2) are of the form

$$\Phi_{0\eta} = 1 - \hat{\zeta}\Psi_{0\hat{\zeta}}, \tag{2.3.4a}$$

$$\Psi_{0\eta} = 0. \tag{2.3.4b}$$

This means that, since $\Psi_0(\hat{\zeta}) = 1$ in the far-field, $\Phi_{0\eta} \sim 1$. It follows that for large η the vertical velocity component in the parabolic solution is of the form

$$\Phi_0 \sim \eta + \delta_B + \delta_{transp}(\hat{\zeta}). \tag{2.3.5}$$

Here $\delta_B \approx -1.2$ is the constant displacement thickness associated with the Blasius solution for flow on a flat plate. There also exists a displacement which is varying in the spanwise direction $\delta_{transp}(\hat{\zeta})$ due to the wall transpiration over a finite spanwise region. If there is no transpiration from the surface, $K = 0$, then $\delta_{transp} = 0$ and there is no $\hat{\zeta}$-dependent perturbation to the Blasius solution, however in general this perturbation must be taken into account.

Now consider the outer region and look for a perturbation to the Blasius similarity solution. In this outer region $\eta = \zeta_0\hat{\eta}$ and $\zeta = \zeta_0\hat{\zeta}$; the vertical velocity component may be written as

$$\Phi(\zeta, \eta) = \Phi_B(\eta) + \phi(\hat{\zeta}, \hat{\eta}), \tag{2.3.6}$$

where Φ_B is the Blasius solution and $\phi = O(1)$ in order to match with the $\delta_{transp}(\hat{\zeta})$ induced by the parabolic solution near to the boundary. Rewriting (2.1.1a) and (2.1.1b) in terms of $\hat{\zeta}$ and $\hat{\eta}$ gives

$$\zeta_0\Phi_B' + \phi_{\hat{\eta}} + \Psi_{\hat{\zeta}} = 2\zeta_0 U, \tag{2.3.7a}$$

$$\Psi_{\hat{\eta}} - \phi_{\hat{\zeta}} = \zeta_0\Theta. \tag{2.3.7b}$$

Numerical evidence suggests that both U and Θ remain $o(\zeta_0^{-2})$ therefore multiplying (2.3.7) by ζ_0 and taking appropriate limits yields

$$\zeta_0^2 \Phi_B' + \zeta_0 \phi_{\hat{\eta}} + \zeta_0 \Psi_{\hat{\zeta}} = 0, \tag{2.3.8a}$$

$$\zeta_0 \Psi_{\hat{\eta}} - \zeta_0 \phi_{\hat{\zeta}} = 0. \tag{2.3.8b}$$

Differentiating (2.3.8a) by η and (2.3.8b) by ζ gives

$$\zeta_0^2 \Phi_B'' + \phi_{\hat{\eta}\hat{\eta}} + \Psi_{\hat{\zeta}\hat{\eta}} = 0, \tag{2.3.9a}$$

$$\Psi_{\hat{\eta}\hat{\zeta}} - \phi_{\hat{\zeta}\hat{\zeta}} = 0. \tag{2.3.9b}$$

Since $\Phi_B \sim \eta + \delta_B$ in this outer region it follows that $\Phi_B'' = 0$ and hence

$$\phi_{\hat{\eta}\hat{\eta}} + \phi_{\hat{\zeta}\hat{\zeta}} = \hat{\nabla}^2 \phi = 0, \tag{2.3.10a}$$

subject to the boundary condition

$$\phi(\hat{\zeta}, \hat{\eta} = 0) = \delta_{transp}(\hat{\zeta}), \tag{2.3.10b}$$

here $\delta_{transp}(\hat{\zeta})$ is determined by solution of the parabolic system (2.3.3). It is also possible to obtain a similar Laplace problem for the corresponding Ψ velocity perturbation $\psi(\hat{\zeta}, \hat{\eta})$.

The solution to the outer problem (2.3.10) can be found by using a Green's function approach. Consider the Dirichlet boundary value problem for Laplace's equation in the domain $D = \{\hat{\eta} \geq 0, -\infty < \hat{\zeta} < \infty\}$ given by

$$\hat{\nabla}^2 \phi = 0 \quad \text{in} \quad D \tag{2.3.11a}$$

with

$$\phi = f(\hat{\zeta}) = \delta_{transp}(\hat{\zeta}) \quad \text{on} \quad S \tag{2.3.11b}$$

where $S = \{\hat{\eta} = 0, -\infty < \hat{\zeta} < \infty\}$. Let the Green's function

$$G(\hat{\zeta}, \hat{\eta}, X, Y) = -\frac{1}{4\pi} \log \left(\frac{\left(\hat{\zeta} - X\right)^2 + (\hat{\eta} - Y)^2}{\left(\hat{\zeta} - X\right)^2 + (\hat{\eta} + Y)^2} \right) \tag{2.3.12}$$

be proposed, noting that setting $\hat{\eta} = 0$ gives $G(\hat{\zeta}, 0, X, Y) = 0$ as required. The solution to the boundary value problem is then given by

$$\phi(X, Y) = -\int_S f \frac{\partial G}{\partial \hat{\eta}} \mathrm{d}S. \tag{2.3.13}$$

The derivative of the Green's function for the boundary $\hat{\eta} = 0$ is required, which is

$$\left.\frac{\partial G}{\partial \hat{\eta}}\right|_S = -\left.\frac{\partial G}{\partial \hat{\eta}}\right|_{\hat{\eta}=0} = -\frac{1}{\pi}\frac{Y}{\left(\hat{\zeta} - X\right)^2 + Y^2}. \tag{2.3.14}$$

Thus

$$\phi(X, Y) = \frac{Y}{\pi}\int_{-\infty}^{+\infty} \frac{\delta_{transp}(\hat{\zeta})}{(\hat{\zeta} - X)^2 + Y^2}\mathrm{d}X, \tag{2.3.15}$$

which may be relabelled to get, in the original variables,

$$\phi(\hat{\zeta}, \hat{\eta}) = \frac{\hat{\eta}}{\pi}\int_{\lambda=-\infty}^{+\infty} \frac{\delta_{transp}(\lambda)}{(\lambda - \hat{\zeta})^2 + \hat{\eta}^2}\mathrm{d}\lambda. \tag{2.3.16}$$

The perturbation to the underlying base state has been described in terms of the spanwise varying displacement $\delta_{transp}(\hat{\zeta})$ which is induced by the wall transpiration.

In the far-field it is known from (2.1.8) that

$$\phi \sim \frac{A\eta}{\zeta^2 + \eta^2} = \frac{\hat{A}\hat{\eta}}{\hat{\zeta}^2 + \hat{\eta}^2}, \tag{2.3.17}$$

where $A = \zeta_0\hat{A}$. This means that $\phi \sim A/r$ as $r \to \infty$ where $r^2 = \zeta^2 + \eta^2$. So the mass flux across the semi-circle $S = r\pi$ is given by $\phi \cdot S$ therefore the radial mass flux at infinity is $A\pi = \hat{A}\zeta_0\pi$. On the other hand the flux from the inner parabolic region induced by the transpiration is $M\zeta_0$ where

$$M = \int_{-\infty}^{+\infty} \delta_{transp}(\lambda)\mathrm{d}\lambda, \tag{2.3.18a}$$

is a function of the injection rate K. Combining these two expressions for the mass flux suggests that

$$A = \frac{M\zeta_0}{\pi}, \tag{2.3.18b}$$

so the mass flux coefficient A is proportional to the blowing width ζ_0 and the integral of the spanwise varying displacement $\delta_{transp}(\hat{\zeta})$.

Figure 2.3.2 shows a comparison between the numerically calculated values of A and the asymptotic prediction given by (2.3.18). In order to determine the spanwise varying transpiration $\delta_{transp}(\hat{\zeta})$ for use in the integral (2.3.18a) the parabolic equations (2.3.3) are marched from an initial Blasius profile in the far-field and use the transverse velocity component for large η given by (2.3.5). Figure 2.3.3 illustrates the connection between the weak injection profile, the spanwise varying displacement and the vertical

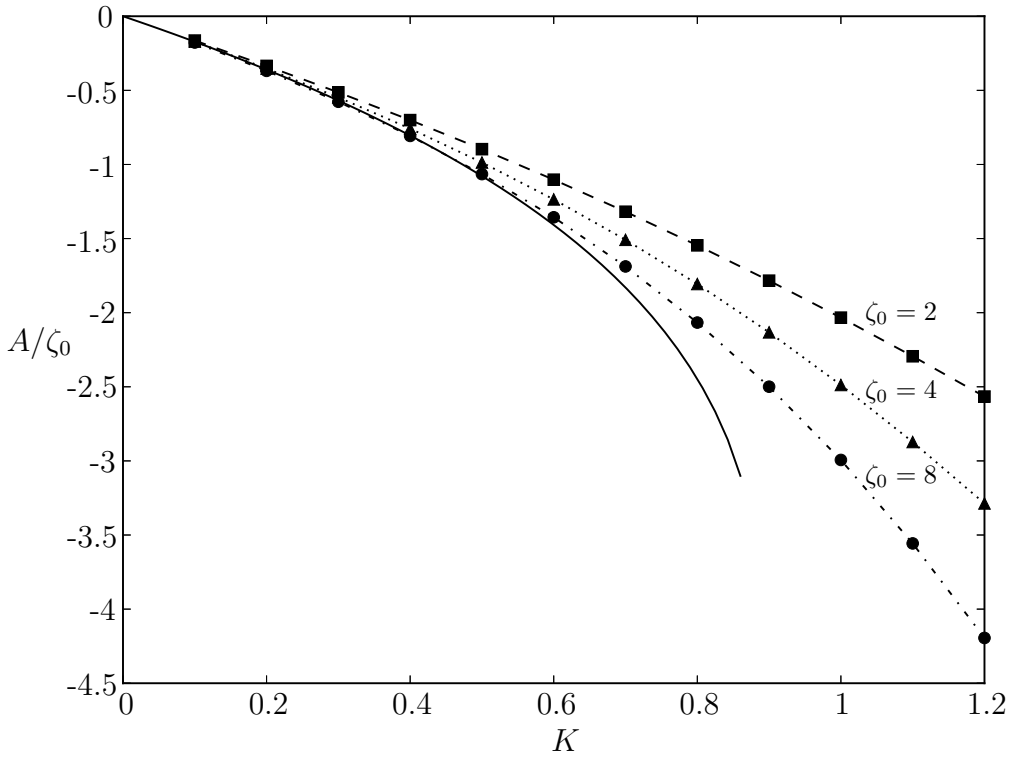

Figure 2.3.2: The solid line shows the asymptotic prediction, M/π, as determined from the parabolic system (2.3.3) and (2.3.18a). The data points show numerically determined values of A/ζ_0 for increasing injection velocities K and injection slot widths $\zeta_0 = 2, 4, 8$.

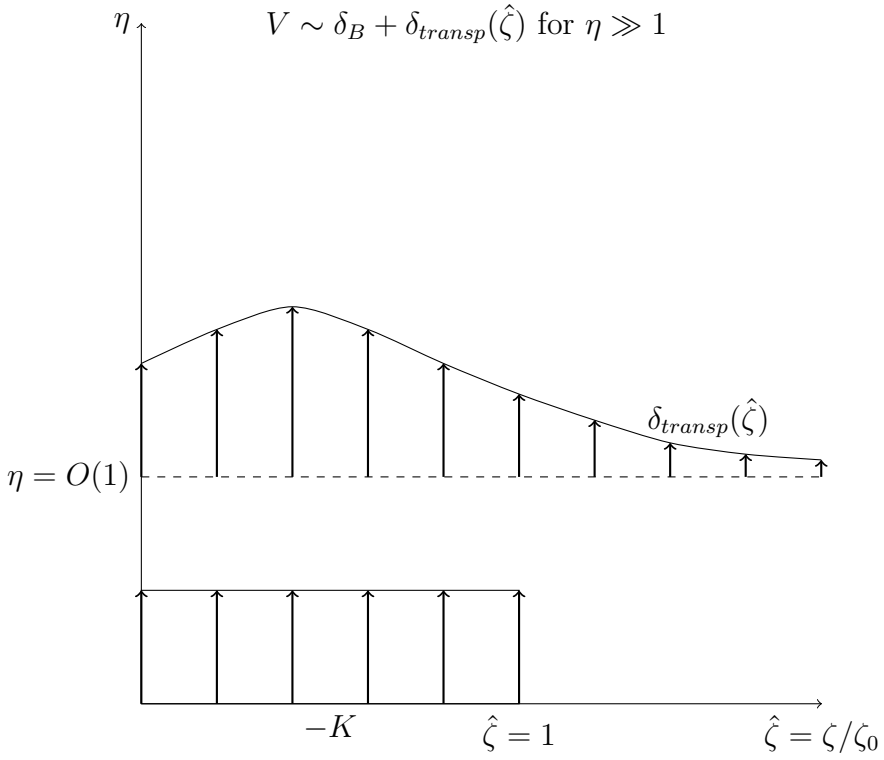

Figure 2.3.3: Schematic diagram for the weak injection asymptotic regime.

velocity component far from the plate surface. The asymptotic relationship between A and ζ_0, at fixed K, is confirmed by the agreement between the numerical data and the asymptotic prediction shown in figure 2.3.2 for sufficiently large ζ_0. The asymptotic prediction ceases to provide a satisfactory description for large ζ_0 upon approaching the critical injection rate $K = K_I \approx 0.876$ indicating a transition into the moderate injection regime.

2.3.2 Strong injection

Examination of the moderate injection regime is postponed for a moment as it acts as an intermediary between the weak and strong injection regimes and is more difficult to describe in isolation. The strong injection regime is produced when the injection rate is large enough, $K > K_{II}$, for a low-speed streak to form as shown in figure 2.2.3. Below an asymptotic description in the limit $\zeta_0 \to \infty$ is presented in which the critical value K_{II} is calculated and the behaviour of the mass flux parameter A is examined. Inside the streak region the $O(1)$ coordinates $\hat{\eta} = \eta/\zeta_0$ and $\hat{\zeta} = \zeta/\zeta_0$ are defined. The numerical calculations suggest the following rescaling of the variables

$U = o(\zeta_0^{-1})$, $\Phi = \Phi^*(\hat{\zeta}, \hat{\eta})$, $\Psi = \Psi^*(\hat{\zeta}, \hat{\eta})$ and $\Theta = \zeta_0^{-1}\Theta^*(\hat{\zeta}, \hat{\eta})$. Applying the rescaling to the continuity equation (2.1.1a) gives

$$\Phi_\eta + \Psi_\zeta = \frac{1}{\zeta_0}\Phi^*_{\hat{\eta}} + \frac{1}{\zeta_0}\Psi^*_{\hat{\zeta}} = 2U, \tag{2.3.19}$$

so since $U = o(\zeta_0^{-1})$, i.e. $U\zeta_0 \to 0$, it follows that

$$\Phi^*_{\hat{\eta}} + \Psi^*_{\hat{\zeta}} = 0 \tag{2.3.20}$$

to leading order. Similarly the vorticity equation (2.1.1b) may be written as

$$\Theta^* = \Psi^*_{\hat{\eta}} - \Phi^*_{\hat{\zeta}}. \tag{2.3.21}$$

The U equation (2.1.1c) has no leading order effect when ζ_0 is large. Applying the rescaling to the Θ equation (2.1.1d) leads to

$$\frac{1}{\zeta_0^3}\Theta^*_{\hat{\eta}\hat{\eta}} + \frac{1}{\zeta_0^3}\Theta^*_{\hat{\zeta}\hat{\zeta}} = 2\left[\zeta_0\hat{\zeta}UU_\eta - \zeta_0\hat{\eta}UU_\zeta\right] - \Phi^*\frac{1}{\zeta_0^2}\Theta^*_{\hat{\eta}} - \Psi^*\frac{1}{\zeta_0^2}\Theta^*_{\hat{\zeta}} - 2U\frac{1}{\zeta_0}\Theta^*. \tag{2.3.22}$$

Multiplying through by ζ_0^2 and using the fact that $U\zeta_0 \to 0$ suggests that

$$\frac{1}{\zeta_0}\Theta^*_{\hat{\eta}\hat{\eta}} + \frac{1}{\zeta_0}\Theta^*_{\hat{\zeta}\hat{\zeta}} = -\Phi^*\Theta^*_{\hat{\eta}} - \Psi^*\Theta^*_{\hat{\zeta}}, \tag{2.3.23}$$

so in the limit $\zeta_0 \to \infty$, to leading order,

$$-\Phi^*\Theta^*_{\hat{\eta}} - \Psi^*\Theta^*_{\hat{\zeta}} = 0. \tag{2.3.24}$$

Applying the rescaling to the governing equations (2.1.1) produces the following leading-order system within the streak:

$$\Phi^*_{\hat{\eta}} = -\Psi^*_{\hat{\zeta}}, \tag{2.3.25a}$$

$$\Theta^* = \Psi^*_{\hat{\eta}} - \Phi^*_{\hat{\zeta}}, \tag{2.3.25b}$$

$$\Phi^*\Theta^*_{\hat{\eta}} + \Psi^*\Theta^*_{\hat{\zeta}} = 0. \tag{2.3.25c}$$

Now let a two-dimensional stream function $G(\zeta, \eta) = \zeta_0 G^*(\hat{\zeta}, \hat{\eta}) + \ldots$, such that $\Psi^* = G^*_{\hat{\eta}}$ and $\Phi^* = -G^*_{\hat{\zeta}}$, be introduced. Then the first equation in (2.3.25) is trivially satisfied and the second and third equations may be written as

$$\hat{\nabla}^2 G^* = \Theta^*, \tag{2.3.26a}$$

$$G^*_{\hat{\eta}}\Theta^*_{\hat{\zeta}} - G^*_{\hat{\zeta}}\Theta^*_{\hat{\eta}} = 0, \tag{2.3.26b}$$

which is the Poisson formulation for an inviscid, rotational, incompressible flow. Introducing the variable s which parametrises a streamline such that $\hat{\eta} = \hat{\eta}(s)$ and $\hat{\zeta} = \hat{\zeta}(s)$ where

$$\frac{\mathrm{d}\hat{\zeta}}{\mathrm{d}s} = G^*_{\hat{\eta}} \quad \text{and} \quad \frac{\mathrm{d}\hat{\eta}}{\mathrm{d}s} = -G^*_{\hat{\zeta}} \tag{2.3.27}$$

then it follows that

$$G^*_{\hat{\eta}}\Theta^*_{\hat{\zeta}} - G^*_{\hat{\zeta}}\Theta^*_{\hat{\eta}} = \frac{\mathrm{d}\hat{\eta}}{\mathrm{d}s}\frac{\partial\Theta^*}{\partial\hat{\eta}} + \frac{\mathrm{d}\hat{\zeta}}{\mathrm{d}s}\frac{\partial\Theta^*}{\partial\hat{\zeta}} = \frac{\mathrm{d}\Theta^*}{\mathrm{d}s} = 0, \tag{2.3.28}$$

so that Θ^* is constant along a given streamline. At the surface boundary, $G^*(\hat{\zeta}, \hat{\eta} = 0) = G^*_w(\hat{\zeta})$, where G^*_w defines the scaled mass flux through the injection slot such that

$$G^*_w(\hat{\zeta}) = -\int_0^{\hat{\zeta}} V_{transp}(\hat{\zeta})\mathrm{d}\hat{\zeta} \tag{2.3.29}$$

where $V_{transp}(\hat{\zeta})$ is defined by (2.1.2).

The above Poisson formulation is defined within the domain $\hat{r} = \sqrt{\hat{\eta}^2 + \hat{\zeta}^2} < \hat{r}_s$ where $r_s = \zeta_0\hat{r}_s$ is the streak radius. In the region outside of the streak, and the shear layer located at $\hat{r} = \hat{r}_s$, the flow is irrotational with $U = 1$ and $\Theta = 0$ to leading order. In the region outside the streak

$$\Phi = \zeta_0\hat{\eta} + \frac{A\hat{\eta}}{\zeta_0\left(\hat{\eta}^2 + \hat{\zeta}^2\right)} + O(\zeta_0^{-2}), \tag{2.3.30a}$$

$$\Psi = \zeta_0\hat{\zeta} + \frac{A\hat{\zeta}}{\zeta_0\left(\hat{\eta}^2 + \hat{\zeta}^2\right)} + O(\zeta_0^{-2}), \tag{2.3.30b}$$

due to the far-field conditions (2.1.8) and the two-dimensional base flow solution. In order to match the solution inside the low-speed streak it is required that both Φ and Ψ be $o(\zeta_0)$ at the shear layer i.e.

$$\frac{\Phi}{\zeta_0} = \hat{\eta} + \frac{A\hat{\eta}}{\zeta_0^2\left(\hat{\eta}^2 + \hat{\zeta}^2\right)} \to 0, \tag{2.3.31a}$$

$$\frac{\Psi}{\zeta_0} = \hat{\zeta} + \frac{A\hat{\zeta}}{\zeta_0^2\left(\hat{\eta}^2 + \hat{\zeta}^2\right)} \to 0. \tag{2.3.31b}$$

Therefore

$$\frac{A}{\zeta_0^2\left(\hat{\eta}^2 + \hat{\zeta}^2\right)} \to -1 \tag{2.3.32}$$

which means that $A \to -\zeta_0^2\left(\hat{\eta}^2+\hat{\zeta}^2\right) = -\zeta_0^2\hat{r}_s^2$ so that the mass flux is specified in terms of the injection width ζ_0 and the scaled streak radius $\hat{r}_s$.

At the interface between the inner and outer regions there exists a shear layer in which there is a rapid change in the streamwise flow velocity. Now the flow field in the shear layer, where all variables are $O(1)$, is to be considered. First propose a change to polar coordinates at the shear layer (R,θ) with radial coordinate $R = r - r_s$, where $r = \sqrt{\eta^2+\zeta^2}$, and θ is the corresponding polar angle such that $\zeta = r\cos\theta$ and $\eta = r\sin\theta$, see figure 2.3.4. Using this change of coordinates the derivatives become

$$\frac{\partial}{\partial\zeta} = \cos\theta\frac{\partial}{\partial r} - \frac{1}{r}\sin\theta\frac{\partial}{\partial\theta}, \tag{2.3.33a}$$

$$\frac{\partial}{\partial\eta} = \sin\theta\frac{\partial}{\partial r} + \frac{1}{r}\cos\theta\frac{\partial}{\partial\theta}. \tag{2.3.33b}$$

Since $R = r - r_s$, whilst assuming no angular variation in the shear layer for $\theta = O(1)$, it follows that

$$\frac{\partial}{\partial\zeta} = \cos\theta\frac{\partial}{\partial R}, \quad \frac{\partial^2}{\partial\zeta^2} = \cos^2\theta\frac{\partial^2}{\partial R^2}, \tag{2.3.34a}$$

$$\frac{\partial}{\partial\eta} = \sin\theta\frac{\partial}{\partial R}, \quad \frac{\partial^2}{\partial\eta^2} = \sin^2\theta\frac{\partial^2}{\partial R^2}. \tag{2.3.34b}$$

This means that the governing equations (2.1.1) become

$$2U = \Phi_R\sin\theta + \Psi_R\cos\theta, \tag{2.3.35a}$$

$$\Theta = \Psi_R\sin\theta - \Phi_R\cos\theta, \tag{2.3.35b}$$

$$U_{RR} = \Phi U_R\sin\theta - \Psi U_R\cos\theta, \tag{2.3.35c}$$

$$\Theta_{RR} = -\Phi\Theta_R\sin\theta - \Psi\Theta_R\cos\theta - 2\Theta U, \tag{2.3.35d}$$

where subscript R indicates the derivative with respect to R. In order for the shear layer flow to match with the regions both inside and outside of the streak it is required that $U\to 0$, $\Theta\to 0$ as $R\to-\infty$ and $U\to 1$, $\Theta\to 0$, $\Phi\to 2R\sin\theta$ and $\Psi\to 2R\cos\theta$ as $R\to\infty$. The last two conditions come from the polar form of (2.3.30) such that

$$\Phi = \zeta_0\hat{\eta} + \frac{A\hat{\eta}}{\zeta_0\left(\hat{\eta}^2+\hat{\zeta}^2\right)} = \left(R+\zeta_0\hat{R}_0\right)\sin\theta\left(1+\frac{A}{R+\zeta_0\hat{R}_0}\right), \tag{2.3.36a}$$

$$\Psi = \zeta_0\hat{\zeta} + \frac{A\hat{\zeta}}{\zeta_0\left(\hat{\eta}^2+\hat{\zeta}^2\right)} = \left(R+\zeta_0\hat{R}_0\right)\cos\theta\left(1+\frac{A}{R+\zeta_0\hat{R}_0}\right), \tag{2.3.36b}$$

and, since $\zeta_0\to\infty$, $R+\zeta_0\hat{R}_0 = 2R$ and $A/\left(R+\zeta_0\hat{R}_0\right)\to 0$ as $R\to\infty$. Here $\hat{R}_0$ is the scaled shear layer radius.

The system (2.3.35) shall be reformulated in terms of the radial flow contribution in the cross-secitional plane,

$$F = \Phi \sin\theta + \Psi \cos\theta, \tag{2.3.37}$$

which implies that $2U = F_R$. Using the this reformulation (2.3.35c) may be written as

$$F_{RRR} + F F_{RR} = 0 \tag{2.3.38}$$

subject to $F_R \to 2$ as $R \to \infty$, $F_R \to 0$ as $R \to -\infty$ and $F = 0$ when $R = 0$. The last condition is due to the fact that the coordinate system is able to be translated with the same equation still being recovered; a value at a specified location must be chosen in order to fix the $O(1)$ contribution to the location of the shear layer. The equation (2.3.38) is the Blasius equation however the boundary conditions are somewhat different than the usual Blasius formulation, in fact the equation describes a laminar mixing layer [59]. Solving the equation numerically subject to the appropriate boundary conditions it is found that $F(-\infty) \approx -1.238$.

It is now necessary to determine Θ along with the individual contributions of Φ and Ψ to the known function F. The Θ equation (2.3.35d) can be written as

$$\begin{aligned} \Theta_{RR} &= -\Theta_R \left(\Phi \sin\theta + \Psi \cos\theta\right) - 2\Theta U \\ &= -\Theta_R F - \Theta F_R \\ &= -\frac{\mathrm{d}}{\mathrm{d}R}\left(\Theta F\right), \end{aligned} \tag{2.3.39}$$

which upon integration gives

$$\Theta_R + \Theta F = \text{constant}. \tag{2.3.40}$$

Using the equation (2.3.35b) and the definition (2.3.37) it follows that

$$\Theta_R + \Theta F = \Psi_{RR} \sin\theta - \Phi_{RR} \cos\theta + \left(\Psi_R \sin\theta - \Phi_R \cos\theta\right)\left(\Phi \sin\theta + \Psi \cos\theta\right). \tag{2.3.41}$$

Evaluating this in the far-field as $R \to \infty$, using the conditions $\Phi \to 2R\sin\theta$ and $\Psi \to 2R\cos\theta$ or simply $\Theta \to 0$, gives

$$\Theta_R + \Theta F = 0 \tag{2.3.42}$$

as $R \to \infty$ therefore the constant in (2.3.40) is zero. From (2.3.38) a solution of (2.3.40) is $\Theta = C_1 F_{RR}$, where C_1 is a constant to be determined.

The function F is the radial velocity contribution from Φ and Ψ with $F < 0$ corresponding to radial outflow. As $R \to -\infty$ this radial flow must match with the radial flow from inside the streak. The stream function describing the flow inside the streak has radial component

$$\frac{1}{\hat{r}}\frac{\partial G^*}{\partial \theta}. \tag{2.3.43}$$

So matching the solution inside streak with the shear layer solution gives the condition

$$\left.\frac{1}{\hat{r}_s}\frac{\partial G^*}{\partial \theta}\right|_{\hat{r}=\hat{r}_s} = -F(-\infty). \tag{2.3.44}$$

Since $F(-\infty)$ is constant for all θ it follows that

$$G^*|_{\hat{r}=\hat{r}_s} = \text{constant} - \hat{r}_s F(-\infty)\theta. \tag{2.3.45}$$

For symmetry of the flow it is required that there is no mass flux across $\hat{\zeta} = 0$ therefore $G^* = 0$ on $\hat{\zeta} = 0$. Since $\zeta_0\hat{\zeta} = r\cos\theta = 0$ this implies that $\theta = \pi/2$, so after determining the constant it follows that

$$G^*(\hat{r}_s, \theta) = -\hat{r}_s F(-\infty)\left(\theta - \frac{\pi}{2}\right). \tag{2.3.46}$$

On assuming that the streak radius is larger than the blowing width, $r_s > \zeta_0$ or $\hat{r}_s > 1$, the scaled mass flux (2.3.29) is approximated by $-K\hat{\zeta}$ for $\hat{\zeta} < 1$ and $-K$ for $\hat{\zeta} \geq 1$ hence $G^*_w(\hat{\zeta} = \hat{r}_s > 1) \approx -K$. In order to match with the boundary condition $G^* = G^*_w$ along $\theta = 0$ it is required that

$$\hat{r}_s F(-\infty)\frac{\pi}{2} = G^*_w(\hat{\zeta} = \hat{r}_s). \tag{2.3.47}$$

Failure of this condition would mean a discontinuity in the streamfunction at $O(\zeta_0)$, so if this is treated as a condition for $\hat{r}_s$ then

$$r_s = \zeta_0\hat{r}_s = -\frac{2K\zeta_0}{\pi F(-\infty)} \approx 0.514K\zeta_0 \tag{2.3.48}$$

and

$$A \sim -\frac{4K^2\zeta_0^2}{\pi^2 F(-\infty)^2} \approx -0.264K^2\zeta_0^2 \tag{2.3.49}$$

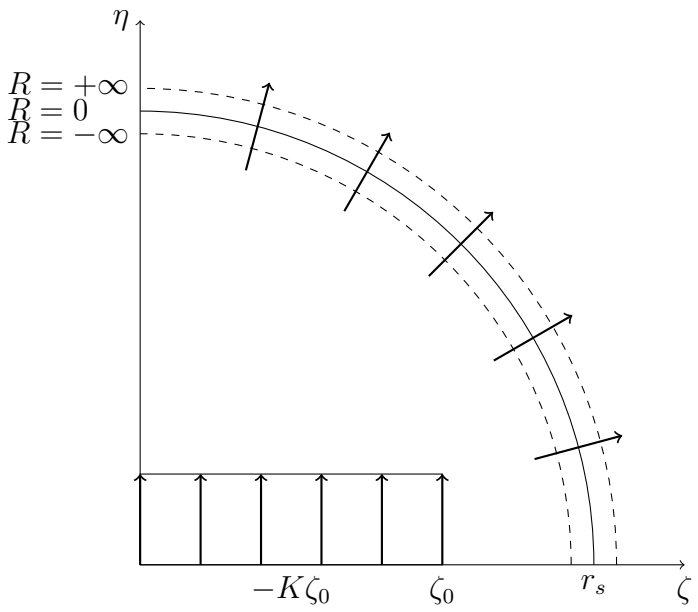

Figure 2.3.4: Schematic diagram for the strong injection asymptotic regime.

for $\zeta_0 \gg 1$ and $K = O(1)$ in the strong injection streak regime where $\hat{r}_s > 1$ (i.e. the streak radius extends past the injection region). If $\hat{r}_s < 1$ then the condition (2.3.47) cannot be satisfied in general since $G_w(\hat{\zeta} = \hat{r}_s) \approx -K\hat{r}_s$. The critical injection rate K_{II}, for which the flow enters into the strong injection regime, is reached when the streak radius is equal to the injection width such that $\hat{r}_s = r_s/\zeta_0 = 1$. Setting $\hat{r}_s = 1$ in (2.3.48) yields

$$K_{II} = -\frac{\pi F(-\infty)}{2} \approx 1.95. \tag{2.3.50}$$

Figure 2.3.4 illustrates the radial flow present in the strong injection regime and the required matching across the shear layer separating the low and high speed regions. Figure 2.3.5 shows a comparison between the asymptotic predictions of the mass flux parameter A and the streak radius r_s and numerically determined values of both of these for increasing injection slot width ζ_0 and injection velocity $K > K_{II}$. As ζ_0 increases excellent agreement is found between the asymptotic predictions and the numerically determined data points, there is however some evidence of an $O(1)$ correction to both A and r_s which has not been determined. Calculations become increasingly computationally expensive as ζ_0 is increased further. Larger values of A require ever larger computational domains and an increasing number of nodal points, at $\zeta_0 = 16$ for example the computational parameters $\hat{\zeta}_\infty = 20$, $\eta_\infty = 400$ and $N_{\hat{\zeta}} = N_\eta = 1201$ have been used. The radius of the streak is determined numerically as the value of

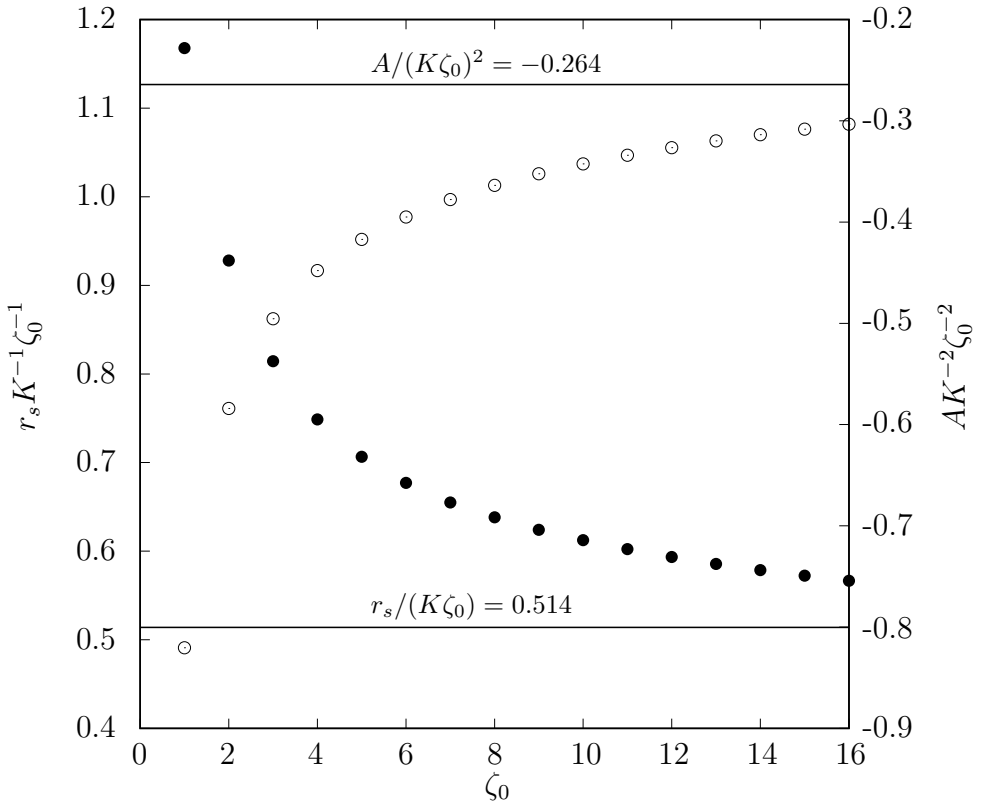

Figure 2.3.5: A comparison of numerically determined values of A and r_s with the asymptotic predictions for $\zeta_0 \gg 1$ given by (2.3.49) and (2.3.48) shown by the solid lines. Here $K = 2.5 > K_{II}$ with values of A (open circles and right-hand scale) and r_s (solid circles and left-hand scale) being shown for increasing injection slot width ζ_0.

r_s at which $U(\zeta = 0, \eta = r_s) = 0.5$ as this is approximately the middle of the shear layer. The asymptotic description given above provides a useful insight into the strong injection regime by giving details of the key components A, r_s and K_{II}.

2.3.3 Moderate injection

The moderate injection regime is more difficult to describe as it exhibits characteristics of both the weak and strong injection regimes thereby providing a transition between the two. As in the strong injection regime a key feature is the presence of a low-speed streak however in the moderate injection regime the streak is not semi-circular as shown in figure 2.2.2. Numerical evidence suggests that instead the low-speed streak is circular up until an angle, measured clockwise from the centreline, that is determined by the rate of injection K. As K increases from the first critical value $K_I \approx 0.876$ towards the second critical value $K_{II} \approx 1.95$ the circular portion of the shear layer continues to expand until the shear layer approaches the plate as predicted by the asymptotic description for the strong injection regime. The increase in the circular portion of the shear layer for increasing injection rates is illustrated in figure 2.3.6 which shows the contour $U(\zeta, \eta) = 0.5$ for an injection slot width $\zeta_0 = 20$ and injection rates $K = 0.9, 1.4, 1.9$.

The critical value K_{II} given by (2.3.50) indicates the injection rate for which the flow enters into the strong regime and the streak radius becomes equal to the injection width. In the moderate injection regime the size of the low-speed streak is smaller than the width of the injection such that $\hat{r}_s = r_s/\zeta_0 < 1$. Near to the plate but outside the low-speed region the flow is characterised by an attached viscous layer where $\eta = O(1)$ as is found in the weak injection regime described by (2.3.2). As previously discussed the parabolic solution (2.3.2) terminates at the centreline $\zeta = 0$ with the classical two-dimensional solution when marched in the spanwise coordinate from $\hat{\zeta} \gg 1$ to $\hat{\zeta} = 0$. This solution only exists when the injection rate is less than the first critical injection rate $K \leq K_I$ therefore when $K > K_I$ as in the moderate injection regime there is no solution at $\zeta = 0$ and the parabolic system (2.3.2) breaks down at a finite value of ζ.

The solution of (2.3.2) assumes that $\Psi_0 \to 1$ as $\eta \to \infty$ so that there is no cross flow at $O(\zeta_0)$ above the layer. This far-field condition holds in the weak injection

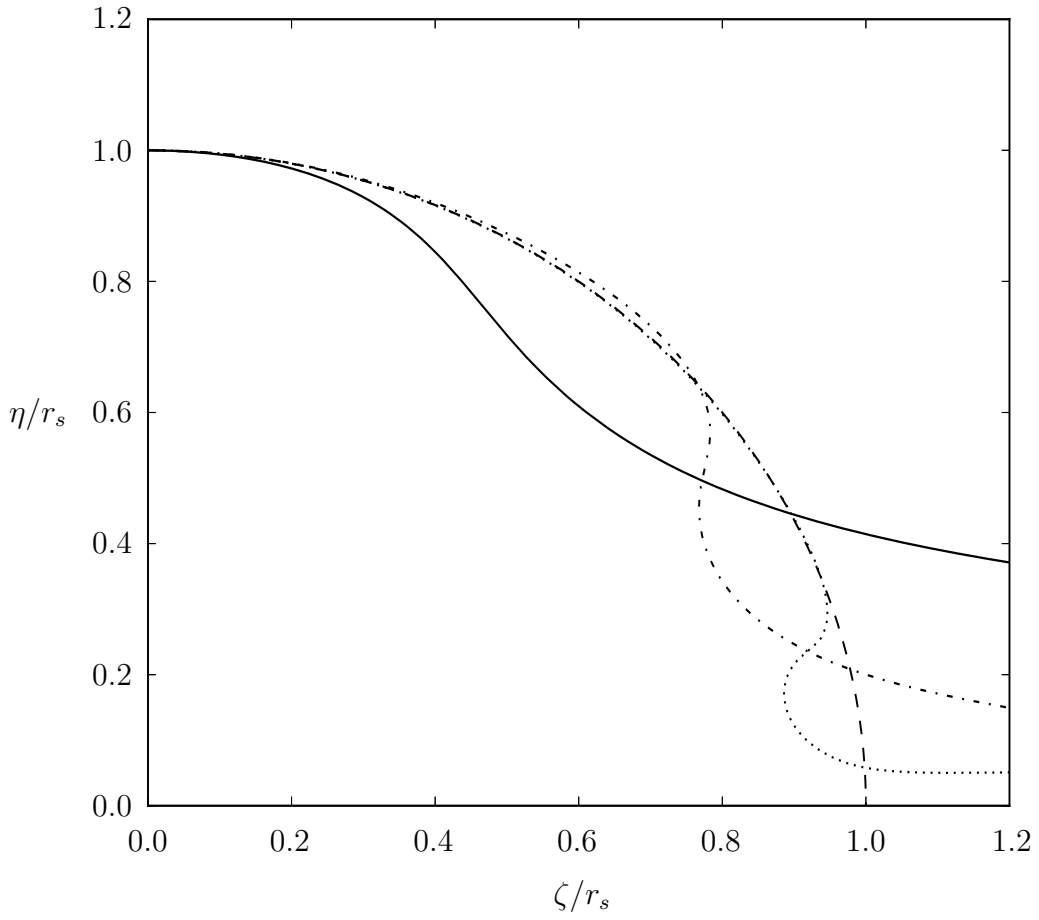

Figure 2.3.6: Streak profiles in the moderate injection regime shown using the contours of $U(\zeta, \eta) = 0.5$ in the rescaled coordinate system $(\zeta/r_s, \eta/r_s)$ where the streak radius r_s is defined by $U(\zeta = 0, \eta = r_s) = 0.5$. The solid, dash-dotted and dotted lines show the $U = 0.5$ contours for $K = 0.9, 1.4$ and 1.9 respectively and $\zeta_0 = 20$. The dashed line shows the circular shear layer location predicted for the strong injection regime when $K > K_{II}$.

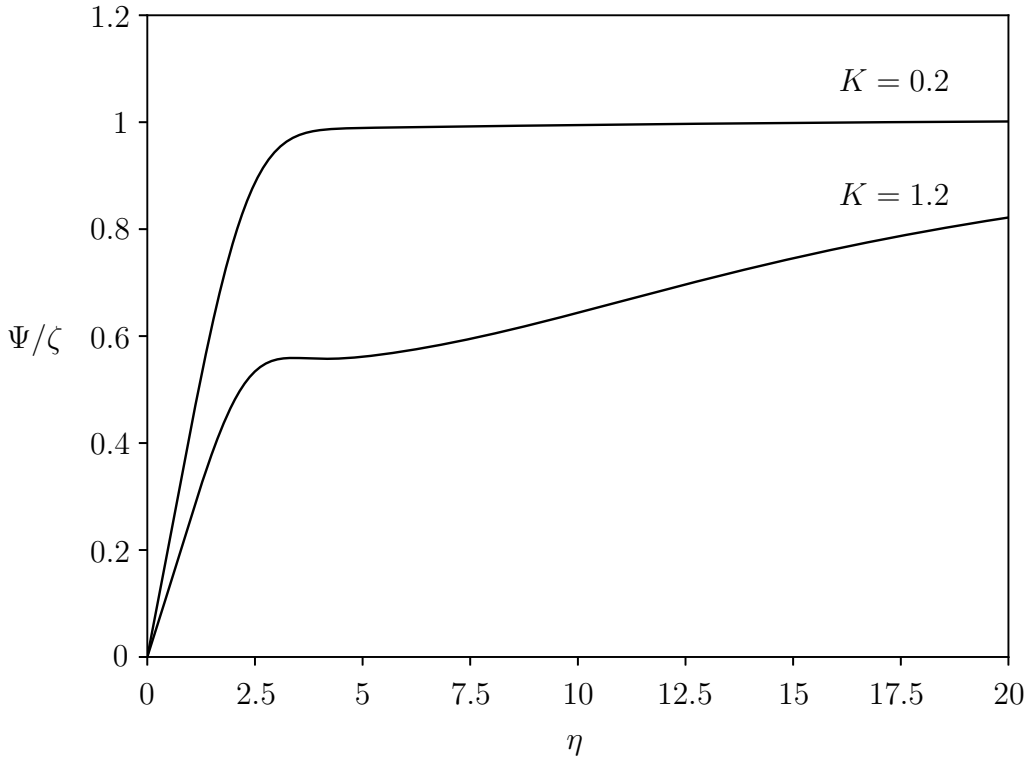

Figure 2.3.7: Profiles of Ψ/ζ in the injection region at $\zeta = 0.7\zeta_0$ for $\zeta_0 = 20$ with $K = 0.2$ (weak injection) and $K = 1.2$ (moderate injection).

regime but is no longer valid in the moderate injection regime due to the shear layer displacement caused by the low-speed streak and the associated cross flow at $O(\zeta_0)$. The profile for $\Psi(\zeta = 0.7\zeta_0, \eta)/\zeta$ is shown in figure 2.3.7 for $\zeta_0 = 20$ and $K = 0.2, 1.2$ (which is $\Psi_0(\hat{\zeta} = 0.7, \eta)$ in (2.3.2) to leading order). For the weak injection $K = 0.2$ the value of $\Psi/\zeta \approx 1$ over most of the η domain. On the other hand for the moderate injection $K = 1.2$ the value of Ψ/ζ is not close to unity even for large values of η which suggests that the far-field cross flow plays an important role in the moderate injection regime.

Outside the streak near to the plate a parabolic solution described by (2.3.2) is still applicable in the moderate injection case however a more general far-field condition is required. The condition is $\Psi_0 \to \Psi_\infty(\hat{\zeta})$ as $\eta \to \infty$ where $\Psi_\infty(\hat{\zeta})$ is a function of the streak geometry describing the distribution of cross-flow velocity. It is not possible to fully determine the size and shape of the streak unless the mass flux into the streak from the parabolic layer is known, it is therefore necessary to solve these intertwined problems simultaneously. An interactive approach which couples the viscous layer on the plate, the streak and the outer region is required; this is a problem of similar complexity to the original governing equations. The moderate injection problem described above will not be attempted in this thesis.

In section 2.3 an asymptotic description of each of the three regimes, and the transitions between them, has been discussed in an attempt to provide an insight into the mechanisms involved in the short-scale injection problem. It is evident however that the descriptions provided do not give an exact account, for example the parabolic system (2.3.2) provides a description of the weak injection regime except in a small region near to $\hat{\zeta} = 0$. In order to provided a more complete picture it is necessary to examine the breakdown of the asymptotic description for $\hat{\zeta} \ll 1$ and the role of spatially unstable eigenmodes.

2.4 Spatial eigenmodes for $\hat{\zeta} \ll 1$

For an increasing injection slot width ζ_0 the weak injection regime $K < K_I$ is approximated, to leading order, by the parabolic system (2.3.2) or (2.3.3). However this asymptotic prediction is not valid for small values of $\hat{\zeta}$, this is illustrated by figure

2.3.1 which shows a deviation from the predicted behaviour of the shear stress distribution near to $\hat{\zeta} = 0$ as the injection slot width is increased. This sharp deviation away from the predicted behaviour is indicative of a spatial 'instability' which grows upon approaching the centreline of the injection at $\hat{\zeta} = 0$.

In order to understand the behaviour near to $\hat{\zeta} = 0$ a description of the spatial evolution of a small perturbation to the parabolic solution of the previous section is provided below. Firstly an expansion is proposed in the form

$$U = U_0(\hat{\zeta}, \eta) + \epsilon u(\hat{\zeta}, \eta), \tag{2.4.1a}$$

$$\Phi = \Phi_0(\hat{\zeta}, \eta) + \epsilon \varphi(\hat{\zeta}, \eta), \tag{2.4.1b}$$

$$\Psi = \zeta_0 \hat{\zeta} \left(\Psi_0(\hat{\zeta}, \eta) + \epsilon \psi(\hat{\zeta}, \eta) \right), \tag{2.4.1c}$$

$$\Theta = \zeta_0 \hat{\zeta} \left(\Theta_0(\hat{\zeta}, \eta) + \epsilon \vartheta(\hat{\zeta}, \eta) \right). \tag{2.4.1d}$$

Setting $\epsilon = 0$ the leading-order system (2.3.2) is recovered which, if started from a state with no cross flow, has a solution with $\Psi_0 = U_0$. Therefore the simpler form (2.3.3) may be used instead. For $\epsilon \ll 1$ the linearised system for $(u, \varphi, \psi, \vartheta)$ is given by

$$2u = \varphi_\eta + \psi + \hat{\zeta} \psi_{\hat{\zeta}}, \tag{2.4.2a}$$

$$\vartheta = \psi_\eta, \tag{2.4.2b}$$

$$u_{\eta\eta} = -\Phi_0 u_\eta - U_{0\eta} \varphi - \hat{\zeta} \left(U_{0\hat{\zeta}} \psi + \Psi_0 u_{\hat{\zeta}} \right), \tag{2.4.2c}$$

$$\begin{aligned} \vartheta_{\eta\eta} = & 2 \left[U_{0\eta} u + U_0 u_\eta \right] - \Theta_{0\eta} \varphi - \Phi_0 \vartheta_\eta - \Psi_0 \left(\vartheta + \hat{\zeta} \vartheta_{\hat{\zeta}} \right) \\ & - \left(\Theta_0 + \hat{\zeta} \Theta_{0\hat{\zeta}} \right) \psi - 2 \left(U_0 \vartheta + \Theta_0 u \right). \end{aligned} \tag{2.4.2d}$$

For $\hat{\zeta} \ll 1$ solutions to these $O(\epsilon)$ perturbation equations exist in the form

$$\left(u(\hat{\zeta}, \eta), \varphi(\hat{\zeta}, \eta), \psi(\hat{\zeta}, \eta), \vartheta(\hat{\zeta}, \eta) \right) = \hat{\zeta}^\lambda \left(u_0(\eta), \varphi_0(\eta), \psi_0(\eta), \vartheta_0(\eta) \right). \tag{2.4.3}$$

The $O(\epsilon^0)$ system reduces to the Blasius equation (1.4.7) with an injection boundary condition such that $U_0 = F'(\eta)$, $\Phi_0 = F(\eta)$, $\Psi_0 = F'(\eta)$, $\Theta_0 = F''(\eta)$ and $F(0) = -K$, along with the other usual boundary conditions. The $O(\epsilon)$ system, with the local form

(2.4.3) leads to an eigenvalue problem

$$2u_0 - \varphi_0' - \psi_0 = \lambda\psi_0, \tag{2.4.4a}$$

$$\vartheta_0 - \psi_0' = 0, \tag{2.4.4b}$$

$$u_0'' + \Phi_0 u_0' + U_{0\eta}\varphi_0 = -\lambda\Psi_0 u_0, \tag{2.4.4c}$$

$$\vartheta_0'' - 2\left[U_{0\eta}u_0 + U_0 u_0'\right] + \Theta_{0\eta}\varphi_0 + \Phi_0\vartheta_0' + \Psi_0\vartheta_0 + \Theta_0\psi_0 + 2(U_0\vartheta_0 + \Theta_0 u_0) = -\lambda\Psi_0\vartheta_0, \tag{2.4.4d}$$

where the prime notation is used to denote derivatives with respect to η. The homogeneous boundary conditions to be imposed are $u_0(0) = \varphi_0(0) = \psi_0(0) = 0$ and $u_0, \psi_0, \vartheta_0 \to 0$ as $\eta \to \infty$. Here $\lambda = \lambda_r + i\lambda_i$ is a complex eigenvalue which must be determined to describe the spatial behaviour of the perturbation on approaching the slot centreline. If the real part of the eigenvalue is negative ($\lambda_r < 0$) as $\hat{\zeta} \to 0$ then the perturbation grows and the corresponding eigenmode is linearly unstable in the context of parabolic marching from $\hat{\zeta} \gg 1$ to $\hat{\zeta} = 0$. In such cases it should not be expected that a Blasius solution near $\hat{\zeta} = 0$ is recovered.

Using a standard central differencing scheme (2.4.4) may be discretised producing a generalised eigenvalue problem of the form $A\mathbf{v}_n = \lambda_n B\mathbf{v}_n$ where A and B are $6N_\eta \times 6N_\eta$ matrices and $n \in \{1, \ldots, 6N_\eta\}$. Performing a generalised Schur decomposition to factorise A and B values of λ_n are able to be found which are numerical approximations to the eigenvalue spectrum of (2.4.4).

Figure 2.4.1 shows the real part of the eigenvalues for a given K for the two-dimensional Blasius solution. When $K \lesssim -0.45$ the real parts of the spatial eigenvalues are positive, $\lambda_r > 0$. For a sufficient suction the parabolic solution is stable to small perturbations upon approaching $\hat{\zeta} = 0$. However when $-0.45 \lesssim K < K_I$ there is solitary eigenvalue with $\lambda_r < 0$ which implies spatial linear instability upon approaching the centreline $\hat{\zeta} = 0$. The eigenvalue value with $\lambda_r < 0$ has an associated eigenfunction such that $\psi_0 \neq u_0$. Upon approaching the centreline the magnitude of the perturbation $\hat{\zeta}^\lambda$ becomes large for the negative eigenvalue. This means that $\Psi \neq U$, since $\psi_0 \neq u_0$, so the flow has a three-dimensional cross-flow component near to $\hat{\zeta} = 0$.

For $\lambda_r < 0$ the two-dimensional Blasius base state $(U_B, \Phi_B, \Psi_B, \Theta_B)$ is unstable as $\hat{\zeta} \to 0$ due to the spatial eigenmode with $\psi_0 \neq u_0$. The spatial eigenmode associated

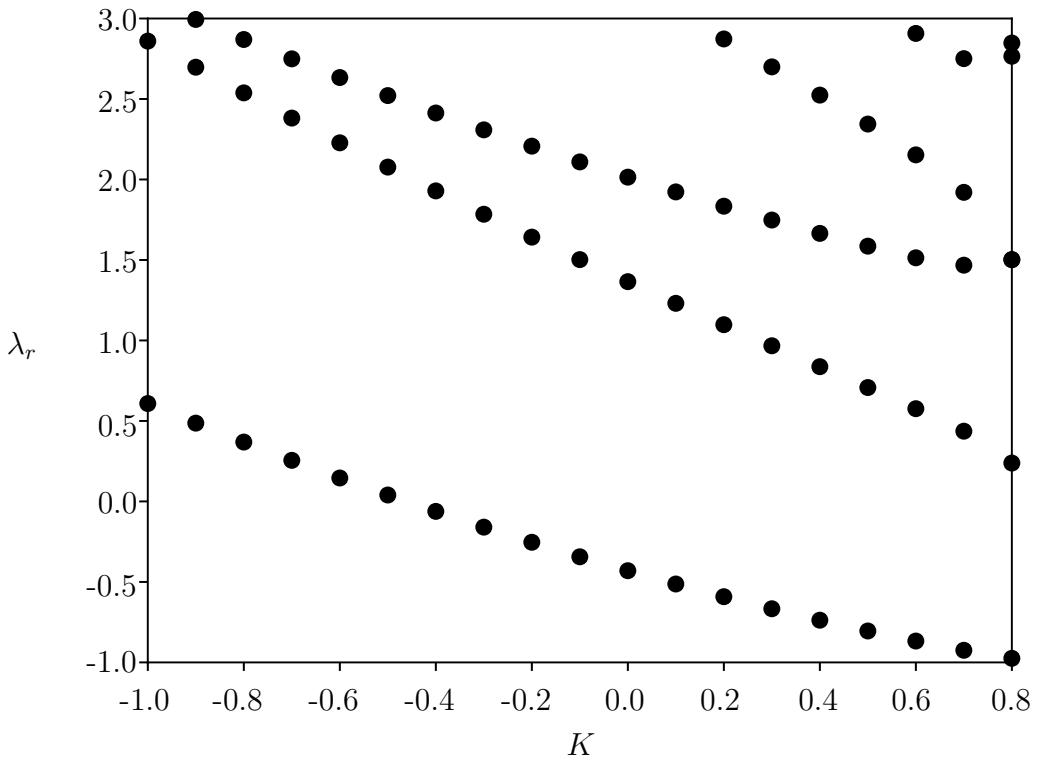

Figure 2.4.1: Real part of the spatial eigenvalues $\lambda = \lambda_r + i\lambda_i$ for the eigenvalue problem (2.4.4). The circles show the values of λ_r associated with the Blasius base flow solution with surface injection/suction $K = -1, -0.9, \ldots, 0.8$.

with the $\lambda_r < 0$ eigenvalue, shown in figure 2.4.1, leads to the discrepancy between the full computational results and the asymptotic prediction given by the parabolic system (2.3.3). This behaviour is not seen in the parabolic solution for large ζ_0 because the starting solution at large $\hat{\zeta}$ is an exactly two-dimensional Blasius state which has no cross-flow and so the amplitude of the unstable eigenmode is forced to be zero.

2.5 Alternative transpiration profiles

In this section the impact of using injection profiles that are different to the 'top-hat' profile described by (2.1.2), especially profiles for which the total mass injection through the plate boundary is zero, will briefly be examined. The asymptotic descriptions given in section 2.3 remain valid and similar arguments will be used when describing alternative transpiration profiles.

The blowing profile described by (2.1.2) can be simplified, for sufficiently large steepness factor γ, so that

$$\Phi_w(\hat{\zeta}) = -V_{transp}(\hat{\zeta}) = \begin{cases} -K, & 0 \leq \hat{\zeta} < 1, \\ 0, & \hat{\zeta} \geq 1. \end{cases} \tag{2.5.1}$$

Then the scaled mass flux through half of the injection slot is given by

$$G^*_w(\hat{\zeta}) = \int_0^{\hat{\zeta}} \Phi_w(\hat{\zeta}) \mathrm{d}\hat{\zeta} = \begin{cases} -K\hat{\zeta}, & 0 \leq \hat{\zeta} < 1, \\ -K, & \hat{\zeta} \geq 1. \end{cases} \tag{2.5.2}$$

The mass flux through the shear layer along the centreline, as described by (2.3.46), is given by $G^*(\hat{r}_s, 0) = \hat{r}_s F(-\infty)\pi/2$. Because the downstream speed in the streak is essentially zero, the mass entering through the injection slot must be matched by the mass leaving through the shear layer. The mass flux constraint (2.3.47) allows the critical injection rate, at which the flow is in the strong injection regime, to be determined. Figure 2.5.1 shows a graphical representation of the mass flux argument. If $K < K_{II}$ there is no intersection of the curves corresponding to the mass flow across the shear layer and the mass entering through the injection slot. The critical value $K = K_{II}$ is the first time when there is intersection of the two curves and when $K > K_{II}$ there is exactly one intersection point, this is the strong injection regime

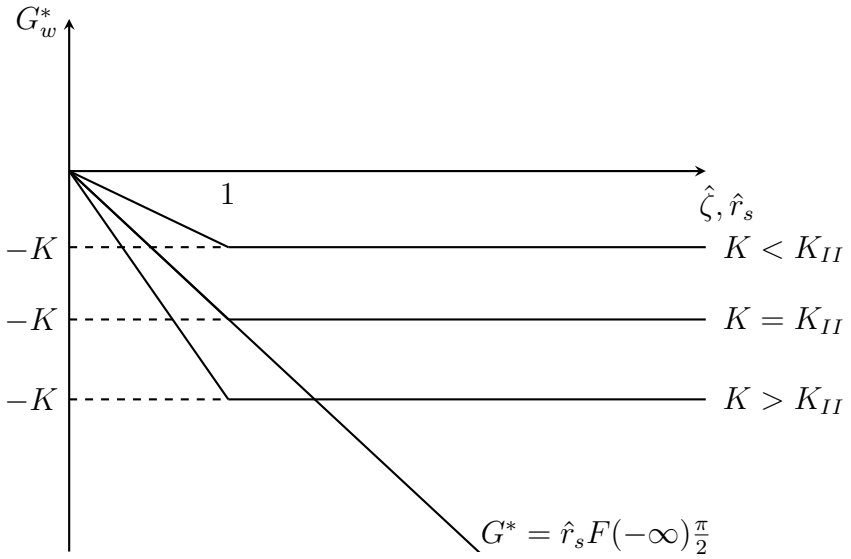

Figure 2.5.1: The mass flux through the injection slot $G_w^*(\zeta)$ for three different injection rates K is compared with the mass flux through the shear layer $G^* = \hat{r}_s F(-\infty)\pi/2$ showing the significance of the critical value K_{II}. Only if $K > K_{II}$ is there an intersection point.

illustrated in figure 2.2.3. The intersection of the curves provides information about the size of the streak since (2.3.47) implies that

$$\hat{r}_s = \frac{-2K}{\pi F(-\infty)} \approx 0.514K \quad \text{for} \quad K \geq K_{II}. \tag{2.5.3}$$

It is possible to suppose that instead of only having blowing through the injection slot there could be regions of both blowing and suction of equal magnitude distributed along the injection slot. Instead of the single blowing section described by (2.1.2) there could instead be multiple blowing and suction regions along the slot described by

$$V_{transp}(\hat{\zeta}) = \frac{K}{2}\left[1 + 2\sum_{i=1}^{N-1}(-1)^i \tanh\left(\gamma\left(\hat{\zeta} - \frac{i}{N}\right)\right) + (-1)^N \tanh\left(\gamma\left(\hat{\zeta} - 1\right)\right)\right], \tag{2.5.4}$$

where N is the total number of combined blowing and suction regions. For example, when $N = 2$ there is blowing of magnitude K for $0 < \hat{\zeta} < 1/2$ and an equal and opposite suction of magnitude K in the region $1/2 < \hat{\zeta} < 1$. For $N = 3$ there are two blowing regions from $0 < \hat{\zeta} < 1/3$ and $2/3 < \hat{\zeta} < 1$ and a suction region for $1/3 < \hat{\zeta} < 2/3$ and so on. For even N there are an equal number of blowing and suction regions and for odd N there are $(N+1)/2$ blowing regions and $(N-1)/2$ suction regions. The injection profiles for which N is an even number are of particular interest as the mean amount of mass injected through the slot is zero.

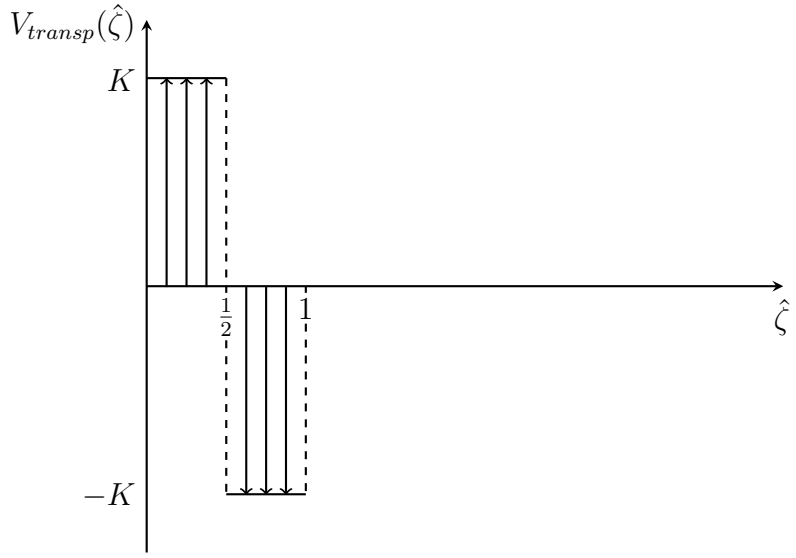

Figure 2.5.2: Injection profile given by (2.5.4) for $N = 2$.

2.5.1 Zero mass injection

The profiles for which there is zero mass injection through the surface are important as in many physical applications it is useful to recirculate fluid by sucking from the boundary layer and injecting the same fluid back into the boundary layer rather than having to have a source of injectant fluid. Boundary-layer suction has been utilised as a method of control since the Second World War, see Braslow (1999) [7], however traditionally the air extracted is vented away from the flow control area. The possibility of using the extracted air to further control flow separation via short-scale injection is of significant interest.

Taking $N = 2$ in (2.5.4) provides an injection profile with both a blowing and a suction in the injection slot region as shown in figure 2.5.2. Figures 2.5.3, 2.5.4 and 2.5.5 show (a) the streamwise velocity U and (b) the perturbation vorticity $\zeta_0\tilde{\Theta}$ along with the particle path lines in the (ζ, η) plane from the numerical solution of the governing equations (2.1.1) with the injection profile (2.5.4) for $N = 2$ and $K = 1, 1.95, 3$ respectively.

The injection profile given by (2.5.4) for $N = 2$, for large γ, is

$$\Phi_w(\hat{\zeta}) = -V_{transp}(\hat{\zeta}) = \begin{cases} -K, & 0 \leq \hat{\zeta} < \frac{1}{2}, \\ K, & \frac{1}{2} \leq \hat{\zeta} < 1 \\ 0, & \hat{\zeta} \geq 1. \end{cases} \tag{2.5.5}$$

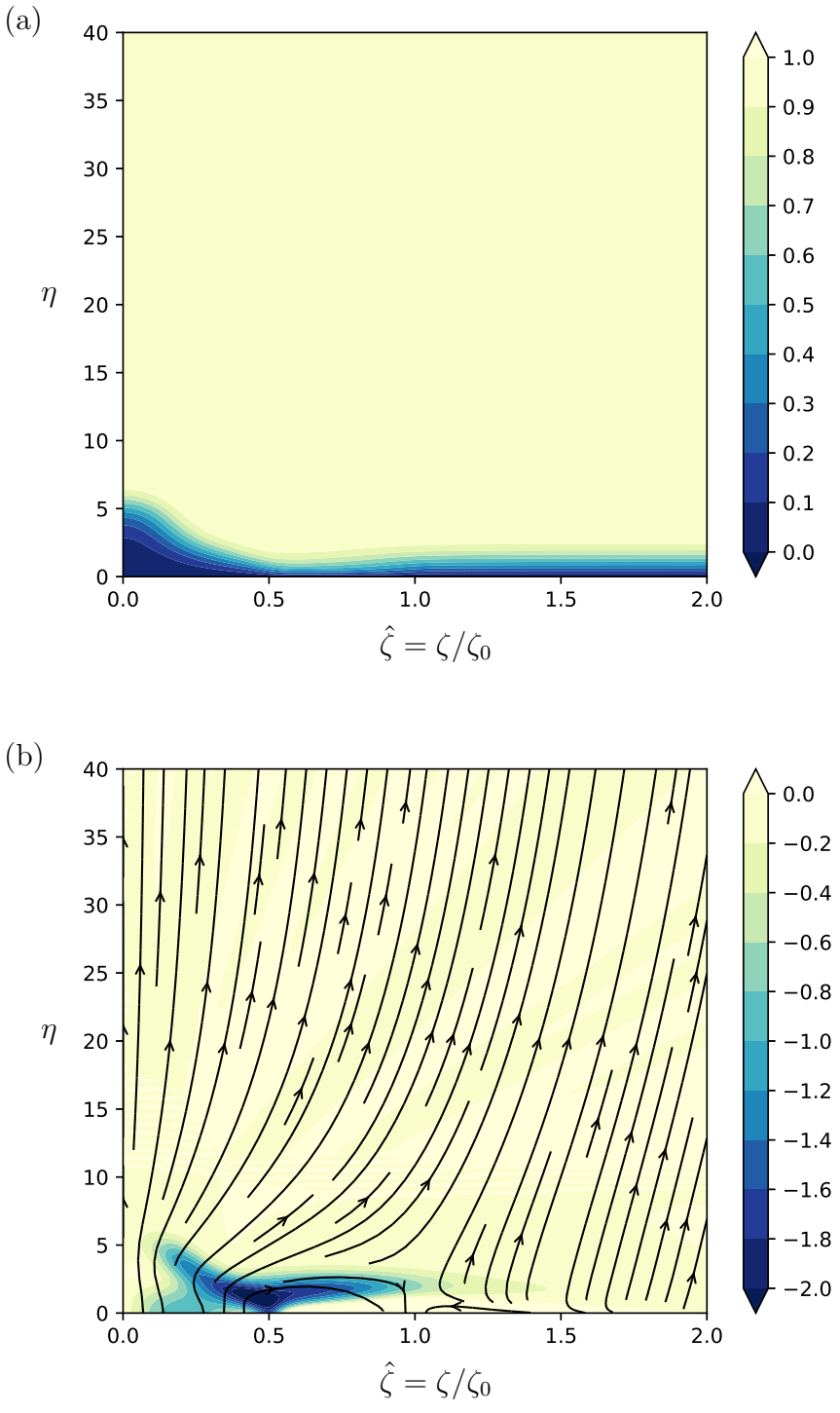

Figure 2.5.3: Results are shown for a wall transpiration (2.5.4), where $K = 1$ and $N = 2$. (a) shows contours of the streamwise velocity U and (b) shows the perturbation vorticity $\zeta_0\tilde{\Theta}$ and the (V, W) particle path lines (1.3.2).

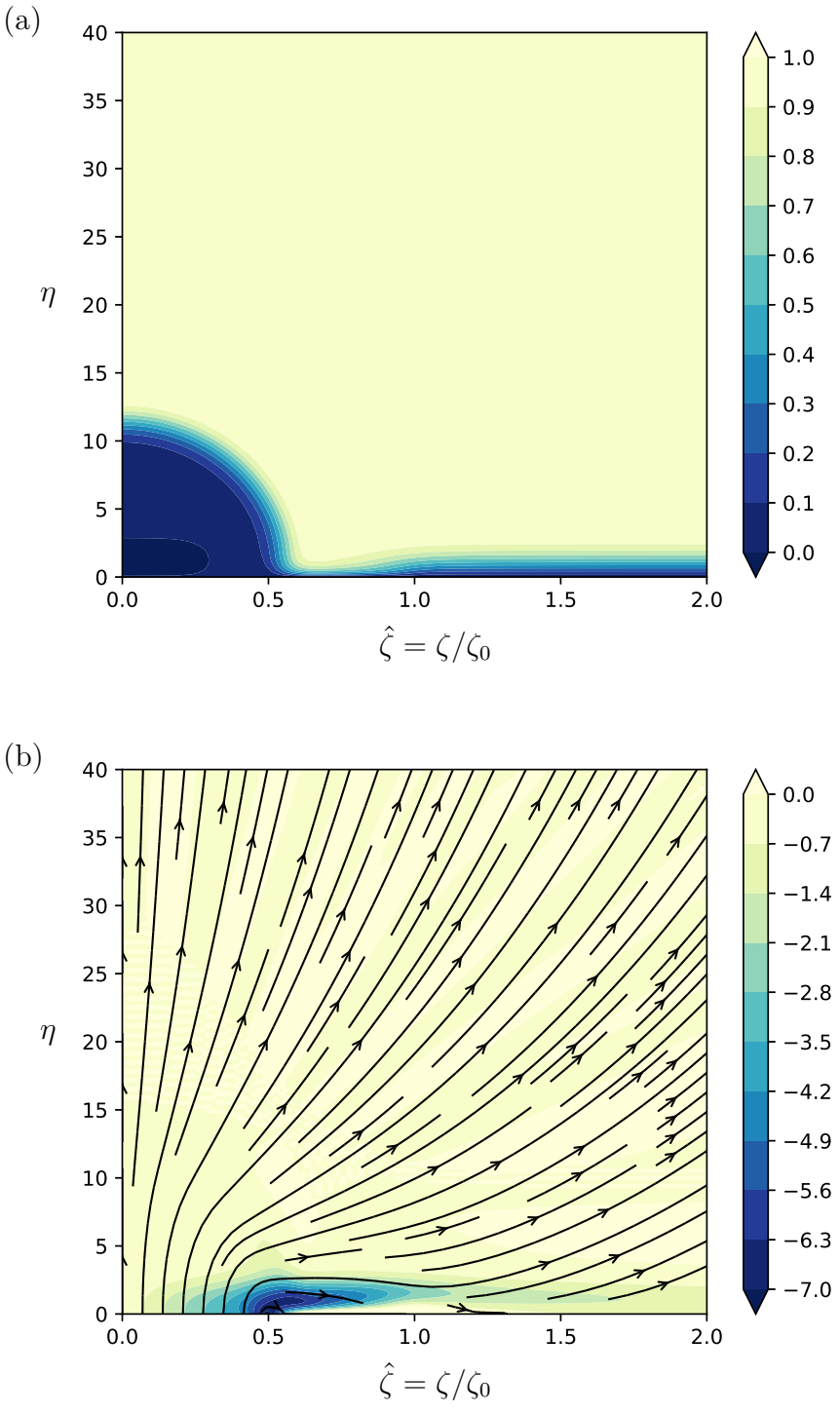

Figure 2.5.4: Results are shown for a wall transpiration (2.5.4), where $K = 1.95$ and $N = 2$. (a) shows contours of the streamwise velocity U and (b) shows the perturbation vorticity $\zeta_0\tilde{\Theta}$ and the (V, W) particle path lines (1.3.2).

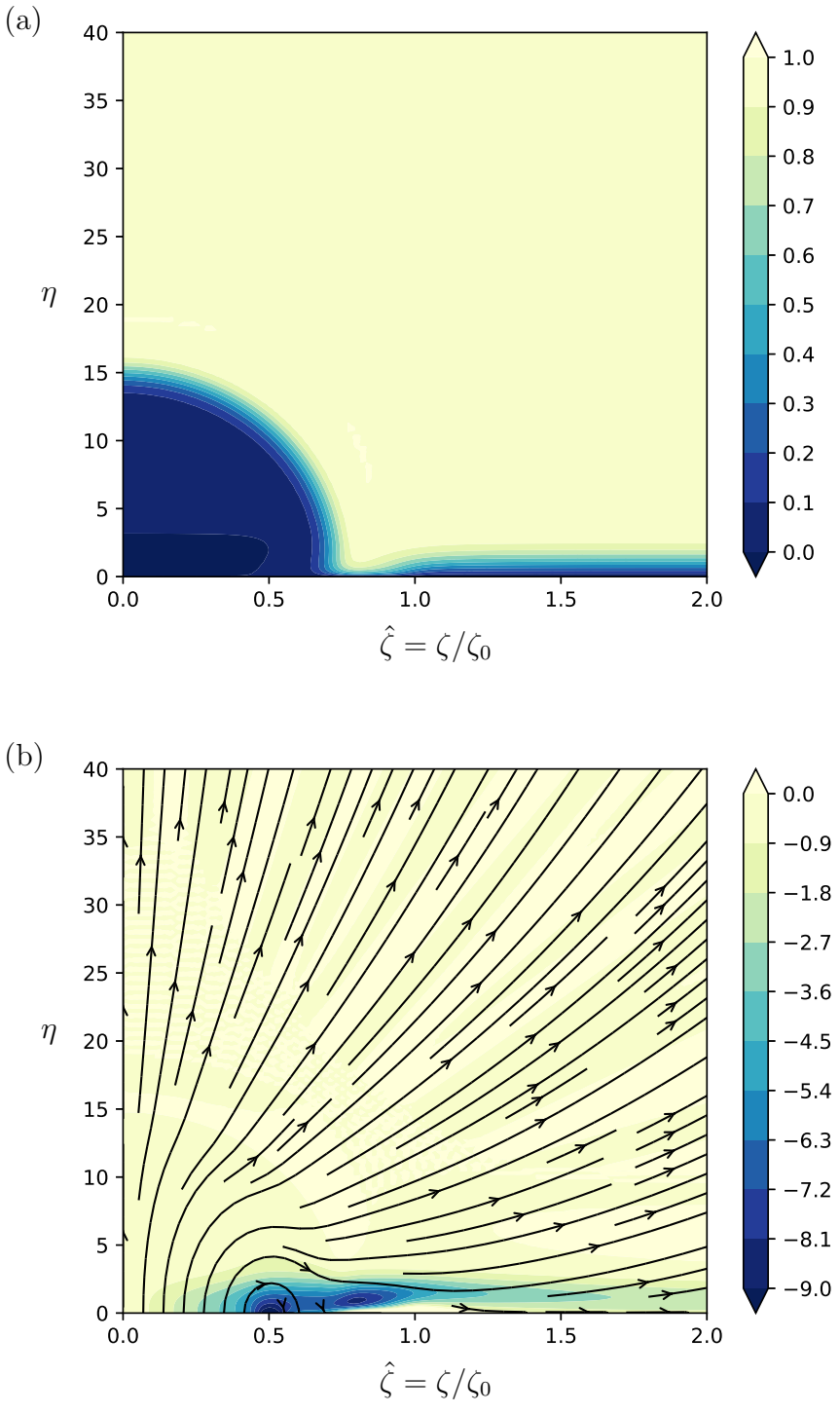

Figure 2.5.5: Results are shown for a wall transpiration (2.5.4), where $K = 3$ and $N = 2$. (a) shows contours of the streamwise velocity U and (b) shows the perturbation vorticity $\zeta_0\tilde{\Theta}$ and the (V, W) particle path lines (1.3.2).

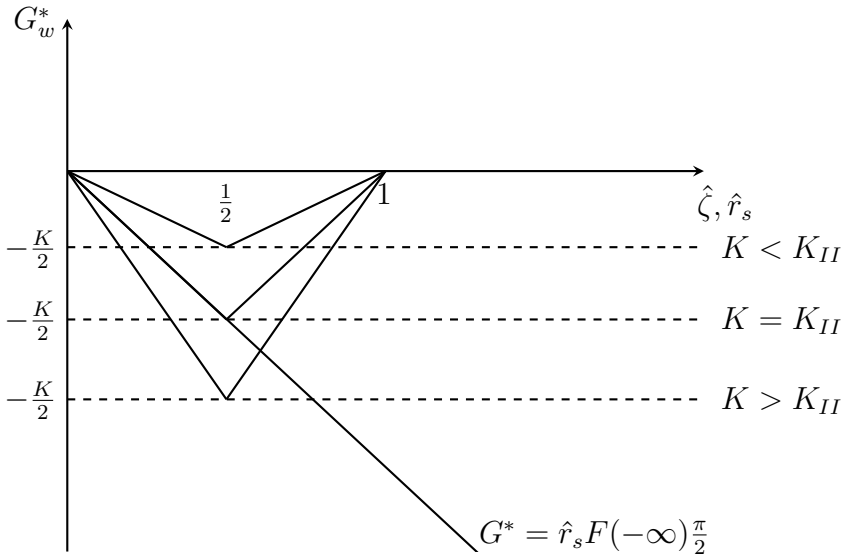

Figure 2.5.6: The mass flux through the injection slot $G_w^*(\zeta)$ for three different injection rates K and injection profile (2.5.4) with $N = 2$ is compared with the mass flux through the shear layer $G^* = \hat{r}_s F(-\infty)\pi/2$.

Then the scaled mass flux through the injection slot is, after requiring matching at the region interfaces, given by

$$G_w^*(\hat{\zeta}) = \int_0^{\hat{\zeta}} \Phi_w(\hat{\zeta})\mathrm{d}\hat{\zeta} = \begin{cases} -K\hat{\zeta}, & 0 \le \hat{\zeta} < \frac{1}{2}, \\ K\hat{\zeta} - K, & \frac{1}{2} \le \hat{\zeta} < 1 \\ 0, & \hat{\zeta} \ge 1. \end{cases} \tag{2.5.6}$$

Figure 2.5.6 shows the three possible cases for matching the mass flux when $N = 2$. Firstly it is possible that K is small enough that $G_w^*(\zeta)$ does not intersect $\hat{r}_s F(-\infty)\pi/2$ therefore the mass flux argument does not hold. The first interesting case is the critical point when the two curves intersect for the first time and $\hat{r}_s F(-\infty)\pi = G_w^*(\zeta) = -K/2$ such that

$$\hat{r}_s = \frac{-K}{F(-\infty)\pi} \approx 0.257K. \tag{2.5.7}$$

This first intersection occurs at $\hat{\zeta} = \hat{r}_s = 1/2$ when $K = -\pi F(-\infty)/2 = K_{II}$, the formation of the semi-circular streak can be seen in figure 2.5.4. Finally when $K > K_{II}$ there is one intersection point in the region $1/2 < \hat{r}_s < 1$ such that $\hat{r}_s F(-\infty)\pi/2 = K\hat{r}_s - K$ which implies that

$$\hat{r}_s = \frac{-2K}{F(-\infty)\pi - 2K}. \tag{2.5.8}$$

As $K \to \infty$ the streak radius $\hat{r}_s \to 1$, this is only an observation as the asymptotic structure breaks down when $K \to \infty$. Unlike the $N = 1$ case it is clear to see that the streak is of bounded extent, as shown in figure 2.5.5, even for large injection rates $K \gg K_{II}$.

Suppose that $N = 2n$ for $n = 1, 2, \ldots$ then N is even and there are an equal number of blowing and suction regions such that

$$\Phi_w(\hat{\zeta}) = -V_{transp}(\hat{\zeta}) = \begin{cases} (-1)^i K, & \frac{i-1}{N} \leq \hat{\zeta} < \frac{i}{N}, \\ 0, & \hat{\zeta} \geq 1, \end{cases} \tag{2.5.9}$$

for $i = 1, 2, \ldots, N$. Then the scaled mass flux through the injection slot is given by

$$G^*_w(\hat{\zeta}) = \int_0^{\hat{\zeta}} \Phi_w(\hat{\zeta}) \mathrm{d}\hat{\zeta} = \begin{cases} (-1)^i K \hat{\zeta} + a_i, & \frac{i-1}{N} \leq \hat{\zeta} < \frac{i}{N}, \\ b, & \hat{\zeta} \geq 1, \end{cases} \tag{2.5.10}$$

where a_i and b are constants. It is known that $G^*_w(\hat{\zeta} = 0) = a_1 = 0$ then matching at the interfaces of the regions $\hat{\zeta} = i/N$ gives

$$(-1)^i K \hat{\zeta} + a_i = (-1)^{i+1} K \hat{\zeta} + a_{i+1}. \tag{2.5.11}$$

Rearranging gives the recursive definition

$$a_{i+1} = \frac{2Ki}{N}(-1)^i + a_i, \tag{2.5.12}$$

with $a_1 = 0$. This means that each of the constants a_i for $i = 1, 2, \ldots, N$ are defined by

$$a_i = -\frac{1}{2}(-1)^i \left(2i + (-1)^i - 1\right) \frac{K}{N}, \tag{2.5.13}$$

which implies that $a_N = -K$ since N is even. Then at $\hat{\zeta} = 1$ $(i = N)$ it is required that $(-1)^i K \hat{\zeta} + a_i = b = 0$. So the mass flux function is given by

$$G^*_w(\hat{\zeta}) = \begin{cases} (-1)^i K \left[\hat{\zeta} - \frac{1}{2N}\left(2i + (-1)^i - 1\right)\right], & \frac{i-1}{N} \leq \hat{\zeta} < \frac{i}{N}, \\ 0, & \hat{\zeta} \geq 1, \end{cases} \tag{2.5.14}$$

for $i = 1, 2, \ldots, N$.

For the mass flux argument when N is even there are a number of cases to consider depending upon the intersections of $\hat{r}_s F(-\infty)\pi/2$ and $G^*_w(\hat{\zeta} = \hat{r}_s)$. Firstly it is possible

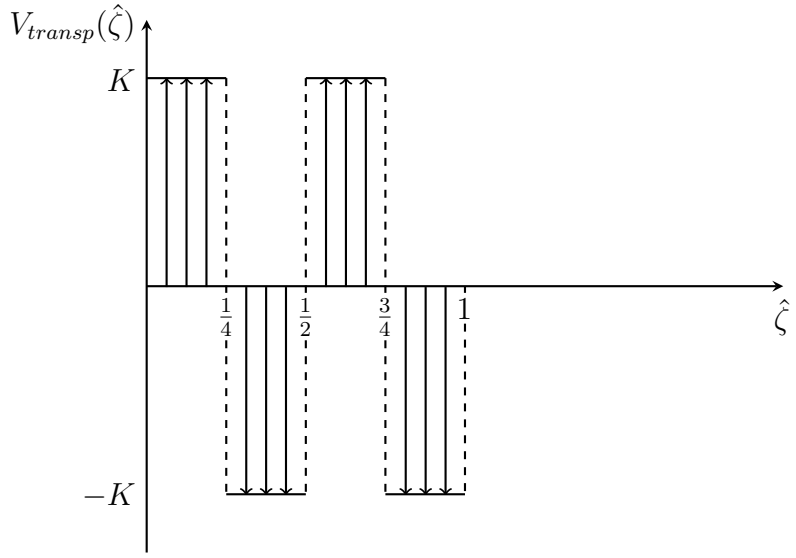

Figure 2.5.7: Injection profile given by (2.5.4) for $N = 4$.

that there are no intersections then the mass flux argument does not hold. Then there are series of critical injection rates for which each of the negative peaks of the $G^*_w(\hat{\zeta})$ function intersect with $\hat{r}_s F(-\infty)\pi/2$ at $\hat{\zeta} = \hat{r}_s = (2j-1)/N$ for $j = 1, 2, \ldots, N/2$. Each of the critical injection rates occurs when

$$\hat{r}_s F(-\infty)\frac{\pi}{2} = -\frac{K}{N}, \tag{2.5.15}$$

so rearranging for K the critical injection rates are

$$K_j = \frac{(1-2j)F(-\infty)\pi}{2}, \tag{2.5.16}$$

for $j = 1, 2, \ldots, N/2$, where $K_1 = -F(-\infty)\pi/2 = K_{II}$. So for example if $N = 4$, see figure 2.5.7, there is the critical injection rate $K_1 = K_{II}$ with $\hat{r}_s = 1/4$ and there is another critical injection rate $K_2 = -3\pi F(-\infty)/2 \approx 5.8$ with $\hat{r}_s = 3/4$.

Figure 2.5.8 shows the streamwise velocity contours when $N = 4$ in (2.5.4) for (a) $K = 3$ and (b) $K = 7$. When $K_1 < K = 3 < K_2$ the low-speed streak is constrained in the spanwise direction and is split into two parts, the main low-speed region near to $\hat{\zeta} = 0$ and a much smaller low-speed near to $\hat{\zeta} = 0.5$. The mass flux argument only predicts the more dominant low-speed streak near to the centre of the injection region. For $K = 7 > K_2$ the two low-speed regions in the previous regime join together to form one much larger streak. Continuing to increase K leads to a more defined streak of increasing size but limited by $\hat{r}_s = 1$.

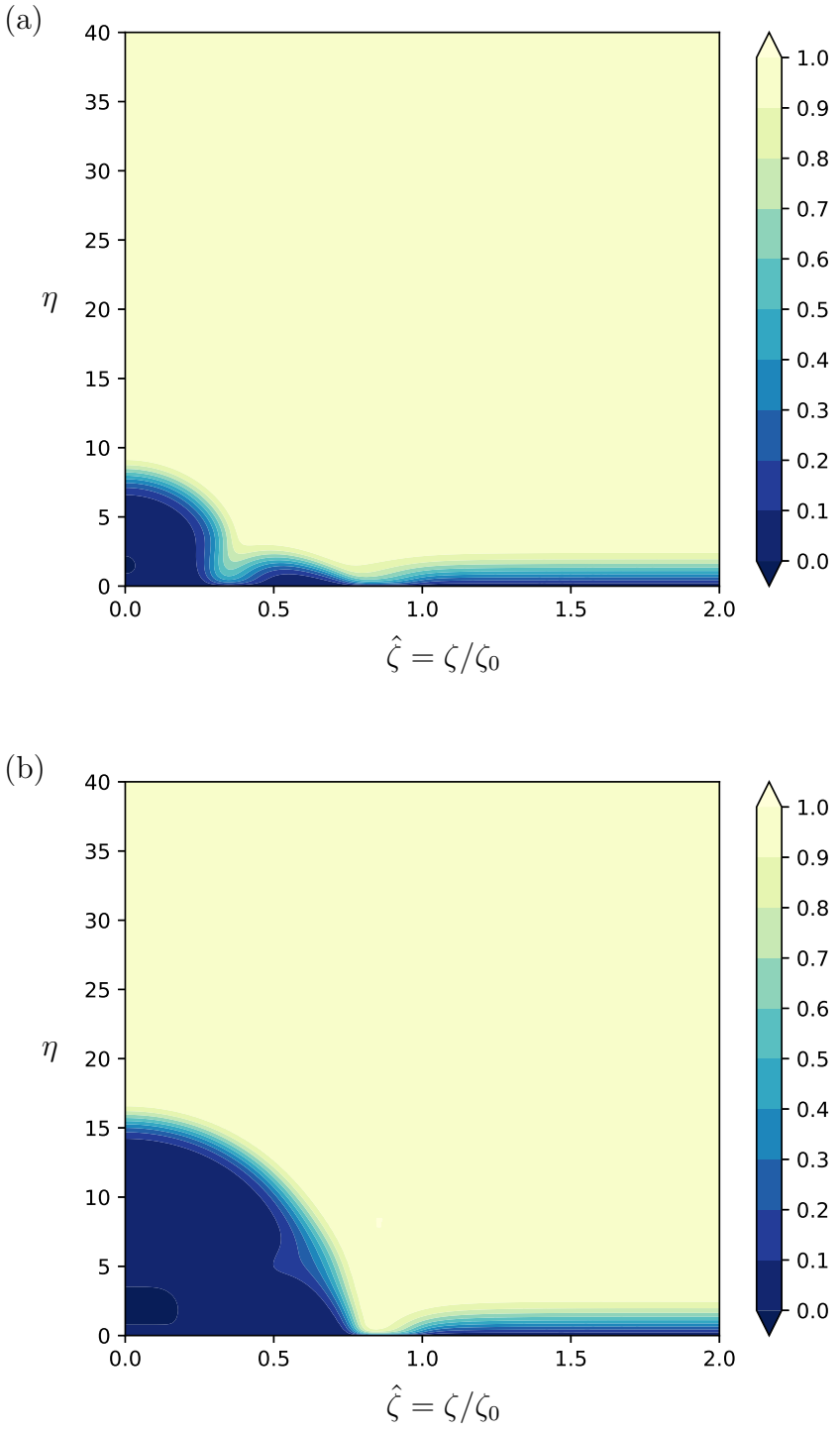

Figure 2.5.8: Streamwise velocity contours U are shown for a wall transpiration (2.5.4), where $N = 4$ and (a) $K = 3$, (b) $K = 7$.

At each critical injection rate K_j there are $2(j-1)$ intersection points of $G_w^*(\hat{\zeta})$ and $\hat{r}_s F(-\infty)\pi/2$ if $j \geq 2$ or one intersection point when $j = 1$. At values of K between the critical injection rates $K_j < K < K_{j+1}$ there are $2j-1$ intersection points for $j \geq 1$. The last intersection point is located in the interval $(2j-1)/N < \hat{r}_s < 2j/N$, here $j = 1, 2, \ldots, N/2$. So for the last intersection point $\hat{r}_s F(-\infty)\pi/2 = K\hat{r}_s - 2jK/N$ which implies that

$$\hat{r}_s = \frac{4jK}{N(2K - F(-\infty)\pi)}, \tag{2.5.17}$$

for $j = 1, 2, \ldots, N/2$. For example if $N = 4$ and $K_1 < K < K_2$ $(j = 1)$ this becomes

$$\hat{r}_s = \frac{K}{2K - F(-\infty)\pi}, \tag{2.5.18}$$

or if $K > K_2$ $(j = 2)$ then

$$\hat{r}_s = \frac{2K}{2K - F(-\infty)\pi}. \tag{2.5.19}$$

Injection profiles of the form (2.5.4) behave in a similar manner to the basic $N = 1$ case. When N is even the low-speed streak is confined to the region $\hat{r}_s < 1$ even for large injection rates and as N is increased there are a larger number of distinct regimes. There is no evidence of non-unique states due to the effect of the blowing outside the streak. There is a smooth transition from the smaller streak radius to the larger streak radius as the blowing at the surface outside the smaller streak disturbs the quiescent fluid outside the streak thereby invalidating the mass flux argument in this region. Moving on from these 'top-hat' like injections the analysis will now turn to a more gradually varying injection profile.

2.5.2 Gaussian injection profiles

Another injection profile which exists over a finite spanwise extent is the Gaussian profile

$$V_{transp}(\zeta) = Ke^{-\zeta^2/\zeta_0^2}, \tag{2.5.20}$$

which replaces (2.1.2) in the formulation. This means that $\Phi_w(\hat{\zeta}) = -Ke^{-\hat{\zeta}^2}$ and therefore the scaled mass flux through the injection slot is given by

$$G_w^*(\hat{\zeta}) = -K\int_0^{\hat{\zeta}} e^{-s^2}\mathrm{d}s = -\frac{K\sqrt{\pi}}{2}\,\mathrm{erf}(\hat{\zeta}), \tag{2.5.21}$$

where $\mathrm{erf}(\hat{\zeta})$ is the error function. As with the 'top-hat' injection profile (2.1.2) the parameter ζ_0 defines the spanwise extent of the injection and K determines the maximum magnitude of the injection velocity. The Gaussian profile (2.5.20) varies much more gradually in the spanwise direction than the 'top-hat' profile and has a smaller total mass flux through the surface. The injection is no longer essentially confined to the region $\hat{\zeta} \leq 1$ but is instead distributed in the $\hat{\zeta}$ domain albeit with the greater injection being located near to $\hat{\zeta} = 0$. It is expected that the critical injection rate, at which transition between the moderate and strong injection regimes takes place, will be different; the mass flux argument used in the 'top-hat' profile case is still valid and will help when describing the critical injection rate for the Gaussian injection profile.

Figure 2.5.9 shows the streamwise velocity contours produced by a Gaussian injection (2.5.20) with (a) $K = 2$ and (b) $K = 3$. It can be seen that for the Gaussian injection with $K = 2$ the flow remains in the moderate injection regime, for the 'top-hat' profile this rate of injection would have pushed the flow into the strong injection regime. For the Gaussian injection with $K = 3$ the flow is definitely in the strong injection regime so there is some intermediate value between $K = 2$ and $K = 3$ which delineates the transition from the moderate to the strong regime.

As for the previous injection profiles, the critical injection rate at which the flow transitions from the moderate to the strong injection regime is sought. For the 'top-hat' transpiration the critical injection rate K_{II} is given by (2.3.50), following the same argument but this time using the Gaussian mass flux (2.5.21) gives

$$\hat{r}_s F(-\infty)\frac{\pi}{2} = -\frac{K\sqrt{\pi}}{2}\,\mathrm{erf}(\hat{r}_s). \tag{2.5.22}$$

Setting $\hat{r}_s = 1$ the critical injection rate for the Gaussian injection function (2.5.20) is found to be

$$K_{II} = -\frac{F(-\infty)\sqrt{\pi}}{\mathrm{erf}(1)} \approx 2.60. \tag{2.5.23}$$

The other critical injection rate remains unchanged when using the Gaussian injection function and is still given by $K_I \approx 0.876$.

The implicit nature of (2.5.22) means that it is difficult to find an exact formula for the streak radius however it is possible to obtain an approximation. The mass flux

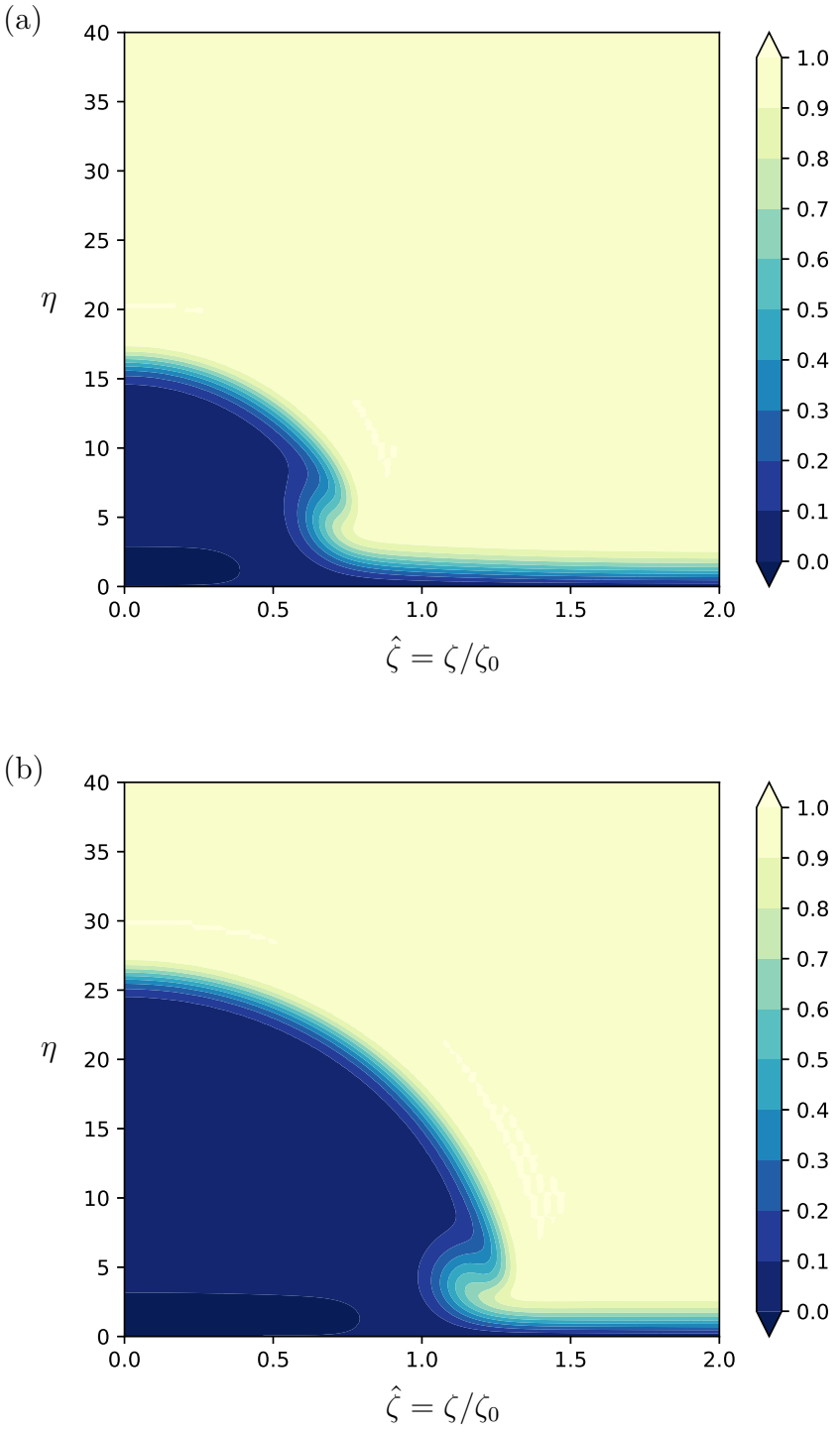

Figure 2.5.9: Streamwise velocity contours U are shown for a Gaussian wall transpiration (2.5.20), where (a) $K = 2$ and (b) $K = 3$.

function (2.5.21) may be approximated by using the substitution $s = t^{1/2}$ so that

$$G_w^*(\hat{\zeta}) = -K\int_0^{\hat{\zeta}} e^{-s^2}\mathrm{d}s = -\frac{K}{2}\int_0^{\hat{\zeta}^2} t^{-\frac{1}{2}}e^{-t}\mathrm{d}t. \tag{2.5.24}$$

The expansion

$$t^{-\frac{1}{2}}e^{-t} = t^{-\frac{1}{2}} - t^{\frac{1}{2}} + \frac{1}{2}t^{\frac{3}{2}} - \frac{1}{6}t^{\frac{5}{2}} + \ldots \tag{2.5.25}$$

converges for all $t \neq 0$ but not at $t = 0$. This series is however asymptotic uniformly for $0 \leq t \leq \hat{\zeta}$ as $\hat{\zeta} \to 0+$. Integrating term-by-term gives

$$G_w^*(\hat{\zeta}) \sim -K\left(\hat{\zeta} - \frac{1}{3}\hat{\zeta}^3 + \frac{1}{10}\hat{\zeta}^5 - \frac{1}{42}\hat{\zeta}^7 + \ldots\right), \quad \hat{\zeta} \to 0+, \tag{2.5.26}$$

describing the behaviour of the mass flux function for small $\hat{\zeta}$. For the behaviour as $\hat{\zeta} \to \infty$ repeated use of integration by parts gives

$$G_w^*(\hat{\zeta}) \sim -\frac{K\sqrt{\pi}}{2} + \frac{Ke^{-\hat{\zeta}^2}}{2\hat{\zeta}}\left[1 + \sum_{n=1}^{\infty}\frac{(-1)^n(1)(3)(5)\ldots(2n-1)}{(2\hat{\zeta}^2)^n}\right], \quad \hat{\zeta} \to \infty. \tag{2.5.27}$$

The asymptotic approximations [3] for small and large $\hat{\zeta}$ means it is possible to define a leading order approximation to $G_w^*(\hat{\zeta})$ as

$$G_w^*(\hat{\zeta}) = \begin{cases} -K\hat{\zeta}, & 0 \leq \hat{\zeta} < \frac{\sqrt{\pi}}{2}, \\ -\frac{K\sqrt{\pi}}{2}, & \hat{\zeta} \geq \frac{\sqrt{\pi}}{2}. \end{cases} \tag{2.5.28}$$

In the strong injection regime $\hat{r}_s \geq 1 > \sqrt{\pi}/2$ therefore it follows that to leading order

$$\hat{r}_s \sim -\frac{K}{F(-\infty)\sqrt{\pi}}. \tag{2.5.29}$$

Since for $\zeta_0 \gg 1$ the mass flux parameter $A \sim -\zeta_0^2\hat{r}_s^2$ it follows that for large ζ_0

$$A \sim -\frac{K^2\zeta_0^2}{F(-\infty)^2\pi}, \tag{2.5.30}$$

to leading order for the Gaussian injection profile.

Figure 2.5.10 plots numerically calculated data points of A/ζ_0^2 as a function of K for different values of ζ_0. It may be seen that as the injection width ζ_0 increases the asymptotic prediction as $\zeta_0 \to \infty$ approximates the numerical data with greater and greater precision. The Gaussian transpiration profile discussed above will be useful later, when downstream evolution of the non-self-similar equations is considered. The Gaussian profile is smoother than the 'top-hat' profile considered earlier and

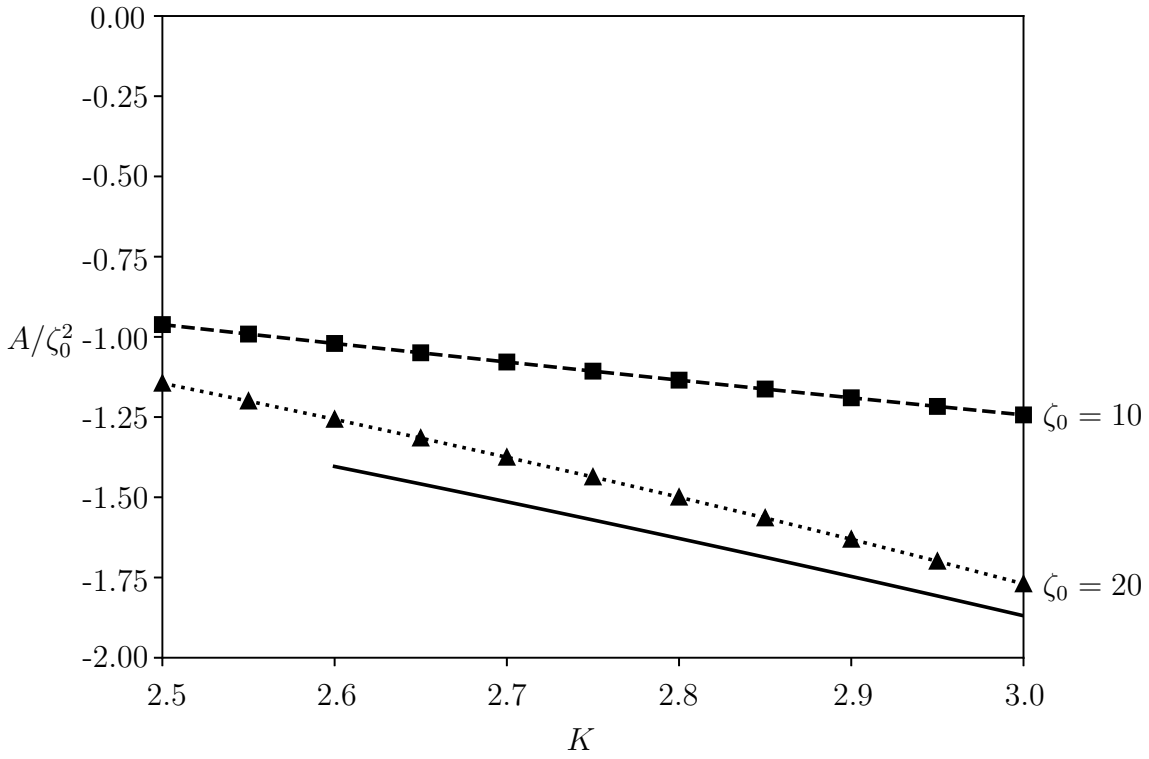

Figure 2.5.10: Numerically calculated values of A/ζ_0^2 for the Gaussian injection profile (2.5.20) with $K \in [2.5, 3.0]$ and $\zeta_0 = 10, 20$. The solid line shows the asymptotic prediction for large ζ_0 given by $-K^2/F(-\infty)^2\pi$.

therefore the computational mesh required for numerical convergence is simpler. With the 'top-hat' profile it is necessary to insert extra points near to the edge of the injection slot thereby creating unnecessary complexities in the cross-sectional mesh. Such complexities are reduced when using a Gaussian transpiration profile and hence numerical calculation is relatively straightforward.

2.6 Discussion

This chapter has investigated a short-scale spanwise injection through a flat plate held parallel to an oncoming unidirectional flow. In the formulation presented the injection slot is of dimensional width $\zeta_0(2x^*\nu*/U^*_\infty)^{1/2}$ and the injection rate is of size $K(U^*_\infty\nu^*/x^*)^{1/2}$ with this choice of slot width and injection rate allowing for solutions that are self-similar in the downstream x^* coordinate. The short-scale injection acts to modify the underlying two-dimensional Blasius base flow boundary layer, which still persists far away from the injection region. Incorporating a short-scale injection modifies the mass flux from the boundary layer into the outer flow, in a similar manner to the narrow gap/plate analysed by Hewitt & Duck (2014) [35], which leads to a modification of the far-field boundary conditions. The self-similar formulation is only for convenience and is not a theoretical restraint; more general injection profiles could be examined by marching in the downstream x^* coordinate: see chapter 4.

For two-dimensional self-similar injection it is known that solutions no longer exist for $K \gtrsim 0.876$ with the boundary layer said to have been 'blown off' the surface of the plate. For the three-dimensional boundary-region equations (2.1.1) governing short-scale spanwise disturbances, there is no evidence of 'blow-off' occurring with solutions continuing to exist past this critical value.

For large injection slot widths numerical evidence suggests the existence of three distinct flow regimes. Whether the flow is in a given regime is determined by the magnitude of the injection parameter K. An asymptotic description of each of the three flow regimes is given in section 2.3. The flow exists in the first regime when the magnitude of the blowing transpiration is small $K \leq K_I \approx 0.876$: in this case there is little deviation from the underlying Blasius base flow. This weak injection state can be determined by parabolic marching from the far-field in the spanwise coordinate

towards the injection region. Upon approaching the centreline of the injection region it would be expected that the Blasius solution with an injection boundary condition is recovered, but this does not occur due to the influence of spatially unstable eigenmodes, see section 2.4.

The moderate injection regime is reached when $K_I < K < K_{II} \approx 1.95$. Here there is significant deviation from the underlying base flow boundary layer, in the form of a low-speed streak, but only in the vicinity of the injection region. Increasing the injection rate past this second critical value the flow enters the strong injection regime. The radius of the low speed streak now becomes larger than the width of the injection slot and the streak takes on a semi-circular geometry. This 'bubble' shaped velocity profile is formed by a thin shear layer connecting the distinct low-speed and high-speed regions, see figure 2.2.3.

Asymptotic descriptions of the weak and strong regimes show clear differences in the mass flux parameter A. Asymptotic analysis indicates that in the strong injection regime the mass flux parameter A is proportional to the square of the injection slot width ζ_0 as shown in (2.3.49). On the other hand, for the weak regime it was found that the mass flux is directly proportional to the injection slot width as shown in (2.3.18b). This means that for a large injection there is a very large increase in the mass flux from the boundary layer into the outer potential flow. This significant increase in the magnitude of the mass flux parameter hints at the difficulty in computing solutions when there is a large injection. Direct comparison between the asymptotically predicted values of A and the values calculated during the numerical routine show good agreement for large values of ζ_0, see figure 2.3.5, showing that the asymptotic results provide a realistic interpretation.

The asymptotic results presented in section 2.3 are robust to changes in the injection profile (2.1.2) as analysis of different profiles can be approached in the same way. In section 2.5 alternative injection profiles are discussed, namely zero-mean mass and Gaussian injections. The zero mass injection profile is of interest due to its applicability to laminar flow control and the Gaussian profile is useful due to its simplicity and smooth spanwise variation. The mass flux arguments presented in section 2.3 apply equally well to the alternative profiles examined in section 2.5 with only a few details needing to be changed.

For large injection widths the geometry of the moderate and strong injection regimes is dictated by the interaction between mass flux through the plate and the mass flux across the bounding shear layer. The streak radius r_s in particular is sensitive to changes in the rate of injection through the plate surface. The results show that short-scale spanwise diffusion can remove the 'blow-off' singularity predicted by the two-dimensional theory with three-dimensional solutions existing for any injection rate. The low-speed streaks that are formed are characterised by very low values of wall shear but despite this no flow reversal is observed in the streamwise direction.

Chapter 3

Applying a favourable pressure gradient

In chapter 2 the classical two-dimensional formulation is extended, in the absence of a pressure gradient, to a three-dimensional formulation by allowing injection over a spanwise length scale which is comparable to the boundary-layer thickness. Counter to the two-dimensional theory, the resulting three-dimensional solutions continue to exist for injection velocities greater than the critical two-dimensional 'blow-off' injection rate. These new solutions take the form of low-speed streamwise-aligned streaks. The streak solutions can be categorised into one of three regimes, where the geometry of the streak is determined by the injection rate, as the width of the injection slot increases.

This chapter again examines the effect of a short-scale injection, but also allows for a favourable pressure gradient. This chapter contains, along with a few extra details, the work presented in Williams & Hewitt (2017) [71]. Generalising the three-dimensional boundary-layer injection solutions to include an applied pressure gradient is important not only because non-uniform external flows are commonplace, but also because it is known that for macro-scale injection the character of the flow is significantly affected by the pressure gradient [44].

3.1 Formulation

Consider a plate defined by $y^* = 0$, $x^* > 0$ which is a planar surface that is aligned with the free stream flow, where the leading edge is located at $x^* = 0$ as shown in

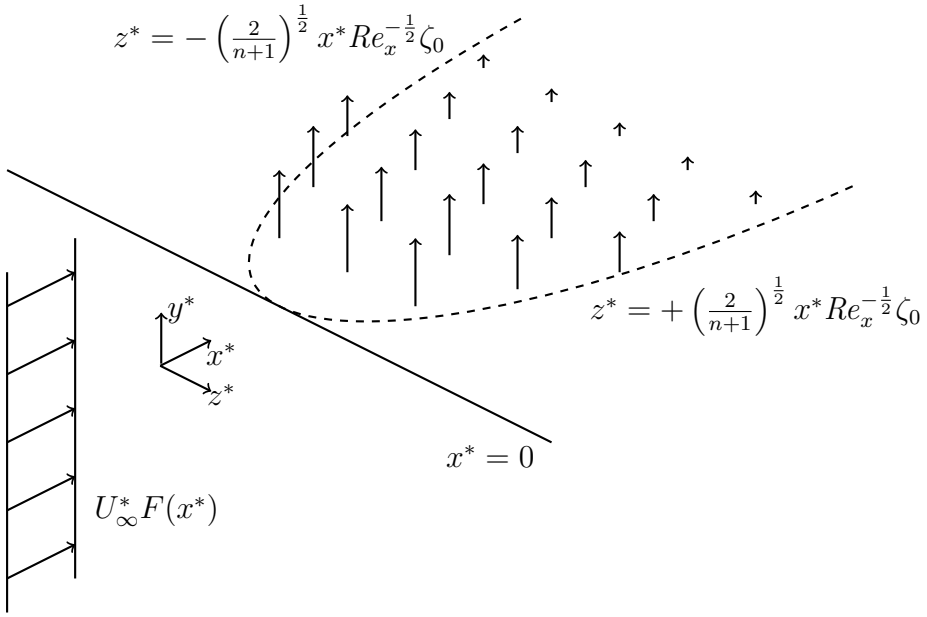

Figure 3.1.1: A schematic representation of the flow domain; the leading edge of the flat plate is located at $x^* = 0$ and the plate is aligned with an oncoming power law flow $U_\infty^* F(x^*)$. An injection perpendicular to the surface of the plate $v^* = v_w^*(x^*, z^*)$ is prescribed on $y^* = 0$ within the spanwise region specified by the dashed curve. The injection region grows downstream at the same rate as the boundary layer thickness with ζ_0 specifying the relative width of the injection slot.

figure 3.1.1. The streamwise velocity at the outer edge of the boundary-layer is given by $U_\infty^* F(x^*)$ where U_∞^* is a free stream reference speed. Power law external flows corresponding to $F(x^*) = (x^*/L^*)^n$ are allowed for where n is the constant pressure gradient parameter and L^* is some arbitrary dimensional length scale. As before at the surface of the plate no-slip boundary conditions $u^* = w^* = 0$ are imposed along with an injection velocity $v^* = v_w^*(x^*, z^*)$ given by (1.3.5). This combination of no-slip and permeable boundary conditions is valid as the injection is $O(Re^{-1/2})$ and therefore has no impact on the no-slip conditions to leading order. As in chapter 2 there is no surface topography so $H = H' = H'' = 0$, the transpiration through the surface of the plate is the only disturbance.

The governing equations (1.3.4) reduce to

$$(2 - \beta)U = \Phi_\eta + \Psi_\zeta, \tag{3.1.1a}$$

$$\Theta = \Psi_\eta - \Phi_\zeta, \tag{3.1.1b}$$

and

$$\nabla^2 U = \beta\left[U^2 - 1\right] - \Phi U_\eta - \Psi U_\zeta, \tag{3.1.2a}$$

$$\nabla^2 \Theta = 2(1-\beta)\left[\zeta U U_\eta - \eta U U_\zeta\right] - \Phi\Theta_\eta - \Psi\Theta_\zeta - (2-\beta)U\Theta, \tag{3.1.2b}$$

where $\beta = 2n/(n+1)$ is the well-known Hartree parameter [30] and ∇^2 is the two-dimensional Laplacian in the (ζ, η) plane. Combining (3.1.1a) and (3.1.1b) and their derivatives with respect η and ζ it is possible to obtain expressions for the Laplacian of both Φ and Ψ given by

$$\nabla^2 \Phi = (2-\beta)U_\eta - \Theta_\zeta, \tag{3.1.2c}$$

$$\nabla^2 \Psi = (2-\beta)U_\zeta + \Theta_\eta. \tag{3.1.2d}$$

Formulating the system of equations (3.1.2) in this way allows for a straightforward discretization scheme for the variables (Φ, Ψ, U, Θ) in the (ζ, η) plane as outlined in section 2.2.1.

Use of the nonlinear correction formulation outlined in section 1.3.2 allows the flow to be split into a response that is free from spanwise variations and a correction that is driven only by the short-scale disturbance. The base solution $(U_B, \Phi_B, \Psi_B, \Theta_B)$ which exists in the absence of any spanwise variation is governed by the system of equations (1.4.1). Here only a base flow solution with no cross flow, see section 1.4, of the form $U_B = F'(\eta)$, $\Phi_B = F(\eta)$, $\Psi_B = (1-\beta)F'(\eta)$, $\Theta_B = (1-\beta)F''(\eta)$ shall be considered where $F(\eta)$ satisfies

$$F''' + FF'' + \beta\left[1 - (F')^2\right] = 0, \tag{3.1.3}$$

which is the Falkner–Skan equation [21] subject to the boundary conditions $F(0) = F'(0) = 0$, $F'(\eta) \to 1$ as $\eta \to \infty$.

The nonlinear correction quantities, induced by any short-scale injection, are governed by

$$\hat{\nabla}^2\tilde{\Phi} = (2-\beta)\tilde{U}_\eta - \tilde{\Theta}_{\hat{\zeta}}, \tag{3.1.4a}$$

$$\hat{\nabla}^2\tilde{\Psi} = (2-\beta)\zeta_0^{-2}\tilde{U}_{\hat{\zeta}} + \tilde{\Theta}_\eta, \tag{3.1.4b}$$

$$\hat{\nabla}^2\tilde{U} = \beta\left[2U_B\tilde{U} + \tilde{U}^2\right] - \left(\hat{\zeta}\Psi_B + \tilde{\Psi}\right)\tilde{U}_{\hat{\zeta}} - \Phi_B\tilde{U}_\eta - \left(U_B' + \tilde{U}_\eta\right)\tilde{\Phi}, \tag{3.1.4c}$$

$$\begin{aligned}\hat{\nabla}^2\tilde{\Theta} = {} & 2(1-\beta)\left\{\hat{\zeta}\left(U_B + \tilde{U}\right)\tilde{U}_\eta + \hat{\zeta}U_B'\tilde{U} - \eta\zeta_0^{-2}\left(U_B + \tilde{U}\right)\tilde{U}_{\hat{\zeta}}\right\} \\ & - \left(\Phi_B + \tilde{\Phi}\right)\tilde{\Theta}_\eta - \hat{\zeta}\Theta_B'\tilde{\Phi} - \hat{\zeta}\Psi_B\tilde{\Theta}_{\hat{\zeta}} - \tilde{\Psi}\left(\Theta_B + \tilde{\Theta}_{\hat{\zeta}}\right) \\ & - (2-\beta)\left[\left(U_B + \tilde{U}\right)\tilde{\Theta} + \hat{\zeta}\Theta_B\tilde{U}\right],\end{aligned} \tag{3.1.4d}$$

where

$$\hat{\nabla}^2 \equiv \frac{\partial^2}{\partial\eta^2} + \frac{1}{\zeta_0^2}\frac{\partial^2}{\partial\hat{\zeta}^2}. \tag{3.1.4e}$$

This system of equations modifies (2.1.4) by including extra terms due to the applied pressure gradient. The surface boundary conditions are given by (1.3.14) which imposes the micro-slot injection profile defined by (2.1.2) with no base flow injection. The symmetry boundary conditions along the centreline $\hat{\zeta} = 0$ are defined by (2.1.7). Far from the injection region it is expected that the flow decays back towards the Falkner–Skan solution hence the far-field conditions (1.3.16) and (1.3.22) are imposed. The equations (3.1.4) governing the perturbation quantities $(\tilde{\Phi}, \tilde{\Psi}, \tilde{U}, \tilde{\Theta})$ must be solved numerically subject to the appropriate boundary conditions mentioned above.

3.2 Numerical results

When there is no injection, $K = 0$, through the surface of the plate the Falkner–Skan solution given by (3.1.3) is recovered and the flow remains two-dimensional throughout the domain. Any non-zero injection through the plate surface, over a finite spanwise extent ζ_0, generates a three-dimensional deviation from the two-dimensional base flow in the neighbourhood of the injection. Results for $K > 0$ and $0 \leq n < 1$, corresponding to $0 \leq \beta < 1$ are presented. When sufficiently far from the injection slot, such that the injection effects are small, the Falkner-Skan solution is recovered where $\beta = 0$ leads to a Blasius flow whilst $\beta \to 1$ leads to a Hiemenz (stagnation point) flow [38].

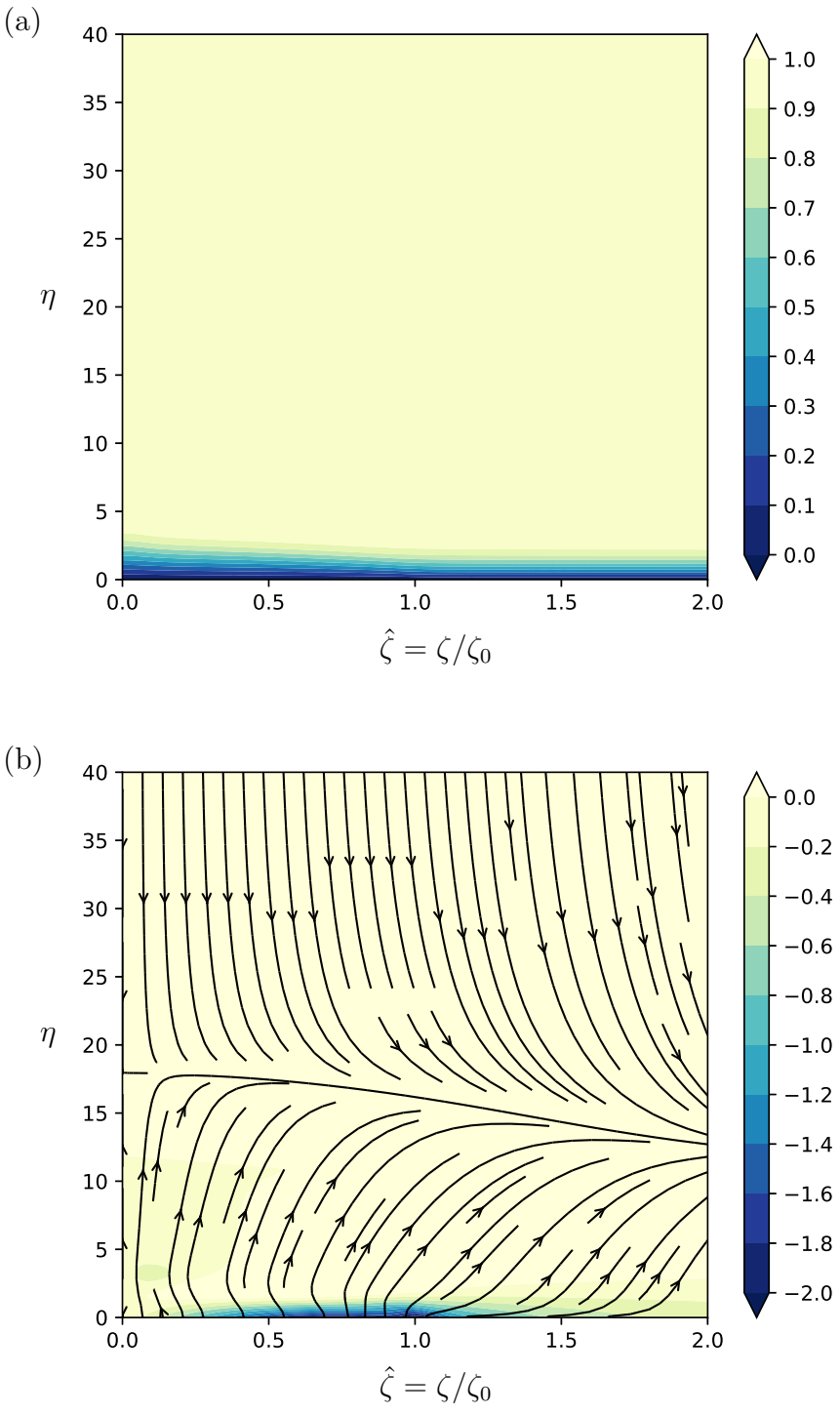

Figure 3.2.1: Results are shown for a wall transpiration (2.1.2), where $K = 0.5$, $\beta = 0.1$ and $\zeta_0 = 20$. (a) shows contours of the streamwise velocity U and (b) shows the perturbation vorticity $\zeta_0\tilde{\Theta}$ and the (V, W) particle path lines (1.3.2).

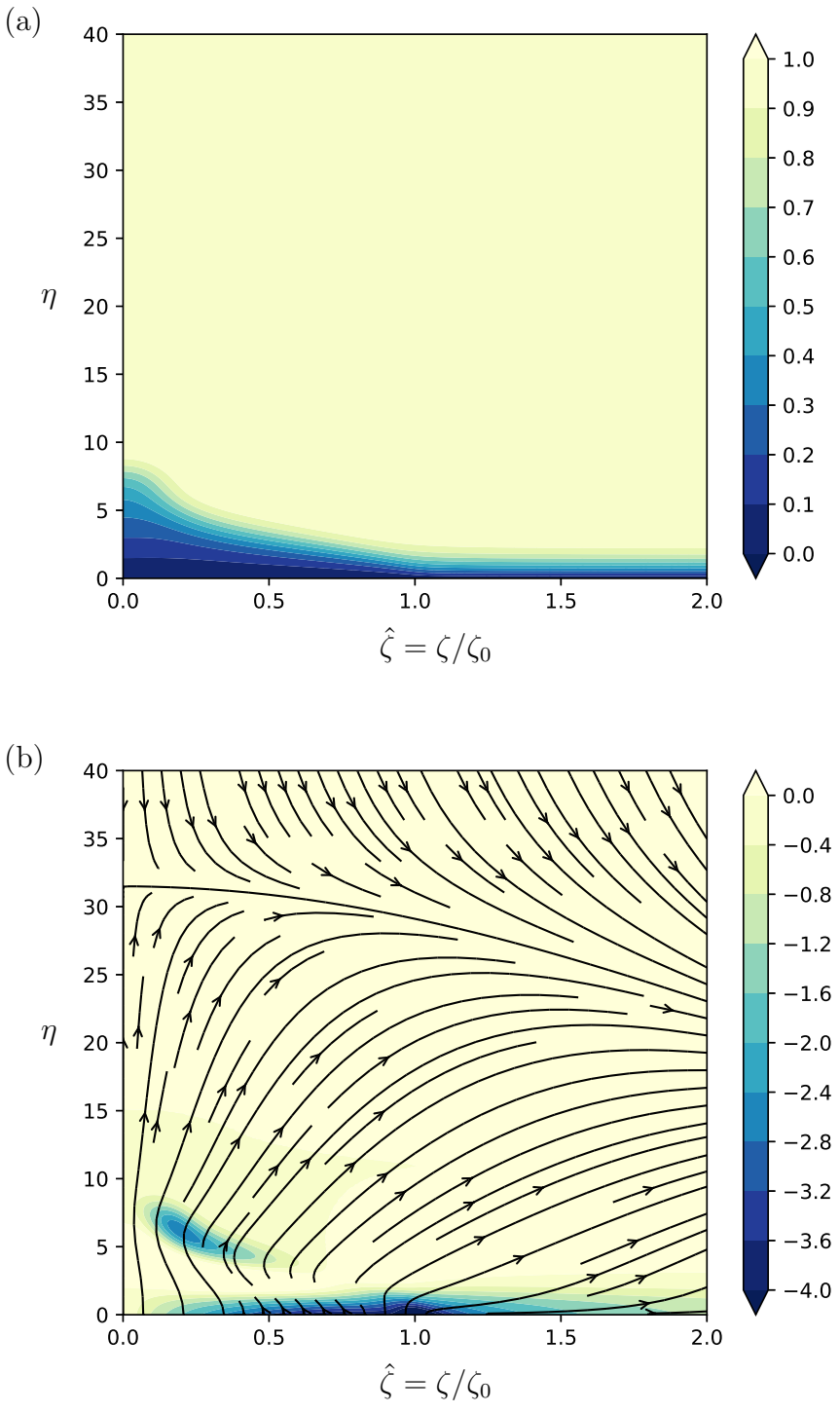

Figure 3.2.2: Results are shown for a wall transpiration (2.1.2), where $K = 1.5$, $\beta = 0.1$ and $\zeta_0 = 20$. (a) shows contours of the streamwise velocity U and (b) shows the perturbation vorticity $\zeta_0\tilde{\Theta}$ and the (V, W) particle path lines (1.3.2).

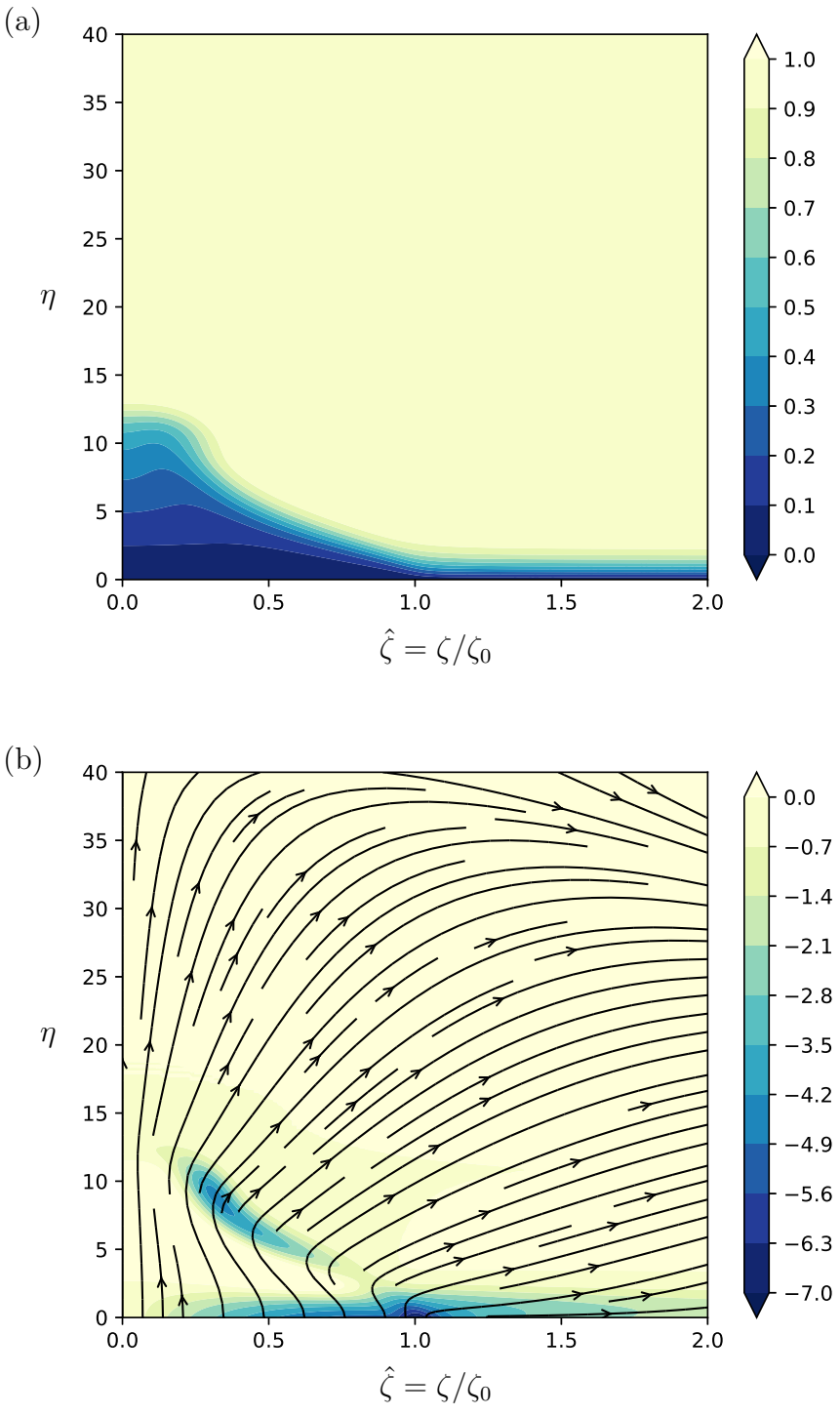

Figure 3.2.3: Results are shown for a wall transpiration (2.1.2), where $K = 2.5$, $\beta = 0.1$ and $\zeta_0 = 20$. (a) shows contours of the streamwise velocity U and (b) shows the perturbation vorticity $\zeta_0\tilde{\Theta}$ and the (V, W) particle path lines (1.3.2).

In chapter 2 it was shown that, for $K > 0$ and no applied pressure gradient ($\beta = 0$), three distinct flow regimes are observed, for a 'top-hat' injection profile, as the injection-slot width ζ_0 is increased. These three regimes are delineated by the injection rates: $0 < K < K_I \approx 0.876$, $K_I < K < K_{II} \approx 1.95$ and $K > K_{II}$. Figures 2.2.1, 2.2.2 and 2.2.3 illustrate the three flow regimes present when $\beta = 0$, the weak, moderate and strong injection regimes respectively. In the weak injection regime $0 < K < K_I$, although a three-dimensional state is obtained, the solution remains qualitatively similar to the underlying Blasius solution with a weak spanwise variation. Near to the centreline $\hat{\zeta} = 0$ there is a slight thickening of the boundary layer, but the injection flow does not have a significant impact on the solution. Increasing the injection amplitude such that $K_I < K < K_{II}$ a low-speed streak develops in the injection region $\hat{\zeta} < 1$. In this moderate injection regime a displaced shear layer separates the low streamwise speeds inside the streak from the high speed outer flow. The size of this streak remains confined to lie within the slot region (ie, $\zeta < \zeta_0$). In the strong injection regime, when $K > K_{II}$, a much more prominent low-speed streak is observed which is separated from the outer flow by a semi-circular free shear layer. Due to the low streamwise velocity inside the streak the mass injected into the layer through the plate must be ejected through the shear layer and this constraint allows one to predict the streak radius as ζ_0 increases.

In the presence of a favourable pressure gradient ($\beta > 0$) the three distinct types of flow, with their prominent low-speed streaks, are not found. The introduction of a non-zero pressure gradient, as shown in figures 3.2.1, 3.2.2 and 3.2.3 (with $\beta = 0.1$), significantly alters the streamwise velocity U in the neighbourhood of the slot ($|\zeta| < \zeta_0$) but not as much as when $\beta = 0$. The two-dimensional Falkner–Skan solution that exists far away from the injection slot ($\hat{\zeta} \gg 1$) is modified in the injection region to a much lesser degree for $\beta > 0$. For large blowing there is no obvious semi-circular low-speed region as shown by comparison of figure 2.2.3 for $\beta = 0$ and figure 3.2.3 for $\beta = 0.1$. Downwards flow towards the plate is seen for large η as shown by the (V, W) streamplots in figures 3.2.1, 3.2.2 and 3.2.3. Since for $\eta \gg 1$ the streamwise velocity $U \sim 1$ and $\Phi \sim \eta + \delta_F + \delta_{transp}(\hat{\zeta})$, where δ_F and δ_{transp} are the displacement thicknesses associated with the Falkner-Skan solution and the spanwise

varying injection respectively, it follows from (1.3.2) that

$$V \sim -\beta\eta - \delta_F - \delta_{transp}(\hat{\zeta}). \tag{3.2.1}$$

This means that for all flows where $\beta > 0$ there is a downwards flow towards the plate for some sufficiently large value of η due to the base flow velocity.

When a favourable pressure gradient is introduced a much less dramatic flow response is obtained, but one that nonetheless has two distinct properties. Either at fixed $K > 0$ (injection) and $\beta > 0$ (i) the solution near the centreline becomes increasingly displaced from the plate as ζ_0 increases or (ii) the low speed region in the slot region $\zeta < \zeta_0$ remains largely unaffected as the slot width is increased. This behaviour is seen in figure 3.2.4 where contours are shown for $K = 4$, $\beta = 0.2$ and $\zeta_0 = 20$ in (a) and $\zeta_0 = 40$ in (b). However, this growing η scale is not observed in all cases, as demonstrated by figure 3.2.5 in the case $K = 4$, $\beta = 0.8$, $\zeta_0 = 20$ in (a) and $\zeta_0 = 40$ in (b). This feature will be explained in the subsequent asymptotic analysis, to identify how the choices of β and K determine the observed behaviour.

Comparing favourable pressure gradient results ($\beta > 0$) to the zero pressure gradient case ($\beta = 0$) it is evident that a favourable pressure gradient acts to inhibit (although not eliminate entirely) the rapid displacement of a low speed layer from the plate surface. The greatly reduced extent of the low-speed streak indicates an increase in the streamwise mass flux and therefore a reduced radial flow into the far field, when compared with the zero pressure gradient case. This reduction in the radial mass flux is reflected in a reduction in the magnitude of the mass flux parameter A contained in the far-field boundary conditions (1.3.16). The phenomena observed here shall be explored in more detail using relevant asymptotic methods.

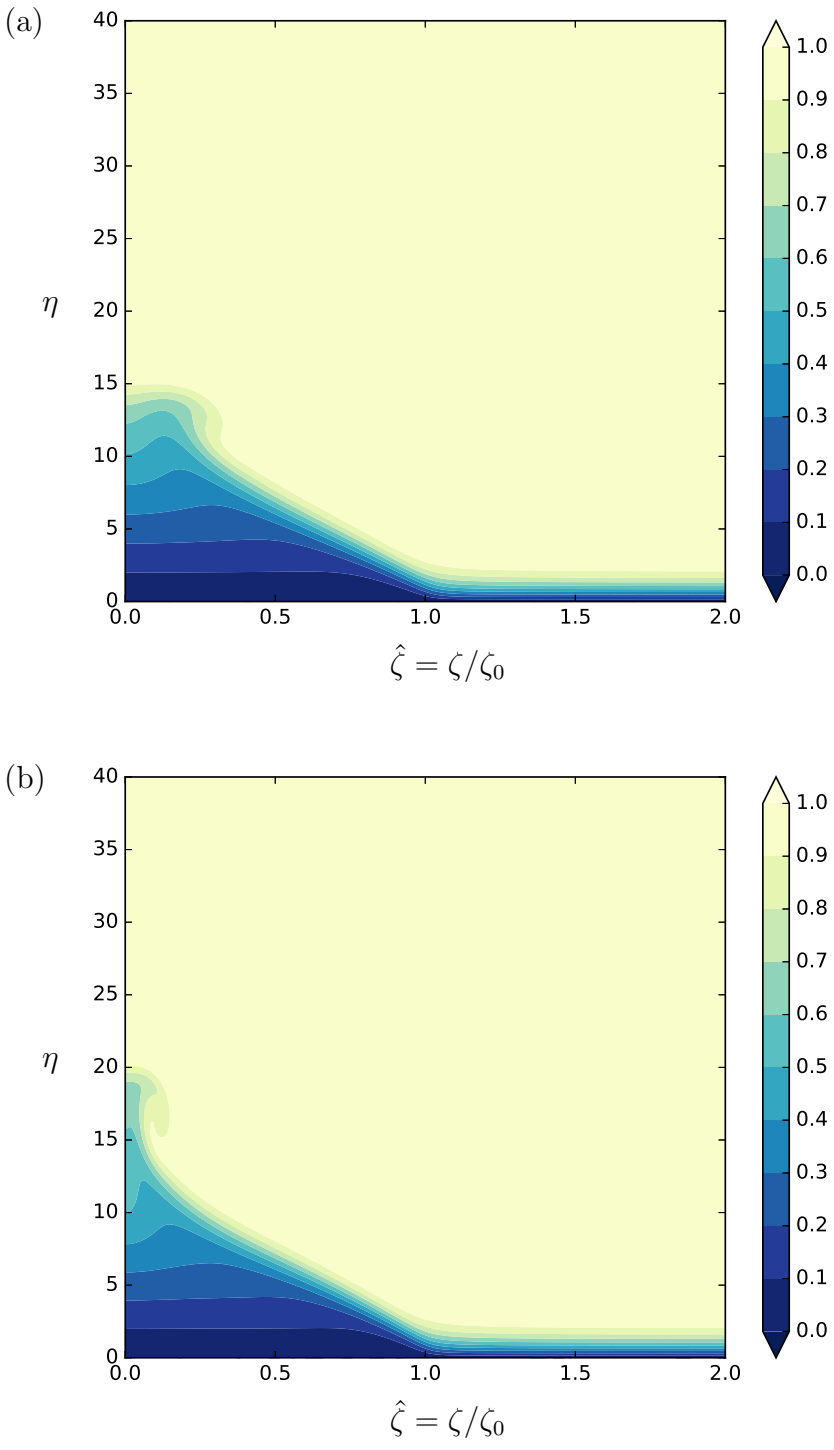

Figure 3.2.4: Contours of the streamwise velocity U are shown for injection rate $K = 4$ and pressure gradient $\beta = 0.2$. The injection slot width is (a) $\zeta_0 = 20$ and (b) $\zeta_0 = 40$. For $\beta = 0.2$ an increasing injection slot width ζ_0 leads to a growing η scale and eruptive behaviour near to $\zeta = 0$.

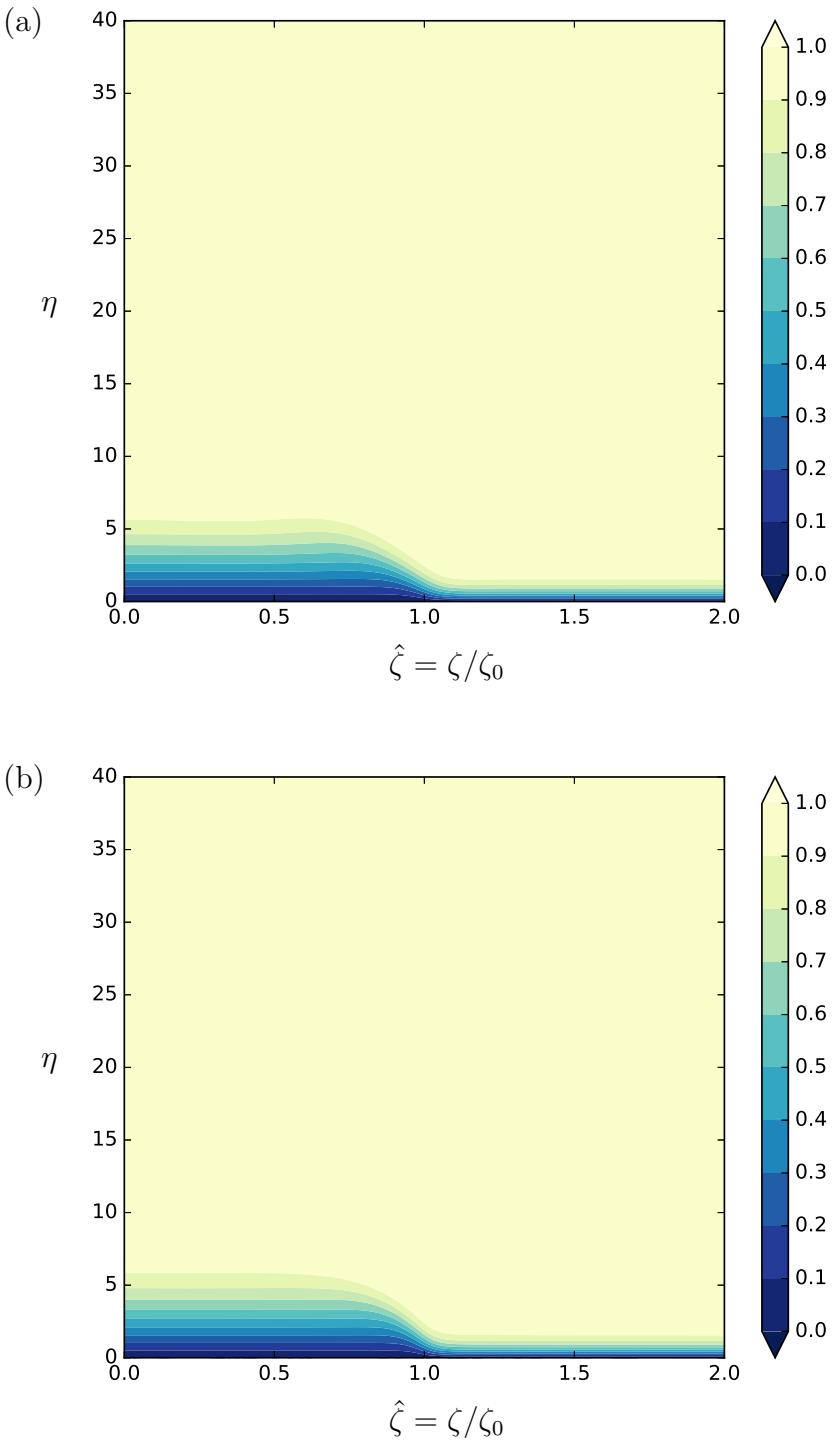

Figure 3.2.5: Contours of the streamwise velocity U are shown for injection rate $K = 4$ and pressure gradient $\beta = 0.8$. The injection slot width is (a) $\zeta_0 = 20$ and (b) $\zeta_0 = 40$. For $\beta = 0.8$ there is no growing η scale for increasing ζ_0 with a benign response seen near to $\zeta = 0$.

3.3 Asymptotic description

The limit of a large injection-slot width, $\zeta_0 \to \infty$, shall now be examined for a short-scale injection with an applied favourable pressure gradient. When $0 < \beta < 1$ a large aspect ratio viscous layer is present, spanned by $\eta = O(1)$ and $\zeta = O(\zeta_0)$ for all values of $K > 0$. To describe the flow the rescaled coordinate $\hat{\zeta} = \zeta/\zeta_0$ is used along with

$$U(\zeta, \eta; \zeta_0) = U_0(\hat{\zeta}, \eta) + \cdots , \tag{3.3.1a}$$

$$\Phi(\zeta, \eta; \zeta_0) = \Phi_0(\hat{\zeta}, \eta) + \cdots , \tag{3.3.1b}$$

$$\Psi(\zeta, \eta; \zeta_0) = \zeta_0 \hat{\zeta} \Psi_0(\hat{\zeta}, \eta) + \cdots , \tag{3.3.1c}$$

$$\Theta(\zeta, \eta; \zeta_0) = \zeta_0 \hat{\zeta} \Theta_0(\hat{\zeta}, \eta) + \cdots . \tag{3.3.1d}$$

Using (3.3.1) and taking the limit $\zeta_0 \to \infty$, it is found that at leading order (3.1.2) reduces to

$$(2 - \beta) U_0 = \Phi_{0\eta} + \hat{\zeta} \Psi_{0\hat{\zeta}} + \Psi_0, \tag{3.3.2a}$$

$$\Theta_0 = \Psi_{0\eta}, \tag{3.3.2b}$$

$$U_{0\eta\eta} = \beta \left[U_0^2 - 1 \right] - \Phi_0 U_{0\eta} - \hat{\zeta} \Psi_0 U_{0\hat{\zeta}}, \tag{3.3.2c}$$

$$\Theta_{0\eta\eta} = 2(1 - \beta) U_0 U_{0\eta} - \Phi_0 \Theta_{0\eta} - \Psi_0 \Theta_0 - \hat{\zeta} \Psi_0 \Theta_{0\hat{\zeta}} - (2 - \beta) U_0 \Theta_0. \tag{3.3.2d}$$

This system is parabolic in $\hat{\zeta}$ and the 'windward' direction is determined by the sign of Ψ_0. When $\beta = 0$ this system reduces to (2.3.2). If $\Psi_0 > 0$ for all $\eta > 0$ then the far-field solution can be extended from $\hat{\zeta} \gg 1$ (where the flow is know to be the classical Falkner–Skan solution) towards $\hat{\zeta} = 0$ by parabolic marching, subject to the conditions

$$U_0 = \Psi_0 = 0, \quad \Phi_0 = \Phi_w \quad \text{on} \quad \eta = 0, \tag{3.3.2e}$$

$$U_0 \to 1, \quad \Theta_0 \to 0, \quad \Psi_0 \to 1 - \beta \quad \text{as} \quad \eta \to \infty. \tag{3.3.2f}$$

In the far field $\hat{\zeta} \gg 1$, the 'initial' state for (3.3.2) is the Falkner–Skan solution, for which $\Psi_0 = (1 - \beta) U_0$, which means that there is no cross flow, $W = 0$. If (3.3.2) is started from a state with no cross flow, then it retains this feature for all subsequent $\hat{\zeta}$, hence the system (3.3.2) can be reduced to a simpler form:

$$U_0 = \Phi_{0\eta} + (1 - \beta) \hat{\zeta} U_{0\hat{\zeta}}, \tag{3.3.3a}$$

$$U_{0\eta\eta} = \beta \left[U_0^2 - 1 \right] - \Phi_0 U_{0\eta} - (1 - \beta) \hat{\zeta} U_0 U_{0\hat{\zeta}}, \tag{3.3.3b}$$

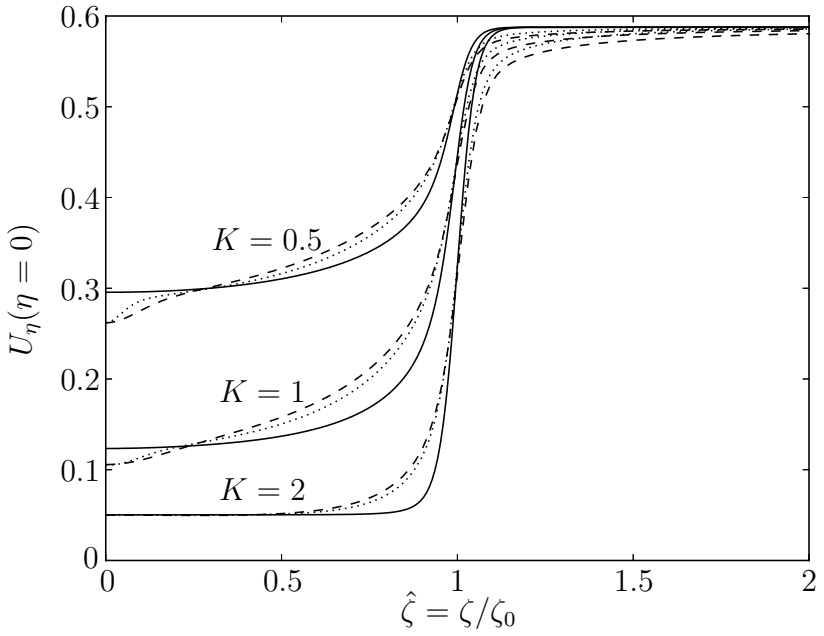

Figure 3.3.1: The shear distribution at the plate surface $U_\eta(\hat{\zeta}, \eta = 0)$, near to the injection region, for various blowing intensities K with the pressure gradient $\beta = 0.1$. The dashed lines are for $\zeta_0 = 20$ and the dotted lines are for $\zeta_0 = 40$; the solid line depicts the shear distribution predicted by the parabolic system (3.3.3).

with $U_0 = 0$, $\Phi_0 = \Phi_w$ on $\eta = 0$ and $U_0 \to 1$ as $\eta \to \infty$. Note that setting $\hat{\zeta} = 0$, under the assumption that $\hat{\zeta}$ derivatives can then be neglected in this limit, reproduces the Falkner–Skan equation (3.1.3), but subject to an injection at the surface of $\Phi_w(\hat{\zeta} = 0) = -K$. This suggests that for sufficiently large slot widths, the classical Falkner–Skan solution may eventually be recovered at the centreline of the injection region. However, this is not always true and, as shall be seen in the next section, small amounts of residual cross flow can dominate for small $\hat{\zeta}$, leading to rather different behaviour in some cases. Nevertheless, it is useful begin by assuming that such cross flow is small and that (3.3.3) is sufficient to describe the flow.

When $\beta = 0$ solutions to (3.1.3) only exist for $K \lesssim 0.876$. Marching of (3.3.3) for $K \gtrsim 0.876$ leads to a singular response at a finite value of $\hat{\zeta} > 0$ because the wall shear stress $U_{0\eta}(\eta = 0)$ becomes equal to zero. When $\beta > 0$, marching of (3.3.3) to $\hat{\zeta} = 0$ can be achieved for *all* values of K. It is the presence of this singularity (when $\beta = 0$) that leads to the other types of low-speed streaks described in chapter 2.

The behaviour of the downstream shear is illustrated in figure 3.3.1. When $\beta \neq 0$ it can be seen that the wall shear stress never reaches zero and instead approaches a

finite value as $\hat{\zeta} \to 0$. For large injection rates K the wall shear $U_\eta(\eta = 0) \sim \beta/K$ in the injection region thus agreeing with the two-dimensional theory [47].

For large η the vertical velocity component in the parabolic solution is of the form

$$\Phi_0 \sim \eta + \delta_F + \delta_w(\hat{\zeta}). \tag{3.3.4}$$

Here δ_F is the constant displacement thickness associated with the Falkner–Skan solution for flow on a flat plate in the absence of injection. A displacement $\delta_w(\hat{\zeta})$ which is varying in the spanwise direction due to the wall injection over a finite spanwise region is also present. If there is no injection though the plate surface then $\delta_w \equiv 0$ for all $\hat{\zeta}$ and there is no $\hat{\zeta}$-dependent perturbation to the Falkner–Skan solution, in general $\delta_w(\hat{\zeta})$ is non-zero and must be taken into consideration.

Now consider the inviscid region defined by $\eta = \zeta_0\hat{\eta}$ and $\zeta = \zeta_0\hat{\zeta}$. In this outer region the vertical velocity component may be rewritten as

$$\Phi(\zeta, \eta) = \zeta_0\hat{\eta} + \delta_F + \phi(\hat{\zeta}, \hat{\eta})\,, \tag{3.3.5}$$

where $\phi = O(1)$ in order to match with the spanwise varying displacement induced by the parabolic solution (2.3.3) and $\zeta_0\hat{\eta} + \delta_F$ is the (outer) $\eta \to \infty$ limit of the (inner) Falkner–Skan solution. Rewriting (3.1.1a) and (3.1.1b) in terms of $\hat{\zeta}$ and $\hat{\eta}$, and since both U and Θ remain $o(\zeta_0^{-2})$, it is found that ϕ is determined by the harmonic problem,

$$\hat{\nabla}^2\phi = 0, \tag{3.3.6a}$$

subject to

$$\phi(\hat{\zeta}, \hat{\eta} = 0) = \delta_w(\hat{\zeta}). \tag{3.3.6b}$$

Here $\delta_w(\hat{\zeta})$ is determined by the solution of the parabolic system (3.3.3). It is also possible to obtain a similar Laplace problem for the corresponding Ψ velocity perturbation $\psi(\hat{\zeta}, \hat{\eta})$. The solution to the problem (3.3.6) is obtained using a Green's function approach

$$\phi(\hat{\zeta}, \hat{\eta}) = \frac{1}{\pi}\int_{z=-\infty}^{+\infty} \frac{\delta_w(z)\hat{\eta}}{\hat{\eta}^2 + (\hat{\zeta} - z)^2}\mathrm{d}z. \tag{3.3.7}$$

It is known from (1.3.16) that in the far-field

$$\phi \sim \frac{\hat{A}\hat{\eta}}{\hat{\zeta}^2 + \hat{\eta}^2} \tag{3.3.8}$$

where $A = \zeta_0 \hat{A}$. Given this far-field behaviour, the total radial mass flux due to the spanwise variation at the edge of the boundary layer is $\hat{A}\zeta_0\pi = A\pi$. On the other hand the flux from the inner parabolic region induced by the injection is $M\zeta_0$ where

$$M = \int_{-\infty}^{+\infty} \delta_w(\hat{\zeta}) \mathrm{d}\hat{\zeta}. \tag{3.3.9}$$

Combining these two expressions for the mass flux gives

$$A = \frac{M\zeta_0}{\pi}, \tag{3.3.10}$$

so the mass flux coefficient A is proportional to the blowing width ζ_0 and the integral of the spanwise varying displacement. The description provided by (3.3.10) applies to the $\beta = 0$ case (provided $K < K_I$), but the difference here lies in the mass flux integral being a function of the pressure-gradient parameter, $M = M(\beta, K)$.

This asymptotic description suggests that, for large injection slot widths $\zeta_0 \gg 1$ and $\beta > 0$, the mass flux coefficient A remains linearly dependent upon ζ_0 for any fixed $K > 0$. This is markedly different to when $\beta = 0$, in which case increased injection ($K \gtrsim 1.95$) leads to a mass flux coefficient A that is proportional to ζ_0^2 and the formation of a low-speed semi-circular 'bubble'.

Computation of $\delta_w(\hat{\zeta})$ by parabolic marching of (3.3.3), allows for the determination of $M(\beta, K)$ via the integral (3.3.9). Figure 3.3.2 shows the asymptotic prediction (3.3.10) for a range of values of $\beta = 0.05, 0.1, 0.4, 0.8$, which effectively shows the reduction in radial mass flux in the (ζ, η) plane as the pressure gradient is increased. The same figure also shows numerically determined values of A, as obtained from (3.1.2), in the particular case $\beta = 0.1$ and increasing injection-slot widths $\zeta_0 = 2, 4$ and 8. The linear relationship between the mass flux coefficient A and the injection width ζ_0 is confirmed with good agreement between the numerically determined values and the asymptotic prediction for the representative value of $\beta = 0.1$.

The leading-order parabolic solution of (3.3.3) captures the full numerical solution for $\hat{\zeta} = O(1)$, as evidenced by the results of figures 3.3.1 and 3.3.2, but there are some additional features that it does not describe. One feature is the influence of spanwise diffusion around the edge of the injection slot, although this region is small compared to the $\hat{\zeta} = O(1)$ scale. A more important issue is the behaviour shown in figures 3.2.4 and 3.2.5. For some choices of β and K, an increasing boundary-layer thickness local to

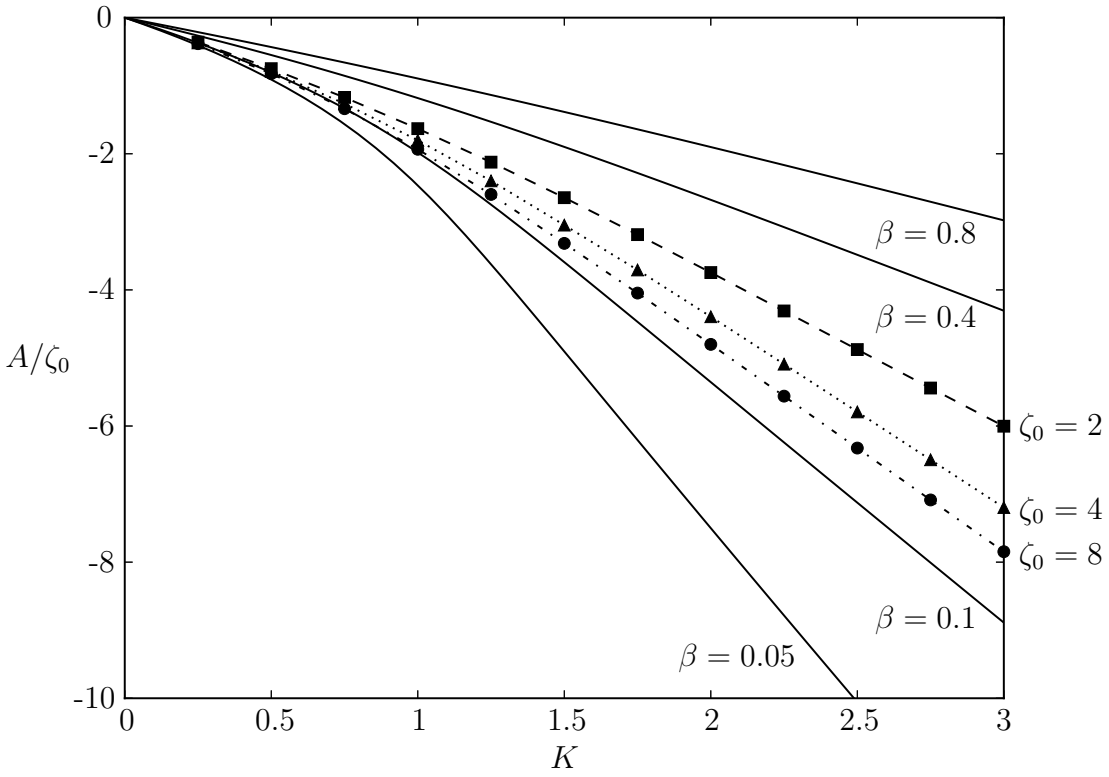

Figure 3.3.2: The solid lines show the asymptotic prediction $A/\zeta_0 \sim M/\pi$ for large ζ_0, as determined from the parabolic system (2.3.3) and (3.3.9) for $\beta = 0.05, 0.1, 0.4, 0.8$. The data points show values of A/ζ_0 for increasing injection rates K and $\beta = 0.1$, as determined numerically from the governing equations (3.1.2) for increasing injection-slot widths $\zeta_0 = 2, 4$ and 8.

the centreline of the slot is found as ζ_0 increases, see figure 3.2.4, however for others this is not found, see figure 3.2.5. The role of cross flow eigenmodes in the parabolic system (3.3.3) now needs to be examined, this will allow for the determination of a critical favourable pressure gradient beyond which this thickening local to the centreline is not found.

3.4 Three-dimensional eigenmodes

Figure 3.4.1 shows the streamwise velocity profiles as measured on the centreline of the injection slot ($\hat{\zeta} = 0$) for $K = 2$, $\beta = 0.1, 0.8$ and $\zeta_0 = 20, 40$. When $\beta = 0.8$ the parabolic solution (3.3.3), in the limit of $\hat{\zeta} \to 0$, is in agreement with the numerical solution of the full equations (3.1.2) for both $\zeta_0 = 20$ and $\zeta_0 = 40$. On the other hand, when $\beta = 0.1$ the parabolic solution and the full solution only agree near to $\eta = 0$ and for large η, whilst at intermediate values of η there is a large discrepancy. Furthermore, increasing the slot width ζ_0 only exacerbates the difference. This reinforces the picture of the flow response presented in figures 3.2.4 and 3.2.5, which similarly show a benign dependence on ζ_0 when $\beta = 0.8$ compared to the eruptive behaviour found for $\beta = 0.2$. Since this deviation from the behaviour predicted by the parabolic solution is confined to a region near to the centreline $\hat{\zeta} \ll 1$, it is necessary to alter the approach in this region. It is clear that, as the slot is widened, some choices of the pressure gradient parameter result in a centreline flow that is consistent with the corresponding injection-affected Falkner–Skan solution, but some instead result in what appears to be an increasing eruptive behaviour in this region.

In order to understand the behaviour near to $\hat{\zeta} = 0$ a description of the spatial evolution of a small perturbation to the parabolic solution of the previous section is sought. Firstly consider an expansion of the form

$$U = U_0(\hat{\zeta}, \eta) + \epsilon u(\hat{\zeta}, \eta), \tag{3.4.1a}$$

$$\Phi = \Phi_0(\hat{\zeta}, \eta) + \epsilon \varphi(\hat{\zeta}, \eta), \tag{3.4.1b}$$

$$\Psi = \zeta_0 \hat{\zeta} \left(\Psi_0(\hat{\zeta}, \eta) + \epsilon \psi(\hat{\zeta}, \eta) \right), \tag{3.4.1c}$$

$$\Theta = \zeta_0 \hat{\zeta} \left(\Theta_0(\hat{\zeta}, \eta) + \epsilon \vartheta(\hat{\zeta}, \eta) \right). \tag{3.4.1d}$$

Setting $\epsilon = 0$ the leading-order system (3.3.2) is recovered which if started from a

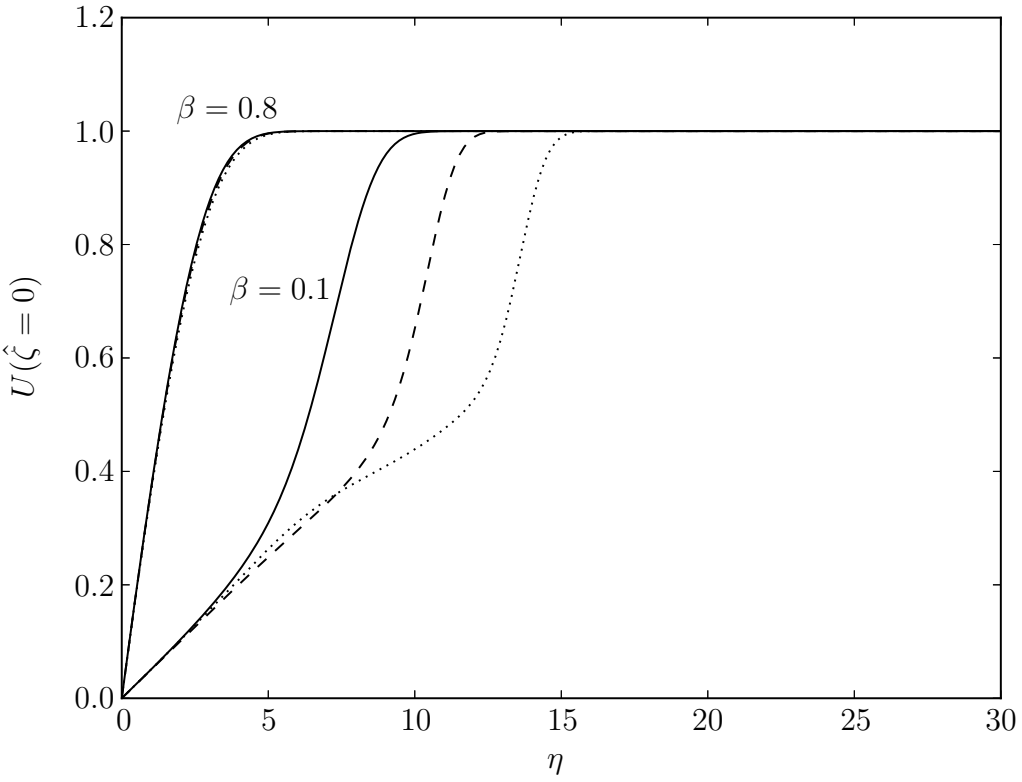

Figure 3.4.1: Streamwise velocity U profiles at the centreline of the injection region $\hat{\zeta} = 0$ for $K = 2$ along with a small favourable pressure gradient, $\beta = 0.1$, and a larger favourable pressure gradient $\beta = 0.8$. For each value of β the solid line shows the Falkner–Skan solution with injection as predicted by (3.3.3), the dashed and dotted lines show the solution of (3.1.2) for $\zeta_0 = 20$ and 40 respectively.

state with no cross flow has a solution with $\Psi_0 = (1-\beta)U_0$, leading to the simpler form (3.3.3). For $\epsilon \ll 1$ the linearised system for $(u, \varphi, \psi, \vartheta)$ is given by

$$(2-\beta)u = \varphi_\eta + \psi + \hat{\zeta}\psi_{\hat{\zeta}}, \tag{3.4.2a}$$

$$\vartheta = \psi_\eta, \tag{3.4.2b}$$

$$u_{\eta\eta} = 2\beta U_0 u - \Phi_0 u_\eta - U_{0\eta}\varphi - \hat{\zeta}\left(U_{0\hat{\zeta}}\psi + \Psi_0 u_{\hat{\zeta}}\right), \tag{3.4.2c}$$

$$\vartheta_{\eta\eta} = 2(1-\beta)\left[U_{0\eta}u + U_0 u_\eta\right] - \Theta_{0\eta}\varphi - \Phi_0\vartheta_\eta - \Psi_0\left(\vartheta + \hat{\zeta}\vartheta_{\hat{\zeta}}\right) - \left(\Theta_0 + \hat{\zeta}\Theta_{0\hat{\zeta}}\right)\psi - (2-\beta)\left(U_0\vartheta + \Theta_0 u\right). \tag{3.4.2d}$$

For $\hat{\zeta} \ll 1$ solutions to these $O(\epsilon)$ perturbation equations exist in the form

$$\left(u(\hat{\zeta},\eta), \varphi(\hat{\zeta},\eta), \psi(\hat{\zeta},\eta), \vartheta(\hat{\zeta},\eta)\right) = \hat{\zeta}^\lambda \left(u_0(\eta), \varphi_0(\eta), \psi_0(\eta), \vartheta_0(\eta)\right) . \tag{3.4.3}$$

The $O(\epsilon^0)$ system merely reduces to the Falkner–Skan equation (3.1.3) with an injection boundary condition such that $U_0 = F'(\eta)$, $\Phi_0 = F(\eta)$, $\Psi_0 = (1-\beta)F'(\eta)$, $\Theta_0 = (1-\beta)F''(\eta)$ and $F(0) = -K$, along with the other usual boundary conditions. The $O(\epsilon)$ system, with the local form (3.4.3) leads to the eigenvalue problem

$$(2-\beta)u_0 - \varphi_0' - \psi_0 = \lambda\psi_0, \tag{3.4.4a}$$

$$\vartheta_0 - \psi_0' = 0, \tag{3.4.4b}$$

$$u_0'' - 2\beta U_0 u_0 + \Phi_0 u_0' + U_{0\eta}\varphi_0 = -\lambda\Psi_0 u_0, \tag{3.4.4c}$$

$$\vartheta_0'' - 2(1-\beta)\left[U_{0\eta}u_0 + U_0 u_0'\right] + \Theta_{0\eta}\varphi_0 + \Phi_0\vartheta_0' + \Psi_0\vartheta_0 + \Theta_0\psi_0 + (2-\beta)(U_0\vartheta_0 + \Theta_0 u_0) = -\lambda\Psi_0\vartheta_0, \tag{3.4.4d}$$

where the prime notation is used to denote derivatives with respect to η. The homogeneous boundary conditions to be imposed are $u_0(0) = \varphi_0(0) = \psi_0(0) = 0$ and $u_0, \psi_0, \vartheta_0 \to 0$ as $\eta \to \infty$. Here $\lambda = \lambda_r + i\lambda_i$ is a complex eigenvalue which must be determined in order to describe the spatial behaviour of the perturbation upon approaching the slot centreline. If the real part of the eigenvalue is negative ($\lambda_r < 0$) as $\hat{\zeta} \to 0$ then the perturbation grows and the corresponding eigenmode is linearly unstable. In such cases it is not expected, in general, that the Falkner–Skan solution is recovered near to $\hat{\zeta} = 0$. The eigenvalue problem (3.4.4) may be discretised and solved numerically as outlined in section 2.4.

Figure 3.4.2(a) shows the real part of the most relevant eigenvalue for various values of the 'injection' parameter K with $\beta = 0.1, 0.2, 0.4, 0.5, 0.6$. The figure covers

$K \in [-2, 3]$ with $K < 0$ indicating suction and $K > 0$ injection. The most relevant eigenvalue in this case is the one with the smallest real part, these are shown in figure 3.4.2(a). When $\beta = 0.1$ (for example) the smallest eigenvalue is positive when K is sufficiently negative (suction) but as K increases the real part of the eigenvalue becomes negative, $\lambda_r < 0$, and approaches a constant negative value for large K (strong injection). With $\lambda_r < 0$ this eigenmode will come to dominate the solution as $|\hat{\zeta}| \to 0$. When sufficiently close to the centreline of the injection slot it is necessary to reintroduce spanwise diffusion and/or nonlinear effects in order to regularise this linear spatial growth. The eigenfunction of this spatial mode is such that there is a non-zero cross flow velocity associated with the perturbation, that is $W \neq 0$.

Figure 3.4.2(a) demonstrates the impact of increasing the pressure gradient on the spatial stability of the solution near to $\hat{\zeta} = 0$. As the value of β increases, λ_r typically increases until at a critical value $\beta_c(K)$ the eigenvalue with the smallest real part has $\lambda_r \geq 0$. This means that only for $\beta \geq \beta_c(K)$ can it be expected that the Falkner–Skan solution is recovered for $|\hat{\zeta}| \ll 1$ if there are perturbations with non-zero cross flow.

Figure 3.4.2(b) shows the functional relationship between the injection and the pressure gradient parameters, such that there exists a spatially neutral mode with $\lambda_r = 0$; as such this represents a neutral curve above which a benign response near to $\hat{\zeta} = 0$ is expected and below which the solution is expected to be affected by these centreline eigenmodes. As can be seen in figure 3.4.2(a) the eigenvalue approaches a constant value for sufficiently large $K > 0$ (strong injection). It is also expected that β_c asymptotes to a constant value as K increases. As shown in 3.4.2(b) the numerical evidence suggests that $\beta_c \approx 1/2$ ($n = 1/3$, right-angle wedge) for large $K > 0$. Asymptotic theory provides evidence to support this assertion about the critical value of β for large injection rates.

3.4.1 Critical eigenvalue for large K

The eigenvalue problem (3.4.4) in the limit $K \to \infty$ shall now be briefly analysed. Firstly the $O(\epsilon^0)$ Falkner–Skan system with a large injection needs to be solved for $(U_0, \Phi_0, \Psi_0, \Theta_0)$. The equation (3.1.3) must be solved subject to the boundary conditions $F(0) = -K$, $F'(0) = 0$ and $F'(\eta) \to 1$ as $\eta \to \infty$ where $K \to \infty$. Pretsch (1944) [54] proposed a solution to this problem which is valid in the region between the wall

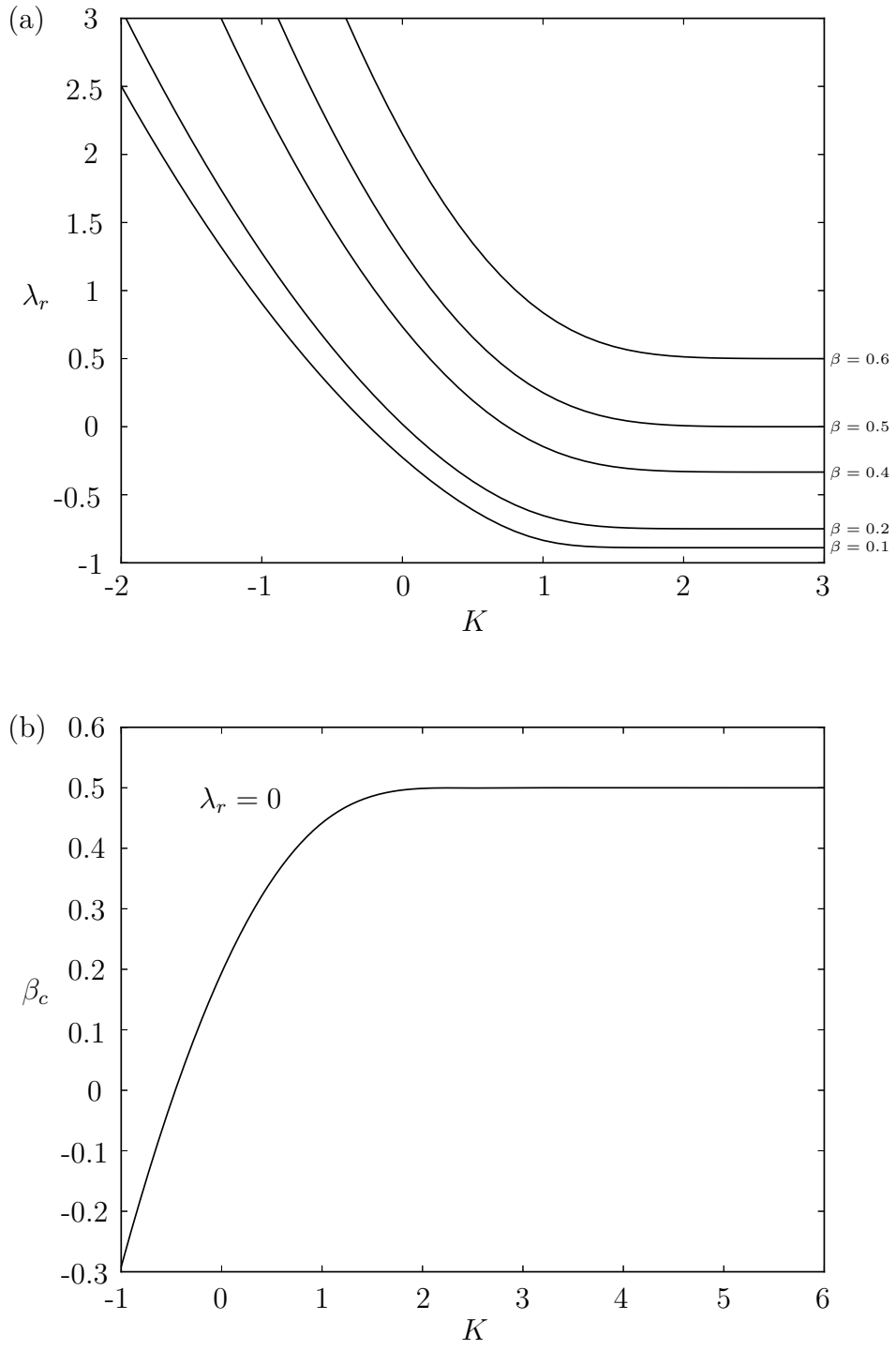

Figure 3.4.2: (a) The real part of the eigenvalues $\lambda = \lambda_r + i\lambda_i$ for perturbations to the parabolic system (2.3.3) as $\hat{\zeta} \to 0$. The eigenvalues are found from the solution of (3.4.4) for injection magnitudes $K \in [-2, 3]$ and pressure gradients $\beta = 0.1, 0.2, 0.4, 0.5, 0.6$. Only the smallest eigenvalues are shown for each of the values of β as all the other eigenvalues remain positive regardless of the value of K. (b) The critical pressure gradient $\beta_c(K)$ at which $\lambda_r = 0$ for $K \in [-1, 6]$.

and the zero streamline which separates the injected fluid from the fluid in the rest of the boundary layer. This solution is only valid in this inner region and does not give any information about the outer region between the zero streamline and the outer inviscid flow.

Firstly new variables are proposed by scaling the old variables using the large injection rate K. Let $f(\xi) = F(\eta)/K$ where $\xi = \eta/K$ then the Falkner–Skan equation (3.1.3) becomes

$$\frac{1}{K^2} f_{\xi\xi\xi} + f f_{\xi\xi} + \beta \left[1 - (f_\xi)^2\right] = 0, \tag{3.4.5}$$

with the boundary conditions $f_\xi(0) = 0$, $f(0) = -1$ and $f_\xi(\infty) \to 1$. Taking an asymptotic expansion, in terms of powers of the small parameter $1/K^2$,

$$f(\xi) = f_0(\xi) + \frac{1}{K^2} f_1(\xi) + \ldots, \tag{3.4.6}$$

at leading order the Falkner–Skan equation becomes

$$f_0 f_{0\xi\xi} + \beta \left[1 - (f_{0\xi})^2\right] = 0, \tag{3.4.7}$$

with $f_{0\xi}(0) = 0$, $f_0(0) = -1$ and $f_{0\xi}(\infty) \to 1$. This equation omits the term $f_{\xi\xi\xi}$ and is essentially an inviscid version of the Falkner–Skan equation. As (3.4.7) is a second order equation only two of the boundary conditions are able to be satisfied in general. Treating f_0 as the independent variable and letting $g_0 = f_{0\xi}$ gives the separable equation

$$f_0 g_0 \frac{\mathrm{d}g_0}{\mathrm{d}f_0} + \beta \left(1 - g_0^2\right) = 0. \tag{3.4.8}$$

Integrating (3.4.8) produces the first order equation

$$\left(\frac{\mathrm{d}f_0}{\mathrm{d}\xi}\right)^2 - 1 = A f_0^{2\beta} \tag{3.4.9}$$

where $A = (-1)^{1-2\beta}$ is a constant. This equation has an implicit general solution in terms of hypergeometric functions but this is not particularly useful here. In order to proceed consider the specific case when $\beta = \beta_c = 1/2$ which has solution

$$f_0(\xi) = \frac{1}{4}\left(\xi^2 - 4\right). \tag{3.4.10}$$

This solution only satisfies the boundary conditions at $\xi = 0$, So the relevant asymptotic expansion is

$$f(\xi) \sim \frac{1}{4}\left(\xi^2 - 4\right) + O\left(\frac{1}{K^2}\right). \tag{3.4.11}$$

Therefore for $K \to \infty$ in the region between the wall and the zero streamline there exists the asymptotic solution

$$F_{in}(\eta) \sim \frac{K}{4}\left(\left(\frac{\eta}{K}\right)^2 - 4\right) + \ldots, \tag{3.4.12}$$

when $\beta = 1/2$ and $\eta \ll 2K$. For the outer region between the zero streamline and the outer inviscid flow a different asymptotic solution is required. The far-field boundary condition $F'(\eta) \to 1$ as $\eta \to \infty$ suggests the asymptotic form

$$F'(\eta) = 1 + F_1'(\eta) + \ldots \tag{3.4.13}$$

where $F_1'(\eta) \ll 1$ as $\eta \to 1$. The Falkner–Skan equation (3.1.3) is satisfied to leading order hence for large η

$$F_{out}(\eta) \sim \eta + c + \ldots, \tag{3.4.14}$$

where c is a constant and $\eta \gg 2K$. The inner and outer solution must match in the overlap region $\eta \to 2K$, so since

$$\lim_{\eta \to 2K} F_{in} = 0 \tag{3.4.15}$$

and

$$\lim_{\eta \to 2K} F_{out} = 2K + c \tag{3.4.16}$$

it follows that $c = -2K$. So for the outer region between the zero streamline and the inviscid flow

$$F_{out}(\eta) \sim \eta - 2K + \ldots. \tag{3.4.17}$$

The solutions presented above are only valid when $\beta = 1/2$; although asymptotic expansions for the case of general β can be determined in terms of parabolic cylinder functions, see Aroesty & Cole (1965) [2], but these are not practically useful in the current context.

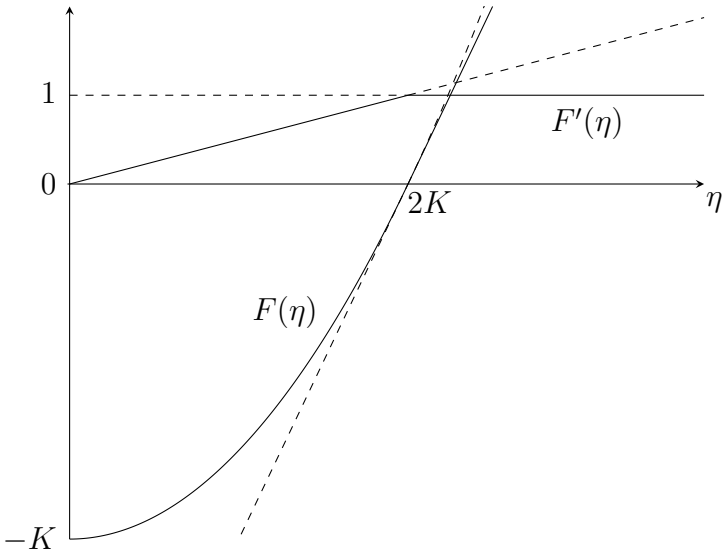

Figure 3.4.3: Solution of the Falkner–Skan equation (3.1.3) in the limit $K \to \infty$ when $\beta = 1/2$. The dashed lines indicate the asymptotic limits in the inner and outer regions. The solid lines indicate the leading order solution for both $F(\eta)$ and $F'(\eta)$.

Figure 3.4.3 shows the leading order asymptotic solution for the Falkner–Skan equation in the limit of large injection. At $\eta = 2K$ the corner in $F'(\eta)$ is actually slightly rounded due to higher order terms. This leading order solution shall now be used to give an approximation to the terms $(U_0, \Phi_0, \Psi_0, \Theta_0)$ in the eigenvalue problem (3.4.4).

Using the coordinate transformation $\eta = Y + 2K$ the asymptotic solutions (3.4.12) and (3.4.17) become

$$F_{in} \sim Y + \frac{Y^2}{4K} + \ldots \quad \text{and} \quad F_{out} \sim Y + \ldots . \tag{3.4.18}$$

Since $K \gg 1$ it follows that $F \sim Y$ to leading order, this means that $\Phi_0 \sim Y$, $U_0 \sim 1$, $\Psi_0 \sim (1 - \beta) = 1/2$ and $\Theta_0 \sim 0$ to leading order. Using this leading order approximation the eigenvalue problem (3.4.4), for $\beta = 1/2$, becomes

$$\frac{3}{2}u_0 - \varphi_0' - \psi_0 = \lambda\psi_0, \tag{3.4.19a}$$

$$\vartheta_0 - \psi_0' = 0, \tag{3.4.19b}$$

$$u_0'' - u_0 + Yu_0' = -\frac{\lambda}{2}u_0, \tag{3.4.19c}$$

$$\vartheta_0'' - u_0' + Y\vartheta_0' + 2\vartheta_0 = -\frac{\lambda}{2}\vartheta_0, \tag{3.4.19d}$$

where $u_0, \varphi_0, \psi_0, \vartheta_0$ are now functions of Y and $'$ indicates the derivative with respect to Y.

It is now possible to show that every eigenvalue is non-negative when $\beta = 1/2$ in the leading order eigenvalue problem (3.4.19). Consider the u_0 equation in (3.4.19)

$$u_0'' + Y u_0' + \left(\frac{\lambda}{2} - 1\right) u_0 = 0 \tag{3.4.20}$$

with the boundary conditions $u_0(-2K) = 0$ and $u_0 \to 0$ as $Y \to \infty$. Let $p(Y) = q(Y) = e^{Y^2/2}$ and $r(Y) = e^{Y^2/2}/2$ then (3.4.20) can be rewritten as

$$\lambda r u_0 = q u_0 - \frac{\mathrm{d}}{\mathrm{d}Y}\left(p u_0'\right). \tag{3.4.21}$$

Multiplying through by u_0 and integrating, by parts, over the domain gives

$$\lambda \int_{-2K}^{\infty} u_0^2 r \mathrm{d}Y = \int_{-2K}^{\infty} u_0^2 q \mathrm{d}Y + \int_{-2K}^{\infty} p u_0'^2 \mathrm{d}Y - \left[u_0 p u_0'\right]_{-2K}^{\infty}. \tag{3.4.22}$$

Since $p, q, r \geq 0$ throughout the domain it follows that every eigenvalue is non-negative if

$$-\left[u_0 p u_0'\right]_{-2K}^{\infty} \geq 0. \tag{3.4.23}$$

Using the boundary conditions it follows that

$$-\left[u_0 p u_0'\right]_{-2K}^{\infty} = 0 \tag{3.4.24}$$

therefore every eigenvalue is non-negative.

It has been shown that when, $\beta = 1/2$ and K is large, the leading order eigenvalue problem (3.4.19) has non-negative eigenvalues. It is expected that for large values of K this is also true for the eigenvalue problem (3.4.4). These findings corroborate the numerical evidence shown in figure 3.4.2(b) which suggests that the critical pressure gradient is $\beta_c \to 1/2$ as $K \to \infty$. Of course this asymptotic approximation does not confirm that this is the case but it does provide support for the notion that for large K and $\beta \geq 1/2$ all the eigenmodes are spatially stable. This means that the two-dimensional Falkner-Skan solution with large injection is recovered at $\hat{\zeta} = 0$ for wide slots provided that $\beta \geq 1/2$.

3.5 Discussion

Three-dimensional similarity solutions have been presented for laminar flow over a flat plate with an applied favourable pressure gradient and injection through a short-scale spanwise slot. The slot and injection velocity scaling mean that the slot width is always a constant ratio of the boundary-layer thickness at all downstream locations. This approach allows for solutions that are self-similar in the the downstream x^* coordinate. Away from the injection slot, at large spanwise distances, the flow is assumed to return back to the classical two-dimensional Falkner–Skan profile.

In the absence of a free stream pressure gradient ($\beta = 0$) in chapter 2 it was shown that an increasing injection-slot width leads to three distinct flow regimes. Selection between these three regimes depends upon the size of the injection velocity which is parametrised by K. The two critical values of $K > 0$ that separate the three regimes are $K = K_I \approx 0.876$ and $K = K_{II} \approx 1.95$. The three flow regimes are exemplified by the streamwise velocity contours shown in the figures 2.2.1, 2.2.2 and 2.2.3. In the presence of a favourable pressure gradient ($\beta > 0$) these three distinct flow responses cease to exist and the low-speed streak structures present in the second and third regimes very rapidly disappear, as shown in figures 3.2.1, 3.2.2 and 3.2.3 for $\beta = 0.1$. The inhibition of the streamwise aligned streaks greatly reduces the radial flow into the far field in the (ζ, η) plane, corresponding to a reduction in the magnitude of the mass flux parameter A defined by (1.3.16). Using an asymptotic analysis it was demonstrated, in (3.3.10), that $A = O(\zeta_0)$ and is proportional to the integral of the spanwise varying displacement (3.3.9) for $\beta > 0$.

Far from the injection slot ($\hat{\zeta} \gg 1$) the flow remains unaffected by the injection, resulting in a two-dimensional solution of Falkner–Skan type. This solution has no cross flow at leading order and can be continued from large $\hat{\zeta}$ towards $\hat{\zeta} = 0$ by parabolic marching of (3.3.3). For sufficiently favourable pressure gradients $\beta_c(K) < \beta < 1$ this results in good agreement with the full numerical solution of (3.1.2) outside of a viscous-dominated layer that straddles the edge of the injection region. For weakly favourable pressure gradients $0 < \beta < \beta_c(K)$ there is still good agreement with the numerical solution, but this agreement fails dramatically near to the centreline of the injection slot.

Chapter 3 highlights some fundamental qualitative differences, in boundary-layer flows with a short-spanwise scale injection, associated with the introduction of a favourable streamwise pressure gradient. For a strongly favourable pressure gradient, above the critical value $\beta_c(K) < \beta < 1$, any residual cross flow does not grow in the injection region and as the slot is widened the classical Falkner–Skan solution is recovered local to the centreline. For $0 < \beta < \beta_c(K)$ this is not the case, any residual cross flow has an increasingly significant impact upon approaching the centreline. This developing cross flow behaviour arises through the appearance of a spatially unstable eigenmode as $\hat{\zeta} \to 0$. The eigenfunction of this spatially unstable mode has non-zero crossflow, and so it is only triggered by the higher-order corrections for large slot widths. This means that in the limit of wide injection slots ($\zeta_0 \to \infty$) the Falkner–Skan solution is only recovered for $\beta_c(K) \geq \beta < 1$ when the real part of the associated eigenvalues λ_r are all non-negative. If $0 < \beta < \beta_c(K)$ an increasingly wide slot results in a cross flow entrainment of fluid from outside the injection region which flows towards the centreline of the slot. For $0 < \beta < \beta_c(K)$ this increased spanwise mass flux towards the injection region leads to collisional behaviour along the centreline. A thin $\hat{\zeta} \ll 1$ eruption region is created which becomes more prominent as the slot widens, this behaviour is observed in figure 3.2.4.

In section 3.4.1 it was argued that in the large injection limit $K \to \infty$ the critical pressure gradient tends to a limiting value of $\beta_c = 1/2$. This suggests that, even for a massive short-scale injection, the Falkner–Skan solution can be recovered at the centreline provided that the pressure gradient is sufficiently favourable. The application of a favourable pressure gradient to a short-scale spanwise injection boundary-layer flow has a significant impact on the flow response. Since the absence of pressure gradients in experimental flows is difficult to achieve it is likely that observation of the pure flow regimes of chapter 2 is unlikely. The next chapter aims to show that the self-similar formulations presented here and in chapter 2 may be generalised to include downstream variation.

Chapter 4

Downstream marching

The self-similar formulation presented in the previous chapters is useful for simplifying the computational requirements of the numerical calculations but it does somewhat restrict the geometry of the short scale features which may be examined. The self-similar structure may be generalised by parabolic marching in the downstream x^* coordinate to create a fully three-dimensional formulation which allows for more general short-scale features. However this non-similar formulation is much more computationally intensive and requires a significant adaptation of the numerical scheme outlined in 2.2.1.

4.1 Formulation

The scaled variables η and ζ are retained as this will allow for the utilisation of many aspects of the self-similar formulation. As before the scaled cross-sectional coordinate system is

$$(\eta,\zeta)=\left(\frac{n+1}{2}\right)^{\frac{1}{2}}x^{*n-1}Re_x^{\frac{1}{2}}\,(y^*,z^*)=\left(\frac{(n+1)U_\infty^*x^{*n-1}}{2\nu^*L^{*n}}\right)^{\frac{1}{2}}(y^*,z^*)\,, \tag{4.1.1a}$$

since $Re_x = x^*U_\infty^*F(x^*)/\nu^*$ where $F(x^*)=(x^*/L^*)^n$. In order to allow for parabolic marching the downstream coordinate is scaled such that $x = x^*/L^*$. The velocity field is given by

$$u^* = U_\infty^*F(x^*)U(x,\eta,\zeta)+\ldots, \tag{4.1.1b}$$

$$(v^*,w^*)=\left(\frac{n+1}{2}\right)^{\frac{1}{2}}U_\infty^*F(x^*)Re_x^{-\frac{1}{2}}\,(V(x,\eta,\zeta)+\ldots,W(x,\eta,\zeta)+\ldots)\,. \tag{4.1.1c}$$

Then the pressure field is described by

$$p^* = -\frac{1}{2}\rho^* \left(U_\infty^* F(x^*)\right)^2 \left[1 + \left(\frac{n+1}{2}\right)^{\frac{1}{2}} Re_x^{-\frac{1}{2}} p_1(x) + \left(\frac{n+1}{2}\right) Re_x^{-1} p_2(x,\eta,\zeta) + \ldots\right]. \tag{4.1.1d}$$

This resembles the self-similar formulation but now the velocity and pressure variables U, V, W, p_2 are allowed to be functions of the scaled downstream coordinate x.

Substituting (4.1.1) into the Navier-Stokes and continuity equations (1.1.1), assuming that $Re_x \gg 1$, and applying the appropriate change of variables results in the governing equations

$$(2-\beta)\left(U + xU_x\right) = \Phi_\eta + \Psi_\zeta, \tag{4.1.2a}$$

$$\Theta = \Psi_\eta - \Phi_\zeta, \tag{4.1.2b}$$

and

$$\nabla^2 U = \beta\left[U^2 - 1\right] + (2-\beta)\, xUU_x - \Phi U_\eta - \Psi U_\zeta, \tag{4.1.3a}$$

$$\nabla^2\Theta = (2-\beta)\, x\left(U_\eta\Psi_x - U_\zeta\Phi_x + U\Theta_x - \Theta U_x\right) + 2\left(1-\beta\right)U\left(\zeta U_\eta - \eta U_\zeta\right) - \Phi\Theta_\eta - \Psi\Theta_\zeta - (2-\beta)\, U\Theta, \tag{4.1.3b}$$

where ∇^2 is the two-dimensional Laplacian in the (η, ζ) plane. As in the self-similar case, combining (4.1.2a) and (4.1.2b) gives expressions for the Laplacian of both Φ and Ψ as

$$\nabla^2\Phi = (2-\beta)\left(U_\eta + xU_{x\eta}\right) - \Theta_\zeta, \tag{4.1.3c}$$

$$\nabla^2\Psi = (2-\beta)\left(U_\zeta + xU_{x\zeta}\right) + \Theta_\eta. \tag{4.1.3d}$$

The system (4.1.3) corresponds to the boundary-region equations (1.3.4), in the absence of surface topography, but also includes x derivatives in order to account for more general downstream variation.

4.1.1 Boundary conditions

In the dimensional coordinates the boundary conditions are $u^* = w^* = 0$, $v^* = v_w^*(x^*, z^*)$ on the wall located at $y^* = 0$. In order to include downstream variation the injection through the surface of the plate is given by

$$v_w^*(x^*, z^*) = (2-\beta)^{-\frac{1}{2}}\, U_\infty^* F(x^*) Re_x^{-\frac{1}{2}} V_{transp}(x,\zeta), \tag{4.1.4}$$

where the transpiration velocity $V_{transp}(x,\zeta)$ will be prescribed later. So in the rescaled coordinate system the surface boundary conditions are

$$\Phi = \Phi_w(x,\zeta), \quad \Psi = U = 0, \quad \Theta = \Psi_\eta - \Phi_{w\zeta} \quad \text{on} \quad \eta = 0, \tag{4.1.5}$$

where $\Phi_w(x,\zeta) = -V_{transp}(x,\zeta)$ and $\Phi_{w\zeta}$ is the derivative of Φ_w with respect to ζ. All the other boundary conditions remain the same as in the self-similar case.

4.1.2 Nonlinear correction formulation

The spanwise coordinate is rescaled using the injection width ζ_0 and the solution is decomposed into the Falkner-Skan base flow and a correction due to the injection so that

$$U(x,\eta,\zeta) = U_B(\eta) + \tilde{U}(x,\eta,\zeta;\zeta_0), \tag{4.1.6a}$$

$$\Phi(x,\eta,\zeta) = \Phi_B(\eta) + \tilde{\Phi}(x,\eta,\zeta;\zeta_0), \tag{4.1.6b}$$

$$\Psi(x,\eta,\zeta) = \zeta_0\hat{\zeta}\Psi_B(\eta) + \zeta_0\tilde{\Psi}(x,\eta,\zeta;\zeta_0), \tag{4.1.6c}$$

$$\Theta(x,\eta,\zeta) = \zeta_0\hat{\zeta}\Theta_B(\eta) + \zeta_0\tilde{\Theta}(x,\eta,\zeta;\zeta_0). \tag{4.1.6d}$$

This leads to (1.4.1) with $K_B = 0$ governing the base flow, which admits a Falkner-Skan solution, and

$$\hat{\nabla}^2\tilde{\Phi} = (2-\beta)\left(\tilde{U}_\eta + x\tilde{U}_{\eta x}\right) - \tilde{\Theta}_{\hat{\zeta}}, \tag{4.1.7a}$$

$$\hat{\nabla}^2\tilde{\Psi} = \left(\frac{2-\beta}{\zeta_0^2}\right)\left(\tilde{U}_{\hat{\zeta}} + x\tilde{U}_{\hat{\zeta}x}\right) + \tilde{\Theta}_\eta, \tag{4.1.7b}$$

$$\begin{aligned}\hat{\nabla}^2\tilde{U} =& \beta\left[2U_B\tilde{U} + \tilde{U}^2\right] - \left(\hat{\zeta}\Psi_B + \tilde{\Psi}\right)\tilde{U}_{\hat{\zeta}} - \Phi_B\tilde{U}_\eta - \left(U_B' + \tilde{U}_\eta\right)\tilde{\Phi} \\ &+ (2-\beta)\,x\left(U_B + \tilde{U}\right)\tilde{U}_x,\end{aligned} \tag{4.1.7c}$$

$$\begin{aligned}\hat{\nabla}^2\tilde{\Theta} =& 2(1-\beta)\left\{\hat{\zeta}\left(U_B + \tilde{U}\right)\tilde{U}_\eta + \hat{\zeta}U_B'\tilde{U} - \eta\zeta_0^{-2}\left(U_B + \tilde{U}\right)\tilde{U}_{\hat{\zeta}}\right\} \\ &- \left(\Phi_B + \tilde{\Phi}\right)\tilde{\Theta}_\eta - \hat{\zeta}\Theta_B'\tilde{\Phi} - \hat{\zeta}\Psi_B\tilde{\Theta}_{\hat{\zeta}} - \tilde{\Psi}\left(\Theta_B + \tilde{\Theta}_{\hat{\zeta}}\right) \\ &- (2-\beta)\left[\left(U_B + \tilde{U}\right)\tilde{\Theta} + \hat{\zeta}\Theta_B\tilde{U}\right] + (2-\beta)\,x\left[(U_B' + \tilde{U}_\eta)\tilde{\Psi}_x\right. \\ &\left. - \frac{1}{\zeta_0^2}\tilde{U}_{\hat{\zeta}}\tilde{\Phi}_x + (U_B + \tilde{U})\tilde{\Theta}_x - \left(\hat{\zeta}\Theta_B + \tilde{\Theta}\right)\tilde{U}_x\right],\end{aligned} \tag{4.1.7d}$$

where

$$\hat{\nabla}^2 \equiv \frac{\partial^2}{\partial\eta^2} + \frac{1}{\zeta_0^2}\frac{\partial^2}{\partial\hat{\zeta}^2}, \tag{4.1.7e}$$

governing the correction. The surface boundary conditions (4.1.5) lead to the conditions

$$\tilde{\Phi} = \tilde{\Phi}_w(x, \hat{\zeta}), \quad \tilde{\Psi} = \tilde{U} = 0, \quad \tilde{\Theta} = \tilde{\Psi}_\eta - \frac{1}{\zeta_0^2}\tilde{\Phi}_{w\hat{\zeta}} \quad \text{on} \quad \eta = 0, \tag{4.1.8}$$

where $\tilde{\Phi}_w(x, \hat{\zeta}) = \Phi_w(\zeta) - \Phi_{Bw}$ is the correction injection function which shall be prescribed later. The other boundary conditions remain the same as in the self-similar problem.

4.2 Numerical results

The scheme for the numerical solution of the above downstream marching equations shall now be outlined. Using the scheme it is possible to examine a number of new fully three-dimensional non-self-similar problems such as an isolated injection region or a constant width slot. The validity of the numerical scheme is checked by recovering the self-similar solutions calculated earlier by using an injection profile that becomes self-similar, for large values of x, and examining the far downstream behaviour.

4.2.1 Numerical scheme

The Crank–Nicolson method [11] is used to step in x starting from the Blasius/Falkner-Skan solution at the leading edge. The Crank–Nicolson method is a second-order method in the downstream x co-ordinate, it is semi-implicit in x and is unconditionally numerically stable [40]. As in section 2.2.1 the cross-sectional discretisation uses a uniform grid in the stretched coordinate plane $(\bar{\eta}, \bar{\zeta})$ such that each of the correction variables are of the form $\tilde{X} = \tilde{X}(x, \bar{\eta}, \bar{\zeta})$. Let Δx be the step size in the downstream x direction. At each downstream location $x_n = n\Delta x$ and the approximation to each $\tilde{X}(x, \bar{\eta}, \bar{\zeta})$ is given by $\tilde{X}^n_{i,j} = \tilde{X}(x_n, \bar{\eta}_j, \bar{\zeta}_i)$ for $n = 0, 1, \ldots$. Each of the equations (4.1.7) is replaced by its finite difference approximation where the cross-sectional discretisation is the same as (2.2.2). The equations are evaluated at the mid-node location $x_{n+\frac{1}{2}}$ so

that

$$\tilde{X} \approx \frac{\tilde{X}^{n+1} + \tilde{X}^{n}}{2}, \tag{4.2.1a}$$

$$\tilde{X}_x \approx \frac{\tilde{X}^{n+1} - \tilde{X}^{n}}{\Delta x}, \tag{4.2.1b}$$

$$\tilde{X}_{\eta x} \approx \frac{\left(\tilde{X}_\eta\right)^{n+1} - \left(\tilde{X}_\eta\right)^{n}}{\Delta x}, \tag{4.2.1c}$$

$$\tilde{X}_{\hat{\zeta} x} \approx \frac{\left(\tilde{X}_{\hat{\zeta}}\right)^{n+1} - \left(\tilde{X}_{\hat{\zeta}}\right)^{n}}{\Delta x}, \tag{4.2.1d}$$

$$\hat{\nabla}^2 \tilde{X} \approx \frac{\left(\hat{\nabla}^2 \tilde{X}\right)^{n+1} + \left(\hat{\nabla}^2 \tilde{X}\right)^{n}}{2}. \tag{4.2.1e}$$

At the boundaries in the cross-sectional plane a slightly different formulae for the finite difference approximation is employed based on Lagrange interpolations as in section 2.2.1. At the leading edge of the plate where $x = 0$ marching is started from the base flow solution where $\tilde{\Phi} = \tilde{\Psi} = \tilde{U} = \tilde{\Theta} = 0$. Starting from $n = 0$ the approximate solution is known at step n however the solution at step $n+1$ is unknown. In order to calculate the solution at step $n + 1$ the variables at $n + 1$ are split into a known/guessed part and a correction such that

$$\tilde{X}^{n+1} = \tilde{X}^{n+1,G} + \tilde{X}^{n+1,C}. \tag{4.2.2}$$

By doing this the governing equations (4.1.7) are linearised to give a system of equations for the correction terms. Iterating allows the known values $\tilde{X}^{n+1,G}$ to be updated until the correction terms are sufficiently small. At the start of each set of iterations, for a given step $n + 1$, initially $\tilde{X}^{n+1,G} = \tilde{X}^{n}$ so that a good guessed value is used from which to start iterating. Essentially this is a modified version of the numerical scheme outlined in 2.2.1 where there are extra terms due to the downstream variation. Extra computation is required to solve the system at different downstream locations as the solutions are no longer self-similar in x. For the numerical calculations presented below, unless otherwise stated, the computational parameters are $\hat{\zeta}_\infty = 16$, $\eta_\infty = 128$, $x_\infty = 100$ and $N_{\hat{\zeta}} = N_\eta = 401$ with $\Delta x = 0.1$ such that $N_x = 1000$. The results presented are for $\zeta_0 = 1$ and $\beta = 0$ and are independent of the above computational parameters and the stretching functions $\bar{\zeta}(\hat{\zeta})$ and $\bar{\eta}(\eta)$.

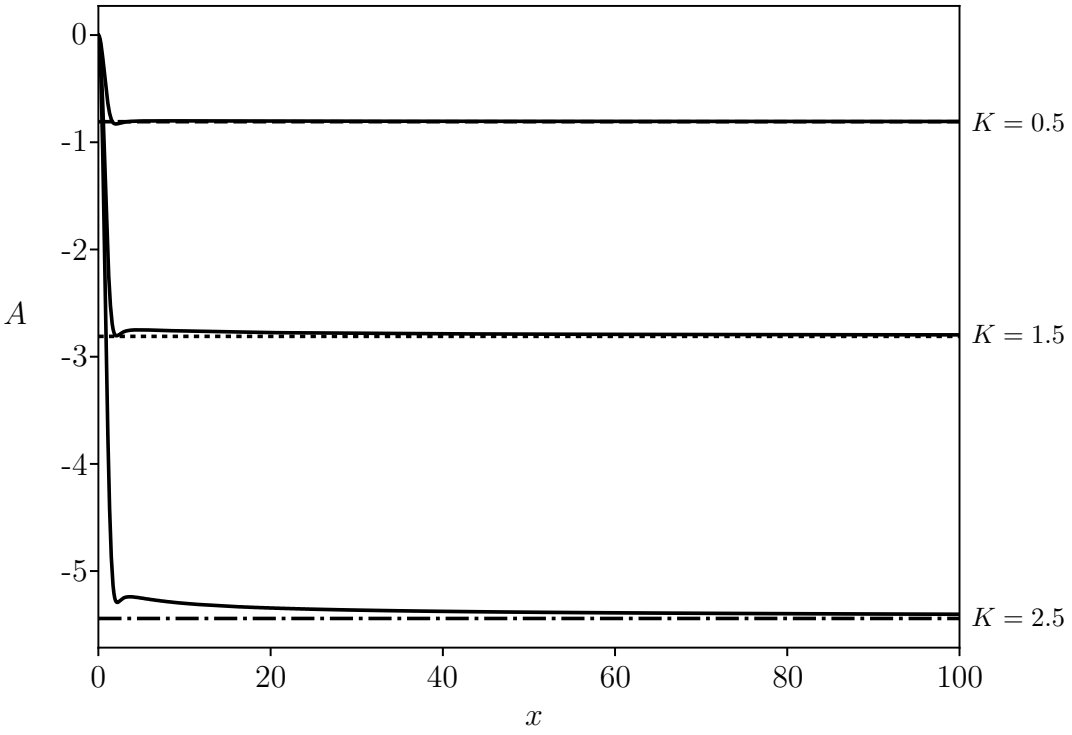

Figure 4.2.1: The mass flux parameter A is plotted as a function of the downstream coordinate x for various injection rates K with $\beta = 0$. The dashed/dotted/dash-dotted lines indicate the value of the mass flux parameter for the corresponding self-similar solution as discussed in chapter 2.

4.2.2 Recovering the self-similar solution

In order to recover the self-similar solution whilst marching downstream it is necessary to use an injection function such as

$$\tilde{\Phi}_w(x, \hat{\zeta}) = -K\left(1 - e^{-x^2}\right) e^{-\hat{\zeta}^2}, \tag{4.2.3}$$

which as x increases becomes the Gaussian injection profile $-Ke^{-\hat{\zeta}^2}$ examined in section 2.5.2. Notice that at the leading edge of the plate ($x = 0$) the injection through the surface given by (4.2.3) is zero. There are many other possible profiles which would recover the self-similar profile far downstream but this one is chosen for convenience.

Solving the downstream marching perturbation equations (4.1.7), with a Blasius base flow, injection function (4.2.3) and slot width $\zeta_0 = 1$, it is possible to determine whether or not the Gaussian self-similar solution from section 2.5 is recovered sufficiently far downstream. One key parameter which may be considered, in order to

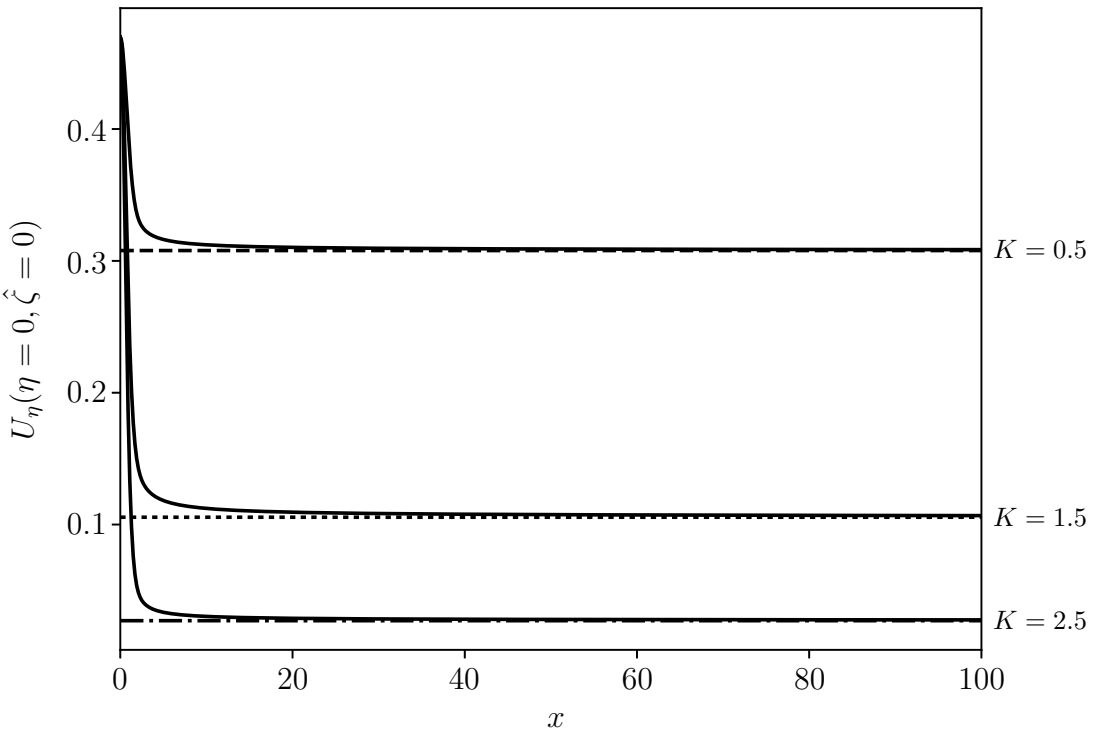

Figure 4.2.2: The wall shear $U_\eta(\eta = 0, \hat{\zeta} = 0)$ is plotted as a function of the downstream coordinate x for various injection rates K with $\beta = 0$. The dashed/dotted/dash-dotted lines indicate the value of the wall shear for the corresponding self-similar solution.

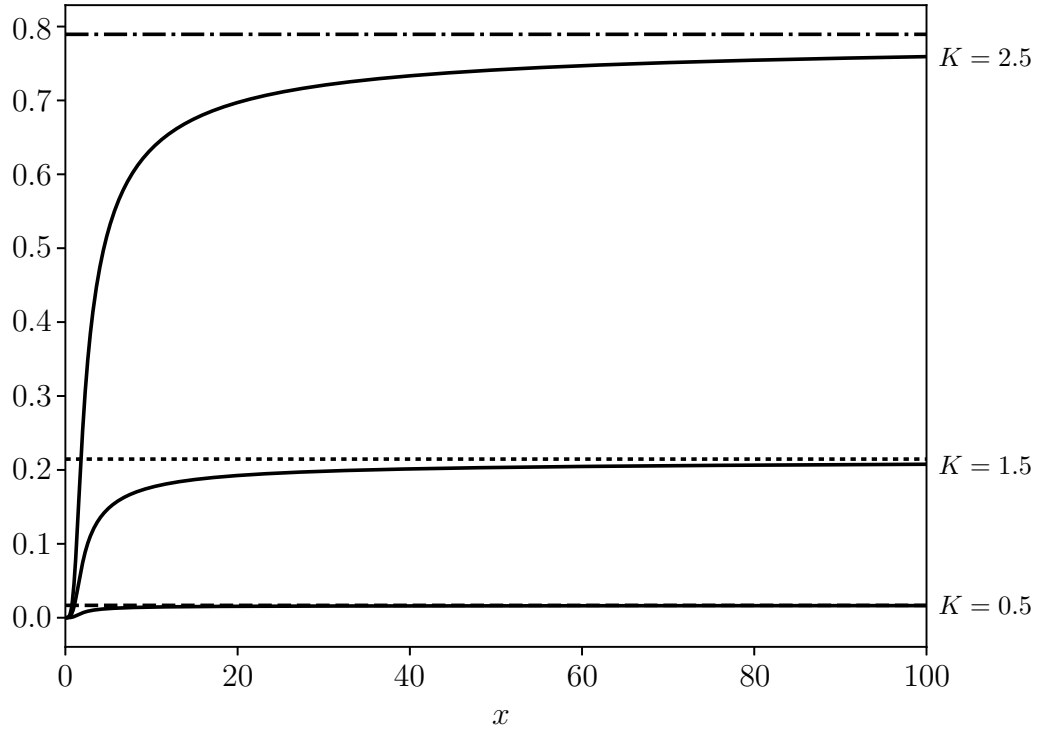

Figure 4.2.3: The integral of the square of the velocity perturbation $\tilde{U}$ over the entire cross-sectional $(\hat{\zeta}, \eta)$ domain is plotted as a function of the downstream coordinate x for various injection rates K with $\beta = 0$. The dashed/dotted/dash-dotted lines indicate the value of the corresponding self-similar solution.

compare the two solutions, is the mass flux coefficient A which is particularly sensitive to variations in the flow. From figure 4.2.1 it is evident that as the flow progresses downstream the mass flux parameter rapidly approaches the self-similar solution for a range of different injection velocities K. However it appears that the flow needs to progress further downstream in order to closely match the self-similar solution as K increases, especially for injection velocities which are in the strong injection regime.

Figure 4.2.2 shows the wall shear stress along the centreline $\eta = \hat{\zeta} = 0$ for a number of injection rates K. At $x = 0$ the wall shear is simply the Blasius wall shear $U_\eta(\eta = 0) \approx 0.4696$ for all injection rates since there is no injection at $x = 0$. Marching downstream the wall shear rapidly approaches the self-similar solution monotonically, even for large injection rates.

A final measure which is useful when comparing the marching solution with the self-similar solution is the integral of the velocity perturbation over the computational domain,

$$\int_0^{\hat{\zeta}_\infty} \int_0^{\eta_\infty} \tilde{U}^2 \mathrm{d}\eta \mathrm{d}\hat{\zeta}. \tag{4.2.4}$$

This measure is analogous to the energy contained in the streamwise velocity correction throughout cross-sectional $(\hat{\zeta}, \eta)$ domain. Figure 4.2.3 shows the value of the integral (4.2.4) at different downstream locations in comparison to the self-similar solution. Again the marching solution approximates the self-similar solution well even for relatively small values of x when K is small but it is necessary to march further downstream to attain the same accuracy as K becomes large.

Clearly using the injection profile (4.2.3) the self-similar solution, found in section 2.5, may be recovered if the equations are marched far enough downstream. Recovering the self-similar solution helps to demonstrate the validity of the marching procedure outlined in section 4.2.1 provided that the streamwise velocity does not become reversed. The effect of using non-self-similar injection profiles may now be investigated with more interesting geometries.

4.2.3 Isolated injection region

Having recovered the self-similar solution attention may now be turned to more geometrically interesting injection profiles. For example the case of an injection concentrated at a particular downstream location on the surface of the plate. For the sake of simplicity suppose that the injection is always along the centreline of the plate on which the symmetry condition is applied. This isolated injection region will take the form of a two-dimensional Gaussian function, which in dimensionless variables is given by

$$v_w(x,z) = Ke^{-(x-x_d)^2}e^{-\left(\frac{z}{\zeta_0}\right)^2}. \tag{4.2.5}$$

Here x_d specifies the downstream location of the centre of the injection region and ζ_0 determines the relative width of the injection. So in terms of the scaled ζ variable this becomes

$$V_{transp}(x,\zeta) = K\left(\frac{2x^{1-2n}}{n+1}\right)^{\frac{1}{2}} e^{-(x-x_d)^2}e^{-\left(\frac{2}{n+1}\right)x\left(\frac{\zeta}{\zeta_0}\right)^2}. \tag{4.2.6}$$

It is assumed, without loss of generality, that there is no basal injection. This means that in the absence of an applied pressure gradient the injection function, for an isolated injection, is taken to be

$$\tilde{\Phi}_w(x,\hat{\zeta}) = -K\sqrt{2x}e^{-(x-x_d)^2}e^{-2x\hat{\zeta}^2}. \tag{4.2.7}$$

The numerical solution of the downstream marching equations (4.1.7) subject to an isolated injection (4.2.7) shall now be examined. The downstream location $x_d = 5$ has arbitrarily been chosen to be the position of the centre of the injection region. Figure 4.2.4 shows that mass flux parameter A as a function of x for $K = 0.5, 1, 2, 4$. As might be expected, the mass flux towards or away from the centreline is only significantly affected near to the injection region, unlike the self-similar scenario, it is found that A tends towards zero as x becomes large. In figure 4.2.4 it is clear that for $x < x_d$ the mass flux parameter becomes increasingly negative as x increases, then when $x \geq x_d$ it is found that A increases until it becomes positive before eventually settling towards zero for large x. A negative value of A indicates that there is a net mass flux away from the centreline which is induced by the injection fluid diverting the oncoming streamwise flow. The mass flux parameter increases and eventually becomes positive

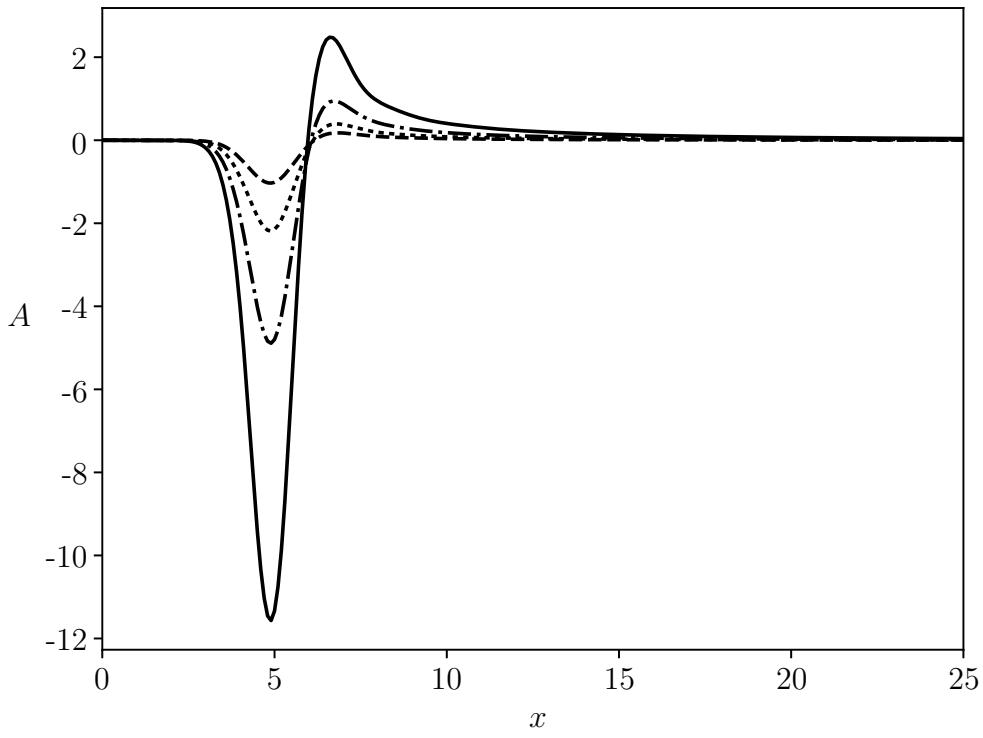

Figure 4.2.4: The mass flux parameter A is plotted as a function of the downstream coordinate x for an injection (4.2.7) with $x_d = 5$ and $\zeta_0 = 1$. The dashed/dotted/dash-dotted/solid lines show the solutions for $K = 0.5, 1, 2, 4$ respectively.

after $x = x_d$ because the magnitude of the injection is decreasing and the low speed region behind the injection causes fluid to be sucked back towards the centreline. In the self-similar case the injection fluid maintains the necessary momentum to force fluid away from the injection region towards the edge of the boundary layer but in the isolated injection case this does not occur.

The changing direction of the transverse and spanwise velocity, due to the influence of the isolated injection, can be seen by examining the (V, W) particle path lines and the vorticity perturbation $\zeta_0\tilde{\Theta}$ at different downstream locations. This phenomenon is illustrated in figure 4.2.5 where it is seen that before the injection region fluid is forced away from the centreline $\hat{\zeta} = 0$; after the injection region the fluid is moving towards the centreline and then being forced upwards as in the usual Blasius boundary layer. The movement of fluid towards the centreline continues further downstream but becomes progressively weaker until the flow becomes essentially two-dimensional with almost vertical path lines.

Figure 4.2.6 shows the shear stress along the centreline $\eta = \hat{\zeta} = 0$. At $x = 0$ the shear stress is equal to the expected two-dimensional Blasius value, then as the injection grows downstream the shear stress drop dramatically. Despite the rapid drop as the injection intensifies the shear stress never becomes equal to zero even for large injection rates, instead the wall shear becomes very small over a finite range of downstream locations. For $x > x_d$ the injection reduces from its peak value and the wall shear stress increases, approaching the Blasius wall shear $U_\eta(\eta = 0) \approx 0.4696$ as x becomes large. Figure 4.2.7 shows the wall shear as a function of the spanwise coordinate $\hat{\zeta}$ at a number of different downstream locations for a large injection rate $K = 8$. At $x = 0$ the wall shear is equal to the Blasius value across the entire spanwise extent as one would expect. Then as the flow proceeds downstream, towards $x = x_d$, the wall shear reduces significantly near to the centreline $\hat{\zeta} = 0$ but approaches the Blasius value for large $\hat{\zeta}$. Proceeding sufficiently far downstream, the influence of the injection on the wall shear reduces significantly, there is only a slight deviation from the Blasius value as shown by the plot for $x = 100$ in figure 4.2.7.

Figure 4.2.8 shows the integral of the square of the streamwise velocity perturbation over the cross-sectional $(\hat{\zeta}, \eta)$ domain for an isolated injection (4.2.7). The flow is only significantly altered in the injection region near to $x = x_d$. The deviation from zero is

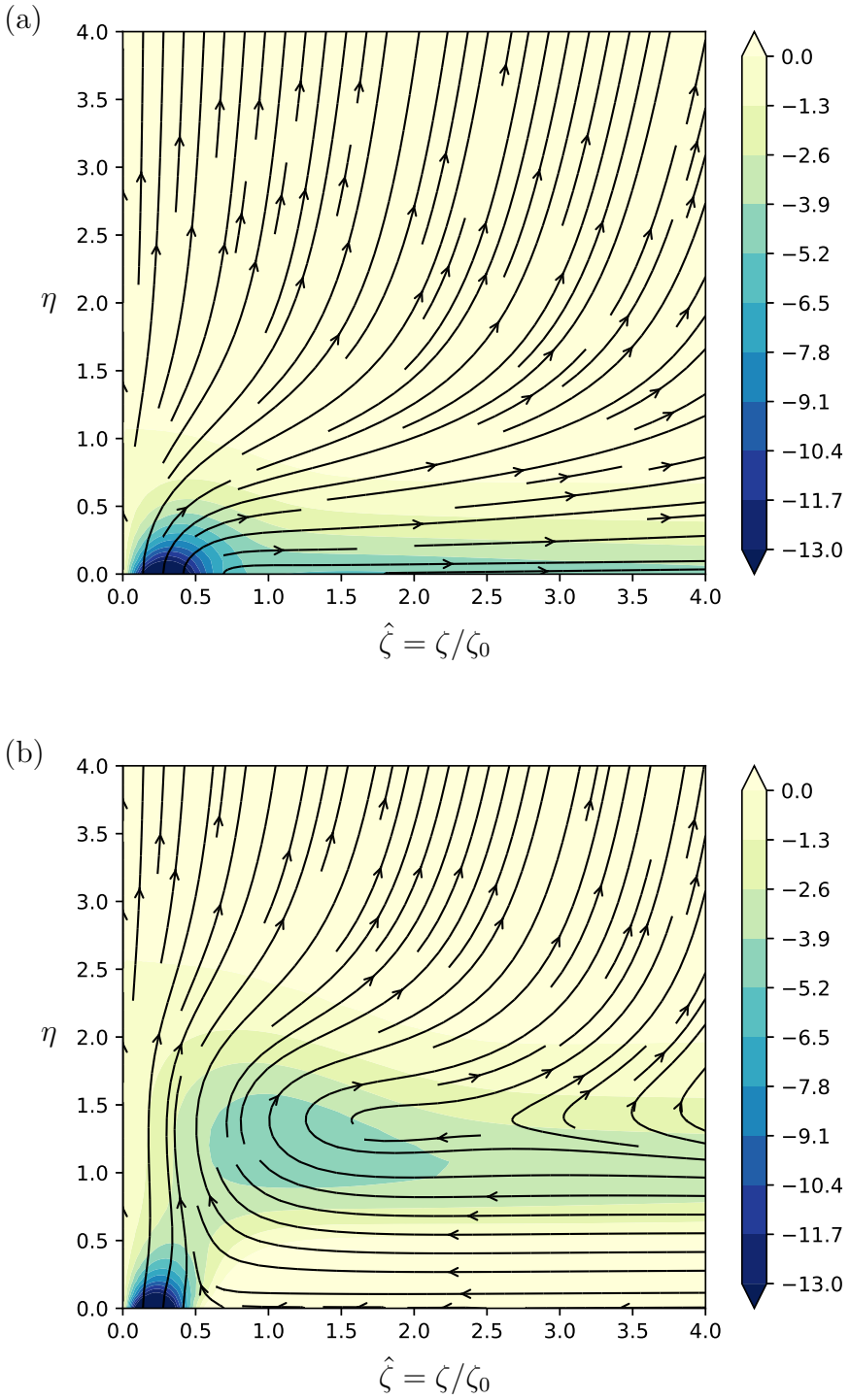

Figure 4.2.5: The perturbation vorticity $\zeta_0\tilde{\Theta}$ and the (V, W) particle path lines are shown for an injection (4.2.7) with $x_d = 5$, $\zeta_0 = 1$ and $K = 4$ at the downstream locations (a) $x = 4$ and (b) $x = 6$.

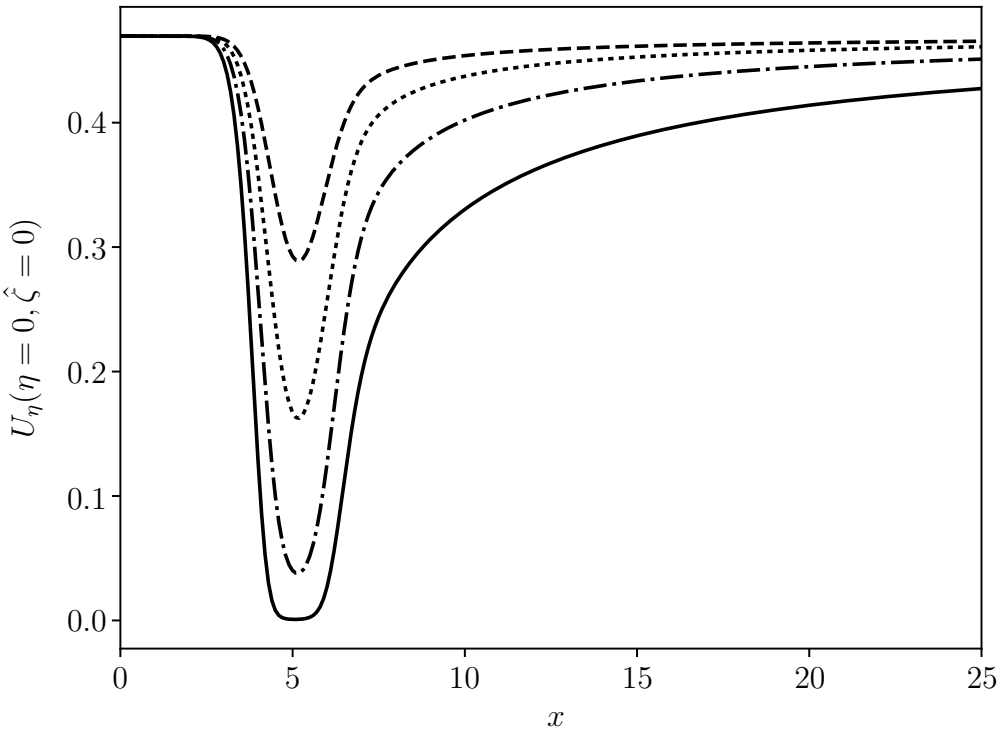

Figure 4.2.6: The wall shear at the centreline $U_\eta(\eta = 0, \hat{\zeta} = 0)$ is plotted as a function of the downstream coordinate x for an injection (4.2.7) with $x_d = 5$ and $\zeta_0 = 1$. The dashed/dotted/dash-dotted/solid lines show the solutions for $K = 0.5, 1, 2, 4$ respectively.

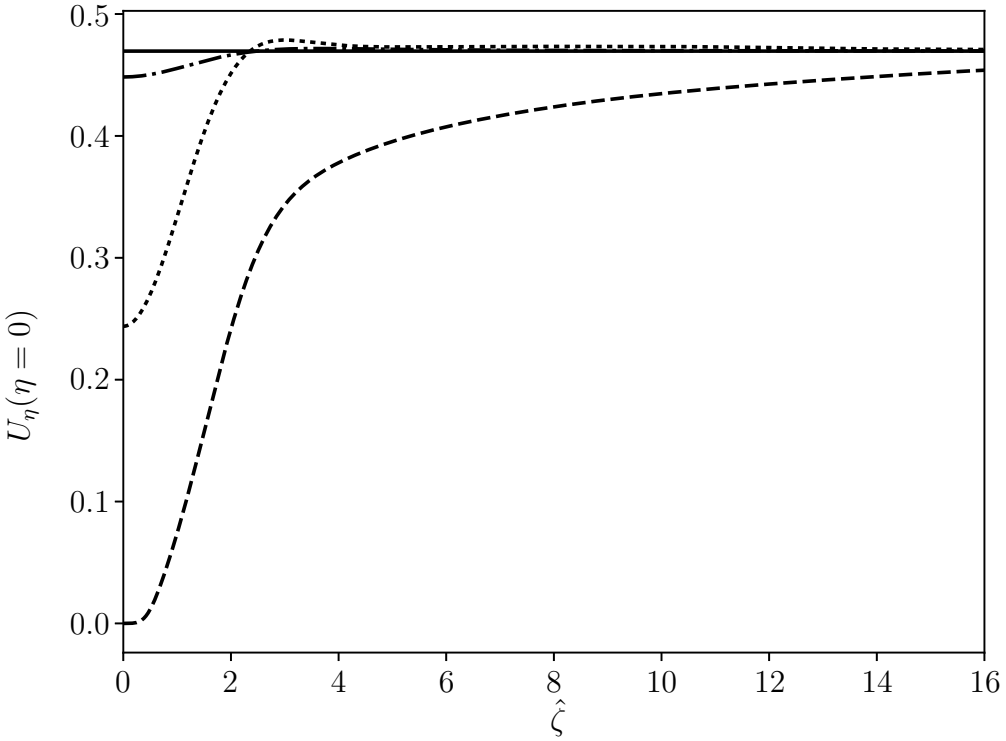

Figure 4.2.7: The wall shear $U_\eta(\eta = 0)$ is plotted as a function of the spanwise coordinate $\hat{\zeta}$ for an injection (4.2.7) with $x_d = 5$, $\zeta_0 = 1$ and $K = 8$. The solid/dashed/dotted/dash-dotted lines show the solutions for $x = 0, 5, 10, 100$ respectively.

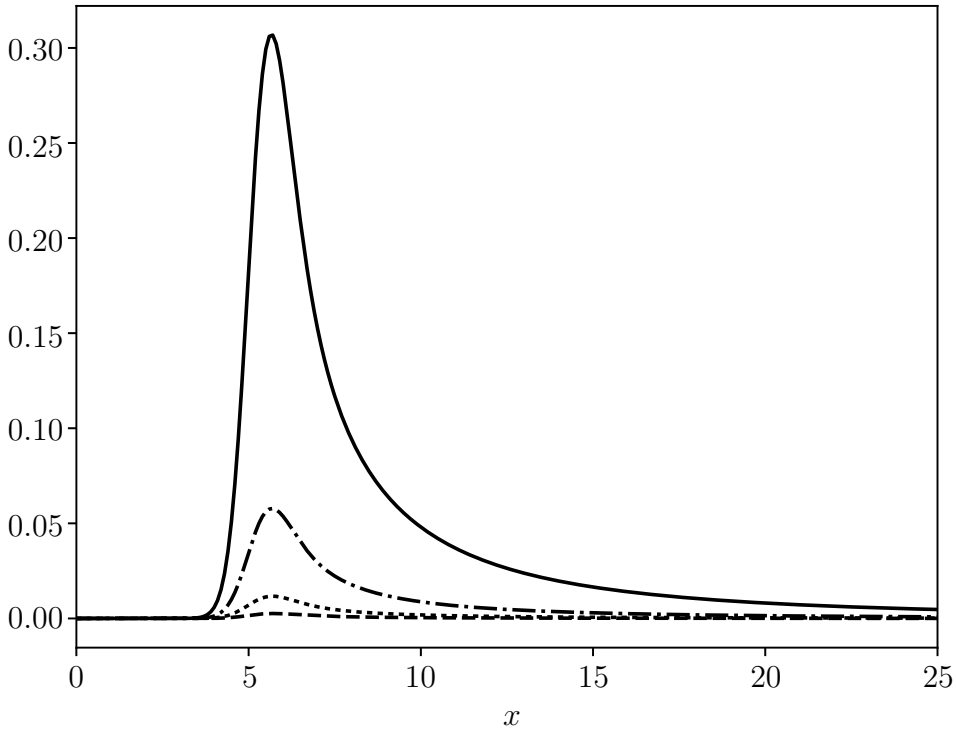

Figure 4.2.8: The integral of the square of the velocity perturbation $\tilde{U}$ over the entire cross-sectional $(\hat{\zeta}, \eta)$ domain is plotted as a function of the downstream coordinate x for an injection (4.2.7) with $x_d = 5$ and $\zeta_0 = 1$. The dashed/dotted/dash-dotted/solid lines show the solutions for $K = 0.5, 1, 2, 4$ respectively.

relatively small when compared with the self-similar case, shown in figure 4.2.3, even for large injection rates. This small deviation, along with the rapid decay back to zero, is due to the fact that much less momentum is being added to the flow when the injection only exists over an isolated downstream region. Even using a larger injection width ζ_0 eventually (4.2.4) will become insignificantly small sufficiently far downstream.

The solution of the downstream marching equations (4.1.3) in the presence of an isolated short-scale injection through the surface of a flat plate has been briefly examined. The influence of the injection only persists significantly for a short distance downstream however this disturbance is exacerbated if the injection rate K and the slot width ζ_0 are increased.

4.2.4 Constant width slot

Another interesting case is that of an injection through a constant width slot in an otherwise uniform flat plate such that the injection velocity is given by

$$v_w(x,z) = K\left(1-e^{-x^2}\right)e^{-(z/\zeta_0)^2}, \tag{4.2.8}$$

where ζ_0 determines the width of the injection slot. The injection is introduced gradually from the zero at the leading edge by the factor $\left(1-e^{-x^2}\right)$. Applying the boundary-layer scaling gives

$$V_{transp}(x,\zeta) = K\left(\frac{2x^{1-2n}}{n+1}\right)^{\frac{1}{2}}\left(1-e^{-x^2}\right)e^{-\left(\frac{2}{n+1}\right)x\left(\frac{\zeta}{\zeta_0}\right)^2}. \tag{4.2.9}$$

So in the absence of an applied pressure gradient ($n = 0$) the nonlinear correction transpiration for the constant width slot is taken to be

$$\tilde{\Phi}_w(x,\hat{\zeta}) = -K\sqrt{2x}\left(1-e^{-x^2}\right)e^{-2x\hat{\zeta}^2}. \tag{4.2.10}$$

The numerical solution of the marching equations (4.1.7) subject to the constant width slot injection (4.2.10) is presented below. The downstream step size and the number of downstream points are taken to be $\Delta x = 0.05$ and $N_x = 2000$. This reduction in the step size helps to avoid so called 'ringing' in the numerical solution which is an oscillation above and below the solution.

Figure 4.2.9 shows the mass flux parameter as a function of the downstream coordinate for increasing injection rates. The mass flux parameter A becomes more negative as the rate of injection increases, as in the previous two cases. Unlike the isolated injection problem, the magnitude of the mass flux remains large far downstream due to the continued presence of the injection. It appears as if A approaches a constant value as x increases but this may not be the case. It is unclear whether A will tend towards a constant value for very large values of x since, in relation to the boundary-layer thickness, the injection becomes increasingly concentrated around the centreline far downstream. The width of the slot will become small in comparison to the boundary-layer thickness at large downstream locations and the injection will take on a delta function-like profile with a very large injection occurring near to $\hat{\zeta} = 0$ but remaining small everywhere else. This concentration near to the centreline at large

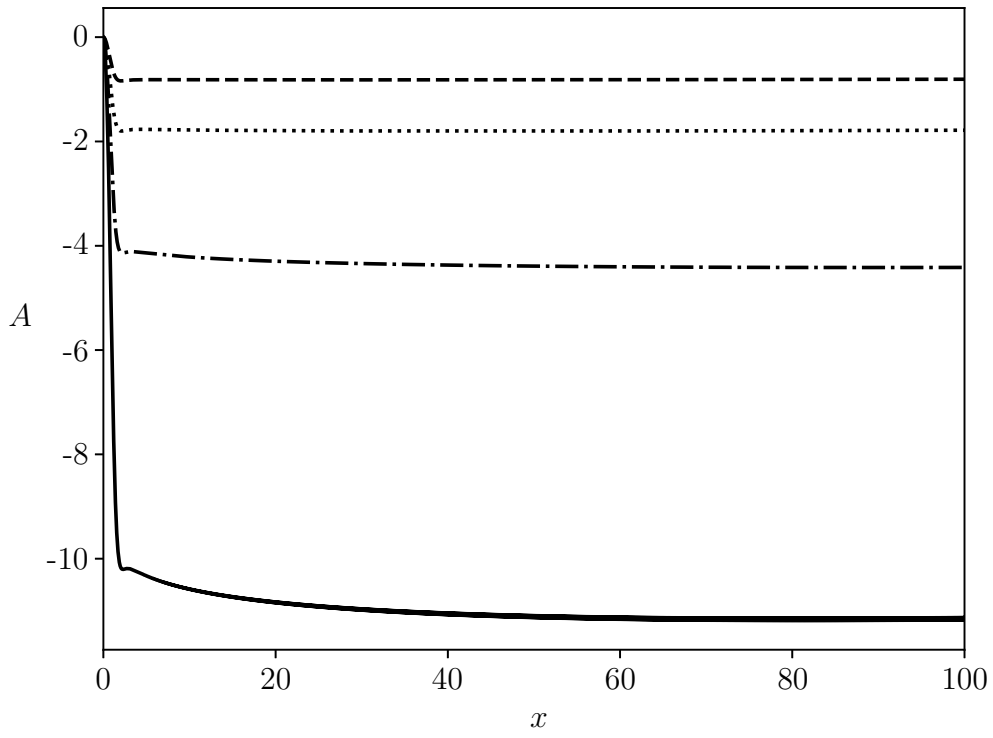

Figure 4.2.9: The mass flux parameter A is plotted as a function of the downstream coordinate x for an injection (4.2.10) with $\zeta_0 = 1$. The dashed/dotted/dash-dotted/solid lines show the solutions for $K = 0.5, 1, 2, 4$ respectively.

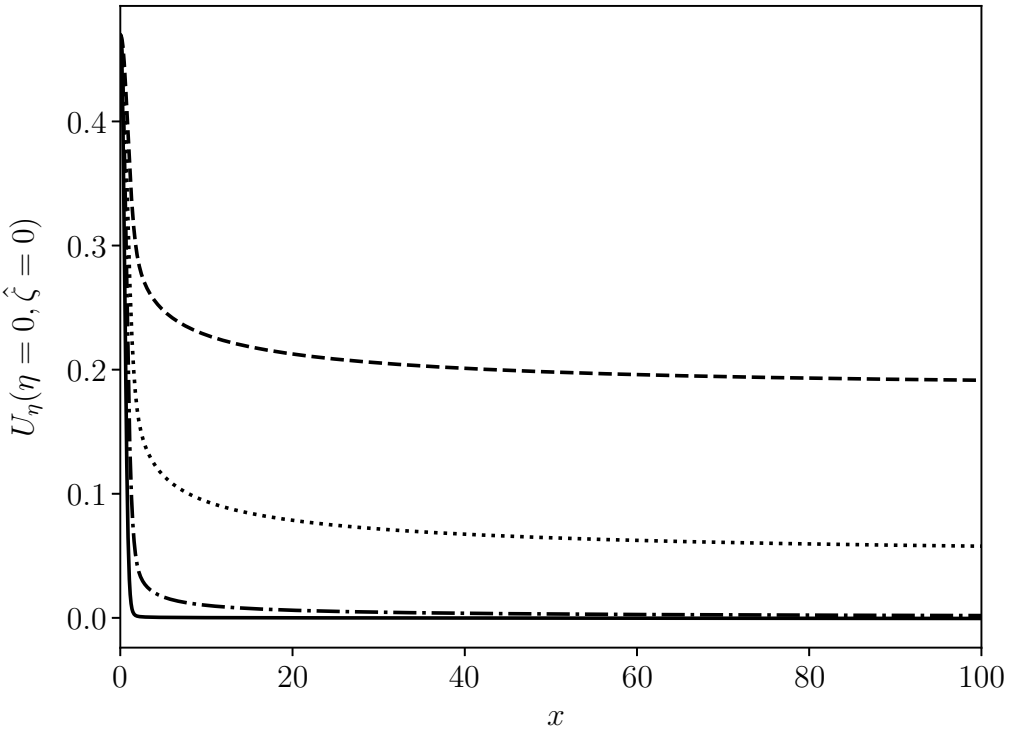

Figure 4.2.10: The wall shear at the centreline $U_\eta(\eta = 0, \hat{\zeta} = 0)$ is plotted as a function of the downstream coordinate x for an injection (4.2.10) with $\zeta_0 = 1$. The dashed/dotted/dash-dotted/solid lines show the solutions for $K = 0.5, 1, 2, 4$ respectively.

downstream locations creates mesh resolution problems, on both uniform and non-uniform meshes, when numerically solving the governing equations for large values of x in the η, $\hat{\zeta}$ coordinates.

The shear stress along the centreline $\eta = \hat{\zeta} = 0$ is shown in figure 4.2.10 for increasing values of K. As predicted, increasing the injection rate reduces the shear stress which becomes very small, but remains positive, for large values of K. Comparing the constant width slot case with the marching self-similar injection (4.2.3) it appears that the shear stress along the centreline is smaller in the constant width slot problem for the same injection rate. It is possible that this is due to the concentrated nature of the injection profile in the constant width slot case since the injection velocity in (4.2.10) is larger than in (4.2.3) near to $\hat{\zeta} = 0$ due to the extra factor of $\sqrt{2x}$. As in the self-similar marching case it appears that the shear stress along the centreline approaches a constant value as x increases.

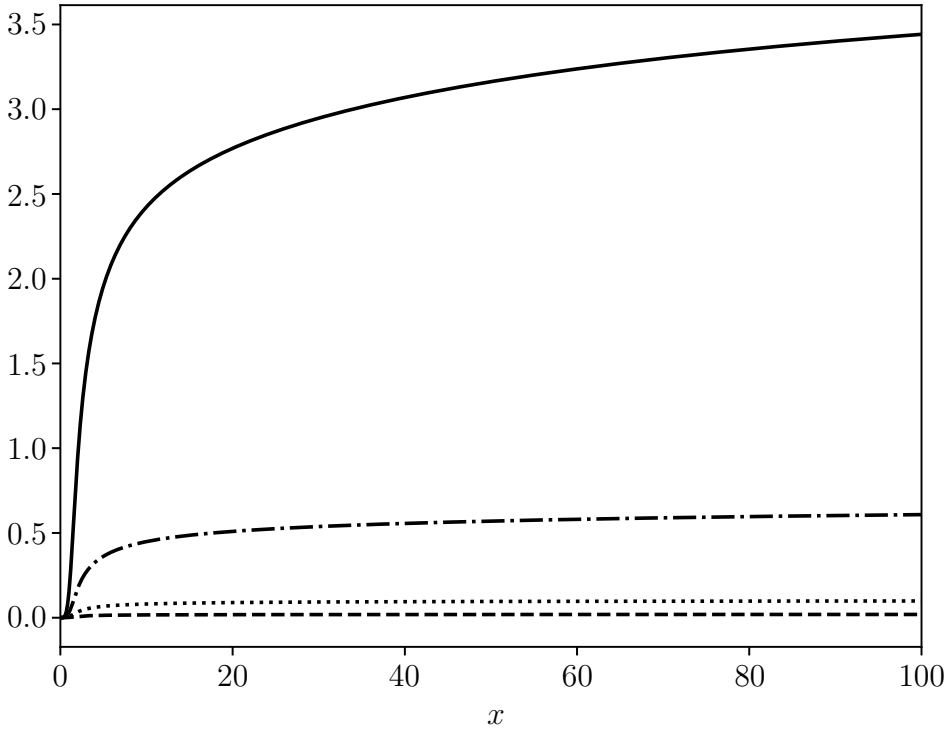

Figure 4.2.11: The integral of the square of the velocity perturbation $\tilde{U}$ over the entire cross-sectional $(\hat{\zeta}, \eta)$ domain is plotted as a function of the downstream coordinate x for an injection (4.2.7) with $\zeta_0 = 1$. The dashed/dotted/dash-dotted/solid lines show the solutions for $K = 0.5, 1, 2, 4$ respectively.

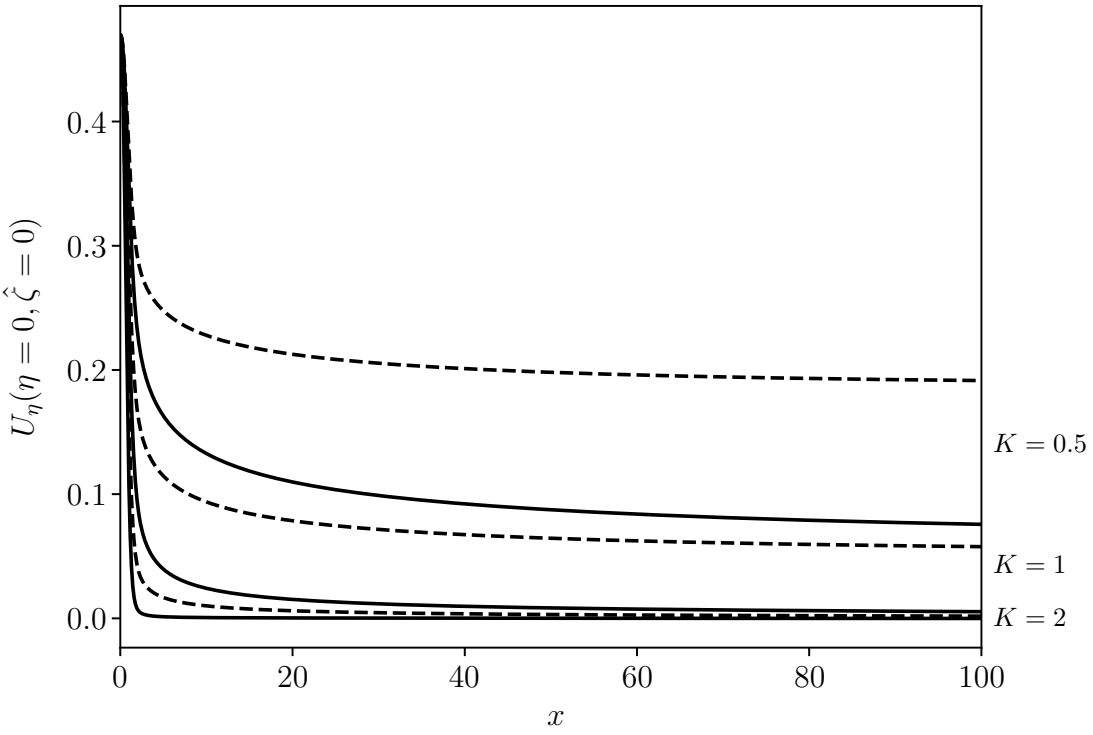

Figure 4.2.12: The wall shear at the centreline $U_\eta(\eta = 0, \hat{\zeta} = 0)$ is plotted as a function of the downstream coordinate x for an injection (4.2.10) with $K = 0.5, 1, 2$. The dashed/solid lines show the solutions for $\zeta_0 = 1, 2$ respectively.

Figure (4.2.11) shows the integral of the square of the streamwise velocity perturbation $\tilde{U}$ defined by (4.2.4). As in the self-similar marching case the value of the integral appears to approach a constant value as x increases. Again it is unclear whether this approach to a constant value will continue at larger downstream locations. However it does appear that the constant width slot solution is qualitatively the same as the self-similar solution in most respects.

Increasing the slot width ζ_0 has a significant impact upon the the flow response for the constant width injection profile (4.2.10). Figure 4.2.12 shows the centreline shear stress for slot widths $\zeta_0 = 1, 2$ and injection rates $K = 0.5, 1, 2$. Doubling the injection slot width greatly reduces the wall shear stress for all values of K, it also significantly increases the magnitude of the mass flux parameter A at all downstream locations. The numerical solution of the downstream marching equations (4.1.3) with an applied constant width injection (4.2.10) produces a different flow response to both the self-similar and isolated injection cases. The constant width slot solution resembles

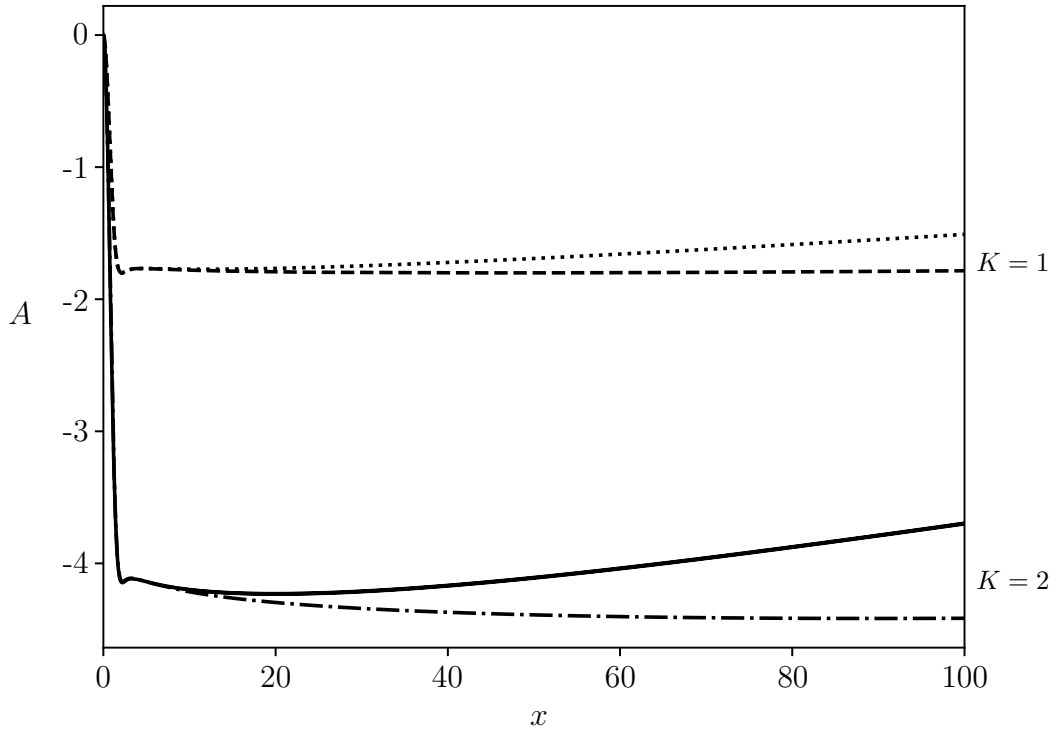

Figure 4.2.13: The mass flux parameter A is plotted as a function of the downstream coordinate x for an injection (4.2.10) with $\zeta_0 = 1$ and $K = 1, 2$. The dashed and dash-dotted lines show the solutions when $N_{\hat{\zeta}} = N_\eta = 401$ and the dotted and solid lines show the solutions when $N_{\hat{\zeta}} = N_\eta = 201$.

the self-similar case in many respects but is quantitatively different. The injection has significant influence over a large range of downstream locations despite the width of the injection becoming smaller in comparison to the thickness of the boundary layer far downstream.

Figure 4.2.13 compares the numerically calculated mass flux parameter A as a function of x for the two meshes $N_{\hat{\zeta}} = N_\eta = 201$ and $N_{\hat{\zeta}} = N_\eta = 401$. For the less refined mesh, $N_{\hat{\zeta}} = N_\eta = 201$, the value of the mass flux parameter increases from a minimum value as x increases and seems to approach zero instead of a constant value. As the injection profile becomes more like a delta function for large values of x the lack of resolution in the mesh means that an increasing extent of the injection near to $\hat{\zeta} = 0$ is effectively ignored. This means that the numerical scheme is behaving as if the injection is decreasing far downstream which leads to the reduction in magnitude of the mass flux witnessed in figure 4.2.13. If the flow response at larger downstream

locations is to be examined it will be necessary to increase the resolution of the mesh, especially near the centreline of the injection. Comparison between the mass flux parameter for the different meshes has been chosen but this phenomenon can also be seen in the shear stress and the integral of the velocity perturbation amongst other measures.

4.3 Discussion

Reintroducing downstream variation to the self-similar equations examined in chapters 2 and 3 adds a great deal of extra complexity. The marching equations (4.1.3) provide a fully three-dimensional description of flows involving short spanwise scale features. This extra dimension increases the computational complexity of the problem and adds a significant amount of time, upto a few weeks depending upon the computer architecture, to the numerical solution of the equations.

In this chapter three test cases were examined, namely self-similar, isolated and constant width slot injections. Using the marching equations to recover the self-similar solution ensures the validity of the numerical formulation and allows for fine tuning of the computational parameters. It was necessary to use a Gaussian injection profile, rather than a 'top-hat', as the smoother transition in the spanwise direction means that stability and convergence of the numerical scheme is easier to achieve. The main reason for introducing downstream variation is to allow more interesting injection profiles such as the isolated injection (4.2.7). The influence of the isolated injection only persists over a limited range of downstream locations, even for large injection rates K. However it is interesting to note the change of sign of the mass flux parameter A, from negative to positive, downstream of the injection region. This change of sign indicates that the usual mass flux away from the centreline created by the injection changes direction when the injection is taken away. The constant width slot behaves much more like the self-similar case since the injection is not confined to a small downstream region. It would be interesting to investigate the behaviour of the flow in the constant width slot problem far downstream: this would require a very refined mesh near to the centreline of the injection region which would be prohibitive computationally.

This collection of examples is by no means exhaustive but merely gives a flavour

of possible avenues of exploration. There are many other possible injection profiles which may be considered such as a non-Gaussian 'top-hat' slot, profiles which vary in intensity downstream, sucking profiles and profiles with zero net mass flux through the surface. The marching equations (4.1.3) could also be modified to include a surface topography which is of a limited spanwise extent, as in the self-similar equations (1.3.4). The fully three-dimensional formulation presented here is an important extension to the self-similar formulation examined earlier. On the other hand a more pressing issue which may be considered is how the self-similar solution, presented in previous chapters, responds to disturbances that might cause instabilities in the laminar flow.

Chapter 5

Streak stability

The previous chapters have examined how the introduction of a short spanwise scale feature impacts the flow profile of an otherwise two-dimensional boundary-layer. It has been shown that short-scale injection into the boundary layer significantly alters the underlying two-dimensional flow, especially the streamwise flow and the mass flux from the boundary layer. The time-independent solutions found are idealised in that they are free from interactions with external excitations that are always present in real world situations.

It is important to consider the stability of the flow response to various forms of disturbance. If the flow responds to an external excitation in an unstable manner the structures found in earlier chapters will breakdown and will therefore be difficult to observe experimentally. Studying the influence of small perturbations on the flow structures gives a sense of how these structures may present themselves and whether or not they will persist in any significant way.

It is necessary to start by stating the non-dimensional governing equations and the streak equations in the scaled Cartesian coordinates (x, Y, Z). The inviscid and viscous stability of the short-scale injection flow to a travelling wave disturbance may then be explored. This will lead to equations governing the stability of the underlying short-scale injection flow which shall be solved numerically.

Firstly the dimensional starred $(^*)$ variables are made non-dimensional using a

representative length L^*, speed U^*_∞ and time L^*/U^*_∞. Thus

$$(x,y,z) = (x^*,y^*,z^*)/L^*, \quad (u,v,w) = (u^*,v^*,w^*)/U^*_\infty,$$
$$p = p^*/\rho^* U^{*2}_\infty, \quad t = t^* U^*_\infty/L^*, \tag{5.0.1}$$

where ρ^* is the constant density of the fluid. Also the global Reynolds number Re is defined by $Re = U^*_\infty L^*/\nu^*$, where ν^* is the kinematic viscosity of the fluid. The above formulation leads to the dimensionless incompressible Navier-Stokes equations

$$u_x + v_y + w_z = 0, \tag{5.0.2a}$$
$$u_t + uu_x + vu_y + wu_z = -p_x + Re^{-1}\left(u_{xx} + u_{yy} + u_{zz}\right), \tag{5.0.2b}$$
$$v_t + uv_x + vv_y + wv_z = -p_y + Re^{-1}\left(v_{xx} + v_{yy} + v_{zz}\right), \tag{5.0.2c}$$
$$w_t + uw_x + vw_y + ww_z = -p_z + Re^{-1}\left(w_{xx} + w_{yy} + w_{zz}\right). \tag{5.0.2d}$$

For the boundary-layer flow the scaled transverse and spanwise variables Y, Z are introduced, these are defined by $(Y,Z) = Re^{1/2}(y,z)$. So the governing equations (5.0.2) are rescaled to be

$$u_x + Re^{\frac{1}{2}} v_Y + Re^{\frac{1}{2}} w_Z = 0, \tag{5.0.3a}$$
$$u_t + uu_x + Re^{\frac{1}{2}} vu_Y + Re^{\frac{1}{2}} wu_Z = -p_x + Re^{-1}u_{xx} + u_{YY} + u_{ZZ}, \tag{5.0.3b}$$
$$v_t + uv_x + Re^{\frac{1}{2}} vv_Y + Re^{\frac{1}{2}} wv_Z = -Re^{\frac{1}{2}} p_Y + Re^{-1}v_{xx} + v_{YY} + v_{ZZ}, \tag{5.0.3c}$$
$$w_t + uw_x + Re^{\frac{1}{2}} vw_Y + Re^{\frac{1}{2}} ww_Z = -Re^{\frac{1}{2}} p_Z + Re^{-1}w_{xx} + w_{YY} + w_{ZZ}. \tag{5.0.3d}$$

5.0.1 Streak/vortex flow

A steady boundary-layer expansion for $Re \gg 1$ is used for the streak flow given by

$$u = \hat{U}(x,Y,Z) + \ldots, \tag{5.0.4a}$$
$$(v,w) = Re^{-\frac{1}{2}}\left(\hat{V}(x,Y,Z) + \ldots, \hat{W}(x,Y,Z) + \ldots\right), \tag{5.0.4b}$$
$$p = -\frac{1}{2}U_e^2(x) + Re^{-\frac{1}{2}}p(x) + Re^{-1}\hat{P}(x,Y,Z) + \ldots, \tag{5.0.4c}$$

where U_e is the (known) outer streamwise velocity such that $(\hat{U},\hat{W}) \to (U_e(x),0)$ as $Y \to \infty$. Substituting (5.0.4) into (5.0.3) leads to the equations governing the streak

flow

$$\hat{U}_x + \hat{V}_Y + \hat{W}_Z = 0, \tag{5.0.5a}$$

$$\hat{U}\hat{U}_x + \hat{V}\hat{U}_Y + \hat{W}\hat{U}_Z = U_e(x)U_e'(x) + \hat{U}_{YY} + \hat{U}_{ZZ}, \tag{5.0.5b}$$

$$\hat{U}\hat{V}_x + \hat{V}\hat{V}_Y + \hat{W}\hat{V}_Z = -\hat{P}_Y + \hat{V}_{YY} + \hat{V}_{ZZ}, \tag{5.0.5c}$$

$$\hat{U}\hat{W}_x + \hat{V}\hat{W}_Y + \hat{W}\hat{W}_Z = -\hat{P}_Z + \hat{W}_{YY} + \hat{W}_{ZZ}. \tag{5.0.5d}$$

The leading-order streamwise pressure gradient is determined by the freestream to be $-U_e(x)U_e'(x)$. This parabolised version of the Navier–Stokes equations can be marched downstream in x provided that there is no flow reversal of the streamwise velocity $\hat{U}$. The equations (5.0.5) are referred to as 'three-dimensional parabolic flow' equations by Patankar & Spalding (1972) [51], as the 'Görtler vortex equations' with $G = 0$ (zero curvature) by Hall (1982, 1983) [28] [29] amongst others and as the 'boundary-region equations' by Kemp (1951) [45], Goldstein et al. (2010, 2016) [24] [26] and Ricco & Dilib [55]. These equations, in self-similar form, have been the subject of chapters 2, 3 and 4. The solution of (5.0.5) in the presence of a short spanwise scale injection will form the basic state which is to be disturbed using a travelling wave, with this allowing the stability of the streak flow to be examined.

5.1 Viscous Stability

The stability of the steady streak flow described by (5.0.5) is examined by superimposing a travelling wave that is periodic in the downstream direction with wavenumber α. Starting with the dimensionless governing equations (5.0.2) a large Reynolds number solution may be suggested of the form

$$u = \hat{U} + \epsilon\left(u'(x,y,z,t) + \text{c.c.}\right) + \ldots, \tag{5.1.1a}$$

$$v = Re^{-\frac{1}{2}}\hat{V} + \epsilon\left(v'(x,y,z,t) + \text{c.c.}\right) + \ldots, \tag{5.1.1b}$$

$$w = Re^{-\frac{1}{2}}\hat{W} + \epsilon\left(w'(x,y,z,t) + \text{c.c.}\right) + \ldots, \tag{5.1.1c}$$

$$p = -\frac{1}{2}U_e^2(x) + Re^{-\frac{1}{2}}p(x) + Re^{-1}\hat{P} + \epsilon\left(p'(x,y,z,t) + \text{c.c.}\right) + \ldots, \tag{5.1.1d}$$

where ϵ is a Reynolds number scaling that is taken to be sufficiently small so that linearisation is a valid procedure [31]. Inserting (5.1.1) into (5.0.2), whilst neglecting higher harmonics of the wave, the equations of a motion can be decomposed into the

$O(1)$ equations governing the streak (5.0.5) and $O(\epsilon)$ equations governing the wave, given by

$$u'_x + Re^{\frac{1}{2}} v'_Y + Re^{\frac{1}{2}} w'_Z = 0, \tag{5.1.2a}$$

$$u'_t + \hat{U}u'_x + Re^{\frac{1}{2}}\hat{U}_Y v' + Re^{\frac{1}{2}}\hat{U}_z w' = -p'_x + Re^{-1}u'_{xx} + u'_{YY} + u'_{ZZ}, \tag{5.1.2b}$$

$$v'_t + \hat{U}v'_x = -Re^{\frac{1}{2}}p'_Y + Re^{-1}v'_{xx} + v'_{YY} + v'_{ZZ}, \tag{5.1.2c}$$

$$w'_t + \hat{U}w'_x = -Re^{\frac{1}{2}}p'_Z + Re^{-1}w'_{xx} + w'_{YY} + w'_{ZZ}, \tag{5.1.2d}$$

using the scaled boundary-layer coordinates (Y, Z). Here the term $\hat{U}_x u'$ in the streamwise momentum equation has been ignored as the parallel flow assumption has been used to presume that the downstream variation of the streak flow is small and therefore any x derivatives of the wave velocity may be neglected. In the inviscid limit all x derivatives are ignored however for the viscous approximation this x dependency will be retained in the wave amplitude and wavenumber.

Since the streak flow is considered parallel the wave perturbation is of the form

$$(u', v', w') = \sigma(x)\,(\tilde{u}(Y,Z), \tilde{v}(Y,Z), \tilde{w}(Y,Z))\exp[iRe^{1/2}\theta(x,t)], \tag{5.1.3a}$$

$$p' = \sigma(x)\tilde{p}(Y,Z)\exp[iRe^{1/2}\theta(x,t)]. \tag{5.1.3b}$$

The wave component of the flow is characterised by a time-scale which is of the same order as that of the streamwise flow and a rapid oscillation on a downstream length scale which is comparable to the boundary-layer thickness. In the above

$$\theta(x,t) = \int \alpha(x)\mathrm{d}x - \Omega t, \tag{5.1.4}$$

such that $\alpha = \theta_x$ and $\Omega = \alpha c = -\theta_t$ where Ω is the frequency of the wave, α is the wavenumber and c is the wave speed. The wave amplitude $\sigma(x)$ is allowed to vary slowly in the downstream direction.

Substituting (5.1.3) into (5.1.2) gives the viscous linearised stability equations

$$i\alpha\tilde{u} + \tilde{v}_Y + \tilde{w}_Z = -\,Re^{-\frac{1}{2}}\frac{\sigma_x}{\sigma}\tilde{u}, \tag{5.1.5a}$$

$$i\alpha\left(\hat{U} - c\right)\tilde{u} + \hat{U}_Y\tilde{v} + \hat{U}_Z\tilde{w} = -\left(i\alpha + Re^{-\frac{1}{2}}\frac{\sigma_x}{\sigma}\right)\tilde{p} + Re^{-\frac{1}{2}}\left(\mathcal{L}\tilde{u} - \frac{\sigma_x}{\sigma}\hat{U}\tilde{u}\right), \tag{5.1.5b}$$

$$i\alpha\left(\hat{U} - c\right)\tilde{v} = -\,\tilde{p}_Y + Re^{-\frac{1}{2}}\left(\mathcal{L}\tilde{v} - \frac{\sigma_x}{\sigma}\hat{U}\tilde{v}\right), \tag{5.1.5c}$$

$$i\alpha\left(\hat{U} - c\right)\tilde{w} = -\,\tilde{p}_Z + Re^{-\frac{1}{2}}\left(\mathcal{L}\tilde{w} - \frac{\sigma_x}{\sigma}\hat{U}\tilde{w}\right), \tag{5.1.5d}$$

where $\mathcal{L}$ is the linear operator

$$\mathcal{L} = \frac{\partial^2}{\partial Y^2} + \frac{\partial^2}{\partial Z^2} - \alpha^2 + 2i\alpha Re^{-\frac{1}{2}}\left(\frac{\sigma_x}{\sigma} + \frac{\alpha_x}{2\alpha}\right) + Re^{-1}\frac{\sigma_{xx}}{\sigma}. \tag{5.1.6}$$

The viscous equations (5.1.5) have extra terms involving negative powers of the Reynolds number when compared with the inviscid stability equations which are recovered in the limit $Re \to \infty$.

Following the method of Tatsumi & Yoshimura (1990) [67], eliminating $\tilde{u}$ and $\tilde{p}$, yields simultaneous equations for the velocity components $\tilde{v}$ and $\tilde{w}$. Taking the Y derivative of (5.1.5b), using (5.1.5a) and substituting into (5.1.5c) leads to

$$\begin{aligned}
&(\hat{U}-c)\left[\tilde{v}_{YY} + \left(i\alpha + Re^{-\frac{1}{2}}\frac{\sigma_x}{\sigma}\right)^2\tilde{v}\right] - \left(1 + \frac{Re^{-\frac{1}{2}}}{i\alpha}\frac{\sigma_x}{\sigma}\right)\hat{U}_{YY}\tilde{v} - \frac{1}{i\alpha}Re^{-\frac{1}{2}}\mathcal{L}\tilde{v}_{YY} \\
&-\frac{1}{i\alpha}Re^{-\frac{1}{2}}\left(i\alpha + Re^{-\frac{1}{2}}\frac{\sigma_x}{\sigma}\right)^2\mathcal{L}\tilde{v} + \frac{1}{i\alpha}Re^{-\frac{1}{2}}\frac{\sigma_x}{\sigma}\hat{U}\left[\tilde{v}_{YY} + \left(i\alpha + Re^{-\frac{1}{2}}\frac{\sigma_x}{\sigma}\right)^2\tilde{v}\right] \\
&\qquad = \frac{1}{i\alpha}Re^{-\frac{1}{2}}\mathcal{L}\tilde{w}_{ZY} - \frac{1}{i\alpha}Re^{-\frac{1}{2}}\frac{\sigma_x}{\sigma}\hat{U}\tilde{w}_{ZY} - (\hat{U}-c)\tilde{w}_{ZY} \\
&\qquad\quad - \left(1 + \frac{Re^{-\frac{1}{2}}}{i\alpha}\frac{\sigma_x}{\sigma}\right)\left[\hat{U}_Y\tilde{w}_Z - \hat{U}_{ZY}\tilde{w} - \hat{U}_Z\tilde{w}_Y\right].
\end{aligned} \tag{5.1.7}$$

Similarly taking the Z derivative of (5.1.5b), using (5.1.5a) and substituting into (5.1.5d) gives

$$\begin{aligned}
&(\hat{U}-c)\left[\tilde{w}_{ZZ} + \left(i\alpha + Re^{-\frac{1}{2}}\frac{\sigma_x}{\sigma}\right)^2\tilde{w}\right] - \left(1 + \frac{Re^{-\frac{1}{2}}}{i\alpha}\frac{\sigma_x}{\sigma}\right)\hat{U}_{ZZ}\tilde{w} - \frac{1}{i\alpha}Re^{-\frac{1}{2}}\mathcal{L}\tilde{w}_{ZZ} \\
&-\frac{1}{i\alpha}Re^{-\frac{1}{2}}\left(i\alpha + Re^{-\frac{1}{2}}\frac{\sigma_x}{\sigma}\right)^2\mathcal{L}\tilde{w} + \frac{1}{i\alpha}Re^{-\frac{1}{2}}\frac{\sigma_x}{\sigma}\hat{U}\left[\tilde{w}_{ZZ} + \left(i\alpha + Re^{-\frac{1}{2}}\frac{\sigma_x}{\sigma}\right)^2\tilde{w}\right] \\
&\qquad = \frac{1}{i\alpha}Re^{-\frac{1}{2}}\mathcal{L}\tilde{v}_{YZ} - \frac{1}{i\alpha}Re^{-\frac{1}{2}}\frac{\sigma_x}{\sigma}\hat{U}\tilde{v}_{YZ} - (\hat{U}-c)\tilde{v}_{YZ} \\
&\qquad\quad - \left(1 + \frac{Re^{-\frac{1}{2}}}{i\alpha}\frac{\sigma_x}{\sigma}\right)\left[\hat{U}_Z\tilde{v}_Y - \hat{U}_{YZ}\tilde{v} - \hat{U}_Y\tilde{v}_Z\right].
\end{aligned} \tag{5.1.8}$$

These may be written more succinctly as the system of equations

$$\mathcal{E}(Y,Z)\tilde{v} = \mathcal{O}(Y,Z)\tilde{w}, \tag{5.1.9a}$$

$$\mathcal{E}(Z,Y)\tilde{w} = \mathcal{O}(Z,Y)\tilde{v}, \tag{5.1.9b}$$

where $\mathcal{E}(Y,Z)$ and $\mathcal{O}(Y,Z)$ are the even and odd operators

$$\begin{aligned}\mathcal{E}(Y,Z) = &-\left[\frac{i}{\alpha Re^{\frac{1}{2}}}\left(\frac{\partial^2}{\partial Y^2}+\frac{\partial^2}{\partial Z^2}-\alpha^2-\frac{\sigma_x}{\sigma}\hat{U}\right)+(\hat{U}-c)-\frac{2}{Re}\left(\frac{\sigma_x}{\sigma}+\frac{\alpha_x}{2\alpha}\right)\right.\\ &\left.+\frac{i}{\alpha Re^{\frac{3}{2}}}\frac{\sigma_{xx}}{\sigma}\right]\left(\frac{\partial^2}{\partial Y^2}+\left(i\alpha+Re^{-\frac{1}{2}}\frac{\sigma_x}{\sigma}\right)^2\right)+\left(1-\frac{i}{\alpha Re^{\frac{1}{2}}}\frac{\sigma_x}{\sigma}\right)\frac{\partial^2\hat{U}}{\partial Y^2},\end{aligned} \tag{5.1.10}$$

$$\begin{aligned}\mathcal{O}(Y,Z) = &\left[\frac{i}{\alpha Re^{\frac{1}{2}}}\left(\frac{\partial^2}{\partial Y^2}+\frac{\partial^2}{\partial Z^2}-\alpha^2-\frac{\sigma_x}{\sigma}\hat{U}\right)+(\hat{U}-c)-\frac{2}{Re}\left(\frac{\sigma_x}{\sigma}+\frac{\alpha_x}{2\alpha}\right)\right.\\ &\left.+\frac{i}{\alpha Re^{\frac{3}{2}}}\frac{\sigma_{xx}}{\sigma}\right]\frac{\partial^2}{\partial Z\partial Y}+\left(1-\frac{i}{\alpha Re^{\frac{1}{2}}}\frac{\sigma_x}{\sigma}\right)\left[\frac{\partial\hat{U}}{\partial Y}\frac{\partial}{\partial Z}-\frac{\partial\hat{U}}{\partial Z}\frac{\partial}{\partial Y}-\frac{\partial^2\hat{U}}{\partial Z\partial Y}\right].\end{aligned} \tag{5.1.11}$$

The system of equations (5.1.9) must be solved subject to appropriate boundary conditions. Due to no-slip and impermeability of the plate it is required that $\tilde{v}=\tilde{w}=\tilde{v}_Y=0$ on $Y=0$. Then due to symmetry of the flow about the centreline it is necessary that $\tilde{w}=\tilde{v}_Z=\tilde{w}_{ZZ}=0$ on $Z=0$, this assumes that the modes are varicose and not sinuous. Then for the far-field boundary conditions $\tilde{v},\tilde{v}_Y,\tilde{w}\to 0$ as $Y\to\infty$ and $\tilde{w},\tilde{w}_Z,\tilde{v}\to 0$ as $Z\to\infty$.

5.1.1 Two-dimensional Orr-Sommerfeld equation

The stability problem may be cast into the self-similar coordinate system such that

$$(Y,Z)=\left(\frac{2x^{1-n}}{n+1}\right)^{\frac{1}{2}}(\eta,\zeta). \tag{5.1.12}$$

Using the self-similar transformation (5.1.12) the system (5.1.9) becomes

$$\mathcal{E}(\eta,\zeta)\tilde{v}=\mathcal{O}(\eta,\zeta)\tilde{w}, \tag{5.1.13a}$$

$$\mathcal{E}(\zeta,\eta)\tilde{w}=\mathcal{O}(\zeta,\eta)\tilde{v}, \tag{5.1.13b}$$

where $\mathcal{E}(\eta,\zeta)$ and $\mathcal{O}(\eta,\zeta)$ are the even and odd operators

$$\begin{aligned}\mathcal{E}(\eta,\zeta) = &-\left[\frac{i}{\hat{\alpha}Re_x^{\frac{1}{2}}}\left(\frac{\partial^2}{\partial\eta^2}+\frac{\partial^2}{\partial\zeta^2}-\hat{\alpha}^2\right)+(U-\hat{c})+\frac{1-\beta}{Re_x}\right]\left(\frac{\partial^2}{\partial\eta^2}-\hat{\alpha}^2\right)\\ &+\frac{\partial^2 U}{\partial\eta^2},\end{aligned} \tag{5.1.14}$$

$$\begin{aligned}\mathcal{O}(\eta,\zeta) = &\left[\frac{i}{\hat{\alpha}Re_x^{\frac{1}{2}}}\left(\frac{\partial^2}{\partial\eta^2}+\frac{\partial^2}{\partial\zeta^2}-\hat{\alpha}^2\right)+(U-\hat{c})+\frac{1-\beta}{Re_x}\right]\frac{\partial^2}{\partial\zeta\partial\eta}\\ &-\frac{\partial U}{\partial\zeta}\frac{\partial}{\partial\eta}+\frac{\partial U}{\partial\eta}\frac{\partial}{\partial\zeta}-\frac{\partial^2 U}{\partial\zeta\partial\eta}.\end{aligned} \tag{5.1.15}$$

Here $Re_x = 2x^{n+1}Re/(n+1)$ is the local Reynolds which is taken to be large and $\hat{\alpha} = \sqrt{2x^{1-n}/(n+1)}\alpha$ and $\hat{c} = x^{-n}\Omega/\alpha = x^{-n}c$ are constants. Terms involving the derivative of the wave amplitude σ_x, σ_{xx} are ignored as the wave amplitude varies slowly as the wave progresses downstream; these terms are small in comparison to the rest of the terms provided that $\alpha = O(1)$. This also applies to the downstream derivative of the wavenumber α_x.

The system of two fourth-order equations (5.1.13) may be rewritten as a system of four second-order equations. Defining the new variables $\tilde{q}$ and $\tilde{s}$ such that

$$\frac{i}{\hat{\alpha}Re_x^{\frac{1}{2}}}\tilde{\nabla}^2\tilde{v} + \left[U - \hat{c} + \frac{(1-\beta)}{Re_x}\right]\tilde{v} = \tilde{q}, \tag{5.1.16a}$$

$$\frac{i}{\hat{\alpha}Re_x^{\frac{1}{2}}}\tilde{\nabla}^2\tilde{w} + \left[U - \hat{c} + \frac{(1-\beta)}{Re_x}\right]\tilde{w} = \tilde{s}, \tag{5.1.16b}$$

the system (5.1.13) may be rewritten as

$$\tilde{q}_{\eta\eta} - \hat{\alpha}^2\tilde{q} + \tilde{s}_{\zeta\eta} + U_\eta\tilde{w}_\zeta - U_\zeta\tilde{w}_\eta - U_{\zeta\eta}\tilde{w} - U_{\eta\eta}\tilde{v} = 0, \tag{5.1.16c}$$

$$\tilde{s}_{\zeta\zeta} - \hat{\alpha}^2\tilde{s} + \tilde{q}_{\eta\zeta} + U_\zeta\tilde{v}_\eta - U_\eta\tilde{v}_\zeta - U_{\eta\zeta}\tilde{v} - U_{\zeta\zeta}\tilde{w} = 0. \tag{5.1.16d}$$

where

$$\tilde{\nabla}^2 = \frac{\partial^2}{\partial\eta^2} + \frac{\partial^2}{\partial\zeta^2} - \hat{\alpha}^2. \tag{5.1.16e}$$

The system of equations (5.1.16) for $\tilde{v}, \tilde{w}, \tilde{q}$ and $\tilde{s}$ is equivalent to (5.1.13) but is easier to implement numerically. Here $\hat{\alpha}$ is a prescribed constant and $\hat{c}$ is the eigenvalue which is to be determined.

Boundary conditions

On the centreline, $\zeta = 0$, the symmetry boundary conditions are $\tilde{w} = \tilde{v}_\zeta = \tilde{w}_{\zeta\zeta} = 0$. This means that $\tilde{s} = 0$ and $\tilde{q}_\zeta = i\tilde{v}_{\zeta\zeta\zeta}/\hat{\alpha}Re_x^{1/2}$ on $\zeta = 0$. However since $\tilde{v}$ is required to be an even function of ζ it follows that $\tilde{v}_{\zeta\zeta\zeta} = 0$ on $\zeta = 0$. So the boundary conditions along the centreline, for each of the variables, are

$$\tilde{v}_\zeta = \tilde{w} = \tilde{q}_\zeta = \tilde{s} = 0 \quad \text{on} \quad \zeta = 0, \tag{5.1.17a}$$

where the condition $\tilde{w}_{\zeta\zeta} = 0$ is implied by the other conditions.

On the surface of the plate at $\eta = 0$ it is required that $\tilde{v} = \tilde{w} = \tilde{v}_\eta = 0$. Substituting these conditions into the system of equations (5.1.16) leads to the surface boundary conditions

$$\tilde{v} = \tilde{w} = \tilde{q} - \frac{i}{\hat{\alpha} Re_x^{\frac{1}{2}}} \tilde{v}_{\eta\eta} = \tilde{s} - \frac{i}{\hat{\alpha} Re_x^{\frac{1}{2}}} \tilde{w}_{\eta\eta} = 0 \quad \text{on} \quad \eta = 0. \tag{5.1.17b}$$

The boundary condition $\tilde{v}_\eta = 0$ is still important however and must be utilised when specifying the boundary conditions numerically.

In the self-similar formulation the far-field boundary conditions become $\tilde{v}, \tilde{v}_\eta, \tilde{w} \to 0$ as $\eta \to \infty$ and $\tilde{w}, \tilde{w}_\zeta, \tilde{v} \to 0$ as $\zeta \to \infty$. This means that the far-field conditions are

$$\tilde{v}, \tilde{w}, \tilde{q} - \frac{i}{\hat{\alpha} Re_x^{\frac{1}{2}}} \tilde{v}_{\eta\eta}, \tilde{s} - \frac{i}{\hat{\alpha} Re_x^{\frac{1}{2}}} \tilde{w}_{\eta\eta} \to 0 \quad \text{as} \quad \eta \to \infty \tag{5.1.17c}$$

and

$$\tilde{v}, \tilde{w}, \tilde{q} - \frac{i}{\hat{\alpha} Re_x^{\frac{1}{2}}} \tilde{v}_{\zeta\zeta}, \tilde{s} - \frac{i}{\hat{\alpha} Re_x^{\frac{1}{2}}} \tilde{w}_{\zeta\zeta} \to 0 \quad \text{as} \quad \zeta \to \infty. \tag{5.1.17d}$$

5.1.2 Numerical formulation

In order to solve the system of equations (5.1.16), along with the boundary conditions, it is appropriate to use a finite-difference scheme which is similar to the scheme outlined in section 2.2. For the equations (5.1.16), which are specified on the internal nodes of the computational grid, the derivatives of the variables $\tilde{v}$, $\tilde{w}$, $\tilde{q}$ and $\tilde{s}$ are approximated by the second-order finite-differences (2.2.2). However special care must be taken with the boundary conditions in order to ensure accuracy of the computational scheme and full application of the boundary conditions.

For the symmetry conditions on $\zeta = 0$ $(i = 0)$ it is sufficient to apply second-order forward difference schemes for the derivative conditions such that the numerical boundary conditions are defined by

$$\begin{aligned} \frac{\bar{\zeta}'}{2\Delta\bar{\zeta}} [-3\tilde{v}_{0,j} + 4\tilde{v}_{1,j} - \tilde{v}_{2,j}] = 0, \quad \tilde{w}_{0,j} = 0, \\ \frac{\bar{\zeta}'}{2\Delta\bar{\zeta}} [-3\tilde{q}_{0,j} + 4\tilde{q}_{1,j} - \tilde{q}_{2,j}] = 0, \quad \tilde{s}_{0,j} = 0. \end{aligned} \tag{5.1.18}$$

For the plate boundary conditions on $\eta = 0$ $(j = 0)$ it is necessary to consider higher order schemes in order maintain accuracy. The boundary condition $\tilde{v}_\eta = 0$ is not applied directly but must differenced and applied within the $\tilde{q}$ condition. Using a

Lagrange interpolation involving the 'ghost' grid point $(i,-1)$ a one-sided difference approximation of $\tilde{v}_\eta = 0$ is given by

$$\frac{\bar{\eta}'}{24\Delta\bar{\eta}}\left[-6\tilde{v}_{i,-1} - 20\tilde{v}_{i,0} + 36\tilde{v}_{i,1} - 12\tilde{v}_{i,2} + 2\tilde{v}_{i,3}\right] = 0. \tag{5.1.19}$$

Since $\tilde{v}_{i,0} = 0$ this leads to the relation

$$\tilde{v}_{i,-1} = 6\tilde{v}_{i,1} - 2\tilde{v}_{i,2} + \frac{1}{3}\tilde{v}_{i,3}. \tag{5.1.20}$$

The second derivative $\tilde{v}_{\eta\eta}$ is then approximated by using the one-sided difference

$$\begin{aligned}\tilde{v}_{\eta\eta} &\approx \frac{\left(\bar{\eta}'\right)^2}{12\left(\Delta\bar{\eta}\right)^2}\left[11\tilde{v}_{i,-1} - 20\tilde{v}_{i,0} + 6\tilde{v}_{i,1} + 4\tilde{v}_{i,2} - \tilde{v}_{i,3}\right] + O\left(\left(\Delta\bar{\eta}\right)^4\right)\\ &= \frac{\left(\bar{\eta}'\right)^2}{18\left(\Delta\bar{\eta}\right)^2}\left[108\tilde{v}_{i,1} - 27\tilde{v}_{i,2} + 4\tilde{v}_{i,3}\right] + O\left(\left(\Delta\bar{\eta}\right)^4\right).\end{aligned} \tag{5.1.21}$$

This formula derived by Briley (1971) [8] leads to the numerical boundary conditions

$$\begin{aligned}\tilde{v}_{i,0} = 0, \quad \tilde{w}_{i,0} = 0,\\ \tilde{q}_{i,0} - \frac{i}{\hat{\alpha}Re_x^{\frac{1}{2}}}\frac{\bar{\eta}''}{\left(\Delta\bar{\eta}\right)^2}\left[6\tilde{v}_{i,1} - \frac{3}{2}\tilde{v}_{i,2} + \frac{2}{9}\tilde{v}_{i,3}\right] = 0,\\ \tilde{s}_{i,0} - \frac{i}{\hat{\alpha}Re_x^{\frac{1}{2}}}\left\{\frac{\left(\bar{\eta}'\right)^2}{\left(\Delta\bar{\eta}\right)^2}\left[-5\tilde{w}_{i,1} + 4\tilde{w}_{i,2} - \tilde{w}_{i,3}\right] + \frac{\bar{\eta}''}{\Delta\bar{\eta}}\left[4\tilde{w}_{i,1} - \tilde{w}_{i,2}\right]\right\} = 0,\end{aligned} \tag{5.1.22}$$

where standard forward-differences have been used for the approximation of $\tilde{w}_{\eta\eta}$.

The far-field conditions at $\eta = \eta_\infty$ $(j = M)$ are very similar to the plate conditions therefore the numerical approximations are given by

$$\begin{aligned}\tilde{v}_{i,M} = 0, \quad \tilde{w}_{i,M} = 0,\\ \tilde{q}_{i,M} - \frac{i}{\hat{\alpha}Re_x^{\frac{1}{2}}}\frac{\bar{\eta}''}{\left(\Delta\bar{\eta}\right)^2}\left[6\tilde{v}_{i,M-1} - \frac{3}{2}\tilde{v}_{i,M-2} + \frac{2}{9}\tilde{v}_{i,M-3}\right] = 0,\\ \tilde{s}_{i,M} - \frac{i}{\hat{\alpha}Re_x^{\frac{1}{2}}}\left\{\frac{\left(\bar{\eta}'\right)^2}{\left(\Delta\bar{\eta}\right)^2}\left[-5\tilde{w}_{i,M-1} + 4\tilde{w}_{i,M-2} - \tilde{w}_{i,M-3}\right]\right.\\ \left. + \frac{\bar{\eta}''}{\Delta\bar{\eta}}\left[-4\tilde{w}_{i,M-1} + \tilde{w}_{i,M-2}\right]\right\} = 0.\end{aligned} \tag{5.1.23}$$

Finally the numerical far-field conditions at $\zeta = \zeta_\infty$ $(i = N)$ are given by

$$\begin{aligned} \tilde{v}_{N,j} = 0, \quad \tilde{w}_{N,j} = 0, \\ \tilde{q}_{N,j} - \frac{i}{\hat{\alpha} Re_x^{\frac{1}{2}}} \left\{ \frac{\left(\bar{\zeta}'\right)^2}{\left(\Delta\bar{\zeta}\right)^2} \left[-5\tilde{v}_{N-1,j} + 4\tilde{v}_{N-2,j} - \tilde{v}_{N-3,j}\right] \right. \\ \left. + \frac{\bar{\zeta}''}{\Delta\bar{\zeta}} \left[-4\tilde{v}_{N-1,j} + \tilde{v}_{N-2,j}\right] \right\} = 0, \\ \tilde{s}_{N,j} - \frac{i}{\hat{\alpha} Re_x^{\frac{1}{2}}} \frac{\bar{\zeta}''}{\left(\Delta\bar{\zeta}\right)^2} \left[6\tilde{w}_{N-1,j} - \frac{3}{2}\tilde{w}_{N-2,j} + \frac{2}{9}\tilde{w}_{N-3,j}\right] = 0. \end{aligned} \tag{5.1.24}$$

All of the numerical approximations to the boundary conditions defined above are at least second-order accurate with the approximations due to Briley (1971) [8] in fact being fourth-order accurate.

Numerical results

The viscous stability equations (5.1.16) are solved for a given self-similar streak flow which is determined by the injection profile

$$\tilde{\Phi}_w(\hat{\zeta}) = -Ke^{-\hat{\zeta}^2}, \tag{5.1.25}$$

where K is the strength of the injection. The system (5.1.16) is solved numerically as a sparse generalised eigenvalue problem, the numerical scheme is discussed in more detail in section 5.2.2. Solving the self-similar streak flow equations (3.1.2) subject to the injection profile (5.1.25) gives a streamwise velocity $U(\eta, \zeta)$ which is required when solving (5.1.16) for a given wavenumber $\hat{\alpha}$ and local Reynolds number Re_x. The local Reynolds number is particularly important as the streak equations are only valid when Re_x is asymptotically large so the value of Re_x used in the numerical scheme must be sufficiently large to give a good approximation. The inviscid eigenvalue problem shall be commented on later in relation to why computation of the viscous form (5.1.16) is preferred.

Figure 5.1.1 shows the imaginary part of the wave speed $\hat{c}_i$ as a function of the self-similar wavenumber $\hat{\alpha}$ when (a) $\beta = 0$ and (b) $\beta = 0.5$ for various injection rates K with $Re_x = 5000^2$. The value of $\hat{c}_i$ is only shown for the most unstable eigenmode for any particular combination of $\hat{\alpha}$ and K. The value $Re_x = 5000^2$ is chosen because it is large enough to give a good approximation to the necessary large Re_x asymptotic limit.

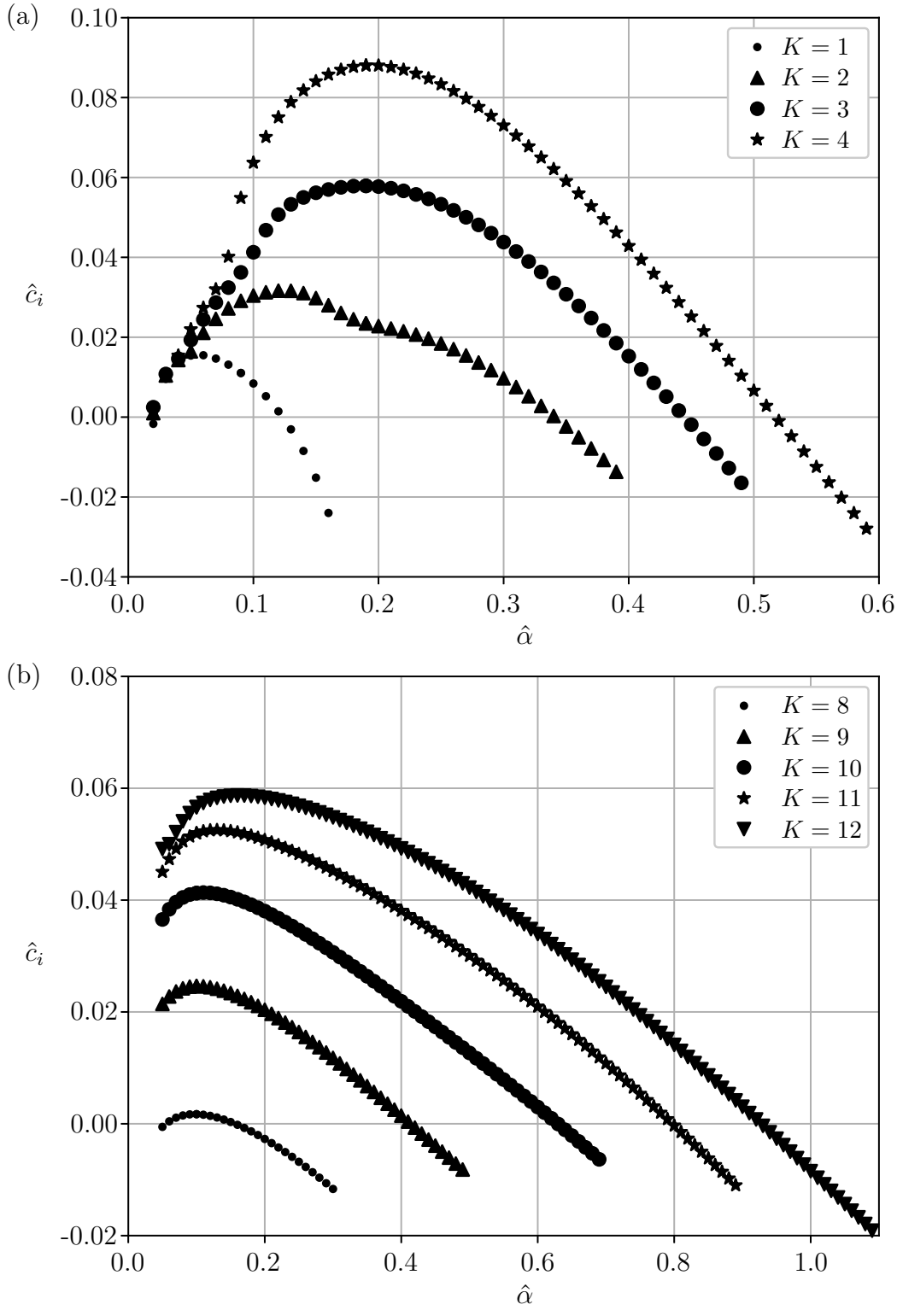

Figure 5.1.1: The imaginary part of the most unstable eigenvalue $\hat{c}_i$ is plotted against the wavenumber $\hat{\alpha}$ for $Re_x = 5000^2$. The self-similar streak flow is determined using the pressure gradient parameter (a) $\beta = 0$ and (b) $\beta = 0.5$ and the Gaussian injection profile (5.1.25) for various injection rates K.

When $\hat{c}_i > 0$ the corresponding eigenmode is temporally unstable; if K is sufficiently large there exists a range of $\hat{\alpha}$ over which there is at least one unstable mode for a particular value of β. When $\hat{\alpha} = 0$ the stability equations (5.1.16) become singular, so if $\hat{\alpha}$ is small the equations become nearly singular and the iterative numerical solver is unable to converge to a solution. As $\hat{\alpha} \to 0$ the wavelength of the travelling wave becomes large so the parallel flow assumption breaks down. If the wavelength becomes large it is necessary to consider downstream variations in the boundary layer, in particular the $\hat{U}_x$ term must be included.

Figure 5.1.2 shows the real and imaginary parts of the most unstable eigenvalue $\hat{c}$ as a function of the injection rate K for various wavenumbers $\hat{\alpha}$ with fixed local Reynolds number. As the wavenumber increases the injection rate required for the flow to become unstable, $\hat{c}_i > 0$, also increases. The value $\hat{c}_r$ indicates the wave speed of the most unstable mode; when the wavenumber is small increasing the injection rate causes the wave speed of the mode to increase monotonically. However for larger wavenumbers the increase is non-monotonic but still the wave speed becomes large when the injection rate is large.

Figures 5.1.1 and 5.1.2 only give a snapshot of a particular value of the local Reynolds number for illustrative purposes. Figure 5.1.3 shows $\hat{c}_i$ for various Re_x and $\hat{\alpha}$ with $K = 9$ and $\beta = 0.5$. As the local Reynolds number increases, the value of $\hat{c}_i$ increases, for a given $\hat{\alpha} = O(1)$, approaching a limiting value as $Re_x \to \infty$. When the local Reynolds number is relatively small the eigenmodes are more stable, as demonstrated by the small/negative values of $\hat{c}_i$ as $\hat{\alpha} \to 0$ when $Re_x = 1000^2$. However as the local Reynolds number becomes large, figure 5.1.3 shows that $\hat{c}_i$ approaches a positive value as $\hat{\alpha} \to 0$.

Figures 5.1.4 show contours of the normalised in-plane wave velocity for (a) $Re_x = 1000^2$ and (b) $Re_x = 20000^2$. It is clear that the main extent of the in-plane wave velocity perturbation is confined to a small region which follows the curvature of the streak flow $U(\eta, \zeta)$. The unstable eigenmode is concentrated in an increasingly thin layer as the local Reynolds number increases. The magnitude of the in-plane wave velocity is not indicated by figure 5.1.4, as the eigenfunctions are normalised, but the structure is clearly evident.

This brief examination of the viscous stability of the short-scale injection streak

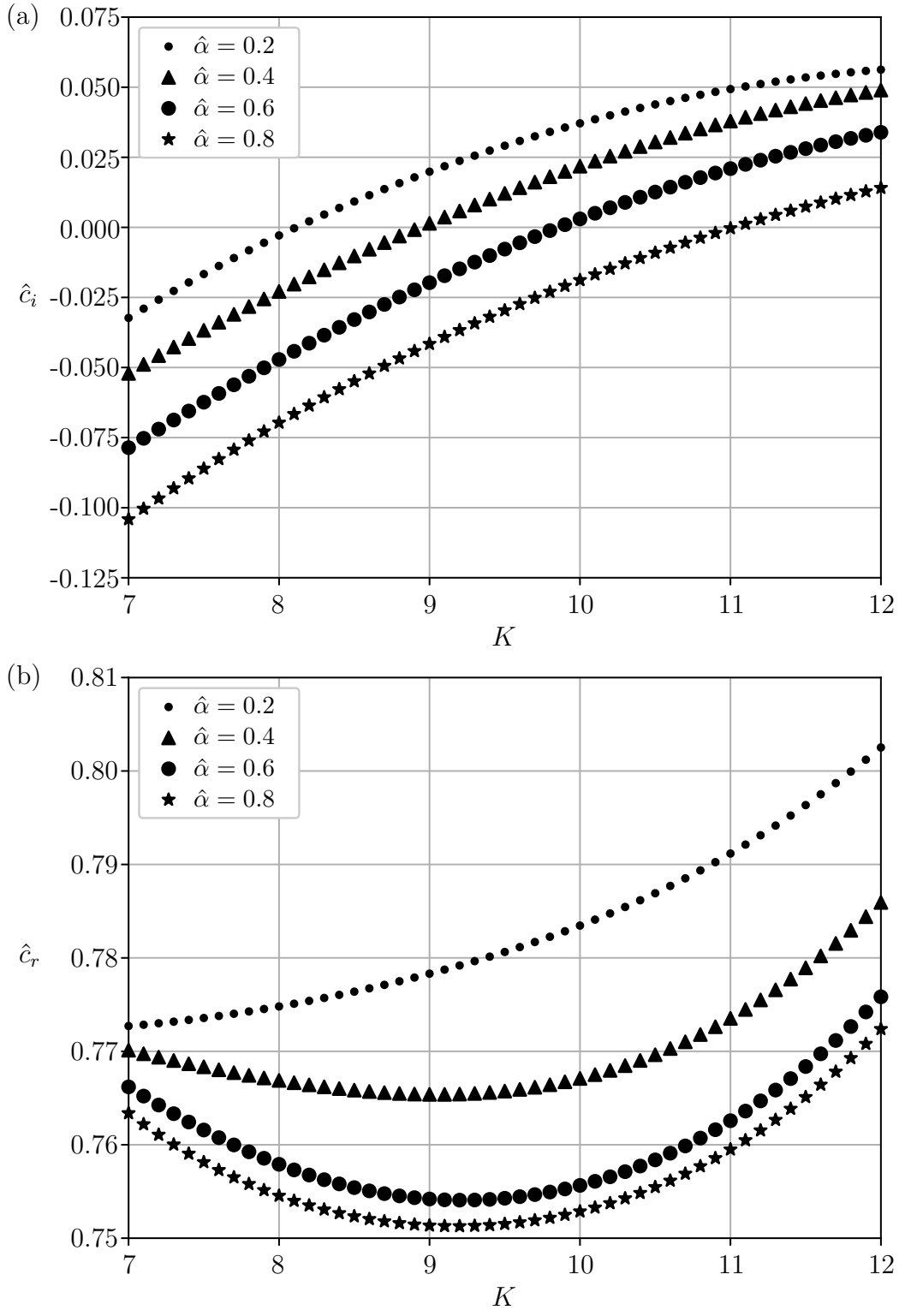

Figure 5.1.2: The most unstable eigenvalue $\hat{c}$ is plotted against the injection rate K for various wavenumbers $\hat{\alpha}$, $\beta = 0.5$ and $Re_x = 5000^2$. The most unstable eigenvalue is split into (a) imaginary $\hat{c}_i$ and (b) real $\hat{c}_r$ parts.

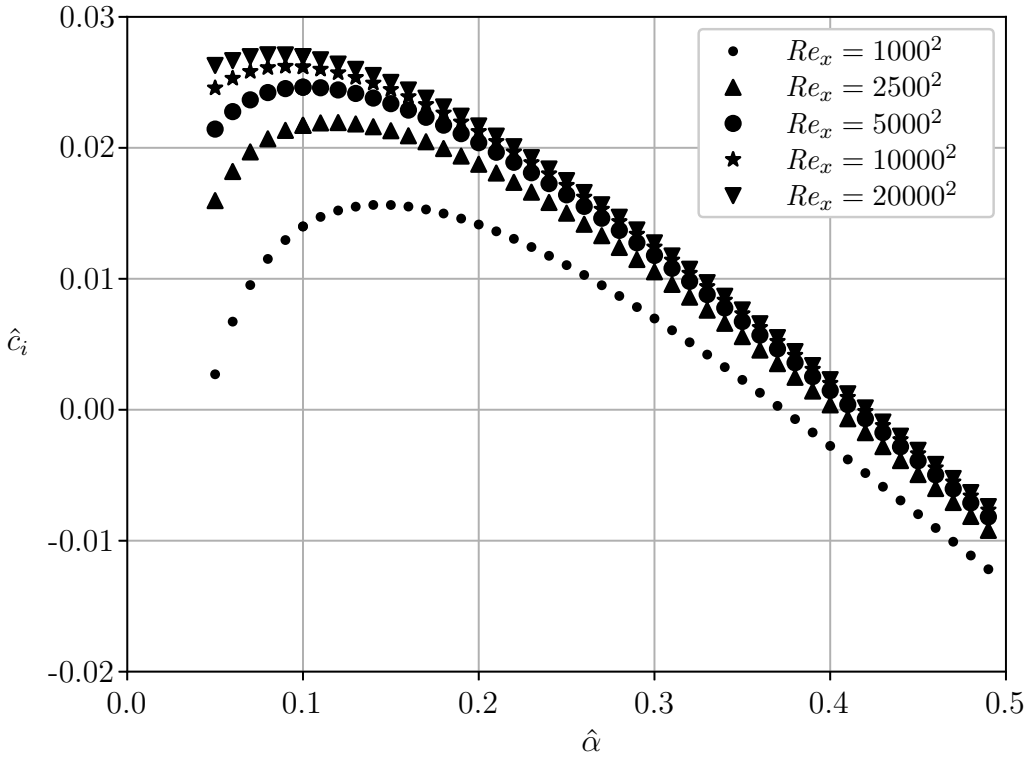

Figure 5.1.3: The imaginary part of the most unstable eigenvalue $\hat{c}_i$ is plotted against the wavenumber $\hat{\alpha}$ for various values of the local Reynolds number Re_x. The self-similar streak flow is determined using the pressure gradient parameter $\beta = 0.5$ and the Gaussian injection profile (5.1.25) with injection rate $K = 9$.

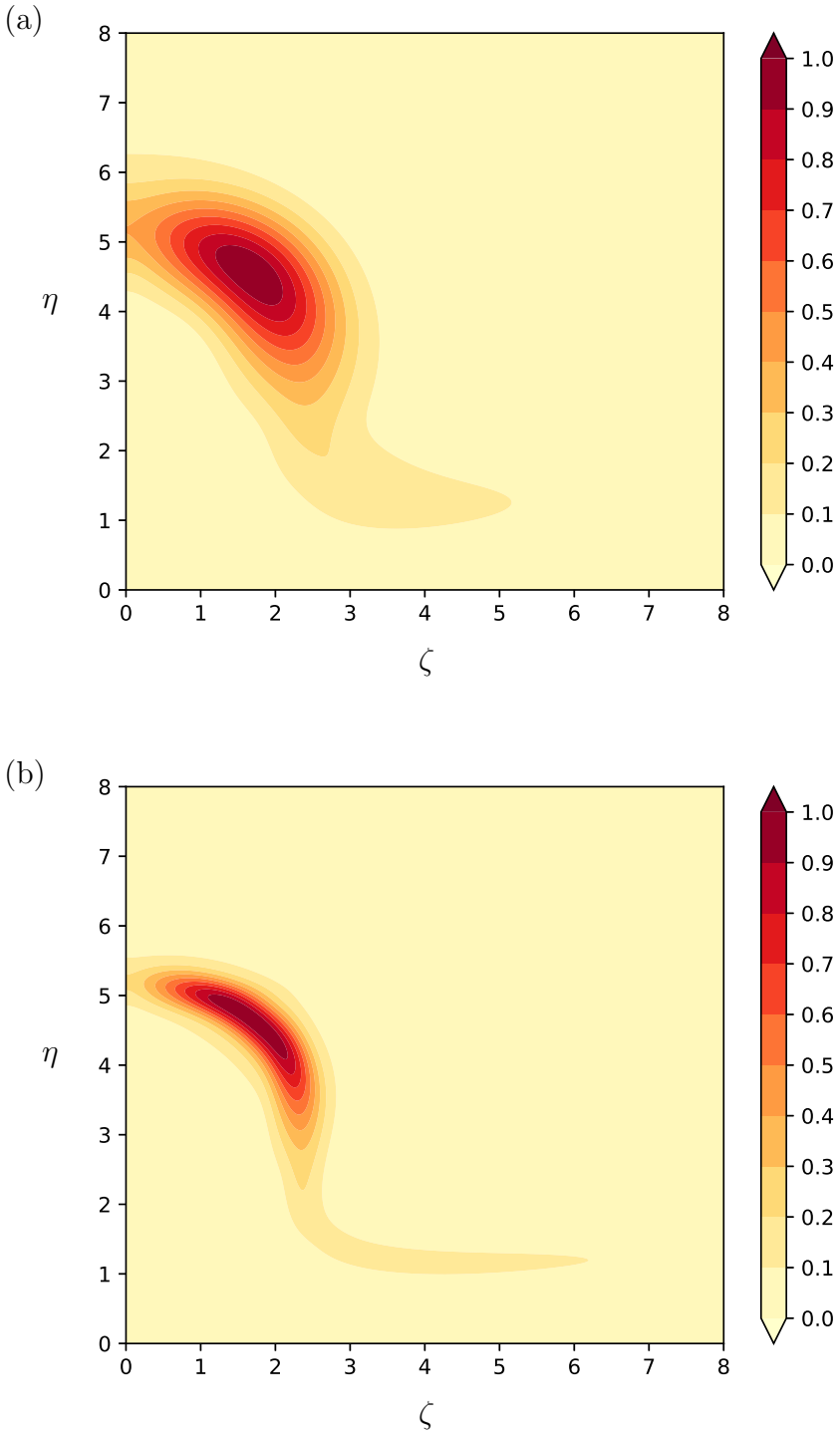

Figure 5.1.4: The solution of (5.1.16) with $\beta = 0.5$, $\hat{\alpha} = 0.23$ and $K = 9$ yields contours of the normalised in-plane velocity $\sqrt{|\tilde{v}|^2 + |\tilde{w}|^2}$ for (a) $Re_x = 1000^2$ and (b) $Re_x = 20000^2$.

flow has given some indication of how a small travelling wave disturbance behaves as it progresses downstream along the streak. The viscous stability analysis presented above is not strictly valid however since the streak flow equations are derived by taking the limit $Re_x \to \infty$. In order for the stability equations to be asymptotically sensible it is necessary to maintain this reasoning thereby reducing the stability equations to their inviscid form.

5.2 Inviscid limit

Here the Reynolds number is taken to be large and the wavelength of the disturbances are fixed on the boundary-layer scale. A steady flow described by (5.0.5) has an inviscid travelling wave, which is periodic in the downstream direction with wavenumber α, superimposed upon it. The limit of (5.1.9) as $Re_x \to \infty$ could be analysed instead but it is simpler to revert to the inviscid form of (5.1.5). The wave component of the flow is characterised by a time-scale, for any disturbances, which is of the same order as that of the streamwise flow and a rapid oscillation on a downstream length scale which is comparable to the boundary-layer thickness. It is well known that inviscid disturbances vary in the streamwise direction on the lengthscale $Re^{-1/2}L^*$ so that their wavelength is comparable with the boundary-layer thickness.

The basic state is perturbed, with an inviscid wave, by writing

$$u = \hat{U} + \epsilon\left(\sigma(x)\tilde{u}(x,Y,Z)E + \text{c.c.}\right) + \ldots, \tag{5.2.1a}$$

$$v = Re^{-\frac{1}{2}}\hat{V} + \epsilon\left(\sigma(x)\tilde{v}(x,Y,Z)E + \text{c.c.}\right) + \ldots, \tag{5.2.1b}$$

$$w = Re^{-\frac{1}{2}}\hat{W} + \epsilon\left(\sigma(x)\tilde{w}(x,Y,Z)E + \text{c.c.}\right) + \ldots, \tag{5.2.1c}$$

where $E = e^{iRe^{\frac{1}{2}}\theta(x,t)}$ and ϵ is a Reynolds number scaling which is taken to be sufficiently small (i.e. $\epsilon = Re^{-7/12}$ [9]) so that linearisation is a valid procedure [31]. The pressure field, with the added wave perturbation, is taken to be of the form

$$p = -\frac{1}{2}U_e^2(x) + Re^{-\frac{1}{2}}p(x) + Re^{-1}\hat{P} + \epsilon\left(\sigma(x)\tilde{p}(x,Y,Z)E + \text{c.c.}\right) + \ldots. \tag{5.2.1d}$$

The scaling factor ϵ is determined by the solution in the critical layer which occurs in a region near to where the wave speed becomes equal to streamwise streak velocity.

Substituting (5.2.1) into the time dependent equations (5.0.3) the boundary-region equations (5.0.5) are recovered at leading order. Then at order ϵ, in the limit $Re \to \infty$,

the inviscid linearised equations are given by

$$i\alpha\tilde{u} + \tilde{v}_Y + \tilde{w}_Z = 0, \tag{5.2.2a}$$

$$i\alpha\left(\hat{U} - c\right)\tilde{u} + \hat{U}_Y\tilde{v} + \hat{U}_Z\tilde{w} = -i\alpha\tilde{p}, \tag{5.2.2b}$$

$$i\alpha\left(\hat{U} - c\right)\tilde{v} = -\tilde{p}_Y, \tag{5.2.2c}$$

$$i\alpha\left(\hat{U} - c\right)\tilde{w} = -\tilde{p}_Z, \tag{5.2.2d}$$

with the condition $\tilde{v} = 0$ at $Y = 0, \infty$. Taking the Y derivative of (5.2.2c) and the Z derivative of (5.2.2d) and using (5.2.2a) gives

$$i\alpha\tilde{u} = \frac{1}{\hat{U} - c}\left(\frac{1}{i\alpha}\tilde{p}_{YY} + \hat{U}_Y\tilde{v} + \frac{1}{i\alpha}\tilde{p}_{ZZ} + \hat{U}_Z\tilde{w}\right). \tag{5.2.3}$$

So substituting into (5.2.2b) yields

$$\frac{1}{i\alpha}\left(\tilde{p}_{YY} + \tilde{p}_{ZZ}\right) + 2\hat{U}_Y\tilde{v} + 2\hat{U}_Z\tilde{w} = -i\alpha\tilde{p}. \tag{5.2.4}$$

Multiplying (5.2.4) by $i\alpha$, using (5.2.2c) and (5.2.2d), gives the Hall & Horseman (1991) [31] pressure Rayleigh equation

$$\tilde{p}_{YY} + \tilde{p}_{ZZ} - \alpha^2\tilde{p} - \frac{2\hat{U}_Y\tilde{p}_Y}{\hat{U} - c} - \frac{2\hat{U}_Z\tilde{p}_Z}{\hat{U} - c} = 0, \tag{5.2.5}$$

which has boundary conditions $\tilde{p}_Y = 0$ on $Y = 0$ and $\tilde{p} \to 0$ as $Y \to \infty$. This equation generalises the pressure form of the Rayleigh equation governing the linear stability of a single variable unidirectional flow [32].

If the wave speed is real ($c_i = 0$) a critical layer occurs at $Y = f(x, Z)$ where the streak velocity $\hat{U}$ is equal to the wave speed c. In this layer the inviscid equations (5.2.2) and (5.2.5) become singular so viscous effects must be taken into account in order to remove the singularities.

The expansion of $\hat{U}$ near to the critical layer ($Y \to f(x, Z)$) is

$$\hat{U} = \hat{U}(x, f(x, Z), Z) + \left.\frac{\partial\hat{U}}{\partial Y}\right|_{Y=f(x,Z)}(Y - f(x, Z)) + \ldots. \tag{5.2.6}$$

Therefore since $\hat{U}(x, f(x, Z), Z) = c$ it follows that

$$\hat{U} - c = \lambda(x, Z)\left(Y - f(x, Z)\right) + O\left(\left(Y - f(x, Z)\right)^2\right), \tag{5.2.7}$$

where $\lambda(x, Z)$ is the transverse shear stress at the critical level. Substituting (5.2.7) into the inviscid equations (5.2.2) suggests that $\tilde{u}, \tilde{v}, \tilde{w} \sim \left(Y - f(x, Z)\right)^{-1}$ as $Y \to f(x, Z)$ as shown by Hall & Smith (1991) [33].

In order to find the appropriate critical level scaling a critical layer variable $\bar{Y}$ is defined such that

$$Y - f(x, Z) = Re^{-\gamma}\bar{Y}, \tag{5.2.8}$$

where γ is a constant which is to be determined. Using the streamwise momentum equation (5.0.3b) it is evident that in the critical layer the wave is governed by

$$\begin{aligned} Re^{\frac{1}{2}-\gamma} i\alpha\lambda(x,Z)\bar{Y}\tilde{u} + Re^{\frac{1}{2}}\hat{U}_Y\tilde{v} + Re^{\frac{1}{2}}\hat{U}_Z\tilde{w} + \hat{U}_x\tilde{u} + \hat{U}\tilde{u}_x + Re^{\gamma}\hat{V}\tilde{u}_{\bar{Y}} \\ + \hat{W}\tilde{u}_Z = -i\alpha Re^{\frac{1}{2}}\tilde{p} - \tilde{p}_x + O(Re^{-1}) + Re^{2\gamma}\tilde{u}_{\bar{Y}\bar{Y}} + \tilde{u}_{ZZ}. \end{aligned} \tag{5.2.9}$$

Taking a dominant balance suggests that $Re^{\frac{1}{2}-\gamma} \sim Re^{2\gamma}$ which implies that $\gamma = 1/6$. So the width of the critical layer is $O(Re^{-1/6})$ as predicted by Brown et al. (1993) [9].

The critical layer occurs when $\hat{U} - c = 0$, so if the flow is of Falkner-Skan type then $\hat{U} \sim x^n$ and $c = \Omega/\alpha$. If the flow is self-similar then the problem may be reduced. For the terms in the pressure equation (5.2.5) to be of the same size downstream it is required that $\tilde{p}_{YY} \sim \tilde{p}_{ZZ} \sim \alpha^2\tilde{p} \sim \hat{U}_Y\tilde{p}_Y/(\hat{U} - c) \sim \hat{U}_Z\tilde{p}_Z/(\hat{U} - c)$ therefore it follows that $\alpha^2 \sim x^{n-1}$. However for a constant frequency wave to exist it is required that $\alpha^2 \sim x^{-2n}$, since $c \sim x^n$, therefore $x^{n-1} \sim x^{-2n}$ which means that $n = 1/3$ (right angle wedge $\beta = 1/2$) therefore $\alpha \sim x^{-1/3}$. Using this value of the pressure gradient parameter means that it is possible to find a solution to the eigenvalue problem that is valid for all downstream locations. If instead a general value for the pressure gradient parameter is chosen a specific downstream location x at which to solve the two-dimensional Rayleigh equation (5.2.5) must be chosen. Changing the value of x will alter the location of the critical layer and the associated eigenvalues as doing so would effectively alter the wavenumber α.

The pressure equation (5.2.5) may be transformed using the similarity variables η and ζ defined by (5.1.12). Since the flow is of Falkner-Skan type $\hat{U}(x, Y, Z) = x^n U(\zeta, \eta)$ then the pressure equation becomes

$$\tilde{p}_{\eta\eta} + \tilde{p}_{\zeta\zeta} - \hat{\alpha}^2\tilde{p} - \frac{2U_\eta\tilde{p}_\eta}{U - \hat{c}} - \frac{2U_\zeta\tilde{p}_\zeta}{U - \hat{c}} = 0, \tag{5.2.10}$$

where $\hat{\alpha} = \sqrt{2x^{1-n}/(n+1)}\alpha$ and $\hat{c} = x^{-n}\Omega/\alpha$. This equation can also be written in the form

$$\frac{\partial}{\partial\eta}\left(\frac{\tilde{p}_\eta}{(U - \hat{c})^2}\right) + \frac{\partial}{\partial\zeta}\left(\frac{\tilde{p}_\zeta}{(U - \hat{c})^2}\right) - \frac{\hat{\alpha}^2\tilde{p}}{(U - \hat{c})^2} = 0. \tag{5.2.11}$$

This specifies an eigenvalue problem for the complex wave speed c or $\hat{c}$ for a given velocity field and wavenumber. Equilibrium solutions are sought where the waves do not grow therefore the wave speed c must be entirely real. If c is complex the interaction of the waves would cause the vortex to grow or decay in the downstream direction at a faster rate than the waves. This means that there are only a finite number of pairs (α, c) or $(\hat{\alpha}, \hat{c})$ which are acceptable for a given streak velocity $\hat{U}$ or U [32].

The linearised inviscid stability equations (5.2.2) may also be writen in self-similar form as

$$i\hat{\alpha}\tilde{u} + \tilde{v}_\eta + \tilde{w}_\zeta = 0, \tag{5.2.12a}$$

$$i\hat{\alpha}\,(U - \hat{c})\,\tilde{u} + U_\eta \tilde{v} + U_\zeta \tilde{w} = -\,i\hat{\alpha}\tilde{p}, \tag{5.2.12b}$$

$$i\hat{\alpha}\,(U - \hat{c})\,\tilde{v} = -\,\tilde{p}_\eta, \tag{5.2.12c}$$

$$i\hat{\alpha}\,(U - \hat{c})\,\tilde{w} = -\,\tilde{p}_\zeta. \tag{5.2.12d}$$

In the above $(\tilde{u}(x, Y, Z), \tilde{v}(x, Y, Z), \tilde{w}(x, Y, Z)) = (\tilde{u}(\zeta, \eta), \tilde{v}(\zeta, \eta), \tilde{w}(\zeta, \eta))$ and the wave pressure $\tilde{p}(x, Y, Z) = x^n \tilde{p}(\zeta, \eta)$. The same notation has been retained in order to avoid excessive switching but it must be observed that the scaled Cartesian wave pressure $\tilde{p}(x, Y, Z)$ grows as the flow progresses downstream.

The singular nature of the inviscid stability equations at the critical level requires that a different approach be taken in this region when considering an interaction between the streak and the wave. However since, at the moment, only the stability of the underlying flow is being considered, and not any reciprocal interactions, the required approach near the critical layer is discussed merely for completeness. It is possible to consider an interaction between the streak and the wave but this scenario will not be examined in this chapter.

5.2.1 Critical layer interaction

In the neighbourhood of the critical level defined by $Y = f(x, Z)$, at which $\hat{U} = c$, the linking between the vortex equations (5.0.5) and Rayleigh's pressure equation (5.2.5) governing the wave is crucial. As the critical layer is approached $\tilde{u}$, $\tilde{v}$ and $\tilde{w}$ all behave like $(Y - f)^{-1}$ but the pressure $\tilde{p}$ is non-singular and remains $O(1)$. Consideration of the forms of (5.2.1) upon approaching the critical level suggests appropriate expansions

in terms of inverse powers of the Reynolds number which can be used to derive relevant jump conditions (see Appendix A of Brown et al. (1993) [9] for details)

It is required that $\hat{U}$, $\hat{V}$, $\hat{W}$, $\hat{U}_Y$ and $\hat{U}_{YY}$ are continuous at the critical level. However the shear stresses in the Y and Z directions are discontinuous at $Y = f(x, Z)$ providing the jump conditions

$$\left[\hat{W}_Y\right]_-^+ = J(x, Z) = \frac{1}{f_Z}\left[\hat{V}_Y\right]_-^+, \tag{5.2.13a}$$

where

$$J(x, Z) = \frac{2\pi\left(\frac{2}{3}\right)^{2/3}\Gamma\left(\frac{1}{3}\right)}{\Delta^5 a^{5/3}}\sigma^2\left\{\left(-\frac{7\Delta_Z}{2\Delta} - \frac{5a_Z}{3a}\right)\left|\frac{\partial\tilde{p}}{\partial Z}\right|^2 + \frac{\partial}{\partial Z}\left(\left|\frac{\partial\tilde{p}}{\partial Z}\right|^2\right)\right\}. \tag{5.2.13b}$$

In the above $\Delta = 1 + f_Z^2$, $a = \lambda\alpha/\Delta$ where $\lambda(x, Z)$ is the unknown transverse shear stress at the critical level and $\Gamma(1/3) \approx 2.68$ is the Gamma function evaluated at $1/3$. The jump in the shear stress is related to the spanwise derivatives of the wave pressure [9]. The pressure function $\hat{P}$ is also discontinuous at the critical surface and the jump condition for the pressure function is given by

$$\left[\hat{P}\right]_-^+ = -\frac{2\pi\left(\frac{2}{3}\right)^{2/3}\Gamma\left(\frac{1}{3}\right)}{\Delta^5 a^{5/3}}\sigma^2 f_{ZZ}\left|\frac{\partial\tilde{p}}{\partial Z}\right|^2. \tag{5.2.14}$$

In the jump conditions (5.2.13) and (5.2.14) the $+$ and $-$ signs denote the values of the prescribed quantity above and below the critical layer respectively.

Due to the introduction of an inviscid travelling wave a critical level $Y = f(x, Z)$ is created at which the velocity field $(\hat{U}, \hat{V}, \hat{W})$ is continuous but $\hat{V}_Y, \hat{W}_Y$ and $\hat{P}$ must satisfy the jump conditions (5.2.13) and (5.2.14). These jump conditions are determined by the wave pressure $\tilde{p}$ which is found from evaluating the two-dimensional Rayleigh pressure equation (5.2.5) on the critical level. However (5.2.5) is non-linearly dependent upon the streak flow so the streak-vortex equations (5.0.5), jump conditions (5.2.13) and (5.2.14) and wave pressure equation (5.2.5) are inextricably linked to one another and hence must be solved in unison when considering an interaction between the wave and the streak-vortex flow.

The derived jump conditions are only relevant when considering how the interaction with the wave disturbance alters the streak-vortex flow but they are not necessary if only the stability of the flow is being considered. The self-similar two-dimensional Rayleigh pressure equation (5.2.10) is sufficient to study the inviscid linear stability of

any self-similar flow characterised by the streamwise velocity component $U(\zeta, \eta)$. It is necessary to develop a numerical scheme for solving the two-dimensional Rayleigh equation.

5.2.2 Two-dimensional Rayleigh equation

The two-dimensional generalisation of Rayleigh's stability equation in pressure form (5.2.5) first derived by Hall & Horseman (1991) [31] may be rewritten in self-similar form as

$$(U - \hat{c})\left(\tilde{p}_{\eta\eta} + \tilde{p}_{\zeta\zeta} - \hat{\alpha}^2\tilde{p}\right) - 2U_\eta\tilde{p}_\eta - 2U_\zeta\tilde{p}_\zeta = 0. \tag{5.2.15}$$

This equation must be solved subject to the boundary conditions

$$\tilde{p}_\zeta = 0 \quad \text{on} \quad \zeta = 0, \qquad \tilde{p}_\eta = 0 \quad \text{on} \quad \eta = 0, \qquad \tilde{p} \to 0 \quad \text{as} \quad \zeta, \eta \to \infty. \tag{5.2.16}$$

For numerical convenience a Robin condition may be used at the large η boundary in the form

$$\tilde{p}_\eta + \hat{\alpha}\tilde{p} = 0 \quad \text{as} \quad \eta \to \infty. \tag{5.2.17}$$

Using a Robin condition ensures a smooth transition from the interior of the domain to the boundary; using a Dirichlet condition on a truncated computational domain often causes a non-smooth transition at the boundary.

It is assumed that the streamwise velocity component U and its derivatives are known throughout the cross-sectional (ζ, η) domain. This is an eigenvalue problem for the unknown complex wave speed $\hat{c}$ given a specified wave number $\hat{\alpha}$ which shall be solved numerically.

Numerical scheme

Rescaling (5.2.15) based on the short scale feature width ζ_0 gives the eigenvalue problem

$$U\left(\tilde{p}_{\eta\eta} + \frac{1}{\zeta_0^2}\tilde{p}_{\hat{\zeta}\hat{\zeta}} - \hat{\alpha}^2\tilde{p}\right) - 2U_\eta\tilde{p}_\eta - \frac{2}{\zeta_0^2}U_{\hat{\zeta}}\tilde{p}_{\hat{\zeta}} = \hat{c}\left(\tilde{p}_{\eta\eta} + \frac{1}{\zeta_0^2}\tilde{p}_{\hat{\zeta}\hat{\zeta}} - \hat{\alpha}^2\tilde{p}\right), \tag{5.2.18}$$

where $\hat{\zeta} = \zeta/\zeta_0$. The equation is solved on a grid which is uniform in the stretched coordinates $(\bar{\zeta}(\hat{\zeta}), \bar{\eta}(\eta))$. The discretisation of the pressure $\tilde{p}$ at given grid point $(\bar{\zeta}_i, \bar{\eta}_j)$

is $\tilde{p}_{i,j}$ and the relevant derivatives in equation (5.2.18) are approximated by the central differences

$$\tilde{p}_{\hat{\zeta}} = \bar{\zeta}' \left(\frac{\tilde{p}_{i+1,j} - \tilde{p}_{i-1,j}}{2\left(\Delta\bar{\zeta}\right)} \right), \tag{5.2.19a}$$

$$\tilde{p}_{\eta} = \bar{\eta}' \left(\frac{\tilde{p}_{i,j+1} - \tilde{p}_{i,j-1}}{2\left(\Delta\bar{\eta}\right)} \right), \tag{5.2.19b}$$

$$\tilde{p}_{\hat{\zeta}\hat{\zeta}} = \bar{\zeta}'' \left(\frac{\tilde{p}_{i+1,j} - \tilde{p}_{i-1,j}}{2\left(\Delta\bar{\zeta}\right)} \right) + \left(\bar{\zeta}'\right)^2 \left(\frac{\tilde{p}_{i+1,j} - 2\tilde{p}_{i,j} + \tilde{p}_{i-1,j}}{\left(\Delta\bar{\zeta}\right)^2} \right), \tag{5.2.19c}$$

$$\tilde{p}_{\eta\eta} = \bar{\eta}'' \left(\frac{\tilde{p}_{i,j+1} - \tilde{p}_{i,j-1}}{2\left(\Delta\bar{\eta}\right)} \right) + \left(\bar{\eta}'\right)^2 \left(\frac{\tilde{p}_{i,j+1} - 2\tilde{p}_{i,j} + \tilde{p}_{i,j-1}}{\left(\Delta\bar{\eta}\right)^2} \right), \tag{5.2.19d}$$

where $\Delta\bar{\zeta}$ and $\Delta\bar{\eta}$ are the grid spacings in the $\bar{\zeta}$ and $\bar{\eta}$ directions respectively. This scheme is not valid at the boundaries of the domain so a different discretisation must be imposed. At $\bar{\zeta} = \bar{\zeta}(0)$ the required condition is $\tilde{p}_{\bar{\zeta}} = 0$ which is discretised as

$$\frac{-3\tilde{p}_{i,j} + 4\tilde{p}_{i+1,j} - \tilde{p}_{i+2,j}}{2\left(\Delta\bar{\zeta}\right)} = 0 \quad \text{where} \quad i = 0. \tag{5.2.20a}$$

Then at $\bar{\eta} = \bar{\eta}(0)$ the boundary condition is $\tilde{p}_{\bar{\eta}} = 0$ which is discretised as

$$\frac{-3\tilde{p}_{i,j} + 4\tilde{p}_{i,j+1} - \tilde{p}_{i,j+2}}{2\left(\Delta\bar{\eta}\right)} = 0 \quad \text{where} \quad j = 0. \tag{5.2.20b}$$

Finally in the far-field at $\bar{\zeta} = \bar{\zeta}(\zeta_\infty)$ and $\bar{\eta} = \bar{\eta}(\eta_\infty)$ it is required that $\tilde{p} = 0$ which is simply discretised as $\tilde{p}_{i,j} = 0$.

The above discretisation leads to a generalised eigenvalue problem of the form $A\tilde{p} = \hat{c}B\tilde{p}$ where A and B are sparsely filled matrices and the complex wave speed $\hat{c}$ is the eigenvalue which is to be determined. There are a number of numerical techniques which have been developed to solve eigenvalue problems, it is therefore necessary to choose a method which is appropriate to a given scenario.

For matrices which are large and sparse, as is the case here, it is most efficient to use numerical methods which preserve this sparsity when solving the eigenvalue problem. Sparsity preserving methods obtain the solution from the information generated by applying a simple function of the matrices A and B to various vectors so that the sparse matrices are only used in matrix-vector products. Maintaining sparsity in this manner greatly reduces the computational cost of solving the eigenvalue problem.

From the full spectrum of solutions of the discretised problem only a few eigenpairs $(\hat{c}, \tilde{p})$ are of any practical relevance. Eigenvalues are sought within a specified region of

the complex plane so iterative methods, which seek specific eigenvalues, are very useful. Here the Krylov-Schur method [64], implemented in SLEPc [34], is used. This is a projection method intended for computing a small number of the possible eigenpairs. The most unstable, or the least stable, eigenvalues are sought.

In order to ensure the accuracy of the numerical scheme for calculating eigenvalues it is necessary to use a large number of nodes. The computational parameters for the results presented below are $\hat{\zeta}_\infty = \eta_\infty = 32$ and $N_{\hat{\zeta}} = N_\eta = 601$ with $\zeta_0 = 1$. For the two-dimensional Rayleigh equation (5.2.15) to be self-similar it is necessary that $\beta = 1/2$ or that the downstream location be fixed, for example setting $\beta = 0$ at $x = 1/2$ retains self-similarity. The iterative scheme used for finding eigenvalues and eigenfunctions, for a specified streak flow, requires an approximate target value in order to converge to a solution. The target value, which approximates $\hat{c}$, is specified using previous knowledge of the eigenvalues for various streamwise velocity profiles $U(\eta, \zeta)$ and by manual searching. The results presented below give an indication of solutions to the eigenvalue problem but are by no means exhaustive as only a limited range of parameters are used.

Numerical results

For the self-similar streak flow, which gives the streamwise velocity component $U(\eta, \zeta)$, the injection function

$$\tilde{\Phi}_w(\hat{\zeta}) = -Ke^{-\hat{\zeta}^2} \tag{5.2.21}$$

is used, where ζ_0 is the width of the injection and K is the strength of the injection. Here $\tilde{\Phi}_w = \Phi_w(\zeta) - \Phi_{Bw}$ where Φ_{Bw} is a base flow transpiration which is taken to be zero. Solving the self-similar streak flow equations (3.1.2) subject to the injection profile (5.2.21) gives a streamwise velocity $U(\eta, \zeta)$ which is required when solving (5.2.18) for a given wavenumber $\hat{\alpha}$.

The stability equation (5.2.15) is solved numerically for a given self-similar streak flow which is determined by the injection profile (5.2.21) and the pressure gradient parameter β. Figure 5.2.1 shows the imaginary part of the wave speed $\hat{c}_i$ as a function of the self-similar wavenumber $\hat{\alpha}$ when (a) $\beta = 0$ $(x = 0.5)$ and (b) $\beta = 0.5$ for various injection rates. The value of $\hat{c}_i$ is only shown for the most unstable eigenmode for

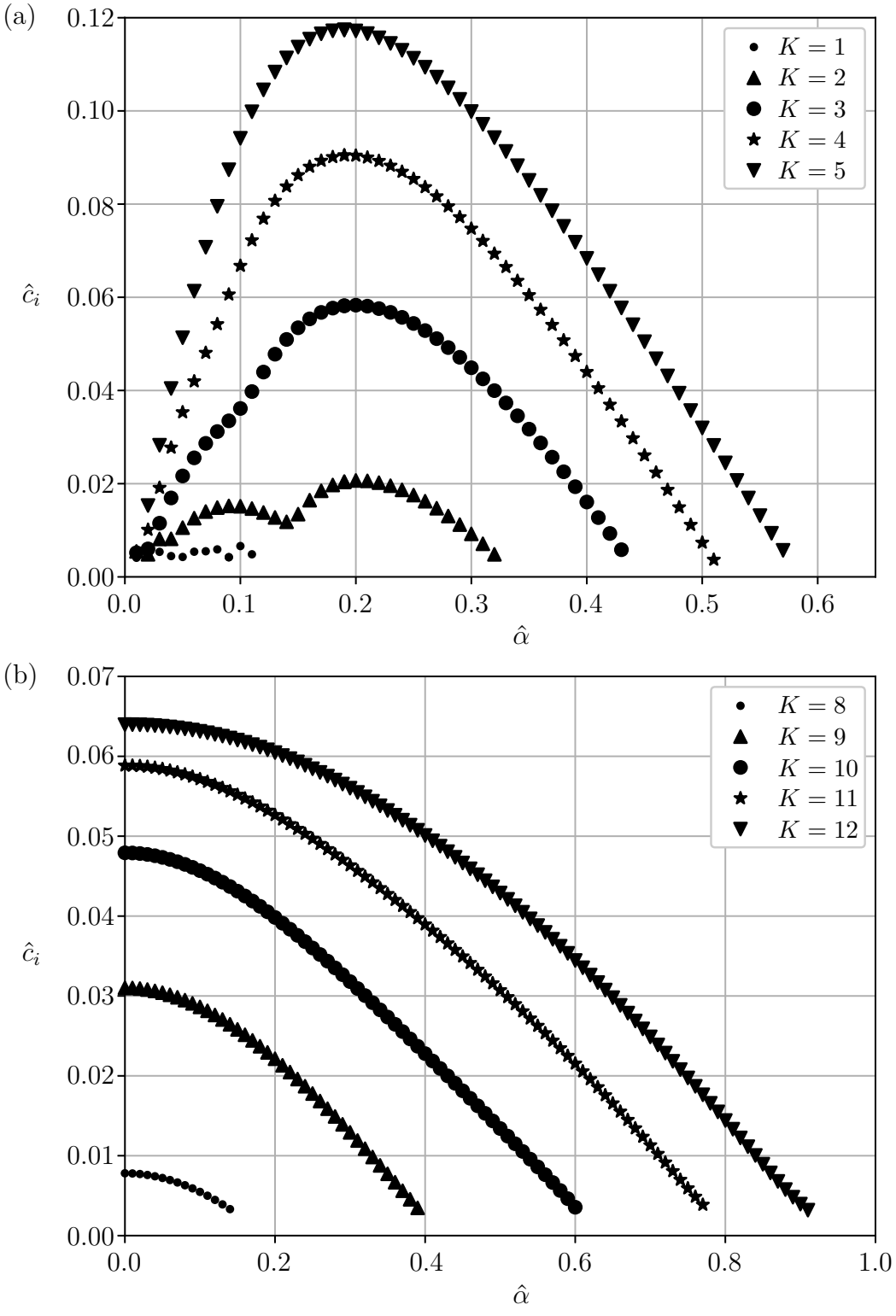

Figure 5.2.1: The imaginary part of the most unstable eigenvalue $\hat{c}_i$ is plotted against the wavenumber $\hat{\alpha}$. The self-similar streak flow is determined using the pressure gradient parameter (*a*) $\beta = 0$ ($x = 0.5$) and (*b*) $\beta = 0.5$ and the Gaussian injection profile (5.2.21) for various injection rates K.

$\beta = 0$			$\beta = 0.5$		
K	$\hat{\alpha}_{max}$	$\hat{\alpha}_{max}\hat{c}_i$	K	$\hat{\alpha}_{max}$	$\hat{\alpha}_{max}\hat{c}_i$
1	0.10	6.6×10^{-4}	8	0.11	5.5×10^{-4}
2	0.23	4.5×10^{-3}	9	0.23	4.5×10^{-3}
3	0.27	1.4×10^{-2}	10	0.33	9.6×10^{-3}
4	0.30	2.2×10^{-2}	11	0.44	1.6×10^{-2}
5	0.32	3.0×10^{-2}	12	0.52	2.1×10^{-2}

Table 5.1: Wavenumber of the fastest growing mode $\hat{\alpha}_{max}$ and the corresponding growth rate $\hat{\alpha}_{max}\hat{c}_i$ for given β and K.

any particular combination of $\hat{\alpha}$ and K. When $\hat{c}_i = 0$ the inviscid stability equation (5.2.15) becomes singular, it is therefore necessary to specify a small value which is used to approximate $\hat{c}_i = 0$. Here the cut-off value for $\hat{c}_i \approx 0$ is set as $\hat{c}_i = \delta = 3\times10^{-3}$. In order to check that this value of δ does not significantly impact the results $\delta/2$ has also been used to check convergence of the solution.

Unstable modes, with $\hat{c}_i > 0$, occur between $\hat{\alpha} = 0$ and some critical value $\hat{\alpha} = \hat{\alpha}_c$ which is determined by the strength of the injection. When $\beta = 0$ and $\hat{\alpha}$ is small $\hat{c}_i$ is also small and the most unstable mode has a very small growth rate. On the other hand when $\beta = 0.5$ and $\hat{\alpha} = 0$ (long wavelength limit) there is at least one unstable mode provided that K is sufficiently large. Table 5.1 shows the wavenumber and growth rate of the fastest growing mode for $\beta = 0, 0.5$ and various values of K.

The solution of the eigenvalue problem (5.2.15) provides the wave speed $\hat{c}$ along with the wave pressure eigenfunction $\tilde{p}$. From the self-similar stability equations (5.2.12) the wave velocities $\tilde{u}, \tilde{v}$ and $\tilde{w}$ may be determined, from $\tilde{p}$, using the relations

$$\tilde{v} = \frac{i}{\hat{\alpha}(U-\hat{c})}\tilde{p}_\eta \tag{5.2.22a}$$

$$\tilde{w} = \frac{i}{\hat{\alpha}(U-\hat{c})}\tilde{p}_\zeta \tag{5.2.22b}$$

$$\tilde{u} = \frac{i}{\hat{\alpha}(U-\hat{c})}\left[i\hat{\alpha}\tilde{p} + U_\eta\tilde{v} + U_\zeta\tilde{w}\right]. \tag{5.2.22c}$$

Figures 5.2.2 and 5.2.3 show contours of (a) the normalised streamwise wave velocity $|\tilde{u}|$ and (b) the normalised in-plane velocity. Figure 5.2.2 shows the contours for $\beta = 0$, $\hat{\alpha} = 0.5$ and $K = 4$ whilst figure 5.2.3 shows the solution when $\beta = 0.5$, $\hat{\alpha} = 0.05$ and $K = 8$ as examples. In both figures it is clear to see that the wave disturbance is concentrated in a thin layer which appears to follow the contours of the streak velocity

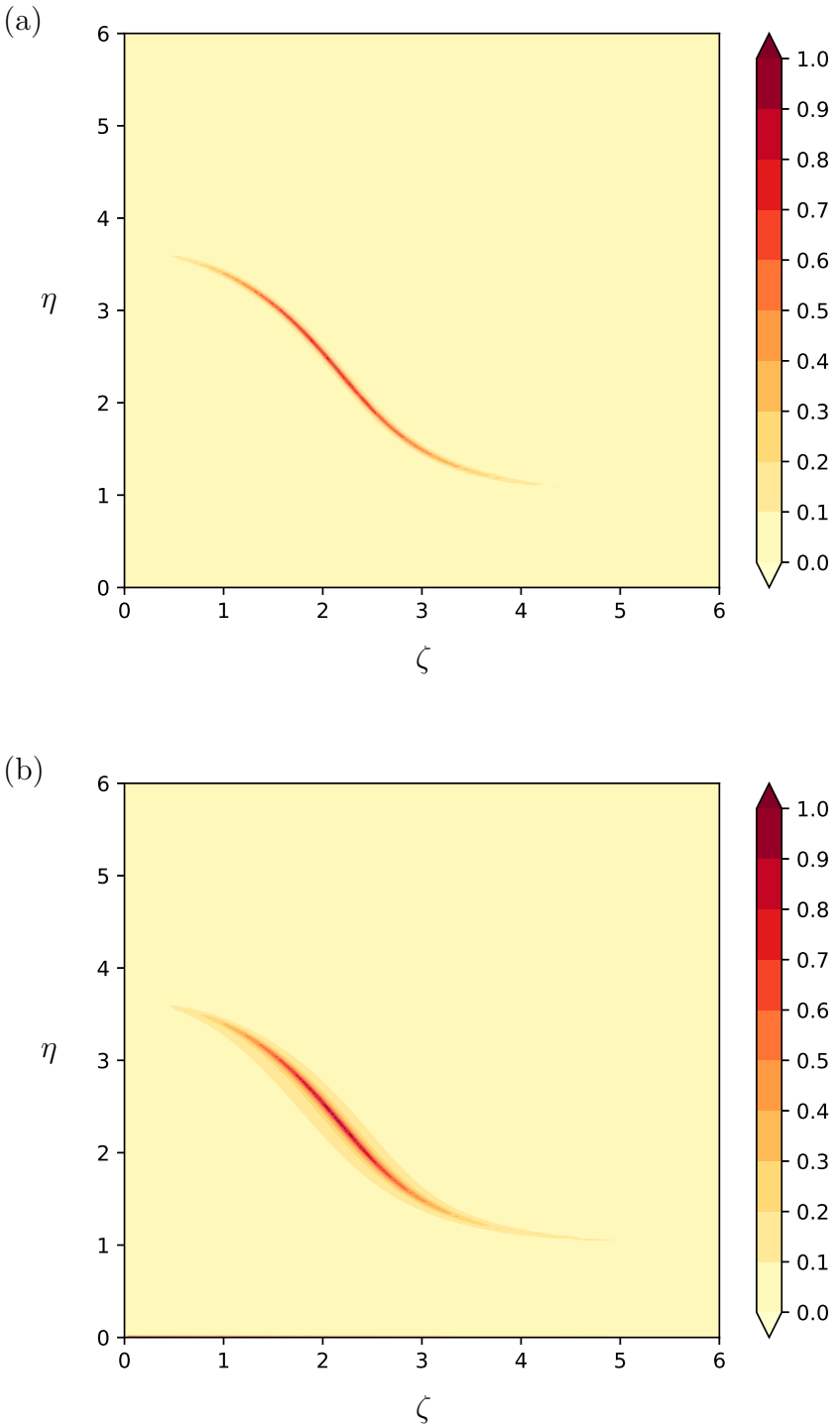

Figure 5.2.2: The solution of (5.2.15) with $\beta = 0$, $\hat{\alpha} = 0.5$ and $K = 4$ yields contours of (a) the normalised streamwise wave velocity eigenfunction $|\tilde{u}|$ and (b) the in-plane velocity magnitude $\sqrt{|\tilde{v}|^2 + |\tilde{w}|^2}$.

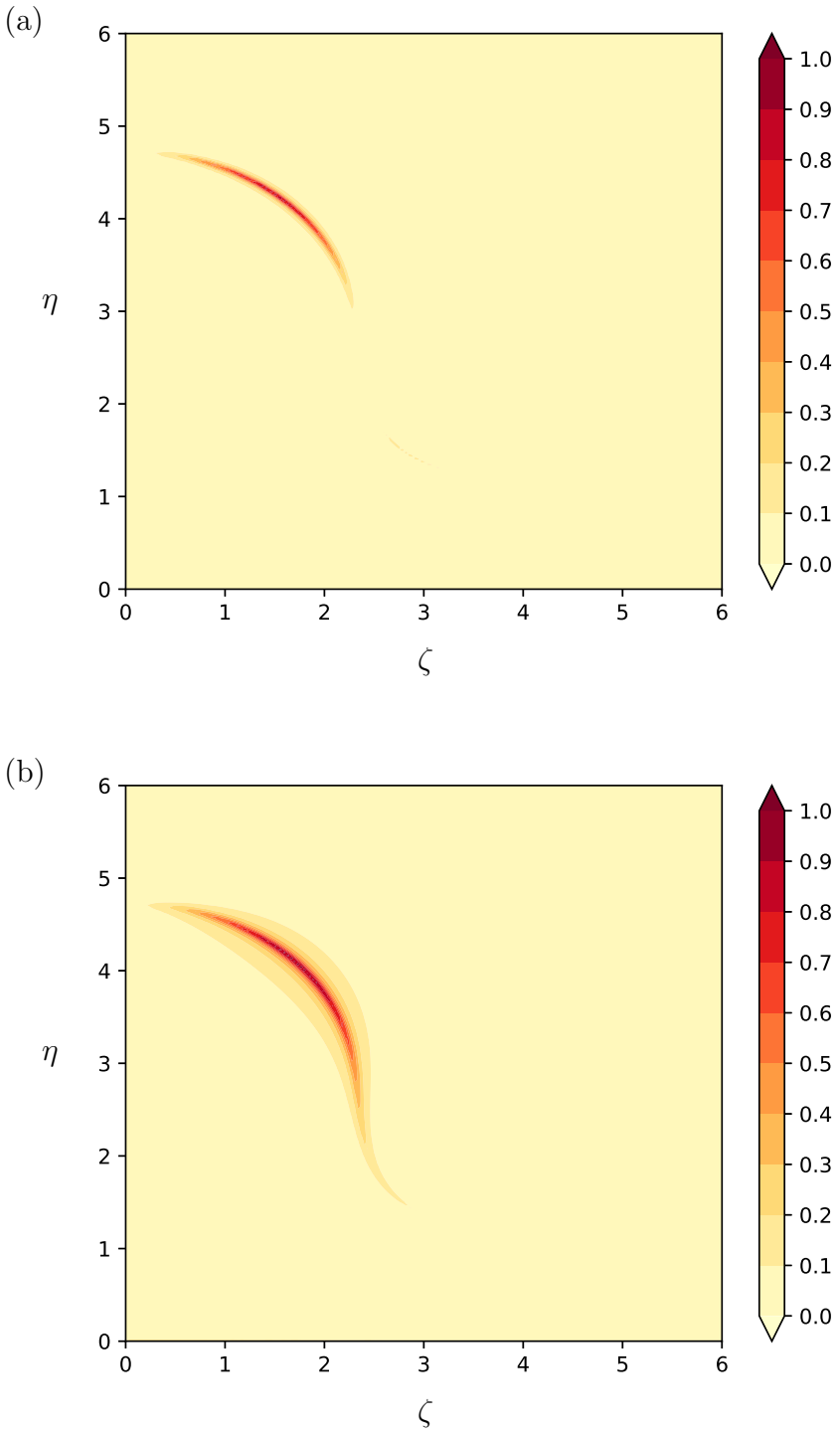

Figure 5.2.3: The solution of (5.2.15) with $\beta = 0.5$, $\hat{\alpha} = 0.05$ and $K = 8$ yields contours of (a) the normalised streamwise wave velocity eigenfunction $|\tilde{u}|$ and (b) the in-plane velocity magnitude $\sqrt{|\tilde{v}|^2 + |\tilde{w}|^2}$.

$U(\eta, \zeta)$. The velocity instability is confined to the critical layer, the solutions presented are illustrative of the general behaviour. When $\beta = 0.5$ the spanwise extent of the instability is significantly constrained in comparison to the $\beta = 0$ case. This tendency for the influence of the wave perturbation to be focused within a critical layer indicates that the unstable behaviour acts within an isolated region, at least initially.

5.3 Discussion

Understanding the stability of the short-scale injection flow is important in order to know whether or not the streak flow will persist when perturbed. The streak flow will only exist in a steady state form if perturbations decay as time progresses. Both the viscous and inviscid stability of the streak flow has been examined for various injection rates K, wavewnumbers $\hat{\alpha}$ and pressure gradients β. For the viscous stability analysis it is necessary to use a finite value of the local Reynolds number Re_x. The numerical calculations were carried out using a selection of different values of Re_x in order to show the effect this has on the results of the viscous stability analysis.

For both the viscous and the inviscid stability solutions at least one unstable eigenmode exists over a range of $\hat{\alpha}$ provided that the injection rate is sufficiently strong. The value of the wavenumber at which all the modes become stable is determined by the rate of injection K for a given value of β. The perturbation eigenvector is concentrated in a layer which conforms to the shape of the short-scale injection. As the local Reynolds number is increased, in the viscous case, this layer becomes thinner and thinner until a critical layer is formed in the inviscid case as $Re_x \to \infty$. When the Reynolds number is sufficiently large the viscous and inviscid results are very similar which means that the viscous equations provide a good approximation to the inviscid equations. The similarity between the viscous and inviscid solutions breaks down when Re_x is too small or if $\hat{\alpha}$ is close to zero. Strictly speaking since the streak equations rely upon taking the asymptotic limit of large Reynolds number, for $O(1)$ values of $\hat{\alpha}$, only the inviscid stability equations are asymptotically consistent.

The analysis presented in this chapter gives an outline of the stability characteristics of the streak flow. The limited selection of β and K values used could be extended

in order to give a more thorough exposition. It might be possible to use an approximation to the streak flow $U(\zeta, \eta)$ in order to analyse the stability equations more deeply in regards to how alterations in the streak flow impact the stability of the eigenmodes. Although this analysis is of limited scope it is sufficient to give a basic understanding of the stability characteristics of the streak flow. The stability analysis presented above also acts as a stepping stone when considering the interaction between the streak and the wave in relation to the formation of a self-sustaining system.

Chapter 6

Conclusions

Three-dimensional similarity solutions have been presented for laminar flow over a flat plate both with and without an applied pressure gradient and a short-scale spanwise injection through a slot of width $O(\zeta_0 ((2-\beta)x^*\nu^*/U^*)^{1/2})$. The injection velocity is $O(K (\nu^*U^*/(2-\beta)x^*)^{1/2})$, with x^* the distance from the leading edge, $U^* = U^*_\infty F(x^*)$ the freestream velocity, ν^* the kinematic viscosity and β the Hartree pressure gradient parameter. This slot width and injection velocity scaling ensures a constant ratio is maintained with the usual boundary-layer scaling in the downstream x^* coordinate, allowing for self-similar solutions. Far from the injection slot, in the spanwise direction, the flow is the usual two-dimensional Blasius/Falkner-Skan boundary-layer flow on a flat plate.

In chapter 2 numerical evidence showed that when $\beta = 0$, for large injection slot widths ζ_0, there exists three distinct flow regimes. The regimes are delineated by two critical injection rates $K_I \approx 0.876$ and $K_{II} \approx 1.95$ separating the weak, moderate and strong injection regimes. For the moderate and strong regimes a low-speed streak is formed in the vicinity of the injection region; the streak radius r_s is determined by the rate of injection through the plate surface with $K = K_{II}$ corresponding to $r_s = \zeta_0$. The weak injection state, $K < K_I$, can be determined by parabolic marching in the spanwise coordinate from the far-field Blasius solution towards the centreline of the injection region. Near to the centreline spatially unstable eigenmodes cause deviation from the expected Blasius solution subject to injection. Asymptotic descriptions are given, in the limit of large slot widths with fixed injection velocities, for each of the regimes. Unlike the two-dimensional boundary layers described in section 1.4 'blow-off'

does not occur and three-dimensional solutions exist for *any* injection rate.

With the introduction of a favourable pressure gradient ($\beta > 0$) in chapter 3 the distinction between the regimes disappears and the low-speed streaks in the moderate and strong regimes is less pronounced. In the limit of a large injection slot width a parabolic solution, marched from the far-field Falkner–Skan flow, exists for all injection rates K. Unlike the zero pressure gradient case, which has a singular response at a finite value of $\hat{\zeta}$ when the wall shear stress is zero, the parabolic solution maintains a non-zero shear stress at all $\hat{\zeta}$ locations. For favourable pressure gradients $\beta_c(K) < \beta < 1$ the parabolic solution gives good agreement with the full numerical solution and the Falkner–Skan solution with injection is recovered near to the centreline. However for weak favourable pressure gradients $0 < \beta < \beta_c(K)$ there is no longer good agreement near the centreline of the injection slot and the full numerical solutions show that for $\hat{\zeta} \ll 1$ (near the centreline) the flow becomes increasingly displaced from the plate as the injection slot width is increased. The critical pressure gradient β_c which separates these two scenarios is a function of the rate of injection K. The discrepancy found when the pressure gradient if sufficiently weak is due to the existence of spatially unstable (in the spanwise direction) eigenmodes which have a large effect on the flow near to the centreline of the injection region. In the limit of large injection $K \to \infty$ it appears that $\beta_c \to 1/2$, so for sufficiently large pressure gradients the flow recovers a two-dimensional Falkner–Skan flow subject to injection, for wide injection slots.

Chapter 4 extends the self-similar formulation of chapters 2 and 3 by allowing for a more general variation in the downstream coordinate x^*. This extension creates a fully three-dimensional formulation which allows more general slot geometries and injection profiles. Including downstream variation requires extra terms in the governing equations, parabolic marching downstream, and therefore necessitates more intensive computations when solving the equations numerically. The main purpose of this chapter is to illustrate how the self-similar formulation can be generalised to allow non-similar injection profiles. The marching formulation does not give much more insight than the self-similar formulation as the examples shown in chapter 4 are treated in less depth. There is a great deal of scope however for further examination of the examples of chapter 4. For example the constant width slot problem is of practical interest but it would be necessary to perform a much more in depth analysis, especially

at far downstream locations, in order to gain some physical insights.

The stability characteristics of parallel shear flows have been extensively studied throughout history since the importance of the transition from stable to unstable flow is widely recognised. The classical Orr-Sommerfeld and Rayleigh equations, along with their two-dimensional analogues, provide an excellent framework for examining the stability characteristics of parallel base flows. Although the base flows considered are not parallel the two-dimensional Orr-Sommerfeld equation provides a good approximation when the Reynolds number is large. Chapter 5 focuses on using the two-dimensional Orr-Sommerfeld and Rayleigh equations to examine the viscous and inviscid stability of the self-similar streak flow defined by the streamwise velocity component $U(\zeta, \eta)$. The stability analysis indicates that for a particular Reynolds number (viscous only), pressure gradient and wavenumber there exists at least one unstable eigenmode provided that the injection rate is sufficiently large. It also clear that as the Reynolds number becomes larger, in the viscous stability analysis, the viscous solution approaches the inviscid solution as expected. This is important because the derivation of the streak equations assumes that the Reynolds number is asymptotically large and therefore the viscous equations are not obtained by a rational asymptotic process. As the Reynolds number increases the eigenmodes associated with the most unstable eigenvalue become concentrated in thin a layer. In the inviscid case, when the Reynolds number becomes infinitely large, a critical layer is formed across which there is jump in the streak pressure and shear stress components, when considering interactions between the wave and streak. In the finite Reynolds number viscous case this jump is smoothed out and the streak pressure and shear stress components remain continuous throughout the cross-sectional domain.

This thesis has investigated the effect of short-scale spanwise disturbances on two-dimensional boundary-layer flows. Formulating the problem in terms of the self-similar boundary-region equations reduces the computational complexity, allowing for numerical solutions to be found for flows both with and without an applied pressure gradient. The self-similar formulation was then extended in order to account for more general downstream variation. Finally the stability of the streak flow produced by the short-scale disturbance, to a travelling wave disturbance, was examined. The work presented here suggests many more possible fruitful avenues of exploration related to short-scale

spanwise disturbances of boundary-layer flows.

6.1 Further work

The formulation presented in chapter 1 allows for a spanwise varying topography of the plate surface H, as well as the surface injection which has been considered throughout this thesis. Only using a simple injection boundary condition makes the governing equations much simpler but it is somewhat restrictive. It is supposed that the results presented in chapters 2-5 have an analogous form where the injection is replaced with a surface topography. Also the surface topography could be combined with an injection profile in order to model real world flow control configurations. Including a surface topography is an obvious means by which this work could be extended.

The stability results presented in chapter 5 could also be extended significantly. The interplay between the pressure gradient β, injection rate K, streamwise wavenumber $\hat{\alpha}$ and the local Reynolds number Re_x parameters is complex and requires more investigation. The singular nature of the inviscid stability equation (5.2.15) in the critical layer is problematic as the streak equations are only valid in the limit $Re \to \infty$.

One of the main reasons for investigating the stability of the streak flow, produced by short-scale spanwise injection, to a travelling wave disturbance was to lay a foundation for examining possible interactions between the streak and the wave. So called 'vortex-wave interactions' are of significant interest when the streak and wave form an interacting system which is self-sustaining. It is possible that the wave interaction could drive a localised streak flow without the need for any short-scale disturbance ($K = 0$).

6.2 Vortex-wave interactions

This section aims to give a brief outline of the interactions between the three-dimensional streak/vortex flows and travelling waves. Interest in this stems from the problem of transition from laminar to turbulent flow. Interactions between streamwise vortices and nonlinear waves are a strongly nonlinear process and are thought to have a great deal of relevance to fully fledged transition [33].

Experimental studies, such as those by conducted by Williams et al. (1984) [72] and Swearingen & Blackwelder (1987) [66], have shown that low-speed regions grow quickly in the wall-normal direction and create inflexional streamwise velocity components. Oscillations, which grow nonlinearly, then develop on these unstable velocity profiles causing a swift transition to turbulence. These experimental observations show the importance of interactions between low-speed regions and the wavy structures which they produce.

In extending their work to the strongly nonlinear regime Hall & Smith (1991) [33] have shown that a boundary-layer mean-flow profile may be modified significantly from its laminar form due to the influence of vortex-wave interactions. The inviscid instability of a longitudinal vortex structure due to Rayleigh waves, studied by Hall & Horseman (1991) [31], leads to unsteady three-dimensional transition to turbulence. Hall & Horseman showed that when the instability has a wavelength which is comparable to the boundary-layer thickness a quasi-parallel approach may be used to derive a two-dimensional generalisation of the Rayleigh equation describing the wave pressure (as shown in section 5.2). Brown et al. (1993) [9] examined the vortex/wave interaction equations of Hall & Smith (1991) in the vicinity of the position where the critical surface forms. At the critical level, where the streamwise velocity is equal to the wave speed, the generalised Rayleigh equation becomes singular and it is necessary to introduce extra constraints on the flow. Brown et al. (1993) determined necessary jump conditions for the shear stresses in the transverse and spanwise directions and the pressure within the streak. In the context of channel flows Waleffe (1997) [68] has examined how streamwise aligned roll/streak flows redistribute the mean shear, thereby creating instabilities, this leads to the production of waves that in turn drive the underlying flow. These so-called 'self-sustaining processes' are analogous to the vortex-wave interaction systems which are investigated herein. It is thought that such systems are responsible for creating structures in the near-wall region which then lead to transition.

In more recent work on Couette flow Hall & Sherwin (2010) [32] have shown that the lower branch state, which plays a central role in determining whether a flow is going to become turbulent, is a finite Reynolds number equivalent of a Rayleigh vortex-wave interaction. Hall & Sherwin found that, even for comparably small Reynolds

numbers, their asymptotic theory agreed well with full numerical solutions of the Navier-Stokes equations, suggesting that vortex-wave interactions are important in turbulent shear flows. Using a hybrid approach, which retains the viscous terms in the wave equations, Blackburn et al. (2013) [5] extended this to a range of spanwise wavenumbers and considered the limit of a large spanwise-wavenumber. In their hybrid approach Blackburn et al. no longer used the artificial forcing introduced by Hall & Sherwin to enforce the jump at the critical layer but instead calculated the forcing functions directly from the Reynolds stresses of the wave velocity field. This is useful as it means that jump conditions are no longer necessary but it does mean that the critical layer structure must be sufficiently resolved.

The aim here is to find a vortex-wave interaction state in the form of a localised streak that is not drive by any injection and is self-similar in its downstream development. In order to ensure that a constant frequency, self-similar wave exists it is necessary to choose the pressure gradient parameter such that $\beta = 1/2$ (or $n = 1/3$) as outlined in section 5.2. The wave interaction acts to modify the streak equations by introducing a forcing term which depends upon the wave eigenfunctions.

6.2.1 Governing equations

In order to determine the system governing the interactions between the streak and the wave a travelling wave disturbance must be added to the three-dimensional self-similar basic flow. The momentum and continuity equations (5.0.3), governing the velocity and pressure fields (u, v, w) and p in the scaled Cartesian coordinates (x, Y, Z), admit solutions of the form

$$u = x^n U(\eta,\zeta) + Re^{-\frac{7}{12}}\sigma(x)\tilde{u}(Y,Z)E + \text{c.c.} + \ldots, \tag{6.2.1a}$$

$$\begin{aligned}(v,w) =& Re^{-\frac{1}{2}}\left(\frac{n+1}{2x^{1-n}}\right)^{\frac{1}{2}}(V(\eta,\zeta),W(\eta,\zeta)) + \\ & Re^{-\frac{7}{12}}\sigma(x)\left(\tilde{v}(Y,Z),\tilde{w}(Y,Z)\right)E + \text{c.c.} + \ldots,\end{aligned} \tag{6.2.1b}$$

$$\begin{aligned}p =& -\frac{1}{2}x^{2n} + Re^{-\frac{1}{2}}p(x) - \frac{1}{2}Re^{-1}\left(\frac{n+1}{2x^{1-n}}\right)p_2(\eta,\zeta) + \\ & Re^{-\frac{7}{12}}\sigma(x)\tilde{p}(Y,Z)E + \text{c.c.} + \ldots,\end{aligned} \tag{6.2.1c}$$

where (U, V, W) is the three-dimensional basic streak flow in the self-similar variables (η, ζ) defined by the transformation (5.1.12). The wave expansion (6.2.1) is the same

as (5.1.1) and (5.2.1) except that the Reynolds number scaling ϵ is specified by the critical layer scaling. Brown et al. [9] calculated the appropriate factor for general boundary-layer and streamwise scales and in this particular case $\epsilon = Re^{-7/12}$ ($\delta = 1/2$ and $b = 0$ in the notation of Brown et al. [9]). Here the wave system is given by the components $\tilde{u}, \tilde{v}, \tilde{w}$ and $\tilde{p}$ along with the downstream varying wave amplitude $\sigma(x)$ and the travelling wave function $E = e^{iRe^{\frac{1}{2}}\theta(x,t)}$ where $\theta(x,t)$ is defined by (5.1.4).

Inserting (6.2.1) into (5.0.3), retaining the mean flow correction but neglecting higher harmonics of the wave gives the system

$$\frac{2}{n+1}U = \Phi_\eta + \Psi_\zeta, \tag{6.2.2a}$$

$$\Theta = \Psi_\eta - \Phi_\zeta, \tag{6.2.2b}$$

$$\nabla^2 U = \frac{2n}{n+1}\left[U^2 - 1\right] - \Phi U_\eta - \Psi U_\zeta + \frac{2}{n+1}x^{1-2n}F, \tag{6.2.2c}$$

$$\begin{aligned}\nabla^2\Theta =& 2\left(\frac{1-n}{n+1}\right)\left[\zeta U U_\eta - \eta U U_\zeta\right] - \Phi\Theta_\eta - \Psi\Theta_\zeta - \frac{2}{n+1}U\Theta \\ &- \left(\frac{2x^{1-n}}{n+1}\right)^{\frac{1}{2}}\left(\frac{1-n}{n+1}\right)\frac{2}{n+1}x^{1-2n}\left(\eta F_Z - \zeta F_Y\right) \\ &- \frac{2}{n+1}x^{1-n}Re^{\frac{1}{2}}\left(\frac{2x^{1-n}}{n+1}\right)\left(G_Z - H_Y\right),\end{aligned} \tag{6.2.2d}$$

where

$$F = Re^{-\frac{7}{6}}\left(2\sigma\sigma_x\tilde{u}\bar{\tilde{u}}\right) + Re^{-\frac{2}{3}}\sigma^2\left(\tilde{v}\bar{\tilde{u}}_Y + \bar{\tilde{v}}\tilde{u}_Y + \tilde{w}\bar{\tilde{u}}_Z + \bar{\tilde{w}}\tilde{u}_Z\right), \tag{6.2.2e}$$

$$\begin{aligned}G =& Re^{-\frac{7}{6}}\sigma\sigma_x\left(\tilde{u}\bar{\tilde{v}} + \bar{\tilde{u}}\tilde{v}\right) \\ &+ Re^{-\frac{2}{3}}\sigma^2\left[i\alpha\left(\bar{\tilde{u}}\tilde{v} - \tilde{u}\bar{\tilde{v}}\right) + \tilde{v}\bar{\tilde{v}}_Y + \bar{\tilde{v}}\tilde{v}_Y + \tilde{w}\bar{\tilde{v}}_Z + \bar{\tilde{w}}\tilde{v}_Z\right],\end{aligned} \tag{6.2.2f}$$

$$\begin{aligned}H =& Re^{-\frac{7}{6}}\sigma\sigma_x\left(\tilde{u}\bar{\tilde{w}} + \bar{\tilde{u}}\tilde{w}\right) \\ &+ Re^{-\frac{2}{3}}\sigma^2\left[i\alpha\left(\bar{\tilde{u}}\tilde{w} - \tilde{u}\bar{\tilde{w}}\right) + \tilde{v}\bar{\tilde{w}}_Y + \bar{\tilde{v}}\tilde{w}_Y + \tilde{w}\bar{\tilde{w}}_Z + \bar{\tilde{w}}\tilde{w}_Z\right].\end{aligned} \tag{6.2.2g}$$

The variables $\bar{\tilde{u}}, \bar{\tilde{v}}, \bar{\tilde{w}}$ are the complex conjugates of the wave velocities $\tilde{u}, \tilde{v}, \tilde{w}$.

Using the transformation (5.1.12), whilst assuming that the Reynolds number is

asymptotically large, the equations (6.2.2) may be rewritten as

$$\frac{2}{n+1}U = \Phi_\eta + \Psi_\zeta, \tag{6.2.3a}$$

$$\Theta = \Psi_\eta - \Phi_\zeta, \tag{6.2.3b}$$

$$\nabla^2 U = \frac{2n}{n+1}\left[U^2 - 1\right] - \Phi U_\eta - \Psi U_\zeta + \left(\frac{2}{n+1}\right)^{\frac{1}{2}} x^{\frac{1-3n}{2}} Re^{-\frac{2}{3}}\sigma^2 \tilde{F}, \tag{6.2.3c}$$

$$\nabla^2\Theta = 2\left(\frac{1-n}{n+1}\right)\left[\zeta U U_\eta - \eta U U_\zeta\right] - \Phi\Theta_\eta - \Psi\Theta_\zeta - \frac{2}{n+1}U\Theta - \frac{2}{n+1}x^{1-n}Re^{-\frac{1}{6}}\sigma^2\left(\tilde{G}_\zeta - \tilde{H}_\eta\right), \tag{6.2.3d}$$

where

$$\tilde{F} = \tilde{v}\bar{\tilde{u}}_\eta + \bar{\tilde{v}}\tilde{u}_\eta + \tilde{w}\bar{\tilde{u}}_\zeta + \bar{\tilde{w}}\tilde{u}_\zeta, \tag{6.2.3e}$$

$$\tilde{G} = i\hat{\alpha}\left(\bar{\tilde{u}}\tilde{v} - \tilde{u}\bar{\tilde{v}}\right) + \tilde{v}\bar{\tilde{v}}_\eta + \bar{\tilde{v}}\tilde{v}_\eta + \tilde{w}\bar{\tilde{v}}_\zeta + \bar{\tilde{w}}\tilde{v}_\zeta, \tag{6.2.3f}$$

$$\tilde{H} = i\hat{\alpha}\left(\bar{\tilde{u}}\tilde{w} - \tilde{u}\bar{\tilde{w}}\right) + \tilde{v}\bar{\tilde{w}}_\eta + \bar{\tilde{v}}\tilde{w}_\eta + \tilde{w}\bar{\tilde{w}}_\zeta + \bar{\tilde{w}}\tilde{w}_\zeta. \tag{6.2.3g}$$

In (6.2.3) the non-parallel and higher order terms have been ignored as these terms will be insignificantly small when compared to the terms which have been retained. The $O(Re^{-2/3})$ term in the streamwise momentum (6.2.3c) is small when compared with the $O(Re^{-1/6})$ term forcing the vorticity equation (6.2.3d) so it can be ignored at leading order when the Reynolds number is large.

In order to remove the downstream dependence present in (6.2.3) it is necessary to choose the downstream varying wave amplitude in order to maintain self-similarity. In order to match with the local Reynolds number formulation of the stability equations (5.1.13) the local Reynolds number $Re_x = 2x^{n+1}Re/(n+1)$ is introduced. It follows that

$$\frac{2}{n+1}x^{1-n}Re^{-\frac{1}{6}}\sigma^2 = \left(\frac{2}{n+1}\right)^{\frac{7}{6}} x^{\frac{7-5n}{6}} Re_x^{-\frac{1}{6}}\sigma^2. \tag{6.2.4}$$

Hence if $\sigma(x)$ is chosen such that

$$\left(\frac{2}{n+1}\right)^{\frac{7}{6}} x^{\frac{7-5n}{6}}\sigma^2 = \hat{\sigma}^2, \tag{6.2.5}$$

where $\hat{\sigma}$ is a constant, then (6.2.3), at leading order, becomes

$$(2-\beta)U = \Phi_\eta + \Psi_\zeta, \tag{6.2.6a}$$

$$\Theta = \Psi_\eta - \Phi_\zeta, \tag{6.2.6b}$$

$$\nabla^2 U = \beta\left[U^2 - 1\right] - \Phi U_\eta - \Psi U_\zeta, \tag{6.2.6c}$$

$$\begin{aligned}\nabla^2\Theta =& 2(1-\beta)\left[\zeta U U_\eta - \eta U U_\zeta\right] - \Phi\Theta_\eta - \Psi\Theta_\zeta - (2-\beta)U\Theta \\ &- Re_x^{-\frac{1}{6}}\hat{\sigma}^2\left(\tilde{G}_\zeta - \tilde{H}_\eta\right),\end{aligned} \tag{6.2.6d}$$

where $\beta = 2n/(n+1)$ is the usual Hartree parameter. The forcing terms may be rewritten in terms of the real and imaginary parts of the wave velocities such that

$$\begin{aligned}\tilde{G} =& 2\left[\hat{\alpha}\left(\Im(\tilde{u})\Re(\tilde{v}) - \Re(\tilde{u})\Im(\tilde{v})\right) + \Re(\tilde{v})\Re(\tilde{v}_\eta) + \Im(\tilde{v})\Im(\tilde{v}_\eta)\right. \\ &\left.+\Re(\tilde{w})\Re(\tilde{v}_\zeta) + \Im(\tilde{w})\Im(\tilde{v}_\zeta)\right],\end{aligned} \tag{6.2.6e}$$

$$\begin{aligned}\tilde{H} =& 2\left[\hat{\alpha}\left(\Im(\tilde{u})\Re(\tilde{w}) - \Re(\tilde{u})\Im(\tilde{w})\right) + \Re(\tilde{v})\Re(\tilde{w}_\eta) + \Im(\tilde{v})\Im(\tilde{w}_\eta)\right. \\ &\left.+\Re(\tilde{w})\Re(\tilde{w}_\zeta) + \Im(\tilde{w})\Im(\tilde{w}_\zeta)\right].\end{aligned} \tag{6.2.6f}$$

The forcing terms $\tilde{G}$ and $\tilde{H}$ are determined by solving the viscous stability equations (5.1.13) or (5.1.16) which requires the self-similar downstream velocity U.

Since $Re \to \infty$ when deriving the streak equations the forcing terms should really be determined by using the inviscid stability equation (5.2.10). This equation, which neglects viscous terms, breaks down at the critical layer where $U = \hat{c}$. In this case it would therefore be necessary to solve (6.2.6) with jump conditions across the critical layer. Hall & Sherwin (2010) [32] enforce the required jump conditions by regularising the forcing terms using an approximate delta-function with a thickness parameter. By using the viscous stability equations (5.1.13) the forcing terms are regularised directly by the Reynolds number and there is no need to introduce an extra regularisation parameter or jump conditions. In this hybrid approach the forcing terms are computed directly from the Reynolds stresses of the wave velocity field and in the limit $Re_x \to \infty$ the forcing will recover the required asymptotic value [5]. This means that using the viscous stability equations with a large Re_x value gives a good approximation to the asymptotic limit whilst also avoiding jump conditions and the regularisation that would otherwise be required in order to resolve solutions near to the critical layer.

So the interaction equations (6.2.6) and the viscous stability equations (5.1.13) form a coupled system since the solution of one relies upon the solution of the other.

It is necessary to solve the two systems simultaneously as one large system in order to find solutions for particular values of $K, \hat{\alpha}$ and $\hat{\sigma}$ however these parameters must be adjusted in order to find equilibrium solutions ($\hat{c}_i = 0$) for the leading wave eigenmode. By reducing the injection rate K but increasing the wave amplitude $\hat{\sigma}$, whilst keeping $\hat{c}_i \approx 0$, it is hoped that a solution may be found where $K = 0$ but the streak structure is maintained. In this case the streak/vortex and the wave form a self-sustaining system in which the injection of fluid into the boundary layer is no longer required in order to maintain the structure.

6.2.2 Proposed numerical scheme

In order to solve the system numerically it will be formulated as a local eigenvalue problem and the stability equations (5.1.16) are split into real and imaginary parts. Each of the four stability variables are split into real and imaginary parts such that $\tilde{v} = \tilde{v}_r + i\tilde{v}_i$ etc. The interaction equations (6.2.6) variables are split into a two-dimensional Falkner-Skan base flow and three-dimensional correction as in previous chapters. The wave speed eigenvalue is also split into real and imaginary parts such that $\hat{c} = \hat{c}_r + i\hat{c}_i$. This leads to the system of equations

$$-\frac{1}{\hat{\alpha} Re_x^{\frac{1}{2}}} \tilde{\nabla}^2 \tilde{v}_i + \left[U_B + \tilde{U} - \hat{c}_r + \frac{(1-\beta)}{Re_x} \right] \tilde{v}_r + \hat{c}_i \tilde{v}_i = \tilde{q}_r, \tag{6.2.7a}$$

$$\frac{1}{\hat{\alpha} Re_x^{\frac{1}{2}}} \tilde{\nabla}^2 \tilde{v}_r + \left[U_B + \tilde{U} - \hat{c}_r + \frac{(1-\beta)}{Re_x} \right] \tilde{v}_i - \hat{c}_i \tilde{v}_r = \tilde{q}_i, \tag{6.2.7b}$$

$$-\frac{1}{\hat{\alpha} Re_x^{\frac{1}{2}}} \tilde{\nabla}^2 \tilde{w}_i + \left[U_B + \tilde{U} - \hat{c}_r + \frac{(1-\beta)}{Re_x} \right] \tilde{w}_r + \hat{c}_i \tilde{w}_i = \tilde{s}_r, \tag{6.2.7c}$$

$$\frac{1}{\hat{\alpha} Re_x^{\frac{1}{2}}} \tilde{\nabla}^2 \tilde{w}_r + \left[U_B + \tilde{U} - \hat{c}_r + \frac{(1-\beta)}{Re_x} \right] \tilde{w}_i - \hat{c}_i \tilde{w}_r = \tilde{s}_i, \tag{6.2.7d}$$

$$\tilde{q}_{r\eta\eta} - \hat{\alpha}^2\tilde{q}_r + \tilde{s}_{r\zeta\eta} = \left(U_B'' + \tilde{U}_{\eta\eta}\right)\tilde{v}_r + \tilde{U}_{\zeta\eta}\tilde{w}_r + \tilde{U}_\zeta\tilde{w}_{r\eta} - \left(U_B' + \tilde{U}_\eta\right)\tilde{w}_{r\zeta}, \tag{6.2.7e}$$

$$\tilde{q}_{i\eta\eta} - \hat{\alpha}^2\tilde{q}_i + \tilde{s}_{i\zeta\eta} = \left(U_B'' + \tilde{U}_{\eta\eta}\right)\tilde{v}_i + \tilde{U}_{\zeta\eta}\tilde{w}_i + \tilde{U}_\zeta\tilde{w}_{i\eta} - \left(U_B' + \tilde{U}_\eta\right)\tilde{w}_{i\zeta}, \tag{6.2.7f}$$

$$\tilde{s}_{r\zeta\zeta} - \hat{\alpha}^2\tilde{s}_r + \tilde{q}_{r\zeta\eta} = \tilde{U}_{\zeta\zeta}\tilde{w}_r + \tilde{U}_{\zeta\eta}\tilde{v}_r + \left(U_B' + \tilde{U}_\eta\right)\tilde{v}_{r\zeta} - \tilde{U}_\zeta\tilde{v}_{r\eta}, \tag{6.2.7g}$$

$$\tilde{s}_{i\zeta\zeta} - \hat{\alpha}^2\tilde{s}_i + \tilde{q}_{i\zeta\eta} = \tilde{U}_{\zeta\zeta}\tilde{w}_i + \tilde{U}_{\zeta\eta}\tilde{v}_i + \left(U_B' + \tilde{U}_\eta\right)\tilde{v}_{i\zeta} - \tilde{U}_\zeta\tilde{v}_{i\eta}, \tag{6.2.7h}$$

$$\nabla^2\tilde{\Phi} = (2-\beta)\tilde{U}_\eta - \tilde{\Theta}_\zeta, \tag{6.2.7i}$$

$$\nabla^2\tilde{\Psi} = (2-\beta)\tilde{U}_\zeta + \tilde{\Theta}_\eta, \tag{6.2.7j}$$

$$\nabla^2\tilde{U} = \beta\left[2U_B\tilde{U} + \tilde{U}^2\right] - \left(\zeta\Psi_B + \tilde{\Psi}\right)\tilde{U}_\zeta - \Phi_B\tilde{U}_\eta - \left(U_B' + \tilde{U}_\eta\right)\tilde{\Phi}, \tag{6.2.7k}$$

$$\begin{aligned}\nabla^2\tilde{\Theta} = {} & 2(1-\beta)\left\{\zeta\left(U_B + \tilde{U}\right)\tilde{U}_\eta + \zeta U_B'\tilde{U} - \eta\left(U_B + \tilde{U}\right)\tilde{U}_\zeta\right\} \\ & - \left(\Phi_B + \tilde{\Phi}\right)\tilde{\Theta}_\eta - \zeta\Theta_B'\tilde{\Phi} - \zeta\Psi_B\tilde{\Theta}_\zeta - \tilde{\Psi}\left(\Theta_B + \tilde{\Theta}_\zeta\right) \\ & -(2-\beta)\left[\left(U_B + \tilde{U}\right)\tilde{\Theta} + \zeta\Theta_B\tilde{U}\right] - Re_x^{-\frac{1}{6}}\hat{\sigma}^2\left(\tilde{G}_\zeta - \tilde{H}_\eta\right),\end{aligned} \tag{6.2.7l}$$

where

$$\tilde{\nabla}^2 \equiv \nabla^2 - \hat{\alpha}^2 \equiv \frac{\partial^2}{\partial\eta^2} + \frac{\partial^2}{\partial\zeta^2} - \hat{\alpha}^2. \tag{6.2.7m}$$

The forcing term in the vorticity equation is written as

$$\begin{aligned}\tilde{G}_\zeta - \tilde{H}_\eta = {} & 4\tilde{v}_{r\zeta}\left(\tilde{v}_{r\eta} + \tilde{w}_{r\zeta}\right) + 4\tilde{v}_{i\zeta}\left(\tilde{v}_{i\eta} + \tilde{w}_{i\zeta}\right) + 2\tilde{v}_r\left(2\tilde{v}_{r\eta\zeta} + \tilde{w}_{r\zeta\zeta} - \tilde{w}_{r\eta\eta}\right) \\ & + 2\tilde{v}_i\left(2\tilde{v}_{i\eta\zeta} + \tilde{w}_{i\zeta\zeta} - \tilde{w}_{i\eta\eta}\right) - 4\tilde{w}_{r\eta}\left(\tilde{w}_{r\zeta} + \tilde{v}_{r\eta}\right) - 4\tilde{w}_{i\eta}\left(\tilde{w}_{i\zeta} + \tilde{v}_{i\eta}\right) \\ & - 2\tilde{w}_r\left(2\tilde{w}_{r\zeta\eta} + \tilde{v}_{r\eta\eta} - \tilde{v}_{r\zeta\zeta}\right) - 2\tilde{w}_i\left(2\tilde{w}_{i\zeta\eta} + \tilde{v}_{i\eta\eta} - \tilde{v}_{i\zeta\zeta}\right).\end{aligned} \tag{6.2.7n}$$

The local eigenvalue problem (6.2.7) is a system of twelve equations in fourteen unknowns so it is necessary to introduce extra conditions for the complex eigenvalue $\hat{c}$. The stability equations are linear so the solutions may be scaled by some arbitrary amplitude. This amplitude may be specified by imposing the extra constraints

$$\tilde{q}_{r\eta}(0,0) = a \quad \text{and} \quad \tilde{q}_{i\eta}(0,0) = 0, \tag{6.2.8}$$

where a is a normalisation factor. These extra conditions provide the additional two equations necessary for the unknowns $\hat{c}_r$ and $\hat{c}_i$.

As before each of the twelve variables are split into a known part and correction, discretised using finite differences and solved using Newton iteration. In order to get a good initial guess the streak (3.1.4) and stability (5.1.16) equations are solved individually, in the absence of any forcing $\hat{\sigma} = 0$. The aim then is to reduce the injection K whilst increasing the wave amplitude $\hat{\sigma}$ so that $\hat{c}_i \approx 0$ until the injection is zero. This computation is non-trivial and is very time consuming.

6.2.3 Discussion

Another method of solving this vortex-wave interaction problem is to leave the streak (6.2.6) and stability (5.1.16) equations separate and use the solution of one in the other until convergence is achieved. This method is problematic due to the slow rate at which the equations settle down to a converged solution, sometimes failing to converge at all. Using the local formulation (6.2.7) eliminates the need for this convergence loop but is extremely computationally expensive.

The system (6.2.7) has twelve variables at each nodal location along with two additional constants, this creates a very large linear system which must be solved. When the mesh has a sufficient number of nodal points to ensure adequate resolution of the computational domain the linear system, which is solved at each Newton iteration, requires an excessive amount of time. Also since the vortex-wave interaction equations are only valid when $\beta = 1/2$ the stepping scheme must start from a large value of K which again increases the amount of computation required. This work is ongoing and may require a new approach in order for a solution to be reached.

Bibliography

[1] Amestoy, P. R., Duff, I. S., Koster, J. & L'Excellent, J.-Y. 2001 *A fully asynchronous multifrontal solver using distributed dynamic scheduling*, SIAM Journal of Matrix Analysis and Applications, Vol 23, No 1, pp 15-41 (2001).

[2] Aroesty, J. & Cole, J.D. 1965 *Boundary-layer flows with large injection rates* (No. RAND/RM-4620-ARPA). RAND CORP SANTA MONICA CA.

[3] Bender, C.M. & Orszag, S.A. 2013 *Advanced mathematical methods for scientists and engineers: Asymptotic methods and perturbation theory*. Springer-Verlag New York, Inc. pp 250-55.

[4] Bigg, G. R. 1981 *Semi-infinite line sources and locally axisymmetric surfaces*. Int. J. Math. Educ. Sci. Technol., 1982, vol. 13, no. 4, 463-465

[5] Blackburn, H.M., Hall, P. and Sherwin, S.J. 2013 *Lower branch equilibria in Couette flow: the emergence of canonical states for arbitrary shear flows*. J. Fluid Mech. 726 R2.

[6] Blasius, H. 1950 *The boundary layer in fluids with little friction*. English translation. NACA Technical Memorandum 1256. (Originally published in 1908).

[7] Braslow, A.L. 1999 *A history of suction-type laminar-flow control with emphasis on flight research*. Monographs in aerospace history, 13, 84.

[8] Briley, W.R. 1971 *A numerical study of laminar separation bubbles using the Navier-Stokes equations*. J. Fluid Mech. 47(4), 713-736.

[9] Brown, P.G., Brown, S.N., Smith, F.T. and Timoshin, S.N. 1993 *On the starting process of strongly nonlinear vortex/Rayleigh-wave interactions*. Mathematika, 40(1), 7-29.

[10] Catherall, D., Stewartson, K. and Williams, P.G. 1965 *Viscous flow past a flat plate with uniform injection*. Proc. R. Soc. Lond. A, 284(1398), 370-396.

[11] Crank, J. & Nicolson, P. 1996 *A practical method for numerical evaluation of solutions of partial differential equations of the heat-conduction type*. Advances in Computational Mathematics, 6(1), 207-226.

[12] Deguchi, K. and Hall, P. 2014 *Free-stream coherent structures in parallel boundary-layer flows*. J. Fluid Mech. 752, 602-625.

[13] Deguchi, K. and Hall, P. 2015 *Free-stream coherent structures in growing boundary layers: a link to near-wall streaks*. J. Fluid Mech. 778, 451-484.

[14] Denier, J.P., Hall, P. & Seddougui, S.O. 1991 *On the receptivity problem for Görtler vortices: vortex motions induced by wall roughness*. Philosophical Transactions of the Royal Society of London A: Mathematical, Physical and Engineering Sciences, 335(1636), 51-85.

[15] Dhanak, M. R. & Duck, P. W. 1997 *The effects of freestream pressure gradient on a corner boundary layer*. Proc. R. Soc. Lond. A 453 (1793).

[16] van Dommelen, L. L. & Yapalparvi, R. 2014 *Laminar boundary-layer separation control by Görtler-scale blowing*. Eur. J. Mech. B, 46, 1-16.

[17] Drazin, P. G. & Reid W. H. 2004 *Hydrodynamic Stability* 2nd Edition. Cambridge University Press.

[18] Duck, P. W., Stow, S. R. & Dhanak, M. R. 2000 *Boundary-layer flow along a ridge: alternatives to the Falkner-Skan solutions*. Phil. Trans. R. Soc. Lond. A 358 (1777), 3075-3090.

[19] Elliott, L. 1968 *Two-dimensional boundary layer theory with strong blowing*. Quart. J. Mech. Appl. Math. 21 (1), 77-91.

[20] Emmons, H. W. & Leigh, D. C. 1954 *Tabulation of the Blasius function with blowing and suction*. Aeronautical Research Council C.P. No. 157.

[21] Falkner, V. M. & Skan, S. W. 1930 *Some Approximate Solutions of the Boundary Layer Equations*. Aero. Res. Coun. Rep. and Mem. no 1314.

[22] Fernandez, E., Kumar, R. & Alvi, F. 2012 *Effect of Microjet Spacing on the Control of a Highly Separated Flowfield*. In 6th AIAA Flow Control Conference, p. 3248.

[23] Gersten, K. & Gross, J. F. 1973 *Increase of boundary-layer heat transfer by mass injection*. AIAA Journal, 11(5), 738-739.

[24] Goldstein, M.E., Sescu, A., Duck, P.W. and Choudhari, M. 2010 *The long range persistence of wakes behind a row of roughness elements*. J. Fluid Mech. 644, 123-163.

[25] Goldstein, M.E., Sescu, A., Duck, P.W. and Choudhari, M. 2011 *Algebraic/transcendental disturbance growth behind a row of roughness elements*. J. Fluid Mech. 668, 236-266.

[26] Goldstein, M.E., Sescu, A., Duck, P.W. and Choudhari, M. 2016 *Nonlinear wakes behind a row of elongated roughness elements*. J. Fluid Mech. 796, 516-557.

[27] Guennebaud G, Benoît J and others (2010) Eigen v3. http://eigen.tuxfamily.org

[28] Hall, P. 1982 *Taylor—Gortler vortices in fully developed or boundary-layer flows: linear theory*. J. Fluid Mech. 124, 475-494.

[29] Hall, P. 1983 *The linear development of Görtler vortices in growing boundary layers*. J. Fluid Mech. 130, 41-58.

[30] Hartree, D. R. 1937 *On an equation occurring in Falkner and Skan's approximate treatment of the equations of the boundary layer*. Mathematical Proceedings of the Cambridge Philosophical Society, 33, 223-239.

[31] Hall, P. and Horseman, N.J. 1991 *The linear inviscid secondary instability of longitudinal vortex structures in boundary layers*. Journal of Fluid Mechanics, 232, 357-375.

[32] Hall, P. and Sherwin, S. 2010 *Streamwise vortices in shear flows: harbingers of transition and the skeleton of coherent structures*. Journal of Fluid Mechanics, 661, 178-205.

[33] Hall, P. and Smith, F.T. 1991 *On strongly nonlinear vortex/wave interactions in boundary-layer transition.* J. Fluid Mech. 227, 641-666.

[34] Hernández, V., Román, J.E., Tomás, A. and Vidal, V. 2007 *Krylov-schur methods in SLEPc.* Universitat Politecnica de Valencia, Tech. Rep. STR-7.

[35] Hewitt, R. E. & Duck, P. W. 2014 *Three-dimensional boundary layers with short spanwise scales.* J. Fluid Mech. 756, 452-469.

[36] Hewitt, R. E., Duck, P. W. & Stow, S. R. 2002 *Continua of states in boundary-layer flows.* J. Fluid Mech. 468, 121–152.

[37] Hewitt, R. E., Duck, P. W. & Williams, A. J. 2017 *Injection into boundary layers: solutions beyond the classical form.* J. Fluid Mech. 822, 617-639.

[38] Hiemenz, K. 1911 *Die Grenzschicht an einem in den gleichformigen Flussigkeitsstrom eingetauchten geraden Kreiszlynder.* Diss. Göttingen 1911, Dingl. Polytech. J. 326, 321-324.

[39] Howison, S. 2005 *Practical Applied Mathematics: Modelling, Analysis, Approximation.* (No. 38). Cambridge University Press. p.125-134

[40] Iserles, A. 2009 *A first course in the numerical analysis of differential equations.* (No. 44). Cambridge university press. p.285

[41] Jordinson, R. 1970 *The flat plate boundary layer. Part 1. Numerical integration of the Orr—Sommerfeld equation.* J. Fluid Mech. 43(4), 801-811.

[42] Kassoy, D. R. 1970 *On laminar boundary layer blowoff.* SIAM Journal on Applied Mathematics 18 (1), 29-40.

[43] Kassoy, D. R. 1971 *On laminar boundary-layer blow-off. Part 2.* J. Fluid Mech. 48, 209-228.

[44] Kassoy, D. R. 1974 *A resolution of the blow-off singularity for similarity flow on a plate.* J. Fluid Mech. 62, 145-161.

[45] Kemp, N. H. 1951 *The laminar three-dimensional boundary layer and a study of the flow past a side edge.* M.Ae.S. thesis Cornell Univ.

[46] Klemp, J. B. & Acrivos, A. 1972 *High Reynolds number flow past a flat plate with strong blowing.* J. Fluid Mech. 51, 337-356.

[47] Kubota, T. & Fernandez, F. L. 1968 *Boundary-Layer Flows with Large Injection and Heat Transfer.* AIAA Journal, 6(1), 22-28.

[48] Kumar, V. & Alvi, F. S. 2006 *Use of high-speed microjets for active separation control in diffusers.* AIAA Journal, 44(2), 273-281.

[49] Pal, A. & Rubin, S.G. (1971) Asymptotic features of viscous flow along a corner. Quart. of Appl. Math. 91–108.

[50] Panton, R. L. 2005 *Incompressible Flow* 3rd Edition. Hoboken, New Jersey: John Wiley and Sons, Inc. p.500-504.

[51] Patankar, S. V., & Spalding, D. B. (1972) A calculation procedure for heat, mass and momentum transfer in three-dimensional parabolic flows. International journal of heat and mass transfer, 15(10), 1787-1806.

[52] Patterson, A. R. 1983 *A First Course in Fluid Dynamics* Cambridge University Press. p.240-243.

[53] Prandtl, L. 1933 *Motion of fluids with very little viscosity.* English translation. NACA Technical Memorandum 452. (Originally published in 1904).

[54] Pretsch, J. 1944 *Grenzen der Grenzschichtbeeinflussung.* ZAMM-Journal of Applied Mathematics and Mechanics/Zeitschrift für Angewandte Mathematik und Mechanik, 24(5-6), 264-267.

[55] Ricco, P. & Dilib, F. 2010 *The influence of wall suction and blowing on boundary-layer laminar streaks generated by free-stream vortical disturbances.* Physics of Fluids, 22(4), 044101.

[56] Ridha, A. 1992 *On the dual solutions associated with boundary-layer equations in a corner.* J. Eng. Math. 26(4), 525-537.

[57] Ridha, A. 2005 *On the three-dimensional alternative to the Blasius boundary-layer solution.* C. R. Mecanique. 333 (2005), 768-772.

[58] Rubin, S. G. 1966 Incompressible flow along a corner. J. Fluid Mech. 26, 97-110

[59] Schlichting, H & Gersten, K. 2000 *Boundary-Layer Theory* 8th Edition. Springer-Verlag Berlin Heidelberg.

[60] Smith, F.T. 1973 *Laminar flow over a small hump on a flat plate.* J. Fluid Mech. 57(4), 803-824.

[61] Smith, F.T., Brighton, P.W.M., Jackson, P.S. & Hunt, J.C.R. 1981 *On boundary-layer flow past two-dimensional obstacles.* Journal of Fluid Mechanics, 113, 123-152.

[62] Smith, F.T. and Stewartson, K. 1973 *Plate-injection into a separated supersonic boundary layer.* J. Fluid Mech. 58(1), 143-159.

[63] Smith, F.T. and Stewartson, K. 1973 *On slot injection into a supersonic laminar boundary layer.* Proc. R. Soc. Lond. A, 332(1588), 1-22.

[64] Stewart, G. W. 2001 *A Krylov–Schur Algorithm for Large Eigenproblems.* SIAM J. Matrix Anal. Appl., 23(3), 601–614.

[65] Stewartson, K. 1974 *Plate-injection into a separated supersonic boundary layer. Part 2. The transition regions.* J. Fluid Mech. 62(2), 289-304.

[66] Swearingen, J.D. and Blackwelder, R.F. 1987 *The growth and breakdown of streamwise vortices in the presence of a wall.* Journal of Fluid Mechanics, 182, 255-290.

[67] Tatsumi, T. and Yoshimura, T. 1990 *Stability of the laminar flow in a rectangular duct.* J. Fluid Mech. 212, 437-449.

[68] Waleffe, F. 1997 *On a self-sustaining process in shear flows.* Physics of Fluids, 9(4), 883-900.

[69] Watson, E. J. 1952 *The asymptotic theory of boundary-layer flow with suction.* HM Stationery Office.

[70] Watson, E.J. 1966 *The equation of similar profiles in boundary layer theory with strong blowing.* Proc. R. Soc. Lond. A 294(1437), 208-234.

[71] Williams, A.J. & Hewitt, R.E., 2017 *Micro-slot injection into a boundary layer driven by a favourable pressure gradient.* J. Eng. Math. 107(1), 19-35.

[72] Williams, D.R., Fasel, H. and Hama, F.R. 1984 *Experimental determination of the three-dimensional vorticity field in the boundary-layer transition process.* J. Fluid Mech. 149, 179-203.

[73] Van Dyke, M. 1975 *Perturbation methods in fluid mechanics.* Parabolic Press, Incorporated.

Appendix A

Governing equations

In the new body fitted coordinate system the derivatives with respect to x^*, y^* and z^* become

$$\frac{\partial()}{\partial x^*} = \left(\frac{n-1}{2x^*}\right)\left[(\eta + H - \zeta H')\,\frac{\partial()}{\partial \eta} + \zeta\frac{\partial()}{\partial \zeta}\right] + \frac{\partial()}{\partial x^*}, \tag{A.0.1}$$

$$\frac{\partial()}{\partial y^*} = \left(\frac{n+1}{2}\right)^{\frac{1}{2}} x^{*-1} Re_x^{\frac{1}{2}}\frac{\partial()}{\partial \eta}, \tag{A.0.2}$$

$$\frac{\partial()}{\partial z^*} = \left(\frac{n+1}{2}\right)^{\frac{1}{2}} x^{*-1} Re_x^{\frac{1}{2}}\left[\frac{\partial()}{\partial \zeta} - H'\frac{\partial()}{\partial \eta}\right], \tag{A.0.3}$$

where H' indicates the derivative of $H(\zeta)$ with respect to ζ.

A.1 Continuity equation

The continuity equation given by

$$\frac{\partial u^*}{\partial x^*} + \frac{\partial v^*}{\partial y^*} + \frac{\partial w^*}{\partial z^*} = 0, \tag{A.1.1}$$

may be reformulated using a boundary-layer approximation using the assumption that $Re_x \gg 1$. So for each of the derivative terms in (A.1.1) it follows that

$$\begin{aligned}
\frac{\partial u^*}{\partial x^*} =& \frac{\partial (U_\infty^* F(x^*))}{\partial x^*} U + U_\infty^* F(x^*) \frac{\partial U}{\partial x^*} \\
=& \frac{U_\infty^* F(x^*)}{2x^*} \left\{ 2nU + (n-1) \left[(\eta + H - \zeta H') U_\eta + \zeta U_\zeta \right] \right\}, && \text{(A.1.2a)} \\
\frac{\partial v^*}{\partial y^*} =& \frac{\partial}{\partial y^*} \left(\left(\frac{n+1}{2} \right)^{\frac{1}{2}} U_\infty^* F(x^*) Re_x^{-\frac{1}{2}} V(\zeta, \eta) \right) \\
=& \frac{U_\infty^* F(x^*)}{2x^*} (n+1) V_\eta, && \text{(A.1.2b)} \\
\frac{\partial w^*}{\partial z^*} =& \frac{\partial}{\partial z^*} \left(\left(\frac{n+1}{2} \right)^{\frac{1}{2}} U_\infty^* F(x^*) Re_x^{-\frac{1}{2}} W(\zeta, \eta) \right) \\
=& \frac{U_\infty^* F(x^*)}{2x^*} (n+1) \left[W_\zeta - H' W_\eta \right]. && \text{(A.1.2c)}
\end{aligned}$$

Since in general $U_\infty^* F(x^*)/2x^*$ is not equal to zero the continuity equation (A.1.1) may be rewritten as

$$2nU + (n-1) \left[(\eta + H - \zeta H') U_\eta + \zeta U_\zeta \right] + (n+1) \left(V_\eta + W_\zeta - H' W_\eta \right) = 0. \quad \text{(A.1.3)}$$

Proposing the change of dependent variables

$$\begin{aligned}
V(\zeta, \eta) =& \frac{(1-n)}{(n+1)} (\eta + H) U(\zeta, \eta) - \Phi(\zeta, \eta), && \text{(A.1.4a)} \\
W(\zeta, \eta) =& \frac{(1-n)}{(n+1)} \zeta U(\zeta, \eta) - \Psi(\zeta, \eta); && \text{(A.1.4b)}
\end{aligned}$$

leaves Φ and Ψ as the variables of interest. Applying the change of variables the continuity equation may be written as

$$\frac{2}{n+1} U = \Phi_\eta + \Psi_\zeta - H' \Psi_\eta. \quad \text{(A.1.5)}$$

A.2 Streamwise momentum equation

The streamwise momentum equation is given by

$$u^* \frac{\partial u^*}{\partial x^*} + v^* \frac{\partial u^*}{\partial y^*} + w^* \frac{\partial u^*}{\partial z^*} = -\frac{1}{\rho^*} \frac{\partial p^*}{\partial x^*} + \nu^* \left(\frac{\partial^2 u^*}{\partial x^{*2}} + \frac{\partial^2 u^*}{\partial y^{*2}} + \frac{\partial^2 u^*}{\partial z^{*2}} \right). \quad \text{(A.2.1)}$$

At leading order each of the terms in (A.2.1) is given by

$$u^*\frac{\partial u^*}{\partial x^*} = \frac{\left(U_\infty^* F(x^*)\right)^2}{2x^*} U\left\{2nU + (n-1)\left[\left(\eta + H - \zeta H'\right)U_\eta + \zeta U_\zeta\right]\right\}, \tag{A.2.2a}$$

$$v^*\frac{\partial u^*}{\partial y^*} = \frac{\left(U_\infty^* F(x^*)\right)^2}{2x^*}(n+1)VU_\eta, \tag{A.2.2b}$$

$$w^*\frac{\partial u^*}{\partial z^*} = \frac{\left(U_\infty^* F(x^*)\right)^2}{2x^*}(n+1)W\left[U_\zeta - H'U_\eta\right], \tag{A.2.2c}$$

$$-\frac{1}{\rho^*}\frac{\partial p^*}{\partial x^*} = \frac{\left(U_\infty^* F(x^*)\right)^2}{2x^*}2n, \tag{A.2.2d}$$

then since $\nu^* = x^* U_\infty^* F(x^*) Re_x^{-1}$ it follows that

$$\nu^*\frac{\partial^2 u^*}{\partial x^{*2}} = O(Re_x^{-1}), \tag{A.2.2e}$$

$$\nu^*\frac{\partial^2 u^*}{\partial y^{*2}} = \frac{\left(U_\infty^* F(x^*)\right)^2}{2x^*}(n+1)U_{\eta\eta}, \tag{A.2.2f}$$

$$\nu^*\frac{\partial^2 u^*}{\partial z^{*2}} = \frac{\left(U_\infty^* F(x^*)\right)^2}{2x^*}(n+1)\left[\left(H'\right)^2 U_{\eta\eta} + U_{\zeta\zeta} - 2H'U_{\eta\zeta} - H''U_\eta\right]. \tag{A.2.2g}$$

Since in general $\left(U_\infty^* F(x^*)\right)^2 / 2x^*$ is not equal to zero the streamwise momentum equation (A.2.1) may be rewritten as

$$\begin{aligned} 2nU^2 + (n-1)\left[\left(\eta + H - \zeta H'\right)U_\eta + \zeta U_\zeta\right] + (n+1)VU_\eta = 2n \\ + (n+1)U_{\eta\eta} + (n+1)\left[\left(H'\right)^2 U_{\eta\eta} + U_{\zeta\zeta} - 2H'U_{\eta\zeta} - H''U_\eta\right]. \end{aligned} \tag{A.2.3}$$

Then applying the change of variables (A.1.4) the streamwise momentum equation (A.2.1) becomes

$$\begin{aligned} \left[1 + \left(H'\right)^2\right]U_{\eta\eta} + U_{\zeta\zeta} - 2H'U_{\eta\zeta} - H''U_\eta = \frac{2n}{n+1}\left[U^2 - 1\right] - \Phi U_\eta \\ - \Psi\left[U_\zeta - H'U_\eta\right]. \end{aligned} \tag{A.2.4}$$

A.3 Transverse and spanwise momentum equations

The transverse and spanwise momentum equations are given by

$$u^*\frac{\partial v^*}{\partial x^*} + v^*\frac{\partial v^*}{\partial y^*} + w^*\frac{\partial v^*}{\partial z^*} = -\frac{1}{\rho^*}\frac{\partial p^*}{\partial y^*} + \nu^*\left(\frac{\partial^2 v^*}{\partial x^{*2}} + \frac{\partial^2 v^*}{\partial y^{*2}} + \frac{\partial^2 v^*}{\partial z^{*2}}\right), \tag{A.3.1a}$$

$$u^*\frac{\partial w^*}{\partial x^*} + v^*\frac{\partial w^*}{\partial y^*} + w^*\frac{\partial w^*}{\partial z^*} = -\frac{1}{\rho^*}\frac{\partial p^*}{\partial z^*} + \nu^*\left(\frac{\partial^2 w^*}{\partial x^{*2}} + \frac{\partial^2 w^*}{\partial y^{*2}} + \frac{\partial^2 w^*}{\partial z^{*2}}\right). \tag{A.3.1b}$$

At leading order each of the terms in the transverse momentum equation (A.3.1a) is given by

$$u^*\frac{\partial v^*}{\partial x^*} = \left(\frac{n+1}{2}\right)^{\frac{1}{2}} \frac{\left(U_\infty^* F(x^*)\right)^2}{2x^*} Re_x^{-\frac{1}{2}}(n-1)U\left[\left(\eta + H - \zeta H'\right)V_\eta + V + \zeta V_\zeta\right] \tag{A.3.2a}$$

$$v^*\frac{\partial v^*}{\partial y^*} = \left(\frac{n+1}{2}\right)^{\frac{1}{2}} \frac{\left(U_\infty^* F(x^*)\right)^2}{2x^*} Re_x^{-\frac{1}{2}}(n+1)VV_\eta, \tag{A.3.2b}$$

$$w^*\frac{\partial v^*}{\partial z^*} = \left(\frac{n+1}{2}\right)^{\frac{1}{2}} \frac{\left(U_\infty^* F(x^*)\right)^2}{2x^*} Re_x^{-\frac{1}{2}}(n+1)W\left[V_\zeta - H'V_\eta\right], \tag{A.3.2c}$$

$$\frac{-1}{\rho^*}\frac{\partial p^*}{\partial y^*} = \left(\frac{n+1}{2}\right)^{\frac{1}{2}} \frac{\left(U_\infty^* F(x^*)\right)^2}{2x^*} Re_x^{-\frac{1}{2}}\left(\frac{n+1}{2}\right)\frac{\partial p_2}{\partial \eta}, \tag{A.3.2d}$$

$$\nu^*\frac{\partial^2 v^*}{\partial x^{*2}} = O\left(Re_x^{-\frac{3}{2}}\right), \tag{A.3.2e}$$

$$\nu^*\frac{\partial^2 v^*}{\partial y^{*2}} = \left(\frac{n+1}{2}\right)^{\frac{1}{2}} \frac{\left(U_\infty^* F(x^*)\right)^2}{2x^*} Re_x^{-\frac{1}{2}}(n+1)V_{\eta\eta}, \tag{A.3.2f}$$

$$\nu^*\frac{\partial^2 v^*}{\partial z^{*2}} = \left(\frac{n+1}{2}\right)^{\frac{1}{2}} \frac{\left(U_\infty^* F(x^*)\right)^2}{2x^*} Re_x^{-\frac{1}{2}}(n+1)\left[\left(H'\right)^2 V_{\eta\eta} + V_{\zeta\zeta} - 2H'V_{\eta\zeta} - H''V_\eta\right]. \tag{A.3.2g}$$

Since in general $((n+1)/2)^{1/2}\left(U_\infty^* F(x^*)\right)^2 Re_x^{-1/2}/2x^*$ is not equal to zero the transverse momentum equation (A.3.1a) may be written as

$$\left(\frac{n-1}{n+1}\right)U\left[\left(\eta + H - \zeta H'\right)V_\eta + \zeta V_\zeta + V\right] + VV_\eta + W\left[V_\zeta - H'V_\eta\right] = \frac{1}{2}\frac{\partial p_2}{\partial \eta} + O(Re_x^{-1}) + \left[1 + \left(H'\right)^2\right]V_{\eta\eta} + V_{\zeta\zeta} - 2H'V_{\eta\zeta} - H''V_\eta. \tag{A.3.3}$$

Then for each of the terms in the spanwise momentum equation (A.3.1b) it follows that, at leading order,

$$u^*\frac{\partial w^*}{\partial x^*} = \left(\frac{n+1}{2}\right)^{\frac{1}{2}} \frac{\left(U_\infty^* F(x^*)\right)^2}{2x^*} Re_x^{-\frac{1}{2}}(n-1)U\left[\left(\eta + H - \zeta H'\right) W_\eta + \zeta W_\zeta + W\right], \tag{A.3.4a}$$

$$v^*\frac{\partial w^*}{\partial y^*} = \left(\frac{n+1}{2}\right)^{\frac{1}{2}} \frac{\left(U_\infty^* F(x^*)\right)^2}{2x^*} Re_x^{-\frac{1}{2}}(n+1)VW_\eta, \tag{A.3.4b}$$

$$w^*\frac{\partial w^*}{\partial z^*} = \left(\frac{n+1}{2}\right)^{\frac{1}{2}} \frac{\left(U_\infty^* F(x^*)\right)^2}{2x^*} Re_x^{-\frac{1}{2}}(n+1)W\left[W_\zeta - H'W_\eta\right], \tag{A.3.4c}$$

$$\frac{-1}{\rho^*}\frac{\partial p^*}{\partial z^*} = \left(\frac{n+1}{2}\right)^{\frac{1}{2}} \frac{\left(U_\infty^* F(x^*)\right)^2}{2x^*} Re_x^{-\frac{1}{2}} \left(\frac{n+1}{2}\right)\left[\frac{\partial p_2}{\partial \zeta} - H'\frac{\partial p_2}{\partial \eta}\right], \tag{A.3.4d}$$

$$\nu^*\frac{\partial^2 w^*}{\partial x^{*2}} = O\left(Re_x^{-\frac{3}{2}}\right), \tag{A.3.4e}$$

$$\nu^*\frac{\partial^2 w^*}{\partial y^{*2}} = \left(\frac{n+1}{2}\right)^{\frac{1}{2}} \frac{\left(U_\infty^* F(x^*)\right)^2}{2x^*} Re_x^{-\frac{1}{2}}(n+1)W_{\eta\eta}, \tag{A.3.4f}$$

$$\nu^*\frac{\partial^2 w^*}{\partial z^{*2}} = \left(\frac{n+1}{2}\right)^{\frac{1}{2}} \frac{\left(U_\infty^* F(x^*)\right)^2}{2x^*} Re_x^{-\frac{1}{2}}(n+1)\left[\left(H'\right)^2 W_{\eta\eta} + W_{\zeta\zeta} - 2H'W_{\eta\zeta} - H''W_\eta\right]. \tag{A.3.4g}$$

This means that the spanwise momentum equation (A.3.1b) may be written as

$$\begin{aligned}\left(\frac{n-1}{n+1}\right) U\left[\left(\eta + H - \zeta H'\right) W_\eta + \zeta W_\zeta + W\right] + VW_\eta + W\left[W_\zeta - H'W_\eta\right] \\ = \frac{1}{2}\left[\frac{\partial p_2}{\partial \zeta} - H'\frac{\partial p_2}{\partial \eta}\right] + O(Re_x^{-1}) + \left[1 + \left(H'\right)^2\right] W_{\eta\eta} + W_{\zeta\zeta} \\ - 2H'W_{\eta\zeta} - H''W_\eta.\end{aligned} \tag{A.3.5}$$

Applying the change of variables (A.1.4), and using the streamwise momentum equation (A.2.4), the momentum equations (A.3.3) and (A.3.5) become

$$\begin{aligned}&\left(\frac{1-n}{n+1}\right)(\eta + H)\left[\left(-\Phi + H'\Psi\right) U_\eta - \Psi U_\zeta - \left(\frac{1-n}{n+1}\right) U^2\right] + \left(\Phi - H'\Psi\right)\Phi_\eta \\ &+ \Psi\Phi_\zeta = \frac{1}{2}\frac{\partial p_2}{\partial \eta} + O(Re_x^{-1}) + \left(\frac{1-n}{n+1}\right) 2U_\eta + \left(\frac{1-n}{n+1}\right)(\eta + H)\left[\frac{2n}{n+1}\left(U^2 - 1\right)\right. \\ &\left. -\Phi U_\eta - \Psi\left(U_\zeta - H'U_\eta\right)\right] - \left[1 + \left(H'\right)^2\right]\Phi_{\eta\eta} - \Phi_{\zeta\zeta} + 2H'\Phi_{\eta\zeta} + H''\Phi_\eta\end{aligned} \tag{A.3.6}$$

and

$$\begin{aligned}
&\left(\frac{1-n}{n+1}\right)\zeta\left[\left(-\Phi+H'\Psi\right)U_\eta-\Psi U_\zeta-\left(\frac{1-n}{n+1}\right)U^2\right]+\left(\Phi-H'\Psi\right)\Psi_\eta+\Psi\Psi_\zeta\\
=&\frac{1}{2}\left[\frac{\partial p_2}{\partial\zeta}-H'\frac{\partial p_2}{\partial\eta}\right]+O(Re_x^{-1})+\left(\frac{1-n}{n+1}\right)2\left(U_\zeta-H'U_\eta\right)\\
&+\left(\frac{1-n}{n+1}\right)\zeta\left[\frac{2n}{n+1}\left(U^2-1\right)-\Phi U_\eta-\Psi\left(U_\zeta-H'U_\eta\right)\right]-\left[1+\left(H'\right)^2\right]\Psi_{\eta\eta}\\
&-\Psi_{\zeta\zeta}+2H'\Psi_{\eta\zeta}+H''\Psi_\eta
\end{aligned}\tag{A.3.7}$$

respectively. Simplifying and ignoring terms which are $O(Re_x^{-1})$ gives

$$\begin{aligned}
&-\left(\eta+H\right)\left(\frac{1-n}{n+1}\right)^2U^2+\left(\Phi-H'\Psi\right)\Phi_\eta+\Psi\Phi_\zeta\\
=&\frac{1}{2}\frac{\partial p_2}{\partial\eta}+\left(\frac{1-n}{n+1}\right)2U_\eta+\left(\eta+H\right)\left(\frac{1-n}{n+1}\right)\frac{2n}{n+1}\left(U^2-1\right)\\
&-\left[1+\left(H'\right)^2\right]\Phi_{\eta\eta}-\Phi_{\zeta\zeta}+2H'\Phi_{\eta\zeta}+H''\Phi_\eta
\end{aligned}\tag{A.3.8}$$

and

$$\begin{aligned}
&-\zeta\left(\frac{1-n}{n+1}\right)^2U^2+\left(\Phi-H'\Psi\right)\Psi_\eta+\Psi\Psi_\zeta\\
=&\frac{1}{2}\left[\frac{\partial p_2}{\partial\zeta}-H'\frac{\partial p_2}{\partial\eta}\right]+\left(\frac{1-n}{n+1}\right)2\left(U_\zeta-H'U_\eta\right)+\zeta\left(\frac{1-n}{n+1}\right)\frac{2n}{n+1}\left(U^2-1\right)\\
&-\left[1+\left(H'\right)^2\right]\Psi_{\eta\eta}-\Psi_{\zeta\zeta}+2H'\Psi_{\eta\zeta}+H''\Psi_\eta
\end{aligned}\tag{A.3.9}$$

Differentiating (A.3.8) with respect to z^* and subtracting the derivative of (A.3.9) with respect to y^* the terms involving the pressure p_2 are eliminated. Then defining the streamwise vorticity function

$$\Theta=\Psi_\eta-\Phi_\zeta+H'\Phi_\eta,\tag{A.3.10}$$

yields

$$\begin{aligned}
&\left[1+\left(H'\right)^2\right]\Theta_{\eta\eta}+\Theta_{\zeta\zeta}-2H'\Theta_{\eta\zeta}-H''\Theta_\eta=\frac{2(1-n)}{(n+1)}\left[\zeta UU_\eta\right.\\
&\left.-\left(\eta+H\right)U\left(U_\zeta-H'U_\eta\right)\right]-\Phi\Theta_\eta-\Psi\left(\Theta_\zeta-H'\Theta_\eta\right)-\frac{2}{n+1}U\Theta.
\end{aligned}\tag{A.3.11}$$

The equations (A.1.5), (A.2.4), (A.3.10) and (A.3.11) form our governing system.

Appendix B

Matching to the outer flow

An increase in the streamwise flow is expected in the region close to the short-scale variation. This increased mass flux must come from outside the short-scale region either from the base flow boundary layer on the plate or from the free-stream flow. The short-scale variation in the plate causes a correction to the outer potential flow which is seen as a line source in the outer length scale. We shall determine the form of this correction and how this affects the far-field boundary conditions for the inner boundary layer solution.

In the outer inviscid region a dimensionless velocity potential $\phi(x, y, z)$ is sought where ϕ and (x, y, z) are made dimensionless with respect to some length scale L^*. Since the flow is incompressible $\nabla \cdot \mathbf{u} = 0$ and since the flow is also inviscid, and thus irrotational, it follows that $\nabla \times \mathbf{u} = 0$. The velocity potential is defined such that $\mathbf{u} = \nabla\phi$ so it follows, using the incompressibility condition, that

$$\nabla \cdot (\nabla\phi) = \nabla^2\phi = 0. \tag{B.0.1}$$

So the velocity potential satisfies Laplace's equation subject to a condition on $y = 0$ due to the boundary layer. There is a transverse flow produced by the boundary layer on $y = 0$ so since the inner and outer solution must match at the edge of the boundary layer it follows that, in dimensional coordinates,

$$\left.\frac{\partial\phi^*}{\partial y^*}\right|_{y^*\to 0, x^*>0} = \left(\frac{n+1}{2}\right)^{\frac{1}{2}} U_\infty^* F(x^*) Re_l^{-\frac{1}{2}} V(\zeta, \eta)\Big|_{\eta\to\infty} \tag{B.0.2}$$

where $Re_l^{-\frac{1}{2}} = (\nu^*/x^* U_\infty^* F(x^*))^{1/2}$. Non-dimensionalising using the freestream velocity

U^*_∞ and the length scale L^* gives

$$\left.\frac{\partial\phi}{\partial y}\right|_{y\to 0,x>0} = \left(\frac{n+1}{2}\right)^{\frac{1}{2}} x^n Re_l^{-\frac{1}{2}} V(\eta,\zeta)\Big|_{\eta\to\infty}$$
$$= \left(\frac{n+1}{2}\right)^{\frac{1}{2}} Re^{-\frac{1}{2}} x^{\frac{n-1}{2}} \left(v_B + \bar{v}(\zeta,\eta\to\infty)\right), \tag{B.0.3}$$

where v_B is the constant transpiration coefficient due to the base flow boundary layer on a semi-infinite plate and $Re = L^*U^*_\infty/\nu^* = Re_l x^{-(n+1)}$ is the global Reynolds number. The $\bar{v}$ transpiration term is an additional unknown transverse velocity.

Let the outer velocity potential be decomposed into a potential flow, a two-dimensional base flow boundary layer correction and an extra three-dimensional contribution due to the additional spanwise boundary layer flow:

$$\phi(x,y,z) = \frac{1}{n+1}x^{n+1} + \phi_B(x,y) + \bar{\phi}(x,y,z). \tag{B.0.4}$$

The correction due to the short-scale spanwise forcing $\bar{\phi}$ is of interest, for which a Green's function solution is sought. Consider the Neumann boundary-value problem for Laplace's equation in the domain defined by $V = \{x \geq 0, y \geq 0, -\infty < z < \infty\}$ given by

$$\nabla^2\bar{\phi} = \frac{\partial^2\bar{\phi}}{\partial x^2} + \frac{\partial^2\bar{\phi}}{\partial y^2} + \frac{\partial^2\bar{\phi}}{\partial z^2} = 0 \quad \text{in} \quad V, \tag{B.0.5a}$$

with

$$\frac{\partial\bar{\phi}}{\partial\mathbf{n}} = \frac{\partial\bar{\phi}}{\partial y} = f = \left(\frac{n+1}{2}\right)^{\frac{1}{2}} Re^{-\frac{1}{2}} x^{\frac{n-1}{2}} \bar{v}(\zeta,\eta\to\infty) \quad \text{on} \quad S, \tag{B.0.5b}$$

where $S = \{y = 0, x \geq 0, -\infty < z < \infty\}$.

Method of images

In order to solve our boundary value problem (B.0.5) in an open region V, with some conditions on the boundary S, a Green's function G is sought such that, in V

$$G(\mathbf{x},\boldsymbol{\xi}) = G_1(\mathbf{x},\boldsymbol{\xi}) + G_2(\mathbf{x},\boldsymbol{\xi}) \tag{B.0.6}$$

where $\nabla^2 G_1 = -\delta(\mathbf{x}-\boldsymbol{\xi})$ (Dirac delta function) and $\nabla^2 G_2 = 0$. The Green's function G_1 does not depend on the boundary conditions and so is the same for all problems involving Laplace's equation. It is necessary to find the function G_2 which satisfies

$$\nabla^2 G_2 = 0 \quad \text{in} \quad V \tag{B.0.7a}$$

with

$$\frac{\partial G_2}{\partial \mathbf{n}} = -\frac{\partial G_1}{\partial \mathbf{n}} \quad \text{on} \quad S \tag{B.0.7b}$$

for Neumann boundary conditions [39].

For this problem the free-space function G_1 is the standard Green's function for the Laplace operator

$$G_1(\mathbf{x}, \boldsymbol{\xi}) = -\frac{1}{4\pi|\mathbf{x} - \boldsymbol{\xi}|} = -\frac{1}{4\pi\sqrt{(x-\xi_1)^2 + (y-\xi_2)^2 + (z-\xi_3)^2}}. \tag{B.0.8}$$

Then for the function G_2 it follows that

$$G_2(\mathbf{x}, \boldsymbol{\xi}) = -\frac{1}{4\pi\sqrt{(x-\xi_1)^2 + (y+\xi_2)^2 + (z-\xi_3)^2}}, \tag{B.0.9}$$

note that

$$\begin{aligned}\frac{\partial G}{\partial y} = \frac{\partial G_1}{\partial y} + \frac{\partial G_2}{\partial y} =& \frac{y-\xi_2}{4\pi\left((x-\xi_1)^2 + (y-\xi_2)^2 + (z-\xi_3)^2\right)^{\frac{3}{2}}} \\ &+ \frac{y+\xi_2}{4\pi\left((x-\xi_1)^2 + (y+\xi_2)^2 + (z-\xi_3)^2\right)^{\frac{3}{2}}}\end{aligned} \tag{B.0.10}$$

therefore

$$\left.\frac{\partial G}{\partial y}\right|_{y=0} = 0. \tag{B.0.11}$$

The solution of the Neumann boundary value problem for Poisson's equation $\nabla^2\bar{\phi} = F$ in V with $\frac{\partial \phi}{\partial \mathbf{n}} = f$ on S is

$$\bar{\phi}(\boldsymbol{\xi}) = -\int_V GF\mathrm{d}V + \int_S Gf\mathrm{d}S + \frac{1}{|V|}\int_V \bar{\phi}\mathrm{d}V. \tag{B.0.12}$$

In this case $F = 0$ and $|V| \to \infty$ therefore the solution is given by

$$\bar{\phi}(\xi_1, \xi_2, \xi_3) = \int_S Gf\mathrm{d}S. \tag{B.0.13}$$

On the surface at $y = 0$ the Green's function is

$$G(x, 0, z, \xi_1, \xi_2, \xi_3) = -\frac{1}{2\pi\sqrt{(x-\xi_1)^2 + \xi_2^2 + (z-\xi_3)^2}}, \tag{B.0.14}$$

this means that the solution is given by

$$\bar{\phi}(\xi_1, \xi_2, \xi_3) = -\frac{1}{2\pi}\int_0^\infty \int_{-\infty}^\infty \frac{\left(\frac{n+1}{2}\right)^{\frac{1}{2}} Re^{-\frac{1}{2}} x^{\frac{n-1}{2}} \bar{v}(\zeta, \eta \to \infty)}{\sqrt{(x-\xi_1)^2 + \xi_2^2 + (z-\xi_3)^2}}\mathrm{d}z\mathrm{d}x. \tag{B.0.15}$$

Relabelling in terms of the original variables gives

$$\bar{\phi}\,(x,y,z) = -\frac{1}{2\pi}\int_{\xi_1=0}^{\infty}\int_{\xi_3=-\infty}^{\infty}\frac{\left(\frac{n+1}{2}\right)^{\frac{1}{2}}Re^{-\frac{1}{2}}x^{\frac{n-1}{2}}\bar{v}(\zeta,\eta\to\infty)}{\sqrt{(x-\xi_1)^2+y^2+(z-\xi_3)^2}}\mathrm{d}\xi_3\mathrm{d}\xi_1. \tag{B.0.16}$$

where $\bar{\zeta} = \xi_3((n+1)/2)^{1/2}Re^{1/2}x^{(n-1)/2}$. Using the $\bar{\zeta}$ definition it follows that

$$\bar{\phi}\,(x,y,z) = -\frac{1}{2\pi Re}\int_{\xi_1=0}^{\infty}\int_{\bar{\zeta}=-\infty}^{\infty}\frac{\bar{v}(\bar{\zeta},\eta\to\infty)}{\sqrt{(x-\xi_1)^2+y^2+\left(z-\bar{\zeta}\left(\frac{2x^{1-n}}{(n+1)Re}\right)^{\frac{1}{2}}\right)^2}}\mathrm{d}\bar{\zeta}\mathrm{d}\xi_1. \tag{B.0.17}$$

The transpiration $\bar{v}$ is a function of the short scale ζ so in the outer flow this transpiration is seen as a volume flux from the half-line $x > 0$, $y = z = 0$. Since $\xi_3 = \bar{\zeta}(2x^{1-n})^{1/2}/\left((n+1)Re\right)^{1/2}$ is small for large Reynolds number Re it is possible to expand about $\xi_3 = 0$ such that

$$\frac{1}{\sqrt{(x-\xi_1)^2+y^2+(z-\xi_3)^2}} = \frac{1}{\sqrt{(x-\xi_1)^2+y^2+z^2}} + \ldots. \tag{B.0.18}$$

So to leading order

$$\bar{\phi}\,(x,y,z) \sim -\frac{M}{2\pi Re}\int_{\xi_1=0}^{\infty}\frac{1}{\sqrt{(x-\xi_1)^2+y^2+z^2}}\mathrm{d}\xi_1. \tag{B.0.19a}$$

where

$$M = \int_{\bar{\zeta}=-\infty}^{\infty}\bar{v}(\bar{\zeta},\eta\to\infty)\mathrm{d}\bar{\zeta} \tag{B.0.19b}$$

is a measure of the flow from the line source/sink. Since the velocity potential is only defined up to some additive constant it follows that

$$\bar{\phi}\,(x,y,z) \sim -\frac{M}{2\pi Re}\int_{\xi_1=0}^{l}\frac{1}{\sqrt{\xi_1^2-2x\xi_1+r^2}}\mathrm{d}\xi_1 + C \tag{B.0.20}$$

where $r = \sqrt{x^2+y^2+z^2}$, $l \to \infty$ and C is a constant. If the constant is given by $C = (M/2\pi Re)\log(2l)$ then evaluating the integral (B.0.20) gives

$$\bar{\phi} \sim \frac{M}{2\pi Re}\log(r-x) + \frac{M}{2\pi Re}\log\left(\frac{2l}{\sqrt{l^2-2xl+r^2}+l-x}\right). \tag{B.0.21}$$

Taking the limit as $l \to \infty$, keeping $r \ll l$, gives the leading order correction to the velocity potential

$$\bar{\phi} \sim \frac{M}{2\pi Re}\log\left(\sqrt{x^2+y^2+z^2}-x\right) \tag{B.0.22}$$

which is equivalent to the velocity potential for a line source/sink [4].

So for the full velocity potential

$$\phi \sim \frac{1}{n+1}x^{n+1} + \phi_B + \frac{M}{2\pi Re}\log\left(\sqrt{x^2+y^2+z^2} - x\right), \tag{B.0.23}$$

hence for the velocity components in the y and z directions

$$\frac{\partial\phi}{\partial y} \sim \frac{\partial\phi_B}{\partial y} + \frac{M}{2\pi Re}\left(\frac{y}{x^2+y^2+z^2-x\sqrt{x^2+y^2+z^2}}\right), \tag{B.0.24a}$$

$$\frac{\partial\phi}{\partial z} \sim \frac{M}{2\pi Re}\left(\frac{z}{x^2+y^2+z^2-x\sqrt{x^2+y^2+z^2}}\right). \tag{B.0.24b}$$

Then for $y, z \ll x$

$$\sqrt{x^2+y^2+z^2} \sim x + \frac{y^2+z^2}{2x} + O(x^{-3}), \tag{B.0.25}$$

using this result the velocity components in the y and z directions are given by

$$\frac{\partial\phi}{\partial y} \sim \frac{\partial\phi_B}{\partial y} + \frac{M}{\pi Re}\left(\frac{y}{y^2+z^2}\right), \tag{B.0.26a}$$

$$\frac{\partial\phi}{\partial z} \sim \frac{M}{\pi Re}\left(\frac{z}{y^2+z^2}\right), \tag{B.0.26b}$$

for $y, z \ll x$. The terms of order Re^{-1} are typically small in most of the outer flow except near the narrow gap at $y = z = 0$. Using this form for the outer flow velocity components gives a more accurate description of the far-field conditions for the boundary layer flow.

Appendix C

Three-dimensional alternative solution

For the three-dimensional alternative to the Falkner-Skan family of solutions a solution of the system (1.4.1) may be suggested in the form

$$\begin{aligned} U_B &= F'(\eta), \\ \Phi_B &= F(\eta) + (2-\beta)G(\eta), \\ \Psi_B &= (1-\beta)F'(\eta) - (2-\beta)G'(\eta), \\ \Theta_B &= (1-\beta)F''(\eta) - (2-\beta)G''(\eta). \end{aligned} \tag{C.0.1}$$

Here the function $G(\eta)$ provides the three-dimensionality and when G and its derivatives are exactly zero the two-dimensional Falkner–Skan solution (1.4.3) is recovered. The first two equations (1.4.1a) and (1.4.1b) are satisfied trivially and the streamwise momentum equation (1.4.1c) becomes

$$F''' + [F + (2-\beta)G]\,F'' + \beta\left[1 - (F')^2\right] = 0. \tag{C.0.2}$$

The Θ_B equation (1.4.1d) may be written as

$$\begin{aligned} F'''' + [F + (2-\beta)G]F''' + [F' + (2-\beta)G']\,F'' + 2\beta F'F'' = \\ \left(\frac{2-\beta}{1-\beta}\right)\{G'''' + [F + (2-\beta)G]\,G''' + 2(1-\beta)G'F'' \\ +(1-\beta)F'G'' + (2-\beta)F'G'' - (2-\beta)G'G''\}\,. \end{aligned} \tag{C.0.3}$$

Using the derivative of (C.0.2) and rearranging the Θ_B equation becomes

$$(G''')' + ([F + (2-\beta)G]\,G'')' - (2-\beta)\left((G')^2\right)' + 2(1-\beta)\,(G'F')' = 0. \tag{C.0.4}$$

Which upon integration may be written as

$$G''' + [F + (2-\beta)G]\, G'' - (2-\beta)\,(G')^2 + 2(1-\beta)G'F' + c = 0. \tag{C.0.5}$$

where c is an arbitrary constant. Evaluating this as $\eta \to \infty$ it follows that $c = 0$ then (C.0.2) and (C.0.5) form a system of third order equations given by

$$F''' + [F + (2-\beta)G]\, F'' + \beta\left[1 - (F')^2\right] = 0, \tag{C.0.6a}$$

$$G''' + [F + (2-\beta)G]\, G'' + [2(1-\beta)F' - (2-\beta)G']\, G' = 0, \tag{C.0.6b}$$

subject to the boundary conditions $F(0) = -K_B$, $F'(0) = G(0) = G'(0) = 0$ and $F'(\eta) \to 1$, $G'(\eta) \to 0$ as $\eta \to \infty$. This form of the base flow equations (1.4.1) emphasises the difference between two and three-dimensional solutions and shows agreement with the formulation given by Ridha (2005) [57]. Rewriting the equations in this form also makes it easier to converge to the three-dimensional solution when solving the equations numerically. The three-dimensional equations (C.0.6) are still solved by the two-dimensional solution so when solving the equations (C.0.6) numerically it is still important to check whether the calculations have converged to the two or three-dimensional solution. The Falkner-Skan solution (1.4.3) and the three-dimensional alternative (C.0.6) provide solutions to the system (1.4.1) which describes the base flow subject to a transpiration and pressure gradient.

C.1 Shear stress

The shear stress on the surface of a plate relates to the friction drag acting on the plate and as such is an important measure of a boundary-layer flow. Also for flow separation it is required that the surface shear stress is zero, so this measure is also useful for predicting flow separation. The surface shear stress is given by $U'_B(\eta = 0) = F''(0)$ and is function of both K_B and β.

For the alternative solution, as shown in figure C.1.1, when the blowing exceed the critical value $K_B \approx 1.18$ only one solution exists whit $\beta > 0$ and no solutions exist with $\beta \leq 0$. At this critical value the solutions becomes singular with the dimensionless wall shear approaching zero and the displacement thickness approaching infinity. In the limit of large blowing a asymptotic expansion of the Falkner-Skan solution can

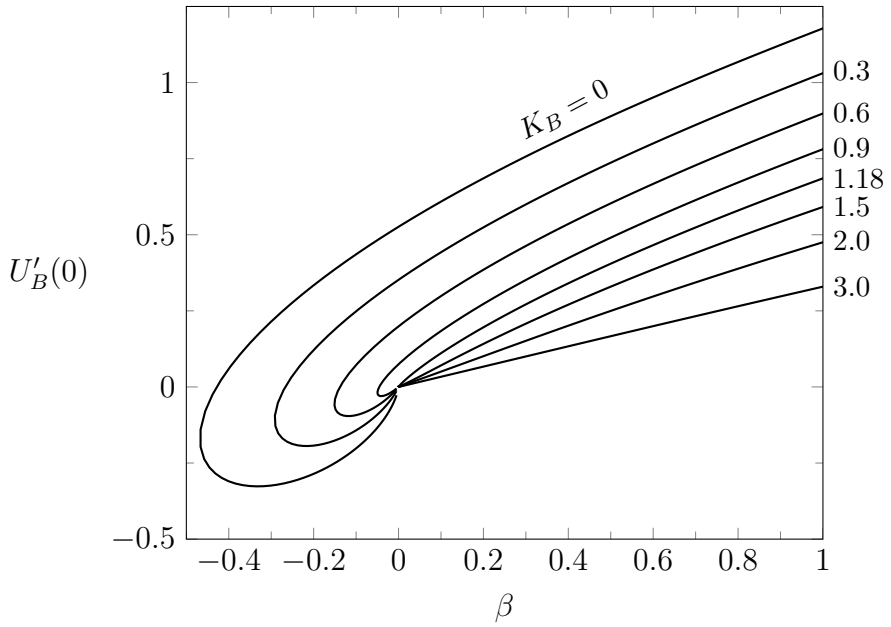

Figure C.1.1: Relation between the scaled shear at the plate $U'_B(\eta = 0)$ and the dimensionless base flow injection amplitude K_B for the alternative solution with Hartree parameter β.

be constructed, Kubota & Fernandez (1968) [47] showed that the leading order wall shear is given by $U'_B(0) \sim \beta/K_B$. This analysis may be adapted in order to find the leading order wall shear for the three-dimensional alternative solution in the limit of large blowing.

Take the alternative solution (C.0.6) with the boundary conditions $F(0) = -K_B$, $F'(0) = G(0) = G'(0) = 0$ and $F'(\eta) \to 1$, $G'(\eta) \to 0$ as $\eta \to \infty$ in the limit $K_B \to \infty$. It is convenient to work in variables defined by

$$Z \equiv (F')^2, \quad X \equiv F + (2 - \beta)G, \tag{C.1.1}$$

such that

$$\frac{\mathrm{d}}{\mathrm{d}\eta} = \frac{\mathrm{d}F}{\mathrm{d}\eta}\frac{\mathrm{d}X}{\mathrm{d}F}\frac{\mathrm{d}}{\mathrm{d}X} = F'\frac{\mathrm{d}}{\mathrm{d}X} = Z^{\frac{1}{2}}\frac{\mathrm{d}}{\mathrm{d}X}. \tag{C.1.2}$$

Then equation (C.0.6a) becomes

$$Z^{\frac{1}{2}}\frac{\mathrm{d}^2 Z}{\mathrm{d}X^2} + X\frac{\mathrm{d}Z}{\mathrm{d}X} + 2\beta\,(1 - Z) = 0 \tag{C.1.3}$$

with boundary conditions $Z(-K_B) = 0$ and $Z(\infty) = 1$. For the inner region, near the wall, a new independent variable $\tilde{X} = X/K_B = \epsilon^{1/2}X$ is introduced. Using this new scaled variable (C.1.3) becomes

$$\epsilon Z^{\frac{1}{2}}\frac{\mathrm{d}^2 Z}{\mathrm{d}\tilde{X}^2} + \tilde{X}\frac{\mathrm{d}Z}{\mathrm{d}\tilde{X}} + 2\beta\,(1 - Z) = 0 \tag{C.1.4}$$

Table C.1: $U_B'(0)$ for various values of K_B with $\beta = 0.5$

K_B	Falkner-Skan	Alternative	β/K_B
0.5	0.659387	0.645441	1
1.0	0.460442	0.457719	0.5
1.5	0.329656	0.329468	0.33333
2.0	0.249789	0.249786	0.25
2.5	0.199994	0.199994	0.2
3.0	0.166667	0.166667	0.166667

with boundary conditions $Z(-1) = 0$ and $Z(\infty) = 1$. The inner solution is valid for fixed $\tilde{X}$ and $\epsilon \to 0$. The variable Z is expanded as

$$Z(X;\epsilon) = \tilde{Z}_0(\tilde{X}) + \epsilon\tilde{Z}_1(\tilde{X}) + \dots . \tag{C.1.5}$$

If the series (C.1.5) is inserted into (C.1.4) a power series in ϵ is obtained which must vanish identically in ϵ. At leading order

$$\tilde{X}\frac{\mathrm{d}\tilde{Z}_0}{\mathrm{d}\tilde{X}} + 2\beta(1 - \tilde{Z}_0) = 0 \tag{C.1.6}$$

with the boundary condition $\tilde{Z}_0(-1) = 0$ (the boundary condition as $\tilde{X} \to \infty$ is abandoned). The ODE (C.1.6) is separable and upon integration it is found that its solution is given by $\tilde{Z}_0 = 1 - (-\tilde{X})^{2\beta}$. In order to determine the shear stress at the wall note that

$$F''(\eta) = \frac{1}{2}\frac{\mathrm{d}Z}{\mathrm{d}X} = \frac{1}{2}\epsilon^{\frac{1}{2}}\frac{\mathrm{d}Z}{\mathrm{d}\tilde{X}} = \frac{1}{2}\epsilon^{\frac{1}{2}}\left(\frac{\mathrm{d}\tilde{Z}_0}{\mathrm{d}\tilde{X}} + \dots\right). \tag{C.1.7}$$

So near the wall

$$F''(\eta) \sim \frac{\beta}{K_B}\left(-\tilde{X}\right)^{2\beta} + O\left(\epsilon^{\frac{3}{2}}\right) \tag{C.1.8}$$

where $\tilde{X}(\eta) = X(\eta)/K_B = (F(\eta) + (2-\beta)G(\eta))/K_B$. So at $\eta = 0$ it is found that to leading order $F''(0) = U_B'(0) \sim \beta/K_B$. This means that, in the limit of large blowing $K_B \to \infty$, the wall shear at the surface is the same for both the Falkner–Skan and the three-dimensional alternative solutions.

In table C.1 numerically calculated values of $U_B'(0)$ are shown for various values of K_B at a fixed value of β for both solutions. It can be seen that for large values of K_B the shear stress at the wall is well approximated by $U_B'(0) = \beta/K_B$. Also for larger values of K_B the shear stress at the wall for the Falkner–Skan solution and the

alternative solution become increasingly similar. Plotting the solution profiles for the base flow variables, $(\Phi_B, \Psi_B, U_B, \Theta_B)$ and selected derivatives, this similarity between the two solutions is not only true for the wall shear but for the entire solution profile. For large values of K_B the Falkner–Skan solution and the three-dimensional alternative solution become indistinguishable.